



HAL
open science

Development and application of new NMR methods for paramagnetic inorganic materials

Kevin Sanders

► **To cite this version:**

Kevin Sanders. Development and application of new NMR methods for paramagnetic inorganic materials. Theoretical and/or physical chemistry. Université de Lyon, 2018. English. NNT : 2018LY-SEN041 . tel-02087299

HAL Id: tel-02087299

<https://theses.hal.science/tel-02087299>

Submitted on 2 Apr 2019

HAL is a multi-disciplinary open access archive for the deposit and dissemination of scientific research documents, whether they are published or not. The documents may come from teaching and research institutions in France or abroad, or from public or private research centers.

L'archive ouverte pluridisciplinaire **HAL**, est destinée au dépôt et à la diffusion de documents scientifiques de niveau recherche, publiés ou non, émanant des établissements d'enseignement et de recherche français ou étrangers, des laboratoires publics ou privés.



N° National de Thèse : 2018LYSEN041

THESE de DOCTORAT DE L'UNIVERSITE DE LYON
opérée par
l'Ecole Normale Supérieure de Lyon
Ecole Doctorale 206
Ecole Doctorale de Chimie (Chimie, Procédée, Environnement)

Spécialité de doctorat : Résonance Magnétique Nucléaire

Discipline : Chimie

Présentée et soutenue publiquement le 28/09/2018

par Monsieur **Kevin J. SANDERS**

**Development and application of new NMR methods for paramagnetic
inorganic materials**

Développement et application de nouvelles méthodes de RMN pour les matériaux inorganiques
et paramagnétiques

Devant le jury composé de :

Ulla Gro NIELSEN	Professeure <i>Syddansk Universitet</i>	Rapporteure
Arno KENTGENS	Professeur <i>Radboud Universiteit Nijmegen</i>	Rapporteur
Chloé THIEULEUX	Directrice de recherche CNRS <i>C2P2, Villeurbanne</i>	Examinatrice
Dominique MASSIOT	Directeur de recherche CNRS <i>CEMHTI-CNRS, Orléans</i>	Examineur
Andrew J. PELL	Professeur <i>Stockholms Universitet</i>	Examineur
Guido PINTACUDA	Directeur de recherche CNRS <i>ISA, Lyon</i>	Directeur de thèse

Acknowledgements

Before getting to the rest, I would like to start by thanking the reviewers of this thesis, Prof. Ulla Gro Nielson and Prof. Dr. Arno Kentgens, for being willing to and having had the patience to read (and perhaps re-read) this thesis and evaluate it, and also to the members of the jury, Dr. Chloé Thieuleux, Dr. Dominique Massiot, and Prof. Andrew J. Pell, for agreeing to take part in the defense committee.

The story of my Ph.D. began on the evening of Wednesday April 17th, 2013, during the ENC conference in Asilomar, California. My advisor at the time, Prof. Philip Grandinetti, was hosting a party for current and former students at the legendary "Casa Linda", together with his housemates for the week, Profs. Brad Chmelka, Dimitris Sakellariou, and Lyndon Emsley. Little did I know that the house would come to be filled with numerous other pillars of the field, and I, an insignificant Masters student, eventually receded to the relative safety of a seat on the couch towards the back of the room. Naturally, I soon found myself seated between Prof. Clare P. Grey and Lyndon, and became involved in a scientific conversation far, far over my head. After some minutes of discussion and maybe a glass or two of wine, Lyndon told me that there was a Ph.D. position available in his lab to study paramagnetic complexes, and encouraged me to apply. I took some time to consider whether it was a good fit for me, whether I saw myself living in a foreign country where I didn't speak the language, and whether I should tell my mom about it. Eventually I decided I was up for the adventure (and yes, I did tell my mother), had an interview over Skype with Guido, Lyndon, and Andy, moved to Lyon a few months later, and skipping a few steps along the way, I now find myself at my desk writing these acknowledgements with no regrets. Truly, this has been the experience of a lifetime, so huge thanks to Phil for the invitation to the party, and, more seriously, for all of his help, guidance, and enlightening discussions over the years. Many thanks to Lyndon for the opportunity to work in such an amazing environment as the CRMN, and for the helpful pushes and prods along the way, well or ill-received, which helped me grow to who I am today.

I would like to take a moment to thank my advisor, Guido, for having taken me on as a grad student and shown me so much about what it means to do good science. Truly, you have been an inspiration, especially with your ability to look at a seemingly sad scientific story at a different angle, and magically spin it in to an exciting story. One may call this the magic-angle story spinning technique. Seriously though, thank you for all of your guidance and patience with me. Sometimes we have had our differences and I know that on more than one occasion it may have been hard to work with me, but I appreciate that you never lost faith in me and always pushed me towards the right direction when I would make mistakes, get off track, or lose optimism in my work. I also really appreciate all of the things outside the lab, like generous opportunities

to travel for conferences, frequent dinner parties, and numerous other flexibilities which made working for you here in Lyon truly a pleasure. Thank you so much.

During my time in the pNMR Marie Curie-Skłodowska project, I had the immense opportunity to visit two great institutions during my two "secondments". First, I spent two months in Cambridge in the group of Prof. Clare P. Grey learning about battery materials and expanding my knowledge of NMR, and this collaboration led to the results given in Chapter 2. Many thanks to Clare for this amazing experience. Second, I spent two months in Karlsruhe, Germany working with Sebastian Wegner and Frank Engelke during the prototype stage of the 0.7 mm MAS probe. I was given access to the full suite of available equipment and knowledge at the Bruker facility, and this led in part to the results given in Chapters 2 and 3. I had an excellent experience there, so many thanks to Sebastian and Frank. Andy Pell has served as a mentor in so many ways since the beginning, when he came to my desk, dropped a stack of classic papers on it, and told me to read them because "it's good for your soul." He's been an endless source of knowledge and support since then, and it's fitting that he is serving on my jury, as he probably knows more than anyone else what I do and do not know. Cheers, Andy. I have had the pleasure of taking part in many collaborative projects during the course of my Ph.D. work. I would especially like to thank Prof. Christophe Copéret for the numerous discussions we've had in the last few years, especially the work on organolanthanide complexes given in Chapter 4. His student, (now Dr.) Florian Allouche, has been a great collaborator and friend as well. I would also like to thank Dr. Pierre-Alain Breuil and the rest of the people at IFPEN, especially Dr. Benjamin Burcher, for all the help with the Fe⁽⁰⁾ complexes. This has turned in to a very exciting project and I am very excited to see where it leads.

All of the past and current members of the CRMN team have contributed to this thesis, whether directly through collaboration or indirectly through contributing to the ambiance of the CRMN. Particularly, I'd like to thank all the members of Guido's group. Early on, Hugh (along with Judith and Andy) were there to welcome me to Lyon, show me around, and invite me out for friendly extra-curricular activities, and I am happy that we have all remain friends. Cécile Gozlan was amazing to work with, was always there when I needed help, and is so much fun otherwise. Besides being an incredibly smart guy, gifted scientist, and amazing colleague, Andrea Bertarello (lalalaaa) has been and continues to be a wonderful friend, and I'm so happy that my choice to come to Lyon allowed us to meet and become friends. Ladislav has been a superb colleague and great friend, and has helped me substantially in my understanding of paramagnetic shift theory. Thank you to all the rest who have come along the way and made this a great place to work: Adrian, Andrea Pica, Arthur, Daniela, Diane, Jan Blahut, Jan Stanek, Kristaps, Loren, Marta, Tanguy, and Tobias, and to those visitors who came to join us for a time, Henry, Magda, and Ryan. I want to give a special shout out to Cécile Chamignon, David, and Lénaïc, who were always there to help sort out technical problems in the spectrometer hall and chemistry lab. Thanks to all the rest of the CRMN/ISA staff as well: Agnès, Alicia, Anne, Audrey, Bénédicte, Cory, Dorothea, Elodie, Georges, Gilles, Houda, Loïc, Lydie, Manhal, Monu, Moreno, Myriam, Olivier, Pierrick, Ribal, Sachin, Sami, Sylvie, Torsten, and Vanessa D.

Friends and family have contributed immensely to the success of my Ph.D. project by helping me retain my sanity during this tough process. I want to thank all the friends I've made along the way who have made life here in Lyon more pleasant, especially Fany, Roland, and Sonia, and a few institutions that made my time here worth living, notably the staff at Cosy Corner (hi Isa and Justine!), The Beers, Bieristan, Les Fleurs du Malt, and Hopstore. While it has at times been difficult to stay in touch, I want to thank all my friends from Ohio who have gone the extra mile to stay close, especially Dave, Fish, Greg, John, Kevin, Lomanno, Lee, Nick Shay, Schwam, and Watson. My brothers from other mothers, David, Nick Frye, and Ryan, have been my best friends since I was 13 years old and I'm very happy to say that they remain so, and have been an endless source of laughs over the past five or so years that I've been in France. My parents, Jeff and Chris, have been there for me since the beginning, and have been an incredible source of inspiration and support in innumerable ways. Thanks to my sisters, Erin and Sara, and the rest of the immediate family, Joe, Abby, James, and Nora, for the endless fun times we've been able to have despite the fact that I live an ocean away. Thanks also to my aunts, uncles, cousins, and extended family, too numerous to mention here. Finally, the person who has contributed the most to my retention of sanity, especially during the writing process, has been Vanessa. You have been more supportive than I probably deserved, and have always been there to help me deal with stress, find ways to make me feel better in my darkest moments, and laugh at my terrible jokes. *Merci beaucoup chérie.* Much love to all of you for always being there.

Abstract

A precise understanding of the coordination geometry and electronic structure around metal centers in catalysts and battery materials is crucial in order to control these complex systems, modify their behavior, and allow rational design of improved sites. However, such systems are not always amenable for diffraction-based structural determination, and even if they are, obtaining atom-specific electronic structure can only be inferred indirectly from the atomic coordinates. As such, a direct probe of the electronic structure is highly desired.

The aim of the present thesis is the investigation of structural and electronic properties of metal sites in catalysts and battery materials by magic-angle spinning nuclear magnetic resonance (MAS NMR) spectroscopy. MAS NMR is a powerful technique for the investigation of local effects in solid materials, and offers a direct probe of highly resolved electronic structures in paramagnetic solids. However, it suffers from limited sensitivity and resolution for nuclei lying close to a paramagnetic center in general.

We address these limitations by first tackling some of the bottlenecks in the acquisition and interpretation of MAS NMR by developing and applying new methodologies to paramagnetic solids using ultra-fast (60-111) kHz MAS rates. A "toolkit" of suitably designed pulse sequences is assembled for broadband detection and interpretation of paramagnetic shifts in crystalline and non-crystalline solids. The potential of this methodology is explored for the elucidation of local geometry and electronic structure around paramagnetic metal sites in homogeneous and heterogeneous catalysts, and a set of mixed-phase Li-ion battery cathode materials.

We anticipate that the approaches described herein form an essential tool to elucidate many outstanding questions about the structure and function of metal sites in modern chemistry.

Résumé

Une compréhension précise de la géométrie de coordination et de la structure électronique autour d'un ion métallique à l'intérieur des catalyseurs et des matériaux de batteries est essentielle pour contrôler ces systèmes complexes, modifier leur fonctionnement, et permettre la conception logique de sites améliorés. Cependant, la structure de ces systèmes n'est pas toujours accessible par des techniques de diffraction, et même si elle l'est, la structure électronique ne peut alors être déduite qu'indirectement des coordonnées atomiques. De ce fait, il est essentiel d'avoir une sonde directe de la structure électronique.

L'objectif de cette thèse est l'étude des propriétés structurales et électroniques des sites métalliques de catalyseurs et de matériaux de batteries par Résonance Magnétique Nucléaire en rotation à l'angle magique (MAS NMR). La MAS NMR est une technique très performante pour l'étude des effets locaux dans les matériaux à l'état solide et permet de sonder directement la structure électronique des matériaux paramagnétiques à haute résolution. Néanmoins, cette approche souffre d'une pauvre résolution et d'une sensibilité limitée pour les noyaux proches d'un site paramagnétique.

Pour dépasser ces limitations, nous avons levé des verrous dans l'acquisition et l'interprétation de la MAS NMR en développant et appliquant de nouvelles méthodes pour l'étude de solides paramagnétiques basées sur des hautes fréquences de rotation (60-111 kHz MAS). Pour ce faire, un répertoire de séquences d'impulsion a été développé pour la détection et l'interprétation des effets paramagnétiques dans des solides cristallins et non cristallins. Le potentiel de cette méthodologie a été examiné pour l'élucidation de la géométrie locale et de la structure électronique autour des sites paramagnétiques de catalyseurs homogènes ou hétérogènes, et des matériaux de cathodes en phase mixte pour des batteries au Lithium.

Nous voyons dans les méthodes présentées ici, un ensemble d'outils indispensables pour l'élucidation de nombreuses questions de la chimie moderne relatives à la structure et la fonction des sites métalliques.

Contents

Acknowledgements	iii
Abstract	vii
Résumé	ix
Introduction	1
1 Solid-state NMR of paramagnetic molecules	7
1.1 Paramagnetic effects in solid-state NMR	7
1.1.1 Magnetic moments of nuclei and electrons	7
1.1.2 Electron and Nuclear Zeeman Interaction	8
1.1.3 The hyperfine Hamiltonian	10
1.1.4 The Curie spin and magnetic susceptibility	13
1.1.5 Spin-orbit effects and the full PNMR Hamiltonian	15
1.1.6 Paramagnetic relaxation enhancement	16
1.1.7 Line broadening from anisotropic bulk magnetic susceptibility	19
1.2 Magic Angle Spinning	20
1.2.1 Adiabatic pulses in MAS experiments	25
1.3 The experimental PNMR toolkit	35
1.3.1 Perspectives moving forward	42
2 Ultrafast MAS applied to mixed-phase olivine-type LiMPO₄ cathode phases	43
2.1 Introduction	43
2.2 ³¹ P NMR of LiFe _{0.25} Mn _{0.75} PO ₄ at 7.05 T and 111 kHz MAS - a proof of concept	47
2.3 The contribution of Mn ²⁺ to the ³¹ P shift in olivine-type LiMg _x Mn _{1-x} PO ₄	51
2.4 Conclusions and Perspectives	60
3 Low-power broadband NMR under fast MAS conditions	61
3.1 Introduction	61
3.2 Inversion pulses in the high-power and low-power limits	63
3.3 Simultaneous irradiation over multiple sidebands	69
3.4 Low-power broadband NMR of ¹⁴ N	74
3.5 Conclusions	79

4	Solid-state NMR applications to heterogeneous catalytic systems	81
4.1	Introduction	81
4.2	Secondary Interactions in organometallic lanthanide complexes	82
4.2.1	Lu[CH(SiMe ₃) ₂] _{3-x} [O-2,6- <i>t</i> Bu ₂ -C ₆ H ₃] _x molecular complexes	84
4.2.2	Grafting Lu[CH(SiMe ₃) ₂] ₃ on to partially dehydroxylated silica	91
4.3	Molecular organoytterbium complexes	94
4.3.1	Solution-state NMR of Yb[CH(SiMe ₃) ₂] ₃	96
4.3.2	Solid-state NMR of Yb[CH(SiMe ₃) ₂] ₃	96
4.3.3	Point-dipole model of the isotropic shifts	98
4.4	Molecular Ti ³⁺ complexes as a model for surface-supported Ti catalysts	104
4.5	Conclusions and perspectives	108
5	Structural studies of paramagnetic Fe⁽⁰⁾-based homogeneous catalysts	111
5.1	Introduction	111
5.2	Stable 16-ve phosphine-stabilized Fe ⁽⁰⁾ olefin complexes	112
5.2.1	Cyclotrimerization of alkynes	112
5.3	De novo structure of Fe(dipe) ₂ (dvtms)	113
5.3.1	Discussion of the PNMR computational protocol	116
5.4	PNMR as a tool for structural determination of complexes 1-4	117
5.4.1	Geometry and electronic structure of 1	117
5.4.2	Resonance assignments of ¹ H and ¹³ C shifts for 1	119
5.4.3	Quantum chemistry calculation of PNMR shifts of 2 and 3	124
5.4.4	Experimental assignments for complex 2 using 100 kHz MAS methodologies	129
5.4.5	Discussion on the structure of 2	131
5.5	Conclusions and outlook	132
	Conclusions and perspectives	133
	List of publications	137
	List of abbreviations	139
A	Experimental details	141
A.1	Solid-state NMR studies LiMPO ₄ cathode phases (Chapter 2)	141
A.2	Low-power broadband NMR (Chapter 3)	141
A.2.1	SHAP, S ³ AP inversions of ⁶⁷ Li	141
A.2.2	S ³ AP inversion of ¹⁴ N	144
A.3	Solid-state NMR applications to heterogeneous catalytic systems (Chapter 4)	145
A.3.1	Yb	145
A.4	Structural studies of paramagnetic Fe ⁽⁰⁾ -based homogeneous catalysts (Chapter 5)	145
A.4.1	Complex 1	146

A.4.2	Complex 2	146
A.4.3	Complex 3	147
A.4.4	Complex 4	148
B	Computational details	149
B.1	DFT calculations of complex 4	149
B.2	Calculations of complexes 1–3	150
C	Synthesis details for complexes 1-4	151
	Bibliography	153

Introduction

Metal ions are present at the active sites of many catalytic processes that are at the core of modern chemistry. Whether they form defined organometallic molecular species or they are supported on surfaces, they are the principal actors in chemical processes such as olefin polymerization, olefin and alkyne metathesis, hydrogenation, and nanostructure synthesis. They also are the key constituents of versatile materials, e.g., molecular magnets, nanodevices such as engines and magnetic resonance imaging contrast agents. As such, they have a tremendous impact on many fields within industry, energy, environment and life sciences. The paramagnetic materials that are found in electrodes in batteries, or in phosphors for solid-state lighting, play an important role in a range of devices that are instrumental in improving the efficiency of energy conversion, storage and use.

A precise understanding of the coordination geometry and electronic structure around metal centers is of the utmost importance in order to control these complex systems, modify their behavior, and allow rational design of improved sites. For example, the coordination geometry around metal centers in catalysts heavily influences catalytic activity, dilute site defects in luminescent materials affect both the efficiency and color of light emitted by these materials, and the local structure around metal centers in lithium-ion battery cathode materials impacts the dynamics of lithium flow within the materials during charging and discharging.

Diffraction methods such as X-ray crystallography remain the primary tools for determining the structure of crystalline materials. However, this methodology fails when materials do not exhibit long-range order, as is the case, for example, in mixed-phase materials, amorphous solids, or structures on surfaces. Even when high-resolution crystal structures are available, often the nature of the metal ion, its oxidation state, or its coordination geometry are not determined. Moreover the most interesting aspects of metallic activity are caused by the electronic structure at the active site, which unfortunately can only be inferred indirectly from the coordinates of the constituent atoms.

A direct probe of electronic structure is thus highly desired. Nuclear magnetic resonance (NMR) spectroscopy is an alternative experimental approach for the determination of molecular structures, as it does not require long-range order. NMR is a particularly powerful tool for analyzing structures of a large variety of molecules, materials, and complex assemblies like proteins. NMR has been particularly successful for studies of molecules in solution, where rapid tumbling of molecules results in relatively simple spectra consisting of a single narrow isotropic resonance for each unique atomic site. More recently, solid-state NMR has proved an efficient tool for the characterization of micro-crystalline, poorly crystalline or disordered inorganic samples, including diamagnetic organometallic complexes, inorganic frameworks, battery materials,

or systems highly pertinent to many areas of modern biology, such as fibrils and membrane proteins. In combination with techniques like EXAFS and IR, NMR can provide unique insights into the analysis of the mechanism of action of catalysts, the description of solution and surface chemistry processes, and in the characterization of binding.

Paramagnetic centers originate from unpaired electrons that are intrinsic features of many transition and lanthanide metal ions. A paramagnetic center interacts with the surrounding nuclear spins and changes the appearance of the NMR spectrum in several ways, most obviously by altering chemical shifts and increasing relaxation rates. NMR of paramagnetic molecules (paramagnetic NMR, PNMR) thus provides a direct probe of the electronic structures in such important compounds. The changes brought in the spectrum by paramagnetism depend in a well-defined manner on the structure of the molecule, providing a variety of structural restraints. In contrast to diamagnetic data, paramagnetic phenomena provide long-range information due to the large value of the electron magnetic moment (the electron gyromagnetic ratio is 658 times larger than that of the proton).

Coupling between the nuclear magnetic dipoles with the (stochastically fluctuating) magnetic dipoles of the surrounding electrons, called the hyperfine coupling, results principally in (1) very large shifts and shift anisotropies, and (2) dramatic nuclear paramagnetic relaxation enhancements (PRE). In solids, this produces NMR spectra that can span many thousands of ppm, with low resolution due to broad, overlapping resonances with broad manifolds of spinning sidebands under magic-angle spinning (MAS) conditions. This hampers both the critical steps of the acquisition of the NMR experiments and the following spectral assignment and interpretation, hindering the full exploitation of the paramagnetic information.

The problem of low resolution due to sideband overlap could simply be addressed by decreasing the external magnetic field strength, as the anisotropic effects scale linearly with the field; however this approach results in decreased sensitivity in general. An alternative solution is to use faster MAS rotation rates, pushing the sidebands further and further away from the isotropic shifts while concentrating the signal in the fewer remaining bands, increasing sensitivity. The recent development of very fast magic angle spinning (MAS) probes with large RF powers has revolutionized this field. Under very-high MAS (>40 kHz), sensitivity and resolution experience a spectacular enhancement as compared to slower rates, allowing efficient detection of previously unobservable nuclei in highly paramagnetic substances [1–4]. Fast MAS, the use of new irradiation schemes, and often the use of nuclei with low gyromagnetic ratios have provided keys to many of the recent solid-state NMR developments in the study of the atomic-level properties of metal complexes, clusters and magnetic frameworks. For example, new efficient RF irradiation schemes have been introduced for broadband population inversion based on adiabatic pulses under fast MAS in the high-power (short, high-power adiabatic pulses, SHAP [5]) and low-power (single-sideband-selective adiabatic pulses, S3AP [6, 7]) regimes. These pulse elements can be incorporated as building blocks into more complex pulse sequences, so as to

obtain high-resolution correlations on highly paramagnetic compounds. This allowed the extraction of site-specific information from which a molecular structure can be calculated (“paramagnetic NMR crystallography” [8]), and to deduce important electronic information on samples as diverse as battery materials [9], or luminescent phosphors [10]. This progress is of particular interest in the area of chemical catalysis, where to monitor electron spin states and ligand conformations in a given metal center is a key step for understanding and controlling a reaction mechanism. For example, paramagnetic solid-state NMR was used to follow the reactivity of supported Cr(II) centers with CO, which is an established platform for assessing the efficiency of chromium-based systems in the field of olefin polymerization [11].

Despite this recent progress, however, a number of issues remain to be addressed before paramagnetic NMR can become a routine tool for the targets of increasing complexity that keep being profiled by modern research in chemistry and materials science. The objectives of my PhD work have been twofold. On one side, I have addressed some of the key remaining bottlenecks to NMR of paramagnetic solids, as concerns the steps of both acquisition and interpretation of the NMR spectra, notably leveraging the advantages offered by new probes capable of MAS rates higher than 100 kHz and the recent progress in the quantitative quantum-mechanical treatments of the parameters of paramagnetic NMR. On the other side, I have explored the potential of this spectroscopy to elucidate the role of metal centers in key areas of science (*e.g.*, battery materials, homogeneous and heterogeneous catalysis,) trying to broaden the range of information that could be successfully accessed by NMR.

To begin this thesis, I start in Chapter 1 with an overview of the current theory of paramagnetic effects in NMR and experimental methodologies used to observe these effects. In the first section, I give a basic introduction to the quantum mechanical framework giving rise to paramagnetic shifts, and review the underlying physics behind the major observables such as the contact shift, shift anisotropy, PRE, and broadening due to anisotropic bulk magnetic susceptibility. The second section is a review of the recent progress in experimental methods for studying paramagnetic samples. These methods primarily revolve about the use of ever-increasing magic-angle spinning rates to simplify the NMR spectra of paramagnetic molecules. Finally, the current “toolkit” of experimental techniques is introduced, which are used primarily to (1) increase the excitation bandwidth of experiments by the use of broadband swept-frequency pulses, (2) improve resolution by the removal of spinning sidebands, and (3) achieve broadband correlation spectroscopies using very high MAS rates.

Chapter 2 outlines work I have carried out during my Ph.D. studies towards the characterization of local geometries and electronic structures in a class of lithium-ion battery cathode materials, the mixed-phase olivine-type lithium metal (M) phosphates, where $M = \text{Mg}^{(\text{II})}$, $\text{Mn}^{(\text{II})}$, $\text{Fe}^{(\text{II})}$, and $\text{Co}^{(\text{II})}$. These samples exhibit 32 distinct chemical environments for ^{31}P , each with unique anisotropies and large line widths, and as a result resolution is typically very poor. Prior studies using MAS rates of 60 kHz and intermediate magnetic fields [9, 12] relied on 2D methods to remove spinning sidebands in ^{31}P NMR spectra to achieve isotropic resolution in the ^{31}P spectra of these materials and the subsequent determination of the relative contributions of each

metal the to the ^{31}P isotropic shift; however these experiments come with a significant cost: these long pulse sequences result in large intensity biasing due to significant relaxation during the sequences, and without careful optimization, can result in spectral artifacts. On the contrary, I show that the combination of 111 kHz MAS and a lower external magnetic field of 7.05 T (300 MHz) results in 1D ^{31}P spectra exhibiting similar resolution and minimal intensity biasing, in a fraction of the time. This methodology results in the determination of the unique contribution of $\text{Mn}^{\text{(II)}}$ to the isotropic ^{31}P shift of these materials, and by extension, the contribution of $\text{Fe}^{\text{(II)}}$, and $\text{Co}^{\text{(II)}}$ to the ^{31}P shift. The results indicate that the local metal geometry may be affected by cation substitution in these mixed phase materials, contrary to what has been concluded in prior studies.

With the advent of faster MAS capabilities, SHAPs become less efficient due to increasing RF field requirements [13]. A low-power alternative would thus be necessary to achieve efficient broadband excitation at extremely high rotation rates. To attack this problem, Chapter 3 outlines recent work I've carried out to improve the bandwidth and selectivity of a class of broadband swept-frequency pulses by the use of multiple frequency sweeps [14].

In this chapter I show, with combined experimental and simulated results, that an alternative, low-power class of swept-frequency pulses, dubbed single-sideband-selective adiabatic pulses (S^3APs , [6]), are an efficient alternative to SHAPs for MAS studies using 60+ kHz spinning rates. This is especially true for low-gamma spin-1/2 nuclei and spin-1 nuclei, due to the fact that solenoid coils fail to provide sufficiently high RF field strengths at low frequency. Additionally, I explored the possibility of sweeping simultaneously over multiple adjacent bands in order to achieve uniform spatial excitation, which improved upon the performance of a pulse that sweeps over only a single band.

Chapter 4 details work I have carried out in applications geared towards the structural analysis of paramagnetic heterogeneous catalysts by solid-state NMR. The chapter begins with the structural examination of an interesting class of organolanthanide complexes that exhibit 3-center-2-electron (3c-2e) secondary bonding interactions in low-temperature crystal structures. The first section details the structural analysis of diamagnetic organolutetium complexes, where it is shown through 2D and J-resolved NMR spectroscopy that this bonding interaction is preserved at room temperature, and that this structural feature is preserved upon grafting to a silica surface, confirmed by EXAFS spectroscopy [15]. The second section is a follow-up of the previous study on the isostructural paramagnetic organoytterbium complex, which exhibits incredibly large line widths in ^1H , ^{13}C , and ^{29}Si NMR spectra and therefore poses a considerable challenge. Nevertheless, I show by 1D ^{29}Si spectra and 2D ^1H - ^{13}C correlations that the isotropic chemical shifts can be predicted using a point-dipole model, thereby confirming that 3c-2e secondary bonding interactions are also present in the case of the organoytterbium complex. This chapter finishes with a brief section detailing work I have carried out towards using small molecules as "spies" of the oxidation state and coordination geometry of $\text{Ti}^{\text{(III)}}$ in small complexes, with potential applications towards the study of Ziegler-Natta catalysts, for example.

Finally, chapter 5 outlines recent work carried out on the structural study towards the determination of the electronic structure of four low-valent Fe⁽⁰⁾-containing homogeneous catalysts. The subtle changes in structure induced by small changes in the composition of the bidentate P-P ligands of these complexes induce large changes in their reactivity. In particular, one of these complexes was comparatively active in a cyclotrimerization reaction of 3-hexyne, however, its structure was unable to be determined by x-ray diffraction. To establish a structure-activity relationship for this complex, a putative de novo structure was built and minimized by density functional theory (DFT) and validated by the agreement of calculated paramagnetic shifts with broadband experimental spectra obtained using a modest MAS rate of about 30 kHz. I then probed the current capabilities and limitations of state-of-the-art computational and experimental PNMR methodologies by a comprehensive study of three other complexes with known X-ray geometry. Two of these three molecules were found to exhibit relatively good agreement between experimental and computational data, however, one molecule exhibited relatively poor agreement, and this was determined to arise from discrepancies between the X-ray structure and the sample analyzed in the NMR experiments.

I then used methodologies afforded by a rotation rate of 100 kHz to achieve broadband ¹H–¹H correlations and ¹H-detected heteronuclear correlations, which permitted identification of ¹H resonances to specific moieties of ligands around the Fe⁽⁰⁾ center and therefore nearly total experimental resonance assignments. Moreover, it was shown that the ¹H-detected heteronuclear correlation experiment exhibited a sensitivity at least equal to that of the more traditional ¹³C-detected experiment, which opens the door for more complex experimental methodologies, such as 3D correlation methods, and is a promising result for future studies of paramagnetic organometallic molecules of increasing complexity.

Chapter 1

Solid-state NMR of paramagnetic molecules

Paramagnetic centers (*i.e.* metals containing unpaired electrons or radicals) induce large generally anisotropic effects on the NMR spectra of nearby nuclei due to strong coupling to the electrons, whose strong magnetic moment is 658 times larger than ^1H . Accurate measurement of these effects can provide a wealth of information about the coordination geometry around the paramagnetic center and the electronic structure of ligands coordinating the metal [1, 3, 16–19]. Three main effects are introduced by the paramagnetic center on NMR spectra: large isotropic shift dispersions and shift anisotropies, each as large as 1000s of ppm, and significant relaxation enhancement, often leading to nuclear relaxation times on the order of 10s-1000s of μs . The combination of these effects can make acquisition and interpretation of paramagnetic NMR (PNMR) spectra difficult because of a loss of resolution resulting from the broadening of resonances by relaxation and shift anisotropy, and the large necessary excitation bandwidths required to cover a spectral range of potentially many thousands of ppm. Ultrafast magic-angle spinning (MAS) [20, 21] can to a certain extent mitigate these problems with resolution [1, 3, 8, 9, 13] by minimizing effects caused by the manifestation of anisotropic interactions in NMR spectra of solids, and the interpretation of these effects is greatly aided by the use of DFT or first-principles calculations of the relevant interactions [3, 9, 12, 18, 19, 22]. This chapter sets out to review the basics of the underlying theory behind these effects, and then describe current state-of-the-art experimental methods used in solid-state NMR to probe paramagnetic effects in solid samples.

1.1 Paramagnetic effects in solid-state NMR

1.1.1 Magnetic moments of nuclei and electrons

In the quantum mechanical framework, objects with a non-zero spin quantum number inherently possess a magnetic dipole moment, μ , which can be related to the spin angular momentum \mathbf{I} , by the expression:

$$\mu_I = \hbar\gamma_I\mathbf{I}, \quad (1.1)$$

where \hbar is the reduced Planck's constant and γ_I is the nuclear gyromagnetic ratio in units of $\text{rad} \cdot \text{s}^{-1} \cdot \text{T}^{-1}$. An analogous expression can be derived for the electron magnetic moment:

$$\begin{aligned}\boldsymbol{\mu}_S &= \hbar\gamma_S\mathbf{S} \\ &= -\mu_B g_e \mathbf{S},\end{aligned}\tag{1.2}$$

where γ_S is the electron gyromagnetic ratio and \mathbf{S} is the electron spin angular momentum. The second expression is more commonly employed in the electron paramagnetic resonance (EPR) community, where $\mu_B = 9.274 \times 10^{-24} \text{ J} \cdot \text{T}^{-1}$ is the Bohr magneton and $g_e = 2.0023$ is the free electron g -factor, and the negative sign indicates that the electron dipole moment is anti-parallel with its spin angular momentum vector.

1.1.2 Electron and Nuclear Zeeman Interaction

The interaction of a magnetic moment, $\boldsymbol{\mu}$, and the external magnetic field, \mathbf{B}_0 , gives rise to an energy of interaction, E , of

$$E = -\mathbf{B}_0 \cdot \boldsymbol{\mu}.\tag{1.3}$$

Consequently, the Hamiltonian describing this interaction is the same expression, with the vector quantity $\boldsymbol{\mu}$ replaced by equivalent vector operator $\hat{\boldsymbol{\mu}}$. This forms the expression for the nuclear Zeeman Hamiltonian, which can be expressed in terms of the spin angular momentum operator, $\hat{\mathbf{I}}$, using equation 1.1:

$$\begin{aligned}\hat{\mathcal{H}}_{IZ} &= -\mathbf{B}_0 \cdot \hat{\boldsymbol{\mu}} \\ &= -\hbar\gamma_I \mathbf{B}_0 \cdot \hat{\mathbf{I}}\end{aligned}\tag{1.4}$$

In much the same way, the electron Zeeman Hamiltonian can be determined to be:

$$\begin{aligned}\hat{\mathcal{H}}_{SZ} &= -\mathbf{B}_0 \cdot \hat{\boldsymbol{\mu}}_S \\ &= -\mu_B g_e \mathbf{B}_0 \cdot \hat{\mathbf{S}}\end{aligned}\tag{1.5}$$

The Hamiltonian describing the nuclear Zeeman interaction in equation 1.4 is only valid for an isolated nucleus. In real samples containing electrons, the external magnetic field causes a motion of electrons which generates magnetic fields opposing the external field, which essentially produces a shielding effect on the nucleus. As such, the nuclear Zeeman Hamiltonian can be adapted with this in mind, by the addition of a term called the nuclear shielding tensor, $\boldsymbol{\sigma}$:

$$\hat{\mathcal{H}}_{IZ} = -\hbar\gamma_I \mathbf{B}_0 \cdot (\mathbf{1} - \boldsymbol{\sigma}) \cdot \hat{\mathbf{I}}\tag{1.6}$$

where $\mathbf{1}$ is the identity tensor. In paramagnetic systems, the nuclear shielding tensor can be decomposed into two terms:

$$\boldsymbol{\sigma} = \boldsymbol{\sigma}^{\text{orb}} + \boldsymbol{\sigma}^{\text{S}} \quad (1.7)$$

where $\boldsymbol{\sigma}^{\text{orb}}$ is Ramsey's orbital shielding tensor [23] for an open-shell system, and where $\boldsymbol{\sigma}^{\text{S}}$ is the temperature-dependent hyperfine contribution to the overall shielding tensor by the paramagnetism of the system.

A brief discussion on notation conventions, and the chemical shift

In order to simplify the description of the anisotropic parts of the shielding tensor and to make description of this tensor easier to understand, it is typical in the field of NMR to describe the shielding tensor not in terms of the three principal values ($\tilde{\sigma}_{xx}$, $\tilde{\sigma}_{yy}$, $\tilde{\sigma}_{zz}$) in the principal axis system (PAS), but rather in terms of three values that describe the isotropic value (trace) of the tensor, the breadth of the average difference between the principal values with respect to one another (referred to as the "anisotropy"), and the distribution of the three principal values (referred to as the "asymmetry"). For the remainder of this thesis the Haeberlen convention [24] is used. Under this convention these three parameters are defined as:

$$\sigma_{\text{iso}} = \text{Tr}[\boldsymbol{\sigma}] = \frac{1}{3}(\tilde{\sigma}_{xx} + \tilde{\sigma}_{yy} + \tilde{\sigma}_{zz}) \quad (1.8)$$

$$\Delta\sigma = \tilde{\sigma}_{zz} - \sigma_{\text{iso}} \quad (1.9)$$

$$\eta = \frac{\tilde{\sigma}_{yy} - \tilde{\sigma}_{xx}}{\Delta\sigma}, \quad (1.10)$$

where $\Delta\sigma$ is the shielding anisotropy and η is the asymmetry parameter. In brief, while it is most useful to discuss paramagnetic effects mathematically in terms of the shielding tensor, what we actually measure in an NMR experiment is the *chemical shift tensor*, $\boldsymbol{\delta}$, the isotropic part of which is equal to the isotropic shielding of a diamagnetic reference compound minus the isotropic shielding of the system:

$$\delta_{\text{iso}} = \sigma_{\text{iso}}^{\text{ref}} - \sigma_{\text{iso}}, \quad (1.11)$$

and the chemical shift anisotropy and asymmetry are defined respectively as:

$$\Delta\delta = \tilde{\delta}_{zz} - \delta_{\text{iso}} = -\Delta\sigma \quad (1.12)$$

$$\eta = \frac{\tilde{\delta}_{yy} - \tilde{\delta}_{xx}}{\Delta\delta}, \quad (1.13)$$

where the ordering of the principal values are assigned as: $|\tilde{\delta}_{zz} - \delta_{\text{iso}}| \geq |\tilde{\delta}_{xx} - \delta_{\text{iso}}| \geq |\tilde{\delta}_{yy} - \delta_{\text{iso}}|$. As such isotropic *shift* in paramagnetic systems can be written in terms of the equation for the nuclear shielding in paramagnetic systems in equation 1.7:

$$\delta_{\text{iso}} = \delta_{\text{iso}}^{\text{orb}} + \delta_{\text{iso}}^S, \quad (1.14)$$

where

$$\delta_{\text{iso}}^{\text{orb}} = \sigma_{\text{iso}}^{\text{ref}} - \sigma_{\text{iso}}^{\text{orb}} \quad (1.15)$$

$$\delta_{\text{iso}}^S = -\sigma_{\text{iso}}^S. \quad (1.16)$$

1.1.3 The hyperfine Hamiltonian

In NMR studies of paramagnetic systems, we are largely concerned with the coupling interaction between unpaired electrons in the vicinity of nuclei in the system of interest, called the hyperfine interaction. The coupling between electrons and nuclei is described by the hyperfine coupling tensor, and the Hamiltonian of this interaction can be expressed as

$$\hat{\mathcal{H}}_{\text{SI}} = \hat{\mathbf{S}} \cdot \mathbf{A} \cdot \hat{\mathbf{I}}, \quad (1.17)$$

where \mathbf{A} is the hyperfine coupling tensor. In the non-relativistic (NR) approximation, the hyperfine coupling tensor can be decomposed into a rank-0 (isotropic) component, the Fermi contact coupling constant, A^{FC} , and a rank-2 component, the spin-dipolar tensor \mathbf{A}^{SD} :

$$\mathbf{A} = A^{\text{FC}}\mathbf{1} + \mathbf{A}^{\text{SD}} \quad (1.18)$$

In general, unpaired electrons are delocalized over ligands through the bonding network. The Fermi contact coupling constant, and the Cartesian components of the spin-dipolar tensor resulting from this delocalization are given by:

$$A^{\text{FC}} = \frac{\mu_0 \mu_{\text{B}} g_e \hbar \gamma_{\text{I}}}{3S} \rho^{\alpha-\beta}(\mathbf{0}), \quad (1.19)$$

$$A_{ij}^{\text{SD}} = \frac{\mu_0 \mu_{\text{B}} g_e \hbar \gamma_{\text{I}}}{8\pi S} \int \frac{3r_i r_j - \delta_{ij} r^2}{r^5} \rho^{\alpha-\beta}(\mathbf{r}) d^3 r, \quad (1.20)$$

where $\rho^{\alpha-\beta}(\mathbf{r})$ is the total spin density (normalized such that $\int \rho^{\alpha-\beta}(\mathbf{r}) d^3 \mathbf{r} = 2S$) at a position \mathbf{r} relative to the nucleus, and δ_{ij} is the Kronecker delta. As a result, we can see that the Fermi contact coupling between unpaired electrons and the nuclei in the sample results from non-zero electron spin density at the site of the nucleus, and as such is exclusively a through-bond interaction. On the other hand, the anisotropic spin-dipolar coupling is exclusively a through-space interaction, and results primarily in spectral broadening due to anisotropic contributions to the nuclear shielding tensor, and an isotropic shift commonly (and somewhat unfortunately) called the pseudocontact shift, δ^{PC} . In the absence of spin-orbit effects and zero-field splitting, the total paramagnetic *shielding* (as written in equation 1.7) can be written as

$$\sigma^S = -\frac{\mu_B g_e S(S+1)}{3\hbar\gamma_I kT} \mathbf{A}. \quad (1.21)$$

From this we can draw a few quick conclusions. First, that the hyperfine nuclear shielding is independent of the nuclear species; although \mathbf{A} does depend on the nuclear species, the ratio $\mathbf{A}/(\hbar\gamma_I)$ is independent of γ_I . Second, we can immediately see that the paramagnetic shift scales as $1/(kT)$, and therefore an increase in temperature corresponds to a smaller resulting isotropic shift, and vice versa. This can be understood in a simplistic way by drawing parallels to the nuclear scalar (J) coupling, as the J -coupling (also historically called the nuclear hyperfine interaction) is mathematically equivalent to the electron hyperfine interaction.

The Hamiltonian describing a coupled spin pair of heteronuclei can be written as

$$\hat{\mathcal{H}} = \hbar\omega_{0,I_1}\hat{I}_{1,z} + \hbar\omega_{0,I_2}\hat{I}_{2,z} + \hbar J\hat{I}_{1,z}\hat{I}_{2,z} \quad (1.22)$$

where the first two terms describe the I_1 -spin and I_2 -spin Zeeman interactions, and the third term is the heteronuclear J -coupling interaction in rad/s. In this formalism we assume that the gyromagnetic ratios of I_1 and I_2 are positive and negative, respectively, that $|\omega_{0,I_2}| > |\omega_{0,I_1}| \gg |J|$, where ω_{0,I_2} and ω_{0,I_1} are the Larmor frequencies of the I_2 -spin and I_1 -spin, respectively, and that J , the heteronuclear scalar coupling constant, is positive. The eigenstates of this Hamiltonian are the functions $|M_{I_1}M_{I_2}\rangle$, which are labelled as $|1\rangle$, $|2\rangle$, $|3\rangle$, $|4\rangle$:

$$\begin{aligned} |1\rangle &= |\alpha\beta\rangle \\ |2\rangle &= |\beta\beta\rangle \\ |3\rangle &= |\alpha\alpha\rangle \\ |4\rangle &= |\beta\alpha\rangle. \end{aligned} \quad (1.23)$$

The two allowed transitions therefore are $|1\rangle \rightarrow |2\rangle$ and $|3\rangle \rightarrow |4\rangle$, which have transition frequencies $\Delta\omega_{1\rightarrow 2}$ and $\Delta\omega_{3\rightarrow 4}$ of:

$$\begin{aligned} \Delta\omega_{1\rightarrow 2} &= -\omega_{0,I_1} + \frac{1}{2}J \\ \Delta\omega_{3\rightarrow 4} &= -\omega_{0,I_1} - \frac{1}{2}J \end{aligned} \quad (1.24)$$

The NMR spectrum of such a coupled system comprises into two lines, separated by the coupling constant J , which is typically of the order of 1–250 Hz. As the energy difference between each transition is small, the lines are observed to be at equal intensity. Upon decoupling of the S -spin, the NMR spectrum collapses to a single line centered at $-\omega_{0,I_1}$. These effects are summarized in Figure 1.1 (a), (c), and (d).

We can treat an isolated spin pair of a spin-1/2 nucleus I and an electron S in the same way, with the corresponding Hamiltonian given by

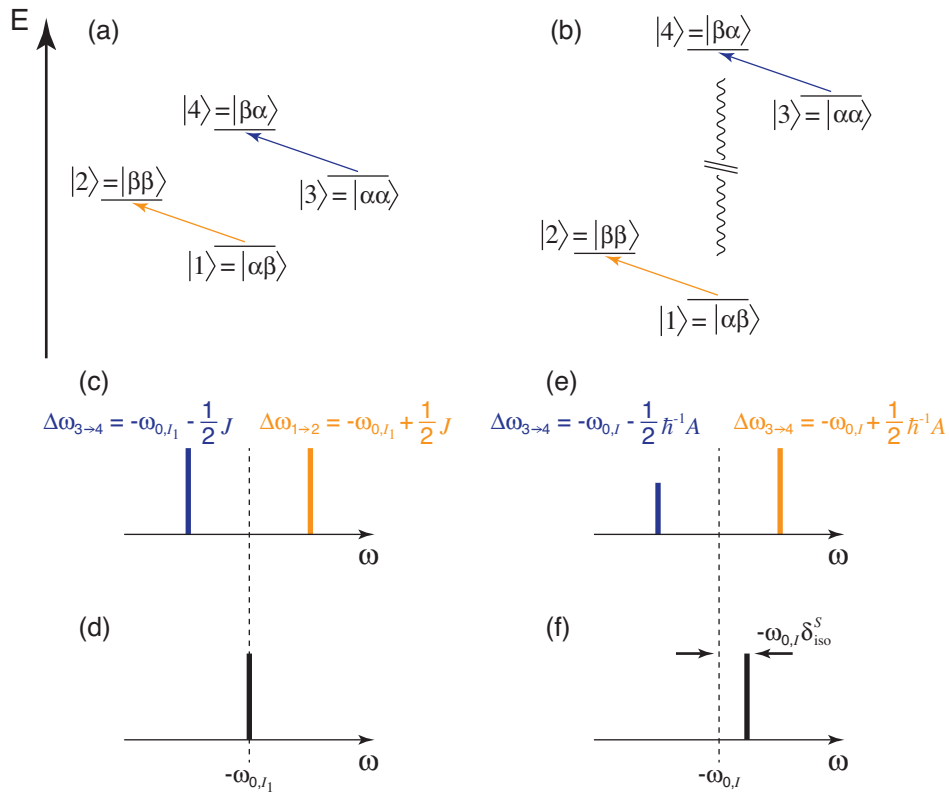


Figure 1.1: An illustration of the spin energy levels of a coupled two-spin system, which illustrates the similarities and differences between (a) two coupled spin-1/2 nuclei, and (b) a spin-1/2 nucleus and an electron with the assumptions that $|\omega_{0,I_2}| > |\omega_{0,I_1}| \gg |J|$, $\omega_{0,I_2} > 0$, $\omega_{0,I_1} < 0$, and in (a), that $J > 0$. The two I -spin transitions are labeled in orange and blue arrows. The resulting NMR spectra of each case are shown in (c)-(f), where (c) exhibits the typical NMR spectrum of a J -coupled spin pair, and (d) shows the resulting NMR spectrum upon I_2 -spin decoupling. The expected NMR spectrum resulting from the transitions shown in (b) is given in (e), where the relative intensities come as a result of the difference in population between higher and lower energy states, while the true NMR spectrum resulting from the transitions in (b) is given in (f), which comes as a result of rapid exchange between Zeeman states due to fast electron relaxation, and where the shift from $\omega_{0,I}$ is the temperature-dependent paramagnetic shift, δ_{iso}^S . Adapted from reference [25].

$$\hat{\mathcal{H}} = \hbar\omega_{0,I}\hat{I}_z + \mu_B g_e \hat{S}_z + A\hat{I}_z\hat{S}_z \quad (1.25)$$

assuming a purely scalar hyperfine coupling constant between I and S . As such the characteristic transition frequencies shown in Figure 1.1 (b) are given as

$$\begin{aligned} \Delta\omega_{1\rightarrow 2} &= -\omega_{0,I} + \frac{1}{2}\hbar^{-1}A \\ \Delta\omega_{3\rightarrow 4} &= -\omega_{0,I} - \frac{1}{2}\hbar^{-1}A \end{aligned} \quad (1.26)$$

In this case, we may therefore expect the NMR spectrum to be composed of two lines with the same intensity, split by A . However, as the hyperfine couplings between electrons and nuclei are typically of the order of MHz, the population of each state cannot be expected to be the same, and therefore the lower energy $\Delta\omega_{3\rightarrow 4}$ is more populated, and would give rise to an NMR spectrum like that shown in Figure 1.1 (e). Furthermore, rapid electron relaxation causes rapid mixing of the Zeeman levels of the electron, which causes the observed NMR lineshape to be composed of a single line at a frequency $-(\omega_{0,I} + \delta_{\text{iso}}^S)$, the weighted average of the two lines split by the scalar coupling. Therefore, the observed temperature dependence of the paramagnetic shift can be explained in the context of electronic Zeeman states: With increasing temperature, the populations of the higher energy states increase, and therefore the observed shift from $\omega_{0,I}$ is less, and vice versa. In the high-temperature limit, the isotropic hyperfine shift tends to zero, and the total paramagnetic shift tends to Ramsey's orbital term.

1.1.4 The Curie spin and magnetic susceptibility

On the timescale of NMR experiments, electronic relaxation processes are typically short. As such, the effects induced by electrons on nuclei in an NMR experiment are typically determined by a "relaxed" electronic spin, which is a thermal average of Zeeman states, and is referred to as the Curie spin, $\langle \mathbf{S}_z \rangle$. The resulting average electron magnetic moment is often best described in terms of the magnetic susceptibility χ , which in general is an anisotropic quantity that determines the magnetization of an object upon interaction with an external magnetic field:

$$\langle \boldsymbol{\mu}_S \rangle = \frac{1}{\mu_0} \boldsymbol{\chi} \cdot \mathbf{B}_0 \quad (1.27)$$

In the high-temperature limit (when the splitting between Zeeman states is small relative to kT , where k is the Boltzmann constant and T is the absolute temperature) and in the absence of spin-orbit effects, only the isotropic part of χ , χ_{iso} , is retained, and the magnetic moment of the Curie spin can be expressed as:

$$\langle \boldsymbol{\mu}_S \rangle = \frac{g_e^2 \mu_B^2 S(S+1)}{3kT} \mathbf{B}_0, \quad (1.28)$$

where S is the electron quantum spin number. Equation 1.28 allows us to define χ_{iso} as:

$$\chi_{\text{iso}} = \frac{\mu_0 g_e^2 \mu_B^2 S(S+1)}{3kT}, \quad (1.29)$$

where μ_0 is the permeability of free space. This equation is the Curie Law. The Curie spin of the paramagnetic center couples to surrounding nuclei, which experience a shielding effect as a result. In the absence of spin-orbit coupling (SOC), the nuclear interaction with the Curie spin only affects the anisotropic part of nuclear shielding, giving rise to the "dipolar shift anisotropy", $\Delta\sigma^{\text{dip}}$, which has an inverse third power dependence on the distance, r , between the paramagnetic center and the nucleus:

$$\Delta\sigma^{\text{dip}} = \frac{\chi_{\text{iso}}}{\hbar\gamma_I r^3} = \frac{\mu_0}{\hbar\gamma_I r^3} \frac{g_e^2 \mu_B^2 S(S+1)}{3kT} \quad (1.30)$$

In a powdered sample, all possible crystallite orientations are present and therefore the observed NMR spectrum is a sum of the contributions from all orientations.

The hyperfine shift

The interaction of the Curie spin with a nuclear spin contributes additional terms to the observed isotropic chemical shift, which is called the hyperfine shift. This is traditionally split into two terms: (1) the contact shift δ^{con} , which results from direct electron spin delocalization on to the nucleus, and (2) the pseudocontact shift (PCS) δ^{pc} , which is a through-space dipolar interaction between unpaired electrons and nuclear spins.

In the simplest case, when spin-orbit coupling (SOC) and zero field splitting (ZFS) effects are negligible, only the contact term contributes to the shift, and is given by the following expression:

$$\delta^{\text{con}} = \frac{A^{\text{FC}}}{\hbar} \frac{g_e \mu_B S(S+1)}{3\gamma_I kT}. \quad (1.31)$$

Equation 1.31 can be re-written in terms of the magnetic susceptibility as

$$\delta^{\text{con}} = \frac{\rho^{\alpha-\beta}(\mathbf{0})}{3S} \chi_{\text{iso}}. \quad (1.32)$$

In systems with orbital degeneracy, or strong spin-orbit coupling (which causes among other things g -shift and zero field splitting (ZFS)), the magnetic susceptibility is a tensorial quantity with rank-0 and rank-2 components:

$$\chi = \chi_{\text{iso}} \mathbf{1} + \Delta\chi \quad (1.33)$$

In its principal axis system, the paramagnetic susceptibility anisotropy tensor, $\Delta\chi$, can be described by its axial and rhombic anisotropy parameters, $\Delta\chi_{\text{ax}}$ and $\Delta\chi_{\text{rh}}$, which are defined as:

$$\Delta\chi_{\text{ax}} = \chi_{zz} - \frac{\chi_{xx} + \chi_{yy}}{2} \quad (1.34)$$

$$\Delta\chi_{\text{rh}} = \chi_{xx} - \chi_{yy} \quad (1.35)$$

The anisotropy of the magnetic susceptibility tensor results in an anisotropy of local magnetic fields experienced by a nuclei in different positions in a molecule, which forms the basis of the PCS, δ^{pc} . Assuming a point-dipole model:

$$\delta^{\text{pc}} = \frac{1}{12\pi r^3} \left[\Delta\chi_{\text{ax}}(3 \cos^2 \theta - 1) + \frac{3}{2} \Delta\chi_{\text{rh}} \sin^2 \theta \cos 2\phi \right], \quad (1.36)$$

where θ and ϕ are polar angles relating the vector between the nucleus and the paramagnetic center to the PAS of χ . In this context, the total observed isotropic chemical shift in paramagnetic systems can be summarized as follows:

$$\delta_{\text{iso}} = \delta_{\text{iso}}^{\text{orb}} + \delta^{\text{con}} + \delta^{\text{pc}} \quad (1.37)$$

1.1.5 Spin-orbit effects and the full PNMR Hamiltonian

When spin-orbit coupling is considered, the previously-scalar quantity g_e becomes a rank-2 tensorial quantity, \mathbf{g} . There are also additional spin-orbit corrections to the hyperfine tensor, outlined below. Furthermore, for paramagnetic centers with an electron spin quantum number greater than $1/2$, $S > 1/2$, ZFS effects should be considered. In an overly simplistic and perhaps naïve way, these effects can be generalized to a short statement: the introduction of spin-orbit effects further splits the electronic spin energy manifold, leading to a change in the magnetic moment of the Curie spin, $\langle \mu_S \rangle$, which in turn affects the measured hyperfine shift in an NMR experiment. For a full description of all these interactions, an effective Hamiltonian, constructed of the nuclear Zeeman and EPR interaction terms, needs to be considered in the form of:

$$\hat{\mathcal{H}}_K^{\text{PNMR}} = \sum_K -\hbar\gamma_K \mathbf{B}_0 \cdot (\mathbf{1} - \boldsymbol{\sigma}_K) \cdot \mathbf{I}_K + \mu_B \mathbf{B}_0 \cdot \mathbf{g} \cdot \mathbf{S} + \sum_K \mathbf{S} \cdot \mathbf{A}_K \cdot \mathbf{I}_K + \mathbf{S} \cdot \mathbf{D} \cdot \mathbf{S} \quad (1.38)$$

for a nucleus K , where \mathbf{D} is the rank-2, symmetric, traceless ZFS tensor. Vaara and coworkers presented a general solution [26] to determine the paramagnetic contributions to the nuclear shielding tensor, which is given below:

$$\boldsymbol{\sigma}_K = \boldsymbol{\sigma}_K^{\text{orb}} - \frac{\mu_B}{\gamma_K \hbar kT} \cdot \mathbf{g} \cdot \langle \mathbf{S}\mathbf{S} \rangle \cdot \mathbf{A}_K. \quad (1.39)$$

where $\langle \mathbf{S}\mathbf{S} \rangle$ is the "spin dyadic", which is a thermal average over all populated electronic Zeeman states. This solution is a result of a re-derivation of the Kurland-McGarvey theory of paramagnetic shifts [27] in terms of EPR property tensors. The individual spin dyadic components are calculated using the equations below:

$$\langle S_a S_b \rangle = \frac{\sum_{nm} Q_{nm} \langle n | S_a | m \rangle \langle m | S_b | n \rangle}{\sum_n \exp(-E_n/kT)} \quad (1.40)$$

Term in $\sigma_{\epsilon\tau}$	Number	Symbol	Order	Tensorial Rank	
				$S = 1/2$	$S > 1/2$
$g_e A^{\text{FC}} \langle S_\epsilon S_\tau \rangle$	1	σ^{con}	$\mathcal{O}(\alpha^2)$	0	0, 2
$g_e \sum_b A_{b\tau}^{\text{SD}} \langle S_\epsilon S_b \rangle$	2	σ^{dip}	$\mathcal{O}(\alpha^2)$	2	0, 2, 1
$g_e A^{\text{PC}} \langle S_\epsilon S_\tau \rangle$	3	$\sigma^{\text{con},2}$	$\mathcal{O}(\alpha^4)$	0	0, 2
$g_e \sum_b A_{b\tau}^{\text{dip},2} \langle S_\epsilon S_b \rangle$	4	$\sigma^{\text{dip},2}$	$\mathcal{O}(\alpha^4)$	2	0, 2, 1
$g_e \sum_b A_{b\tau}^{\text{as}} \langle S_\epsilon S_b \rangle$	5	σ^{as}	$\mathcal{O}(\alpha^4)$	1	2, 1
$\Delta g_{\text{iso}} A^{\text{FC}} \langle S_\epsilon S_\tau \rangle$	6	$\sigma^{\text{con},3}$	$\mathcal{O}(\alpha^4)$	0	0, 2
$\Delta g_{\text{iso}} \sum_b A_{b\tau}^{\text{SD}} \langle S_\epsilon S_b \rangle$	7	$\sigma^{\text{dip},3}$	$\mathcal{O}(\alpha^4)$	2	0, 2, 1
$A^{\text{FC}} \sum_a \Delta \tilde{g}_{\epsilon a} \langle S_a S_\tau \rangle$	8	$\sigma^{\text{c,aniso}}$	$\mathcal{O}(\alpha^4)$	2, 1	0, 2, 1
$\sum_{ab} \Delta \tilde{g}_{\epsilon a} A_{b\tau}^{\text{SD}} \langle S_a S_b \rangle$	9	σ^{pc}	$\mathcal{O}(\alpha^4)$	0, 2, 1	0, 2, 1

Table 1.1: The 9 contributions to the nuclear shielding tensor by the hyperfine coupling when considering spin-orbit effects, in terms of EPR property tensors. Rank-0, 2, and 1 contributions correspond to the isotropic, anisotropic symmetric, and anisotropic anti-symmetric terms, respectively. [26]

$$Q_{nm} = \begin{cases} \exp(-E_n/kT) & ; E_n = E_m \\ -\frac{kT}{E_m - E_n} [\exp(-E_m/kT) - \exp(-E_n/kT)] & ; E_n \neq E_m \end{cases} \quad (1.41)$$

The \mathbf{g} and \mathbf{A} tensors can be decomposed into 3 and 5 terms, respectively:

$$\mathbf{g} = (g_e + \Delta g_{\text{iso}}) \mathbf{1} + \Delta \tilde{\mathbf{g}} \quad (1.42)$$

$$\mathbf{A} = (A^{\text{FC}} + A^{\text{PC}}) \mathbf{1} + \mathbf{A}^{\text{SD}} + \mathbf{A}^{\text{dip},2} + \mathbf{A}^{\text{as}} \quad (1.43)$$

where \mathbf{g} consists of the $\mathcal{O}(\alpha^0)$ free electron g_e factor and the $\mathcal{O}(\alpha^2)$ g shift tensor $\Delta \mathbf{g}$ (where $\Delta \mathbf{g} = \mathbf{g} - g_e \mathbf{1}$), the isotropic and anisotropic parts of which are Δg_{iso} and $\Delta \tilde{\mathbf{g}}$, respectively. The hyperfine coupling tensor contains the non-relativistic, $\mathcal{O}(\alpha^2)$ contribution $A^{\text{FC}} \mathbf{1} + \mathbf{A}^{\text{SD}}$, and the relativistic $\mathcal{O}(\alpha^4)$ spin-orbit term $A^{\text{PC}} \mathbf{1} + \mathbf{A}^{\text{dip},2} + \mathbf{A}^{\text{as}}$. The combination of these terms using Equation 1.39 results in 15 total terms that contribute to the paramagnetic nuclear shielding tensor, and, when truncated to $\mathcal{O}(\alpha^4)$, results in 9 terms, which are summarized in table 1.1. Terms 1, 3, 6, and 8 contribute to the contact shielding, whereas terms 2, 4, 5, 7, and 9 contribute to the dipolar shielding. To relate to terms previously discussed, terms 1 and 2 are the NR Fermi-contact and spin-dipolar terms given in equations 1.31 and 1.30 respectively, whereas the rank-0 component of term 9 is the traditional pseudocontact shielding.

1.1.6 Paramagnetic relaxation enhancement

The following discussion makes extensive use of the excellent review of paramagnetic relaxation enhancement given in chapter 4 of the book by Bertini and coworkers from the Florence group [16], and as such the citation is given here only once to avoid overcrowding. Paramagnetic relaxation enhancement (PRE) is among the earliest paramagnetic effects observed, and

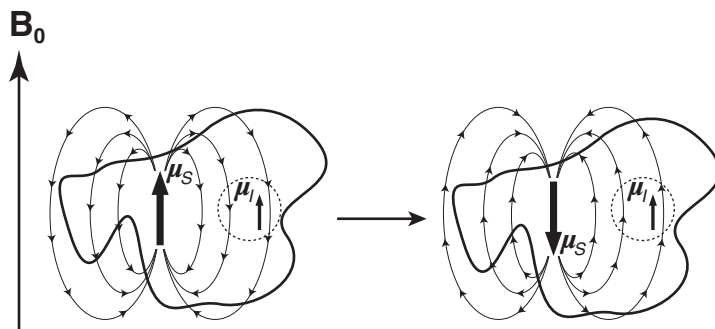


Figure 1.2: A simplistic but illustrative illustration showing how the effect of fluctuating magnetic field of a rapidly-relaxing electron spin relaxes the nuclear spin via dipolar hyperfine coupling in a molecule of generic shape. Adapted from reference [16].

was originally exploited to decrease relaxation times in NMR samples for the measurement of gyromagnetic ratios of nuclear isotopes [28]. Due to the hyperfine coupling between the strong electron magnetic moment ($\gamma_S \approx -660\gamma_{\text{H}}$) and the nucleus, stochastic fluctuations in the electronic magnetic moment cause large fluctuations in the local magnetic field experienced by the nucleus, which provides efficient relaxation. This effect is illustrated in a simplistic way in Figure 1.2. In general, this effect is dependent on the correlation time, which describes the evolution of the populations of the spin states in the system of interest. This correlation time is itself a function of three independent time constants: (1) the electron spin relaxation correlation time, τ_s , (2) the rotational correlation time, τ_r , and (3) the exchange correlation time, τ_M , by the following relationship:

$$(\tau_c^{-1})^{\text{dip}} = \tau_s^{-1} + \tau_r^{-1} + \tau_M^{-1}. \quad (1.44)$$

In solids, the lack of molecular tumbling results in the total correlation time being to the electron correlation time, *i.e.* $\tau_c = \tau_s$. As a result, the nuclear relaxation times are directly dependent on the electron spin relaxation correlation time, which is manifested by two principle mechanisms: (1) dipolar hyperfine coupling to distant electrons, the so-called Solomon mechanism, which is typically treated by a point-dipole approximation, and which is the dominant relaxation mechanism for nuclei far from the metal center, and (2) Fermi-contact coupling to electrons at the site of the nucleus, the so-called Bloembergen mechanism, which is particularly strong for nuclei up to a few bonds away from the metal center. These two mechanisms are discussed briefly in the following paragraphs.

Assuming a point-dipole approximation and neglecting spin-orbit coupling effects, the nuclear longitudinal and transverse relaxation rates¹ resulting from dipolar couplings to distant electrons, R_{1M}^{dip} and R_{2M}^{dip} , respectively, can be determined to be

¹It should be noted here that although relaxation rates are typically given units of s^{-1} and correlation times in units of s , implicit in the following equations is that the rates are calculated to have units of $\text{rad}\cdot s^{-1}$ with the correlation times having units of $s\cdot\text{rad}^{-1}$, and the gyromagnetic ratios with units of $\text{rad}\cdot s^{-1}\cdot T^{-1}$.

$$R_{1M}^{\text{dip}} = \frac{2}{15} \left(\frac{\mu_0}{4\pi} \right)^2 \frac{\gamma_I^2 g_e^2 \mu_B^2 S(S+1)}{r^6} \left[\frac{\tau_c}{1 + (\omega_I - \omega_S)^2 \tau_c^2} + \frac{3\tau_c}{1 + \omega_I^2 \tau_c^2} + \frac{6\tau_c}{1 + (\omega_I + \omega_S)^2 \tau_c^2} \right] \quad (1.45)$$

$$R_{2M}^{\text{dip}} = \frac{1}{15} \left(\frac{\mu_0}{4\pi} \right)^2 \frac{\gamma_I^2 g_e^2 \mu_B^2 S(S+1)}{r^6} \left[4\tau_c + \frac{\tau_c}{1 + (\omega_I - \omega_S)^2 \tau_c^2} + \frac{3\tau_c}{1 + \omega_I^2 \tau_c^2} + \frac{6\tau_c}{1 + (\omega_I + \omega_S)^2 \tau_c^2} + \frac{6\tau_c}{1 + \omega_S^2 \tau_c^2} \right], \quad (1.46)$$

where ω_I and ω_S are the nuclear and electron Larmor frequencies, respectively. Assuming that $\tau_c = \tau_s$, and with terms containing ω_S in the denominator collected, as $|\omega_S| \gg |\omega_I|$, this can be simplified to the following two expressions:

$$R_{1M}^{\text{dip}} = \frac{2}{15} \left(\frac{\mu_0}{4\pi} \right)^2 \frac{\gamma_I^2 g_e^2 \mu_B^2 S(S+1)}{r^6} \left[\frac{7T_{2e}}{1 + \omega_S^2 T_{2e}^2} + \frac{3T_{1e}}{1 + \omega_I^2 T_{1e}^2} \right] \quad (1.47)$$

$$R_{2M}^{\text{dip}} = \frac{1}{15} \left(\frac{\mu_0}{4\pi} \right)^2 \frac{\gamma_I^2 g_e^2 \mu_B^2 S(S+1)}{r^6} \left[4T_{1e} + \frac{13T_{2e}}{1 + \omega_S^2 T_{2e}^2} + \frac{3T_{1e}}{1 + \omega_I^2 T_{1e}^2} \right] \quad (1.48)$$

where T_{1e} and T_{2e} are the longitudinal and transverse electron relaxation times, respectively.

Due to the previously-mentioned large electronic magnetic moment, the dipolar PRE can occur over very large distances, and as the effect scales by r^6 , this relaxation mechanism is particularly strong for those nuclei lying close to the metal center. Moreover, in solids the efficient spin diffusion mechanism among protons causes this effect to be further spread over a long distance, resulting in short and largely uniform proton relaxation times. The enhanced nuclear transverse relaxation rates causes line broadening, which diminishes the resolution of the spectra. However, the delay time between repeated NMR experiments is governed by the nuclear longitudinal relaxation rate, which is also greatly enhanced by the PRE. Therefore, although the PRE generally decreases the resolution of experimental NMR spectra, the same effect allows the acquisition of more scans per unit time compared to NMR experiments of diamagnetic systems. This feature of the PRE is used extensively in the results discussed in the following chapters, and is particularly useful in the case of two-dimensional experiments utilizing polarization transfer from protons, as the PRE is proportional to γ_I^2 .

Near the metal center ($\sim 1-4$ bonds away from the metal atom) stochastic variations of electron magnetic moments *at the site of the nucleus* cause considerable nuclear relaxation due to relatively strong Fermi contact couplings. In this regime, the nuclear relaxation rates can be expressed as

$$R_{1M}^{\text{con}} = \frac{2}{3}S(S+1)\left(\frac{A^{\text{FC}}}{\hbar}\right)^2 \frac{T_{2e}}{1 + \omega_S^2 T_{2e}^2} \quad (1.49)$$

$$R_{2M}^{\text{con}} = \frac{1}{3}S(S+1)\left(\frac{A^{\text{FC}}}{\hbar}\right)^2 \left[T_{1e} + \frac{T_{2e}}{1 + \omega_S^2 T_{2e}^2} \right]. \quad (1.50)$$

Thus, it can be seen that for nuclei with large Fermi contact coupling constants, this relaxation mechanism can be considerable, as (A^{FC}/\hbar) is often of the order of MHz whereas T_{1e} is typically of the order of $10^{-8} - 10^{-13}$ s. This often results in proton relaxation times of the order of $\mu\text{s} - \text{ms}$ for nuclei experiencing strong hyperfine couplings, permitting rapid repetition of experiments but often compromising spectral resolution in extreme cases.

1.1.7 Line broadening from anisotropic bulk magnetic susceptibility

Following the preceding discussion on PRE effects, we may expect that metals exhibiting very short correlation times, such as the lanthanide series (except Gd^{3+}) and some transition metals (such as Co^{2+} or Fe^{2+}) will not contribute significantly to the line width of resonances in an NMR spectrum of samples containing these metal ions. While it is true that the relaxation effects tend to be small, a much more significant effect arises due to the anisotropy of the bulk magnetic susceptibility (ABMS). BMS effects on the line widths in NMR spectra have been analyzed in detail over the years following pioneering work by the group of Lippmaa [29–31], and have been recently extensively reviewed by Pell, Pintacuda, and Grey [25].

The ABMS broadening comes as a result of the fact that the magnetic susceptibilities of paramagnetic centers are in general anisotropic, and as such can contribute to the isotropic shift of nearby resonances by the through-space PCS. In powdered crystals, the crystallite size is in general non-uniform, and all spatial orientations of crystallites exist within the NMR rotor. As a result, when placed inside a strong magnetic field, each crystallite will generate a unique magnetic field depending on the crystal structure, g , the crystallite size, and necessarily, its orientation. This in turn generates a non-uniform distribution of magnetic fields within the sample [29–31]. In the case that the susceptibility tensor is isotropic, this effect can be efficiently averaged to zero by magic angle spinning.

However, in the case of a general anisotropic magnetic susceptibility tensor, the problem is not so easily solved. The nuclei surrounding an individual crystallite interact with an orientation-dependent magnetic dipole. During MAS, this manifests as a periodic modulation of the magnetic field experienced by each nucleus within the sample which is not averaged by MAS [31]. The result is an inhomogeneously broadened line shape in the MAS NMR spectra, and is illustrated in Figure 1.3. As will be seen in subsequent chapters, this effect often results in NMR line widths of the order of 10-100 ppm.

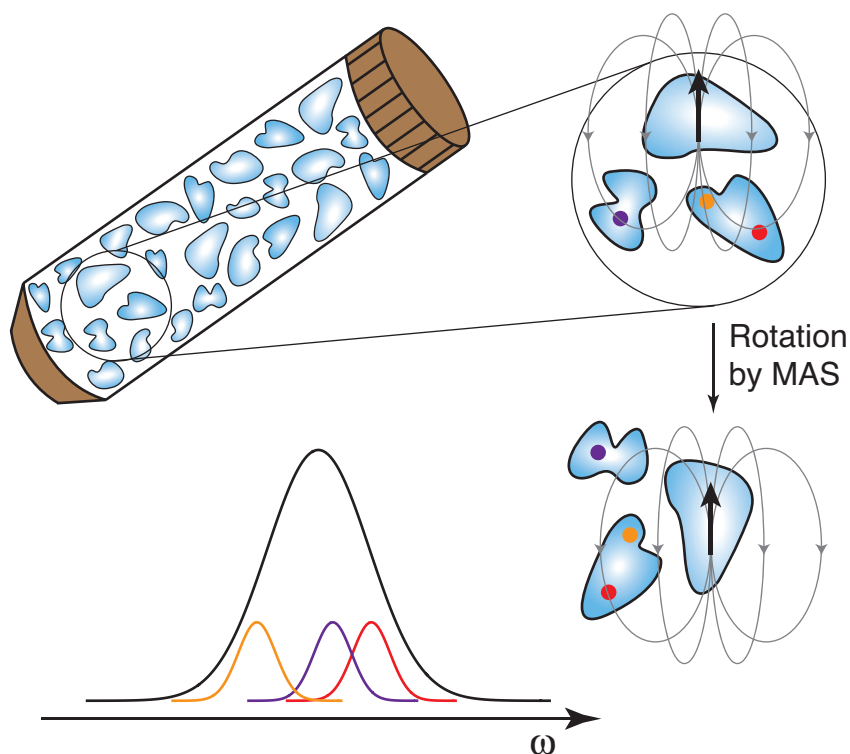


Figure 1.3: An illustration of the anisotropic bulk magnetic susceptibility broadening. During MAS, the nuclei in the positions denoted by orange, red, and purple circles do not feel the same magnetic field, and thus resonate at different frequencies. This results in a bulk broadening of the NMR line. Adapted from reference [32].

1.2 Magic Angle Spinning

There is a long history in the literature of NMR being used to probe paramagnetic effects in molecular complexes and biological assemblies. The PRE effect was first described in 1948 by Bloembergen, Purcell, and Pound and was used to reduce the nuclear T_1 during measurements of gyromagnetic ratios [28]. Paramagnetic effects on the nuclear isotropic shifts were observed as early as 1950 [33], with the first papers detailing how these shifts may be theoretically understood for d -block metal ions given by McConnell in 1958 [34, 35]. Solution-state NMR has long been used to probe the electronic structure and coordination geometries in paramagnetic complexes and metalloproteins, and has been reviewed extensively [16, 36, 37]. On the other hand, solid-state NMR studies of paramagnetic complexes were virtually non-existent until the 1980s. Due to the strong hyperfine coupling between electrons and nuclei, large shift anisotropies and Fermi-contact shifts cause NMR spectra of paramagnetic solids to exhibit very low resolution. Dramatic improvements in the resolution of solid-state NMR spectra of paramagnetic samples can be achieved by using magic-angle spinning (MAS) [20, 21], which is a method whereby the sample is placed in a cylindrical rotor and subsequently spun about its axial dimension at a rate ν_R at the so-called "magic angle" from the external magnetic field, B_0 , where the magic angle, θ_M , is $\theta_M = \cos^{-1}(\sqrt{1/3}) \approx 54.74^\circ$ (see Figure 1.4 (a)).

The most important effect of MAS for paramagnetic solids is the partial or total averaging of frequency components arising from shift anisotropy in the NMR spectrum. Under MAS the

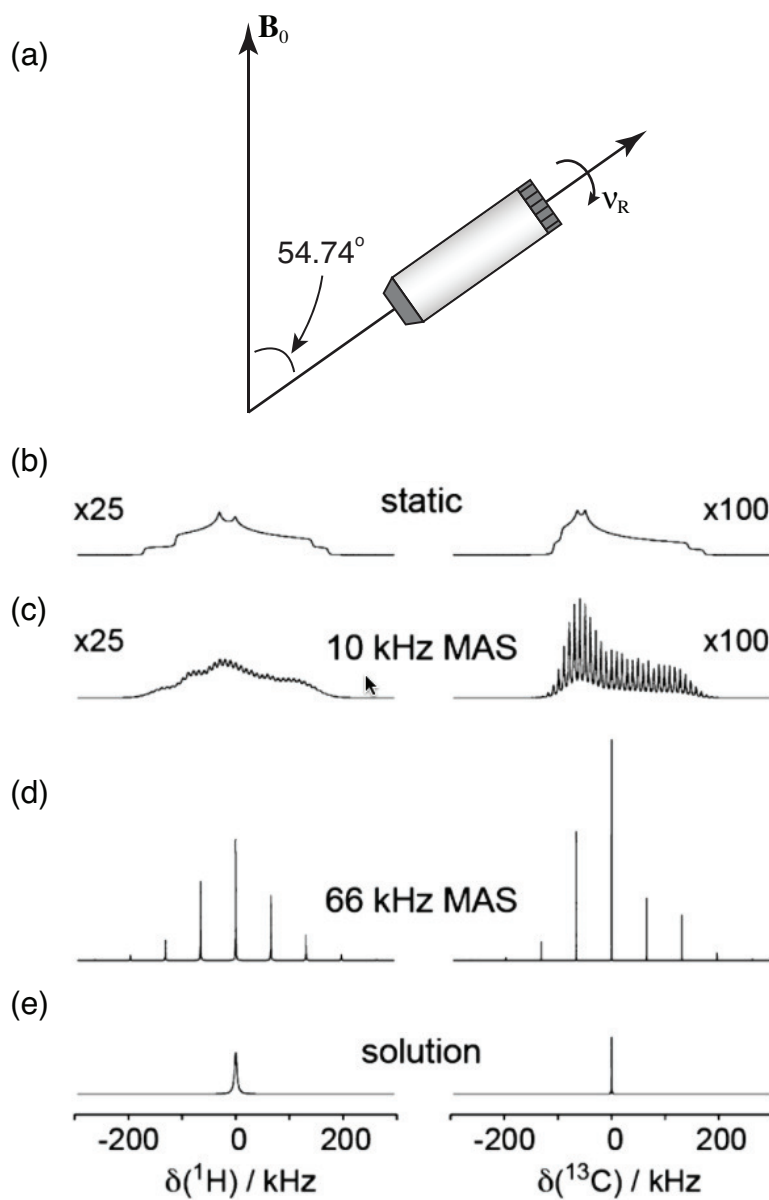


Figure 1.4: (a) Depiction of a magic-angle spinning rotor. (b-e) Simulated ^1H (left) and ^{13}C (right) NMR spectra for a ^1H - ^{13}C spin pair located 5 \AA from a paramagnetic ion ($S = 3/2$, $\tau_e = 10^{-11} \text{ s}$) with the following experimental conditions: (b) static solid, (c) 10 kHz MAS, (d) 66 kHz MAS, and (e) solution. (b-e) Reprinted with permission from [4]. Copyright 2013 American Chemical Society.

chemical shift Hamiltonian is the sum of two parts:

$$\hat{\mathcal{H}}_{\text{CS}}(t) = \Omega_0 \hat{\mathbf{I}}_z + \Omega_c^{\text{SA}}(\gamma; t) \hat{\mathbf{I}}_z, \quad (1.51)$$

where Ω_0 is the isotropic frequency for all crystallites present in the sample, and is time-independent, and $\Omega_c^{\text{SA}}(\gamma; t)$ is the anisotropic frequency, which is time-dependent, periodic over the rotor period, and is generally different for all crystallites with orientations (α, β, γ) . For a single crystallite, these frequencies are given by:

$$\Omega_0 = -\omega_0 \sigma_0, \quad (1.52)$$

$$\Omega_c^{\text{SA}}(\gamma; t) = \sum_{k=-2, k \neq 0}^{+2} \omega_c^{(k)}(\gamma) \exp(-ik\omega_r t), \quad (1.53)$$

where ω_0 is the Larmor frequency, σ_0 is the isotropic nuclear shielding, and the coefficients $\omega_c^{(k)}(\gamma)$ are expressed as

$$\omega_c^{(k)}(\gamma) = -\sqrt{\frac{2}{3}} \omega_0 \sum_{l=-2}^{+2} \tilde{\sigma}_{2l} \exp(-i\alpha l) d_{lk}^{(2)}(\beta) d_{k0}^{(2)}(\theta_M) \exp(-ik\gamma), \quad (1.54)$$

where $d_{lk}^{(2)}(\theta)$ are the elements of the reduced Wigner rotation matrix of rank l , and where the crystallite orientation is given by the orientation of the PAF of the nuclear shielding tensor relative to the rotor. The term $\tilde{\sigma}_{2l}$ denotes the symmetric anisotropic components of the nuclear shift tensor, which are given by:

$$\tilde{\sigma}_{20} = \sqrt{\frac{1}{6}} (3\tilde{\sigma}_{zz} - \sigma_0) = \sqrt{\frac{3}{2}} \Delta\sigma \quad (1.55)$$

$$\tilde{\sigma}_{2\pm 1} = 0 \quad (1.56)$$

$$\tilde{\sigma}_{2\pm 2} = -\frac{1}{2} \eta \Delta\sigma \quad (1.57)$$

where $\Delta\sigma$ and η are the anisotropy and asymmetry of the shift tensor, defined previously in Equations 1.8-1.10.

For powder samples under moderate MAS rates relative to the size of the SA tensor (*i.e.* $\omega_r < \Delta\sigma$), the effect of MAS is to split the resonances into a series of narrower bands with the same phase, separated by the rotational frequency [38, 39]. This effect is illustrated in Figure 1.4. Static NMR line shapes of a ^1H - ^{13}C spin pair are given in Figure 1.4 (b), where the line shapes shown are a result of a combination of chemical shift anisotropy and heteronuclear dipolar coupling. Upon rotation about the magic angle, anisotropic contributions to the NMR observables, such as chemical shift anisotropy and homo- and heteronuclear dipolar couplings, begin to be averaged. Once the MAS rate exceeds the magnitude of these anisotropic interaction, total coherent averaging is achieved and only the isotropic frequencies remain in the spectra [38].

For example, when rotating about the magic angle at a relatively low rotation rate of 10 kHz (Figure 1.4 (c)), the previously broad ^{13}C line shape is split into a series of relatively narrow bands referred to as spinning sidebands or rotational sidebands, which are separated by the rotational frequency, each of which are slightly broadened by residual effects of the ^1H - ^{13}C dipolar coupling, which is typically around 20 kHz in magnitude. On the other hand, the ^1H spectrum is not significantly enhanced by this relatively slow MAS rate of 10 kHz, primarily due to the fact that homonuclear ^1H - ^1H are not sufficiently averaged and as a result, broaden the ^1H spinning sidebands significantly [1, 2]. Upon rotation at a much higher frequency (Figure 1.4 (d)), both homonuclear and heteronuclear dipolar couplings are sufficiently removed to give narrow spinning sidebands, and as the number of spinning sidebands is also reduced, the sensitivity is increased. Contrary to what may be expected, the line width for each nucleus solid-state spectrum is comparatively more narrow than what is observed in solution (Figure 1.4 (e)). This is due to the fact that the so-called Curie relaxation broadening, present in solution due to molecular tumbling [16] and which broadens the solution-state resonances, is not present in the solid state [40]. As such it is often seen in solid-state PNMR spectra that the line widths are more narrow than solution-state measurements, so long as ABMS broadening is not significant.

Despite the fact that MAS was discovered in the late 1950s, MAS probe designs at that time did not permit sufficient MAS rotation rates for high resolution solid-state studies of paramagnetic complexes. Technological advances in MAS probe design in the 1980s finally permitted adequate magic-angle spinning speeds (3-4 kHz) to obtain high resolution NMR spectra of some paramagnetic complexes, shown first by Chacko *et al.* in 1983 [41] on ^{13}C spectra of lanthanide acetate complexes. Subsequent experimental studies of lanthanide-containing pyrochlores [42-44] proved the utility of solid-state NMR as a technique to study the effects of paramagnetic centers in molecular complexes, as at this point it became possible to obtain well-resolved NMR spectra and identify the contribution of the size of Fermi contact shifts in molecular complexes, with representative spectra begin given in Figure 1.5.

However, due to the strong anisotropic effects induced by paramagnetic centers, traditional solid-state MAS NMR techniques used to give further resolution and/or sensitivity improvements such as cross polarization (CP) [45] and heteronuclear decoupling [46] are inefficient or even detrimental in the worst cases due to the fact that these techniques require long periods of RF irradiation, and these RF fields are not sufficiently strong to dominate the anisotropic interactions exhibited by such samples. An alternative experimental approach to obtain high resolution MAS spectra of nuclei in paramagnetic complexes was suggested by Ishii *et al.* [1, 2], where it was argued that the maximum available rotation rate (in the so-called "fast MAS regime", $\nu_{\text{R}} > 20$ kHz) should be used in order to (1) suppress contributions from dipolar couplings on the NMR spectral line widths and (2) to minimize the number and intensity of spinning sidebands. This naturally leads to the development of MAS probes that are capable of faster and faster spinning rates by the use of smaller rotors, leading to the current maximum rates of 130+ kHz. The use of smaller rotors has an additional benefit, in that smaller solenoidal coils are used for excitation and receiving, and which in turn are able to generate stronger RF fields thereby improving excitation

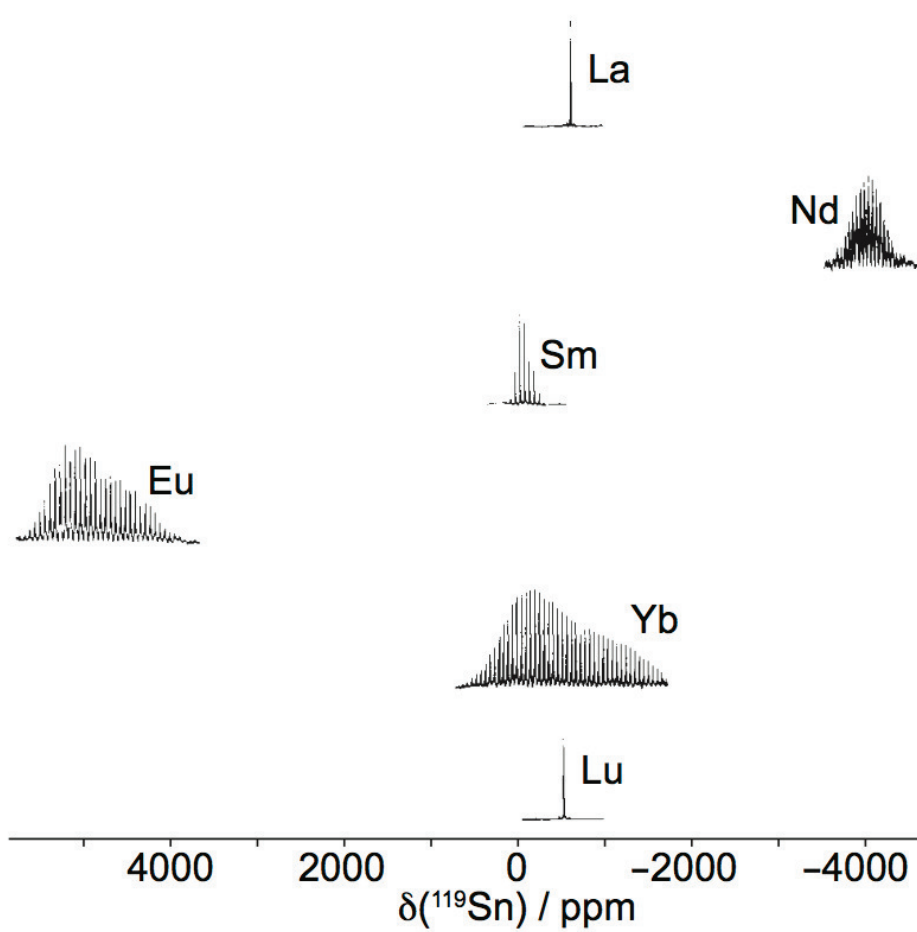


Figure 1.5: ^{119}Sn MAS NMR spectra of the pyrochlores $\text{Ln}_2\text{Sn}_2\text{O}_7$ at spinning speeds of 3-4 kHz, where Ln = La, Nd, Sm, Eu, Yb, and Lu. The chemical shifts are referenced to tetramethyltin. Adapted with permission from [43]. Copyright 1989 American Chemical Society.

band widths and efficiencies of conventional short RF pulses. Indeed, it has been shown that among the most effective 1D MAS NMR techniques applied to paramagnetic systems are those that use high-power, short RF pulses, such as the spin-echo sequence [47] for direct excitation, or the transferred-echo double resonance (TEDOR) method for polarization transfer [3, 48]. The advantages of the use of fast MAS rates and the use of high-power RF pulses are primarily twofold: (1) fast MAS rates suppress the intensity and number of rotation sidebands, and thereby increase resolution and sensitivity, and (2) the recycle delay can be considerably shortened due to the absence of concerns about the probe duty cycle when using long spin-lock pulses (as in CP and decoupling sequences), and as such, the relaxation benefits induced by the PRE can be exploited in order to increase the number of scans acquired per unit time. Thus, resolution and sensitivity are simultaneously increased by this approach. Indeed, fast MAS techniques form the foundation on which most paramagnetic NMR methods have been based.

1.2.1 Adiabatic pulses in MAS experiments

Typically we consider a pulse to be performing well if it achieves an excitation of 90% or higher. For conventional pulses using a RF field strength of ω_1 to excite spins with an offset Ω , it can be shown that 90% excitation can be achieved for $\pi/2$ pulses over a quite broad range of $-1.58\omega_1 < \Omega < +1.58\omega_1$ [49] whereas π pulses suffer from a much more narrow effective range of $-0.23\omega_1 < \Omega < +0.23\omega_1$ [50]. For paramagnetic samples, this limitation in the effective bandwidth of π pulses often renders conventional NMR methodology useless, as the pulse often only excites a narrow range of the frequencies in a PNMR spectrum. As such it is necessary to update the experimental methodology to include broadband pulses to replace conventional π pulses for inversion and refocusing applications.

One potential way to attack this problem is with the use of phase-modulated (swept-frequency) adiabatic pulses [51–53]. Unlike a conventional RF pulse, which utilizes a constant amplitude and phase to perturb nuclear spins, adiabatic pulses typically utilize a ramped amplitude and a non-linear phase sweep to adiabatically "lock" the nuclear magnetization to the pulse effective field field in order to invert spin coherences [54]. Examples of such pulses include the hyperbolic secant pulse [51], the tanh/tan pulse [52], and the Wide, Uniform-Rate, Smooth Truncation (WURST) pulse [53]. Each of these three types of pulses are symmetric to time reversal, so the time-dependent amplitude and phase are symmetric about the middle of the pulse:

$$\omega_1(t) = \omega_1(\tau_p - t) \quad (1.58)$$

$$\phi_p(t) = \phi_p(\tau_p - t) \quad (1.59)$$

The amplitude is generally increased from zero to its maximum value, ω_1^{\max} , halfway through the pulse, and then is symmetrically reduced back to zero during the second half of the pulse,

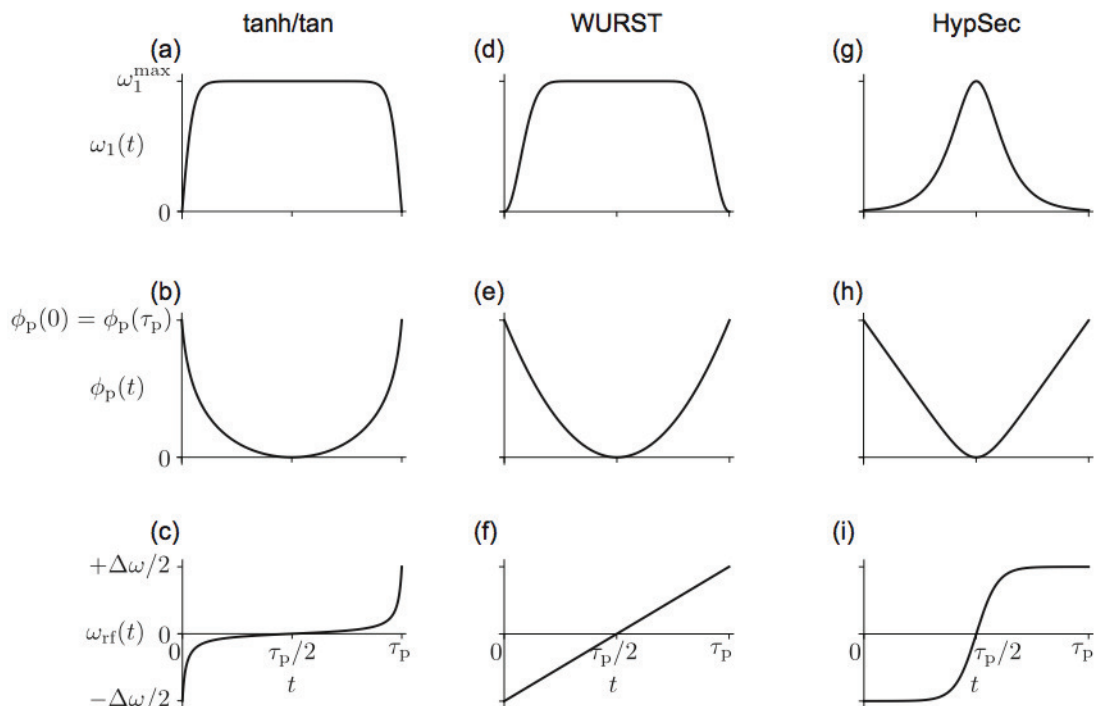


Figure 1.6: The amplitude, phase, and frequency sweep profiles of (a-c) tanh/tan pulse, (d-f) WURST pulse, and (g-i) hyperbolic secant pulse. Reprinted with permission from [25].

which ensures that the effective field is parallel to $\pm z$ at the beginning and end of the pulse. The symmetric phase-sweep profile results in a variation of the transmitter offset so that

$$\omega_{\text{rf}}(t) = -\omega_{\text{rf}}(\tau_p - t), \quad (1.60)$$

which results in a frequency sweep from $-\Delta\omega/2$ to $+\Delta\omega/2$, where $\Delta\omega$ is the sweep width of the pulse. The amplitude, phase, and frequency sweep profiles for each pulse are given in Figure 1.6, with the mathematical expressions for each given in Appendix A, Table A.1.

Short, High-powered Adiabatic Pulses (SHAPs)

Adiabatic pulses have been used with great success in solution-state NMR, MRI, and static solid-state NMR; however, these pulses tend to be quite long (many milliseconds in length) using low RF field strengths. This is problematic for PNMN, as rapid relaxation prevents the use of such long pulses. One brute force approach to achieve broadband inversion and refocusing in the study of paramagnetic samples during MAS experiments was introduced by Kervern *et al.* in 2007 [5], whereby short pulses (tens of μs) using very high RF fields (100s of kHz) are used to invert or refocus spins in paramagnetic samples. These pulses were dubbed Short, High-powered Adiabatic Pulses (SHAPs).

It is necessary to examine these pulses mathematically in order to establish an adiabatic condition, which is used to grade the performance of the pulse. Before developing the mathematical description of SHAPs it is necessary to start with the descriptions of basic RF pulses. First we

consider the Hamiltonian of an RF pulse in a reference frame that is rotating synchronously with the transmitter frequency of the resonant component of the RF field:

$$\hat{\mathcal{H}}_p(t) = \omega_1(t) \hat{\mathbf{R}}_z(\phi_p(t)) \hat{\mathbf{I}}_x \hat{\mathbf{R}}_z(\phi_p(t))^{-1} \quad (1.61)$$

$$= \omega_1 \left[\cos(\phi_p(t)) \hat{\mathbf{I}}_x + \sin(\phi_p(t)) \hat{\mathbf{I}}_y \right], \quad (1.62)$$

where $\omega_1(t)$ and $\phi_p(t)$ are the time-dependent amplitude and phase of the pulse. The time dependence of the phase modulation becomes more clear if the Hamiltonian $\hat{\mathcal{H}}_p(t)$ is transformed into the modulated frame, which is a frame which precesses so that it follows the phase [49]:

$$\hat{\tilde{\mathcal{H}}}_p(t) = -\frac{d\phi_p(t)}{dt} \hat{\mathbf{I}}_z + \hat{\mathbf{R}}_z(\phi_p(t))^{-1} \hat{\mathcal{H}}_p(t) \hat{\mathbf{R}}_z(\phi_p(t)) \quad (1.63)$$

$$= \omega_{\text{rf}}(t) \hat{\mathbf{I}}_z + \omega_1(t) \hat{\mathbf{I}}_x, \quad (1.64)$$

where a frequency offset $\omega_{\text{rf}}(t)$ appears, given by

$$\omega_{\text{rf}}(t) = \frac{d\phi_p(t)}{dt}. \quad (1.65)$$

The two magnetic field components in Equation 1.64 combine to give an effective RF field $\omega_{\text{eff}}(t)$ given by:

$$\omega_{\text{eff}}(t)^2 = \omega_{\text{rf}}(t)^2 + \omega_1(t)^2 \quad (1.66)$$

which is tilted with respect to the z-axis by an angle $\theta(t)$, which is given by

$$\tan(\theta(t)) = -\frac{\omega_1(t)}{\omega_{\text{rf}}(t)} \quad (1.67)$$

For conventional pulses, the RF field amplitude is constant, *i.e.* $\omega_1(t) = \omega_1$, while the phase varies as $\phi_p(t) = \phi_0 - \Omega t$, which results in the pulse having an effective transmitter offset of $-\Omega$. For static samples, this results in a pulse Hamiltonian in the modulated frame of

$$\hat{\tilde{\mathcal{H}}}_p(t) = \Omega \hat{\mathbf{I}}_z + \omega_1 \hat{\mathbf{R}}_z(\phi_0) \hat{\mathbf{I}}_x \hat{\mathbf{R}}_z^{-1}, \quad (1.68)$$

and the effective field and tilt angles are given respectively by

$$\omega_{\text{eff}}^2 = \Omega^2 + \omega_1^2, \quad (1.69)$$

and

$$\tan(\theta) = \frac{\omega_1}{\Omega}. \quad (1.70)$$

In order to develop an expression for the adiabatic condition of a generic adiabatic pulse, we start from the Hamiltonian $\hat{\mathcal{H}}(t)$ in the rotating frame, which is a sum of the RF Hamiltonian $\hat{\mathcal{H}}_p(t)$ and a term taking in to account the possible time-dependence of the chemical shift:

$$\hat{\mathcal{H}}(t) = \Omega(t)\hat{\mathbf{I}}_z + \hat{\mathcal{H}}_p(t) \quad (1.71)$$

$$= \Omega(t)\hat{\mathbf{I}}_z + \omega_1(t)\hat{\mathbf{R}}_z(\phi_p(t))\hat{\mathbf{I}}_x\hat{\mathbf{R}}_z(\phi_p(t))^{-1}, \quad (1.72)$$

where $\Omega(t)$ is a term containing the isotropic and anisotropic contributions to the shift. This Hamiltonian can then be transformed into the frequency-modulated frame:

$$\hat{\mathcal{H}}^{(0)}(t) = [\Omega(t) - \omega_{\text{rf}}(t)]\hat{\mathbf{I}}_z + \omega_1(t)\hat{\mathbf{I}}_x \quad (1.73)$$

$$= \omega_{\text{eff}}^{(0)}(t)\hat{\mathbf{R}}_y(\theta^{(0)}(t))\hat{\mathbf{I}}_z\hat{\mathbf{R}}_y(\theta^{(0)}(t))^{-1}, \quad (1.74)$$

where the effective field $\omega_{\text{eff}}^{(0)}(t)$ and its tilt angle $\theta^{(0)}(t)$ are given by:

$$\omega_{\text{eff}}^{(0)}(t)^2 = [\Omega(t) - \omega_{\text{rf}}(t)]^2 + \omega_1(t)^2, \quad (1.75)$$

$$\tan(\theta^{(0)}(t)) = \frac{\omega_1(t)}{\Omega(t) - \omega_{\text{rf}}(t)} \quad (1.76)$$

A second transformation is now possible in to a frame which follows the effective field, referred to as the adiabatic frame [55]. This transformation gives

$$\hat{\mathcal{H}}^{(1)}(t) = \hat{\mathbf{R}}_y(\theta^{(0)}(t))^{-1}\hat{\mathcal{H}}^{(0)}(t)\hat{\mathbf{R}}_y(\theta^{(0)}(t)) - \dot{\theta}^{(0)}(t)\hat{\mathbf{I}}_y \quad (1.77)$$

$$= \omega_{\text{eff}}^{(0)}(t)\hat{\mathbf{I}}_z - \dot{\theta}^{(0)}(t)\hat{\mathbf{I}}_y. \quad (1.78)$$

This Hamiltonian is the sum of two terms, a large field along the z-axis and a comparatively small field along the y-axis. At this point, we can define a way to grade the pulse by the definition of the so-called quality factor $Q^{(1)}$:

$$\frac{1}{Q^{(1)}} = \max \left| \frac{\dot{\theta}^{(0)}(t)}{\omega_{\text{eff}}^{(0)}(t)} \right| \quad (1.79)$$

$$= \max \left| \frac{\dot{\omega}_1(t)[\Omega(t) - \omega_{\text{rf}}(t)] - \omega_1(t) [\dot{\Omega}(t) - \dot{\omega}_{\text{rf}}(t)]}{\omega_{\text{eff}}^{(0)}(t)^3} \right|. \quad (1.80)$$

If the pulse is efficient (*i.e.* $Q^{(1)} \gg 1$), this implies that rate of change of $\theta^{(0)}$ is negligible with respect to the effective field, then the Hamiltonian in the adiabatic frame simplifies to

$$\hat{\mathcal{H}}^{(1)}(t) \approx \omega_{\text{eff}}^{(0)} \hat{\mathbf{I}}_z \quad (1.81)$$

For a spin in a static sample (thus making $\Omega(t)$ time-independent), the adiabatic condition is most likely to be violated when the carrier frequency is exactly resonant with the spin, at which point the effective field is at its lowest while the tilt angle is changing most rapidly. At this point the adiabatic condition can be rewritten as

$$\frac{1}{Q^{(1)}} = \frac{\dot{\omega}_{\text{rf}}(t)}{(\omega_1^{\text{max}})^2} \quad (1.82)$$

Thus, the adiabatic condition is $\dot{\omega}_{\text{rf}}(t) \ll (\omega_1^{\text{max}})^2$. In other words, this means that the rate at which the pulse is swept must be much lower than the square of the maximum RF amplitude. Thus, a shaped pulse can be improved simply by increasing the RF field amplitude or by decreasing the sweep rate of the pulse in static experiments.

Finally, we can consider the effects of MAS on the quality of the pulse. During magic angle spinning we must consider the effect of the periodic modulation of the SA during MAS. As such, the time-dependent offset $\Omega(t)$ must be replaced with the explicit for the SA during MAS as given in Equation 1.53. This offset is now a term comprising both the isotropic and SA terms, which when combined with the RF field results in an effective field $\omega_{\text{eff,c}}^{(0)}(\gamma; t)$ and tilt angle $\dot{\theta}_c(\gamma; t)$ of

$$\omega_{\text{eff,c}}^{(0)}(\gamma; t) = \sqrt{(\Omega_{\text{iso}} + \Omega_c^{\text{SA}}(\gamma; t) - \omega_{\text{rf}})^2 + \omega_1(t)^2}, \quad (1.83)$$

$$\dot{\theta}_c(\gamma; t) = \frac{\dot{\omega}_1(t) [\Omega_{\text{iso}} + \Omega_c^{\text{SA}}(\gamma; t) - \omega_{\text{rf}}] - \omega_1(t) [\dot{\Omega}_c^{\text{SA}}(\gamma; t) - \dot{\omega}_{\text{rf}}(t)]}{\omega_{\text{eff,c}}^{(0)}(\gamma; t)^2}. \quad (1.84)$$

Thus, in order to evaluate the performance of a SHAP we must determine the point at which the ratio $|\dot{\theta}_c(\gamma; t)/\omega_{\text{eff,c}}^{(0)}(\gamma; t)|$ is at its largest, which gives an expression for the quality factor $Q^{(1)}$ of

$$\frac{1}{Q^{(1)}} = \max \left| \frac{\dot{\omega}_1(t) [\Omega_{\text{iso}} + \Omega_c^{\text{SA}}(\gamma; t) - \omega_{\text{rf}}] - \omega_1(t) [\dot{\Omega}_c^{\text{SA}}(\gamma; t) - \dot{\omega}_{\text{rf}}(t)]}{\omega_{\text{eff,c}}^{(0)}(\gamma; t)^3} \right|, \quad (1.85)$$

which is a difficult expression to evaluate in general [13]. The modulation of the SA during MAS causes both the magnitude of the effective field and the tilt angle to change rapidly, which effectively reduces $Q^{(1)}$ and therefore the adiabaticity of the pulse. For the case of an axially symmetric SA, it was proposed that the effective adiabatic condition for SHAPs can be given as [5]

$$\omega_{1, \text{max}} > \sqrt{1.41 \Delta \sigma \omega_0 \omega_r}. \quad (1.86)$$

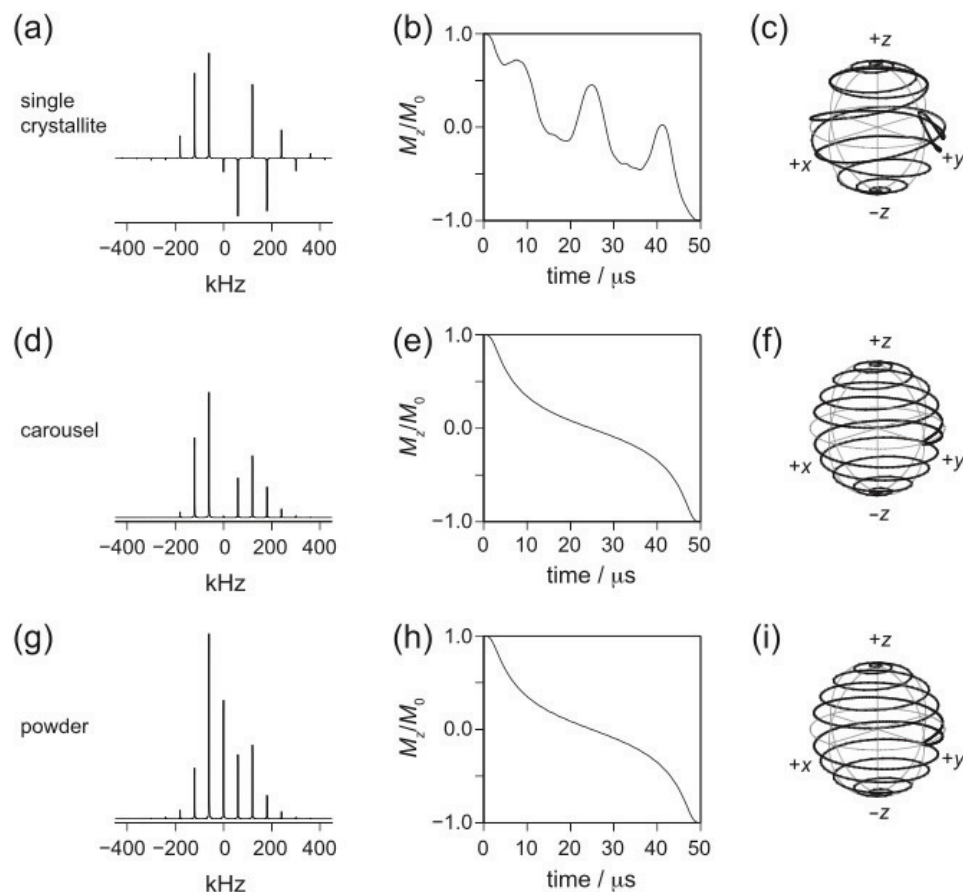


Figure 1.7: Simulations of the magnetization trajectory during inversion by a SHAP [5]. Trajectories are shown for a single crystallite orientation (a-c), a whole carousel (d-f), and a powder (g-i) using SA tensor components of $\delta = 0$, $\Delta\delta = 200$ kHz, $\eta = 0.3$ and a MAS rate of 60 kHz. A simulated spectrum of a single crystallite with an orientation of $(\alpha, \beta, \gamma) = (0^\circ, 50^\circ, 0^\circ)$ is shown in (a). The inversion trajectory of the z-component of the magnetization during the SHAP is shown in (b), and exhibits oscillations in the inversion trajectory due to modulation of the SA during MAS. A 3D representation of the trajectory is shown in (c). The 1D spectrum of the carousel of crystallites with orientation $(\alpha, \beta) = (0^\circ, 50^\circ)$ is given in (d), with the corresponding z-component and 3D magnetization trajectories given in (e) and (f), respectively. The oscillations observed in (b) and (c) have been averaged out, and now result in smooth inversion trajectories. The simulated spectrum of a full powder is given in (g), with corresponding 1D and 3D magnetization trajectories given in (h) and (i). In all cases, the simulated SHAP utilized a tanh/tan shape [52] sweeping through 5 MHz in 50 μs with a maximum RF field amplitude of 400 kHz. Reprinted from Reference [13] with permission from Elsevier.

To compensate for this decrease in pulse efficiency, it is necessary to dramatically increase the pulse sweep width (to 1-10 MHz) and RF field strength (to 100s of kHz), and these combined permit a much shorter pulse to be used, on the order of 10s of μs . The effects of SA oscillations on the inversion profile of a SHAP applied to a spin with a large anisotropy during MAS can be appreciated in Figure 1.7.

Despite the fact that extremely high RF fields are required to obtain efficient SHAPs, when applied properly SHAPs can effectively invert or refocus spins spanning a frequency range of a few MHz [5, 13]. SHAPs have proven to be particularly versatile, and have been applied to a number of traditional solid-state NMR sequences, such as the spin-echo sequence [5], the multiple-echo acquisition CPMG sequence [40], the TEDOR sequence [5], and the magic-angle turning (MAT) sequence [9].

Single-sideband-selective Adiabatic Pulses (S^3APs)

The high RF field requirements for SHAPs, typically many times the rotational frequency [13], can be a limitation for studies where such high RF fields cannot be practicably achieved, such as for low-gamma nuclei like ^6Li , ^{13}C , ^{15}N , or ^{29}Si . Using this as motivation, a second, lower-power class of broadband swept-frequency RF pulses was introduced in 2011 by Pell *et al.* and were dubbed the single-sideband-selective adiabatic pulses (S^3APs) [6]. These pulses typically utilize the WURST pulse shape with a frequency sweep width equal to the MAS rotation rate. By sweeping only over a single spinning sideband are able to achieve broadband inversions using very low RF field strengths, over a frequency range that more than an order of magnitude greater than the applied RF field strength [6, 14, 56], and have recently been shown to be particularly powerful when using high MAS rates of 60-111 kHz [13, 14, 56].

This section sets out to give a basic review of the mathematical treatment of S^3APs . The same analysis of the pulse performance used for SHAPs is not possible for S^3APs due to the complicated spin dynamics resulting from a pulse which is frequency-selective to a single sideband. Before considering the underlying theory, the complicated effects on the spin dynamics produced by S^3APs during spin inversions can be appreciated by first examining the magnetization trajectories of a spin system subjected to a large SA of 200 kHz with a rotation rate of 60 kHz, shown in Figure 1.8. When applied to a single crystallite orientation, the resulting magnetization trajectory during the S^3AP exhibits wild oscillations due to the modulation of the SA during MAS, shown in Figure 1.8 (b) and (c). The quality factor of this pulse is much less than 1, indicating that the magnetization is not locked to the effective field of the pulse, and thus is not adiabatic. However, the inversion trajectories in the case of a carousel of crystallites, shown in Figure 1.8 (e) and (f), and a full powder, shown in Figure 1.8 (h) and (i), do not exhibit the same oscillations, indicating that oscillations are cancelled upon averaging over γ . It is noteworthy that these trajectories resemble those observed in the case of SHAPs in Figure 1.7, and provide a hint that the pulse may be treated as adiabatic given an appropriate description of the pulse.

S^3APs are frequency-swept pulses which are selective to a single sideband and operate in the low-power limit, *i.e.* $\omega_1 \ll \omega_r$. These pulses are best described in the so-called jolting

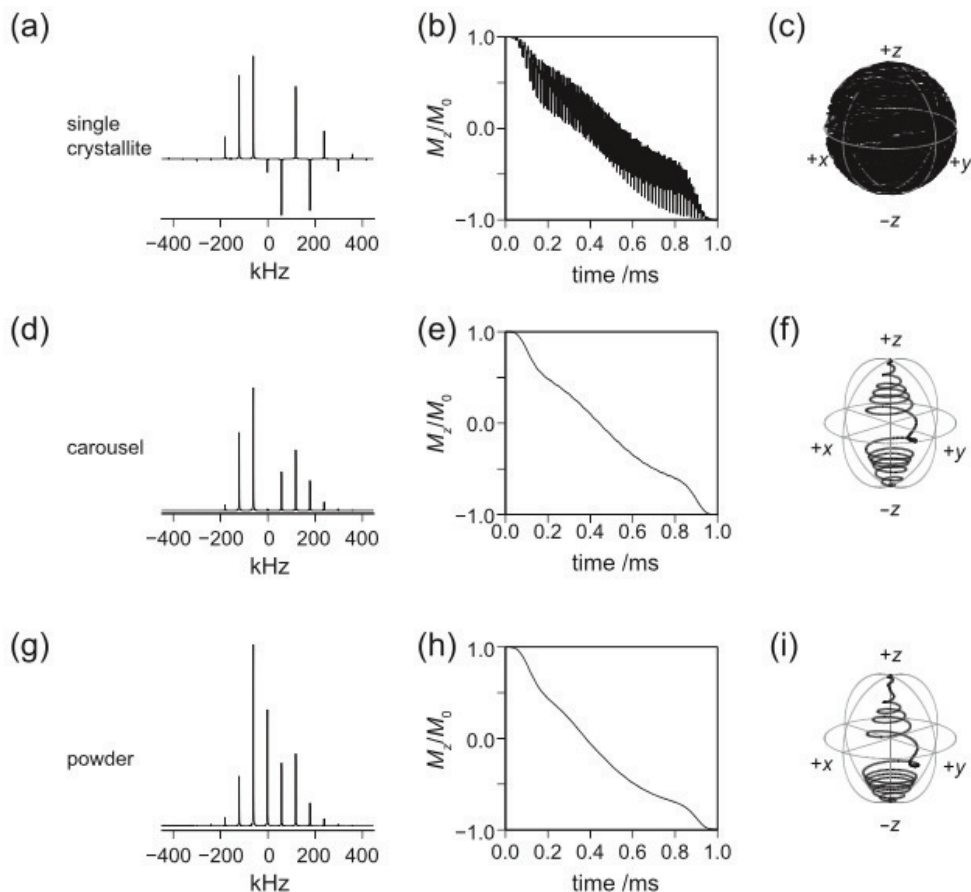


Figure 1.8: Simulations of the magnetization trajectory during inversion by a S^3 AP [6]. Trajectories are shown for a single crystallite orientation (a-c), a whole carousel (d-f), and a powder (g-i) using SA tensor components of $\delta = 0$, $\Delta\delta = 200$ kHz, $\eta = 0.3$ and a MAS rate of 60 kHz. A simulated spectrum of a single crystallite with an orientation of $(\alpha, \beta, \gamma) = (0^\circ, 50^\circ, 0^\circ)$ is shown in (a). The inversion trajectory of the z-component of the magnetization during the S^3 AP is shown in (b), and exhibits large, violent oscillations due to modulation of the SA during MAS. A 3D representation of the trajectory is shown in (c). The magnetization vector wildly oscillates during the pulse and crosses itself many times, resulting in the crowded nature of (c). The 1D spectrum of the carousel of crystallites with orientation $(\alpha, \beta) = (0^\circ, 50^\circ)$ is given in (d), with the corresponding z-component and 3D magnetization trajectories given in (e) and (f), respectively. The oscillations observed in (b) and (c) have been averaged out, and now result in smooth inversion trajectories. The simulated spectrum of a full powder is given in (g), with corresponding 1D and 3D magnetization trajectories given in (h) and (i). In all cases, the simulated S^3 AP utilized a WURST-20 shape [53] sweeping through 60 kHz in 1 ms, applied to the +2 order sideband, with a maximum RF field amplitude of 50 kHz. Reprinted from Reference [13] with permission from Elsevier.

frame, which is a frame of the interaction representation of the time-dependent chemical shift interaction, and is generally applicable to pulses in the low-power limit [57] which are selective to a single band. In this frame, the Hamiltonian of an amplitude and phase modulated pulse applied to the n^{th} sideband is given as

$$\begin{aligned} \hat{\mathcal{H}}(t) = & \omega_1(t) \hat{\mathbf{R}}_z(\phi_p(t)) \left\{ \sum_{m=-\infty}^{+\infty} A_c^{(m)} \hat{\mathbf{R}}_z(\phi_c^{(m)}(\gamma) + (m-n)\omega_r t)^{-1} \right. \\ & \left. \times \hat{\mathbf{I}}_x \hat{\mathbf{R}}_z(\phi_c^{(m)}(\gamma) + (m-n)\omega_r t) \right\} \hat{\mathbf{R}}_z(\phi_p(t))^{-1}, \end{aligned} \quad (1.87)$$

which describes a pulse with RF field amplitude $\omega_1(t)$ and phase $\phi_p(t)$ applied to the n^{th} order sideband with an offset of $(m-n)\omega_r t$, and where $A_c^{(m)}$ and $\phi_c^{(m)}(\gamma)$ describe the intensity and phase of the m^{th} order sideband [6, 13]. From this we can see that the Hamiltonian can be described as a superposition of RF fields with carrier frequencies separated by ω_r , and with relative amplitudes and phases given by the sideband amplitudes and phases. To be more specific, the field that is applied with a carrier frequency of $(m-n)\omega_r$ relative to the n^{th} -order sideband has a RF field amplitude of $\omega_1(t)A_c^{(m)}$ and a phase that is offset from $\phi_p(t)$ by a constant value of $-\phi_c^{(m)}(\gamma)$. This Hamiltonian can accordingly be separated into a sum of terms with $m \neq n$ superimposed upon the smooth variation of the sweep (which gives rise to the oscillations seen in Figure 1.8 (b)), and a term for $m = n$ that does not oscillate. For conventional pulses this last term is given by the first-order average Hamiltonian [58, 59], however average Hamiltonian theory is not applicable due to the rapid variations of phase and amplitude relative to the timescale of the NMR experiment [60] and so Floquet theory must be used [61], which is used to describe the smooth part of the inversion trajectory in the low-power regime, given by the term with $m = n$:

$$\hat{\mathcal{H}}(t) = \omega_1(t) A_c^{(n)} \hat{\mathbf{R}}_z(\phi_p(t) - \phi_c^{(n)}) \hat{\mathbf{I}}_x \hat{\mathbf{R}}_z(\phi_p(t) - \phi_c^{(n)})^{-1}, \quad (1.88)$$

which has the relatively simple form of an adiabatic pulse applied on resonance with an RF field amplitude scaled by $A_c^{(n)}$ and with a constant phase of $-\phi_c^{(n)}$ added to the time-dependent phase.

This Hamiltonian can subsequently be transformed back to the frequency-modulated frame, then to the adiabatic frame, and the quality factor $Q^{(1)}$ can be determined:

$$\frac{1}{Q^{(1)}} = \max \left| \frac{\dot{\theta}^{(0)}(t)}{\omega_{\text{eff}}^{(0)}(t)} \right| \quad (1.89)$$

$$= \max \left| \frac{\omega_1(t) \dot{\omega}_{\text{rf}}(t) - \dot{\omega}_1(t) \omega_{\text{rf}}(t)}{[\omega_{\text{rf}}(t)^2 + (\omega_1(t) A_c^{(n)})^2]^{3/2}} \right| A_c^{(n)}. \quad (1.90)$$

As before, this condition is most likely violated when the transmitter is on resonance in the jolting frame and the effective field is maximal, resulting in the most rapid change in the tilt angle. In this case the adiabatic condition simply becomes

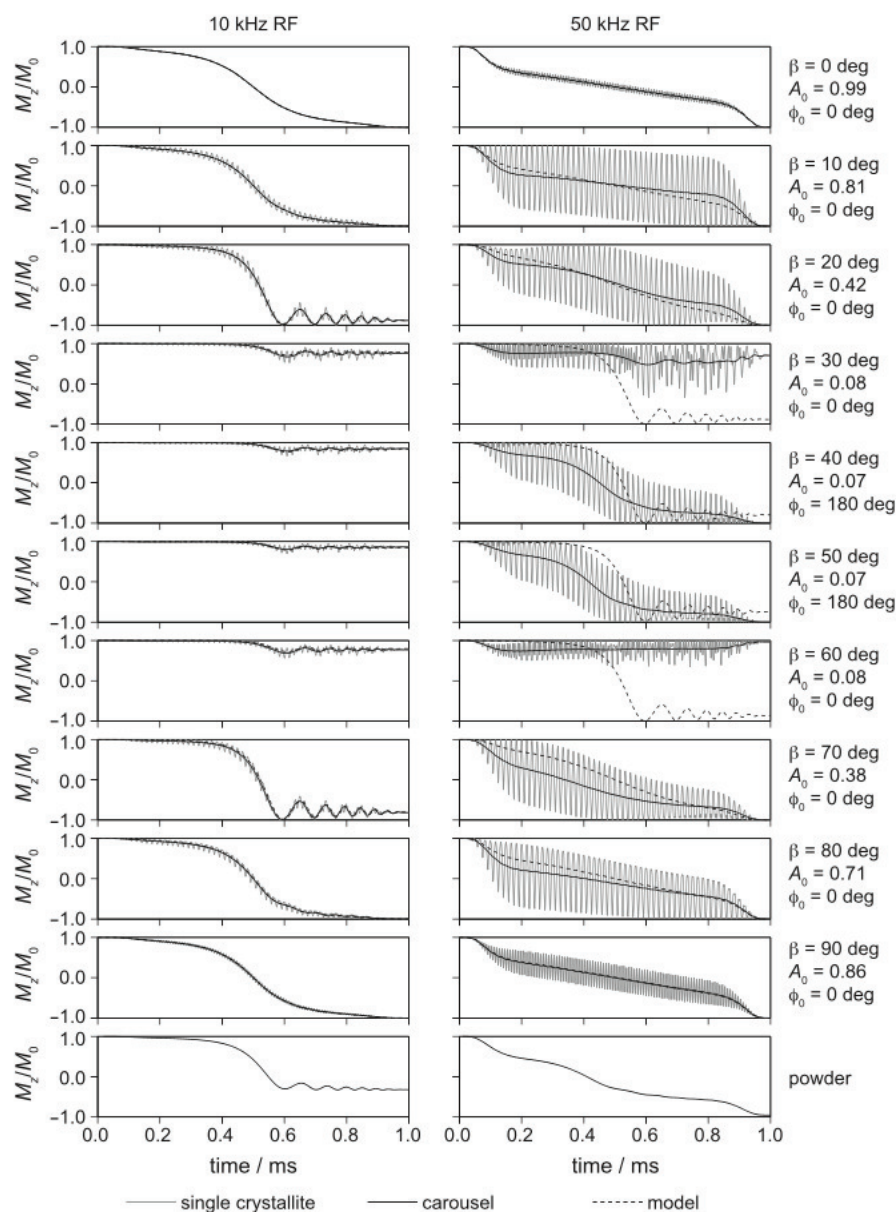


Figure 1.9: Comparison of exact simulation of the inversion trajectories produced by a S^3AP under MAS with a simple isotropic model for different crystallite orientations. The shift tensor parameters used were $\delta = 0$, $\Delta\delta = 200$ kHz, and $\eta = 0.3$. The MAS rate was 60 kHz. The S^3AP is a WURST-20 pulse applied to the centerband which sweeps through 60 kHz in 1 ms at RF field amplitudes of 10 kHz (left-hand column) and 50 kHz (right-hand column). Simulated results are shown for a range of ten values of β from 0° to 90° in steps of 10° ; while α and γ were held constant at 0° . The inversion pathways are shown for the single crystallite (grey full line) and the carousel (black full line), and are shown with the inversion pathways simulated assuming an isotropic spin system in which the RF field amplitude is scaled down by the centerband intensity $A_c^{(0)}$ as shown in Eq. (145) (black dashed line). The match between the exact simulated and model for the WURST pulse at the RF field amplitude of 10 kHz (left-hand column) is excellent. However, only partial inversion is seen for the powder resulting from the effective scaling down of the RF field as discussed in the text. Raising the RF field amplitude to 50 kHz delivers 100% inversion, but the inversion trajectories for some of the crystallites depart from those calculated in the low-power approximation. Reprinted from Reference [13] with permission from Elsevier.

$$\dot{\omega}_{\text{rf}}(\tau_{\text{p}/2}) \ll (A_{\text{c}}^{(n)}\omega_1^{\text{max}})^2, \quad (1.91)$$

which is the same as in the static case, except with the RF field amplitude scaled by the intensity of the irradiated sideband, $A_{\text{c}}^{(n)}$.

As such, the quality factor, and thus the performance, of the pulse depends heavily on the sideband intensity. As the sideband intensity varies as a function of the crystallite orientation, it may be expected that S³APs do not work uniformly for all crystallites. Figure 1.9 gives simulated inversion trajectories during a WURST-20 S³AP during 60 kHz MAS for a spin experiencing a large SA in a series of crystallite orientations, each with $(\alpha, \gamma) = (0^\circ, 0^\circ)$, while β was varied from 0° to 90° in steps of 10° for two RF field strengths: 10 kHz and 50 kHz, with a simulation for the full powder given at the bottom. Irradiation with 10 kHz results in severe spatial biasing, as the crystallites with $\beta = 30$ -60 kHz have very low sideband intensities, and thus do not satisfy the adiabatic condition, whereas a higher RF field strength greatly improves the performance. This feature will be explored in more detail in Chapter 3.

1.3 The experimental PNMN toolkit

1D methods

As with conventional NMR characterization of diamagnetic materials in solution and the solid-state, 1D experiments are the most widely used for basic characterization of paramagnetic materials in the solid state. The simplest one-pulse experiment shown in Figure 1.10 (a) would be ideal for paramagnetic samples due to the large bandwidth achievable with short RF excitation pulses, yet it often fails for paramagnetic systems due to the receiver delay, δ_{e} , which is often about 5 μs in length and serves to protect the receiver from acquiring the RF pulse. During this delay time, rapid signal dephasing typical of paramagnetic samples causes the acquired signal to exhibit a significant distortion in the line shape due to the necessity of applying a large first-order phase correction, exhibited in the one-pulse ⁷Li and ³¹P spectra of LiFe_{0.5}Mn_{0.5}PO₄ given in Figure 1.11 (a) and (b). The use of the spin echo sequence [47] in Figure 1.10 (b) mitigates this issue by absorbing δ_{e} in to an echo shift period, τ_{echo} , and therefore a flat baseline can be achieved, as seen in the ⁷Li spectrum in Figure 1.11 (c). This approach has a serious drawback, though, because the π pulse used for refocusing has a very limited band width, which is typically less than the RF field amplitude of the pulse. This effect is exhibited in the ³¹P spin echo spectrum in Figure 1.11 (d). In this case, the spectrum is convoluted with the excitation band width profile of the π pulse used in the experiment, which had an RF field amplitude of 417 kHz. This problem can in turn be mitigated by the use of adiabatic SHAP refocusing pulses using the double adiabatic echo sequence shown in Figure 1.10 (c), with the resulting ⁷Li and ³¹P spectra given in Figure 1.11 (e) and (f). The ⁷Li spectrum is largely unchanged compared to the spin echo case, with very minor improvements increases in the extremal sidebands. A huge improvement in the line shape is observed for the ³¹P spectrum, though, owing to the increased band width of the refocusing

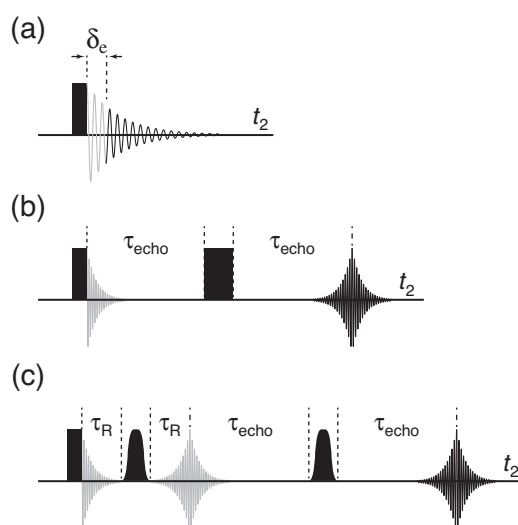


Figure 1.10: (a) The one pulse experiment. The term δ_e denotes the receiver delay, a hardware limitation that prevents acquisition immediately following the excitation pulse, denoted by the narrow filled black rectangle. (b) The spin echo sequence [47], with the π refocusing pulse denoted by the broader filled black rectangle. The echo evolution time, τ_{echo} , may be set as short as a single rotor period to prevent sensitivity losses for samples with very short coherence lifetimes, while this evolution time may be set much longer in principle to allow acquisition of the full echo. (c) The double adiabatic echo sequence [5]. As given, this sequence assumes that the swept frequency pulse, denoted by the shape between dashed lines, has a length equal to an integer multiple of rotor periods. As in the case of the spin echo sequence given in (b), the echo evolution time, τ_{echo} , may be set as short as a single rotor period or to any multiple of rotor periods as desired. In all cases the simulated free induction decays given in light grey denote those which are not observed, whereas those given in black indicate that the receiver is on.

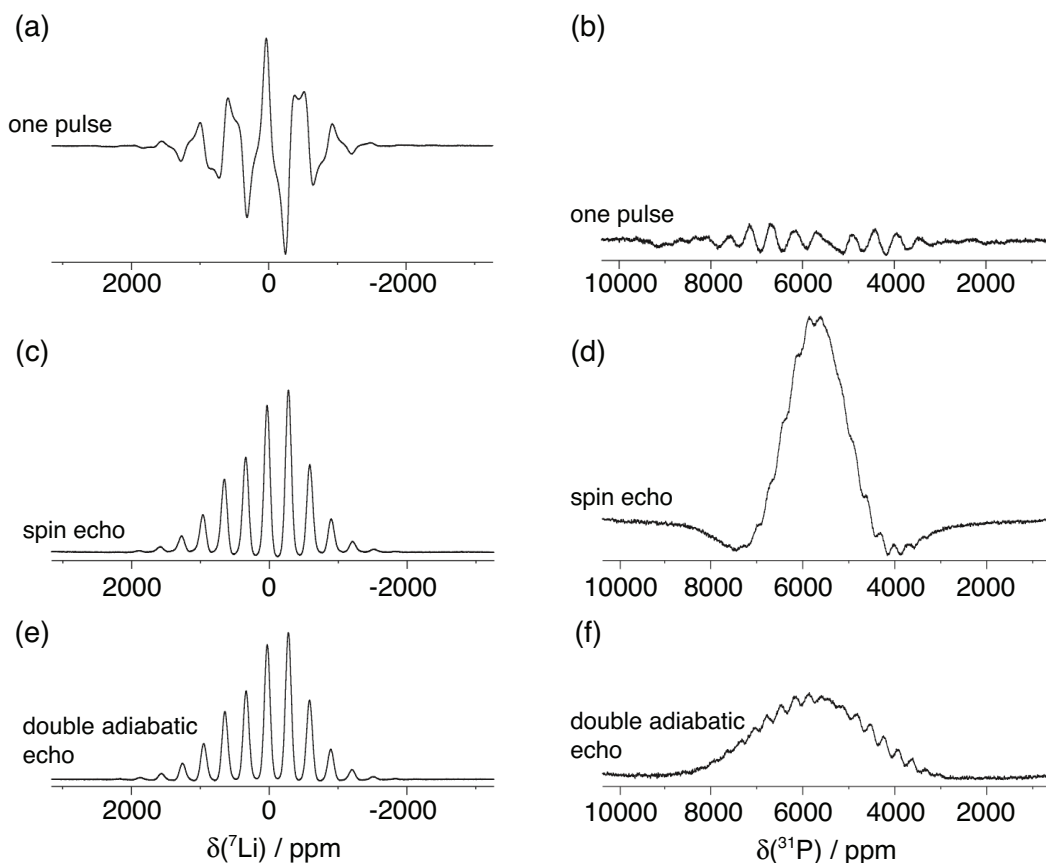


Figure 1.11: A collection of one-pulse (a, b), spin echo (c,d), and double adiabatic echo (e, f) spectra of $\text{LiFe}_{0.5}\text{Mn}_{0.5}\text{PO}_4$ for ^7Li (a, c, e) and ^{31}P (b, d, f). Nominal $\pi/2$ pulses were used for excitation in all cases, and nominal π pulses were used for refocusing in (c) and (d). The SHAPs used in (e) and (f) were tanh/tan shape sweeping through 5 MHz with a length of 50 μs . The RF field amplitudes for all pulses were 455 and 417 kHz for ^7Li and ^{31}P , respectively. Adapted and reprinted from Reference [13] with permission from Elsevier.

SHAPs. Although the double adiabatic echo sequence is used most widely throughout this thesis for 1D acquisitions, it should be noted that it is not a perfect solution. All adiabatic pulses have a large excitation band width relative to the RF field used, and this increase in bandwidth is paid for by a significant increase in the pulse length compared to conventional RF pulses. As such the use of SHAPs comes at a cost: significant sensitivity losses can be observed in samples with strong PRE due to the the relatively (and necessarily) long length of the pulse. While in general this sequence is the most robust, the spin echo sequence is often more sensitive for spectra which exhibit a narrow range of observed frequencies relative to the maximum available RF field amplitude for a given nucleus and probe.

2D methods

Although 1D NMR methods are most commonly used for basic characterization of paramagnetic materials, 2D methods, like homo- and heteronuclear correlation (HETCOR) experiments or 2D sideband-separation experiments, are often necessary to achieve site-specific resolution and experimental resonance assignments. Because CP-based dipolar polarization transfers for

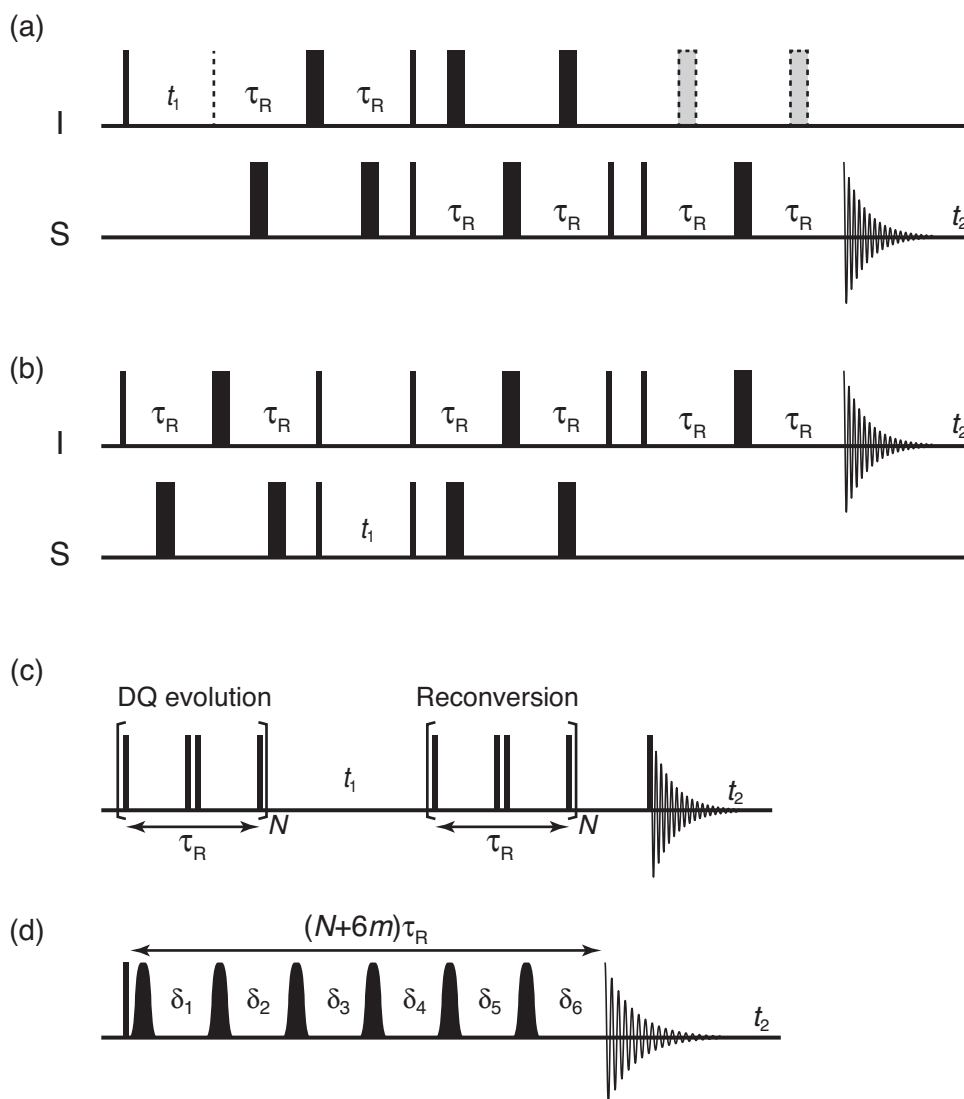


Figure 1.12: (a) The 2D TEDOR sequence [3, 48]. The narrow and broader filled black rectangles indicate $\pi/2$ and π pulses, respectively. The grey rectangles bordered by dashed black lines on the I-channel are dephasing pulses, which can be optionally used to distinguish between CH, CH₂, and CH₃ groups [3]. (b) The 2D HSQC-like TEDOR spectrum, conceptually the same as before however the t_1 evolution is on the S channel, followed by a transfer back to the I channel for acquisition. (c) The 2D BABA sequence [62]. Double quantum coherences are generated during the first block of $\pi/2$ pulses, followed by t_1 evolution, and then reconversion back to zero-quantum coherence and subsequent excitation for detection by the final $\pi/2$ pulse. (c) the 2D aMAT sequence [9, 63] where the total time of the sequence is equal to the sum of the isotropic evolution time, $N\tau_R$ (where $N \neq 3n$ and where n is an integer), and the length of 6 SHAPs each having a length $m\tau_R$. The odd-numbered SHAPs are kept constant in time whereas the even-number SHAPs are incremented forward in time for positive time evolution of the isotropic shift (echo type) or backward in time for negative time evolution (anti-echo type) [9]. The combination of both echo and anti-echo type acquisition results in an absorption-mode lineshape in the indirect dimension.

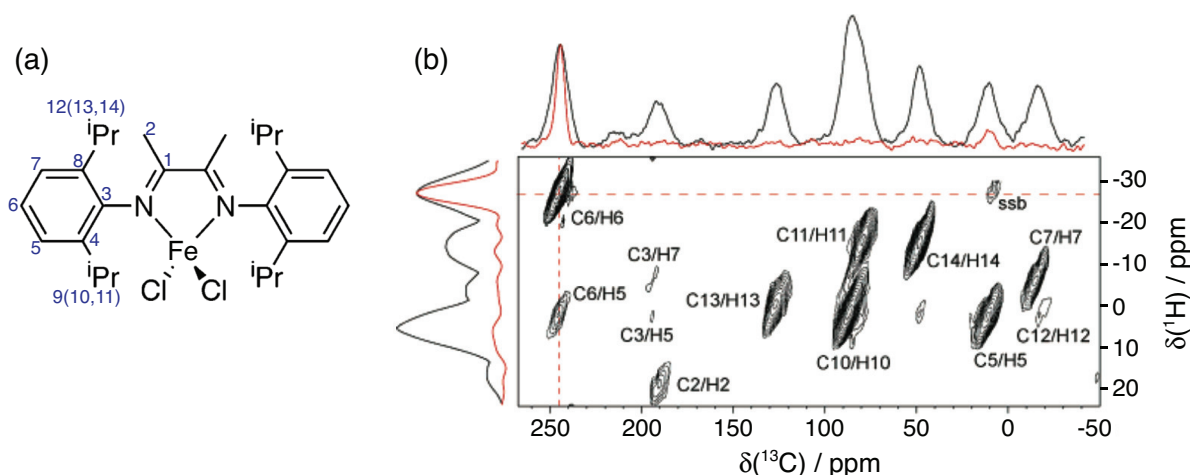


Figure 1.13: (a) The structure of DIAD-Fe^(II) with labels given by each carbon nucleus in blue. For the ¹Pr moieties, the two values in parenthesis correspond to the two inequivalent methyl groups. The molecule exhibits *C_s* symmetry, and as such the two sides of the DIAD ligand are equivalent. (b) The 2D TEDOR ¹H–¹³C heteronuclear correlation spectrum of DIAD-Fe^(II) using a MAS rotation rate of 33 kHz (recoupling time 60 μs). The red spectra set in to the axis projections correspond to the traces along the red dashed lines in the spectrum. Adapted with permission from Reference [3]. Copyright 2006 American Chemical Society.

paramagnetic materials are typically inefficient, it is necessary to achieve transfer of polarization from protons via short dipolar-recoupling sequences that use high-powered short RF pulses, such as the HETCOR variant of the TEDOR sequence [3, 48], the Dipolar Insensitive Nucleus Enhanced by Polarization Transfer (DINEPT) sequence [64], or the Dipolar Heteronuclear Single-Quantum Correlation (DHSQC) sequence [65]. The 2D TEDOR sequence in Figure 1.12 (a) has been proven to be particularly effective due to the relatively short and efficient dipolar recoupling period. An example 2D TEDOR spectrum of the Fe^(II) (*S* = 2) containing complex DIAD-Fe^(II) dichloride (DIAD: 2,3-dimethyl-1,4-[(2',6')-diisopropylphenyl]-*N,N'*-diazediene, Figure 1.13 (a)) is given in Figure 1.13 (b) [3]. Eight major resonances corresponding to eight of the nine C–H pairs in the molecule are observed, as well as a few additional weaker resonances corresponding to more distant coupled C–H pairs. These results powerfully illustrate the potential of the TEDOR sequence for broadband H–C correlations, though it should be noted that the quality of these results may not be always observed. In this sample the ¹³C nuclei directly bonded to protons have chemical shifts spanning a range of less than 300 ppm, and as such conventional π pulses using large albeit practicable RF fields provide sufficient bandwidth to cover this range. This cannot be expected to be generally true for all paramagnetic complexes, as will be shown in later chapters for larger spans of ¹³C resonances.

Heteronuclear correlations achieved by 2D TEDOR or similar techniques represent a major step towards assignment of resonances in small to medium-sized paramagnetic complexes, and indeed, with the aid of computational techniques may permit full assignment of the observed resonances [3]. However, homonuclear correlations, in particular correlations between nearby ¹H atoms in organic ligands, would help to clarify the assignment perhaps without the need of computational methods. The most widely used technique for this in solid-state NMR is the Radio

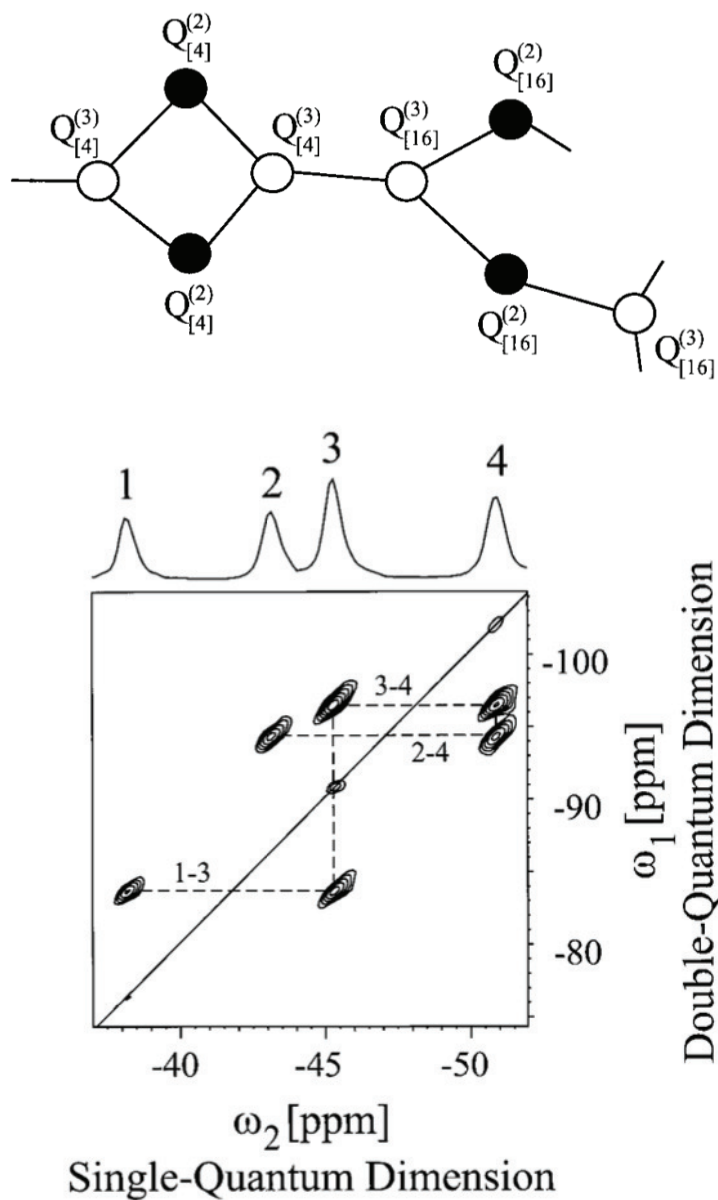


Figure 1.14: (above) A schematic representation of the $\text{MgP}_4\text{O}_{11}$ network, which consists of four nonequivalent phosphate groups. The structure of $\text{MgP}_4\text{O}_{11}$ consists of corrugated sheets of linked rings containing 4 or 16 PO_4 tetrahedra. (below) The 2D BABA spectrum of $\text{MgP}_4\text{O}_{11}$ recorded using an MAS rotation rate of 14.2 kHz using a 4 mm Bruker MAS probe [62]. The spectrum exhibits three correlated pairs of ^{31}P nuclei, consistent with the structure given above. Reprinted from [62] with permission from Elsevier.

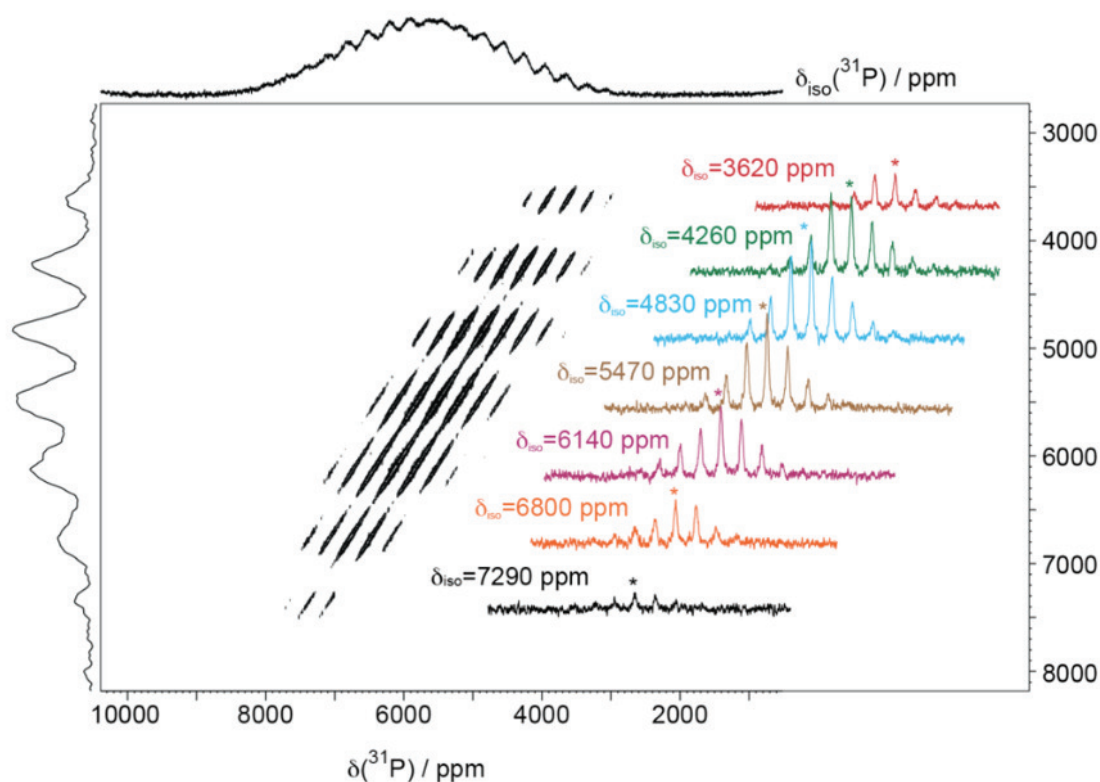


Figure 1.15: The 2D aMAT spectrum of $\text{LiFe}_{0.5}\text{Mn}_{0.5}\text{PO}_4$ acquired with a MAS rotation rate of 60 kHz using a Bruker 1.3 mm probe [9]. Reprinted with permission from [9]. Copyright 2012 American Chemical Society.

Frequency-driven Dipolar Recoupling (RFDR) experiment [66], which mixes nuclear coherences by way of a train of π pulses. Due to the limited excitation bandwidth of π pulses in general, a long train of 50 or more pulses over 100s or 1000s of μs will result not only in spectral biasing due to accumulated pulse bandwidth issues, but potentially significant relaxation losses due to T_1 relaxation during this period. A method using $\pi/2$ pulses, which have much greater bandwidth than π pulses, over a shorter recoupling period is the single-quantum (SQ) – double-quantum (DQ) back-to-back experiment [62], with the pulse sequence given in Figure 1.12 (b). This experiment correlates the single-quantum resonance of two nuclei by way of the evolution of the a double quantum resonance of the pair; as such, the two single quantum resonances with frequencies ω_1 and ω_2 in the direct dimension will both have a frequency of $\omega_1 + \omega_2$ in the indirect dimension. This is illustrated on the 2D ^{31}P BABA spectrum of $\text{MgP}_4\text{O}_{11}$ in Figure 1.14 [62]. When applied to protons in paramagnetic organometallic complexes, the BABA experiment is a powerful method to resolve and assign ^1H peaks, as will be shown in Chapter 5.

Finally, due to large anisotropic effects induced by paramagnetic centers on the NMR resonances of nuclei in paramagnetic complexes, a significant number of sidebands or some or all of the resonances may be observed. This often results in spectra consisting of many isotropic resonances overlapping with spinning sidebands. Of course, this problem can be addressed simply by rotating at a faster rate, but in extreme cases even MAS rates up to 60 kHz cannot resolve this issue. 2D sideband separation experiments like the Magic Angle Turning (MAT) sequence

[63] or the Phase Adjusted Spinning Sidebands (PASS) sequence [67] address this issue by suppressing spinning sidebands in the direct (PASS) or indirect (MAT) dimensions, thus achieving a 2D spectrum correlating pure isotropic frequencies to mixed isotropic/anisotropic frequencies, the latter of which can be transformed to pure anisotropic frequencies with an appropriate shearing transformation. These experiments use a train of π refocusing pulses with unique timings in order to result in pure isotropic evolution, but the aforementioned bandwidth problems with π pulses can cause these experiments to not work properly for paramagnetic samples. Clément *et al.* addressed this problem in the MAT experiment by the inclusion of SHAP refocusing pulses, which was dubbed the adiabatic MAT (aMAT) sequence [9], and is given in Figure 1.12 (c). The authors applied this methodology to untangle the ^{31}P resonances in the olivine-type mixed phase lithium-ion battery cathode materials with the stoichiometries $\text{LiFe}_x\text{Mn}_{1-x}\text{PO}_4$. The ^{31}P MAS NMR spectra of these mixed-phases are composed of up to 32 unique isotropic resonances, each with potentially unique principle components of the anisotropy of their shift tensors. To make matters worse, significant ABMS broadening of the lines caused severe line broadening, resulting in a 1D MAS spectrum completely devoid of any appreciable resolution. The use of aMAT (shown in Figure 1.15 on the $\text{LiFe}_{0.5}\text{Mn}_{0.5}\text{PO}_4$ composition) greatly enhanced the spectral resolution by suppression of spinning sidebands. Subsequent fitting of the isotropic projection of this spectrum permitted the identification of isotropic shifts for each of the 32 possible sites.

1.3.1 Perspectives moving forward

Astounding progress has been achieved in the field of solid-state NMR of paramagnetic systems since the groundbreaking work of Ishii *et al.* Particular progress has been made towards the structural studies of paramagnetic metalloproteins or proteins with a paramagnetic tag bound to the surface, where structural constraints from PRE and/or PCS measurements have led to a resurgence in solid-state NMR being used for the determination of protein structures [4, 17, 68–77], to name but a few examples. Applications to molecular complexes have been relatively more sparse in the literature, but nevertheless impressive progress has been made towards the determination of coordination geometries and electronic structures in paramagnetic complexes [1, 3, 8, 10, 17, 18, 65, 78–83], battery materials [9, 12, 22, 84–88], and in applications towards NMR crystallography using paramagnetic constraints [8, 89–91]. This approach has been particularly effective when coupled with state-of-the-art computational methods for calculating paramagnetic effects [3, 9, 12, 18, 19, 92–97]. The following chapters explore and expand the limits of the current PNMR methodologies with a particular focus on the use of the currently-available MAS rates of more than 100 kHz.

Chapter 2

Ultrafast MAS applied to mixed-phase olivine-type LiMPO_4 cathode phases

2.1 Introduction

World-wide demand for efficient, long-lasting, and safe Li-ion batteries (LIBs) has in recent years led to an incredible surge in research committed to this topic, with possible applications to mobile devices, electric vehicles, and grid storage. A major early advancement was made with the development of the layered oxide cathode material Li_xCoO_2 in 1980 [98], which to this day remains the most commonly used cathode material in LIBs due to its high operating voltage, despite the fact that it is unstable towards O_2 loss for $x > 0.5$ [99]. As such there has been considerable work focusing on better-performing cathode materials, with olivine-type LiMPO_4 ($M = \text{Fe}, \text{Co}, \text{Mn}, \text{or Ni}$) compositions emerging as strong candidates for the replacement of Li_xCoO_2 in LIBs. LiFePO_4 (LFP) was determined to be a particularly attractive alternative to Li_xCoO_2 due to the low toxicity of Fe compared to Co, high stability, fast charging rates, and high reversible theoretical capacity, though its low voltage (with the $\text{Fe}^{2+/3+}$ redox couple being 3.45 V vs. Li^+/Li) remains a major disadvantage as this results in a low energy density of the material [100]. LiMPO_4 phases where $M = \text{Mn}, \text{Co}, \text{or Ni}$ have comparatively higher operating voltages (4.1 V, 4.8V, and 5.0 V vs. Li^+/Li , respectively) than LFP [101–104], but slow kinetics make these pure phases undesirable, especially for applications requiring fast, sudden discharges. Mixed-phase olivine-type LiMPO_4 compositions, with one or more substitutions of other transition metals (LTMPs, TMs = Mn, Co, Ni) for Fe^{2+} in LFP, have garnered considerable interest in recent years [9, 12, 95] due to their relatively higher operating voltage compared to LFP and improved kinetics versus other pure-phase LiMPO_4 compositions. This increased performance has been proposed to arise from distortions in the local and long-range structure caused by cation substitution. It is thus crucial to determine how the local electronic structure is affected by cationic substitution in order to understand the electrochemical properties of mixed-phase LiMPO_4 .

NMR spectroscopy is, by its nature, particularly well-suited to study and understand the local variations in geometry and electronic structure in LiMPO_4 compositions that come as a result of partial cationic substitutions by studying the variations in the ^6Li and ^{31}P spectra resulting from this substitution. However, the same paramagnetic interactions between nuclei which, in principle, provide critical insight (as discussed in Chapter 1) to local variations in structure also make

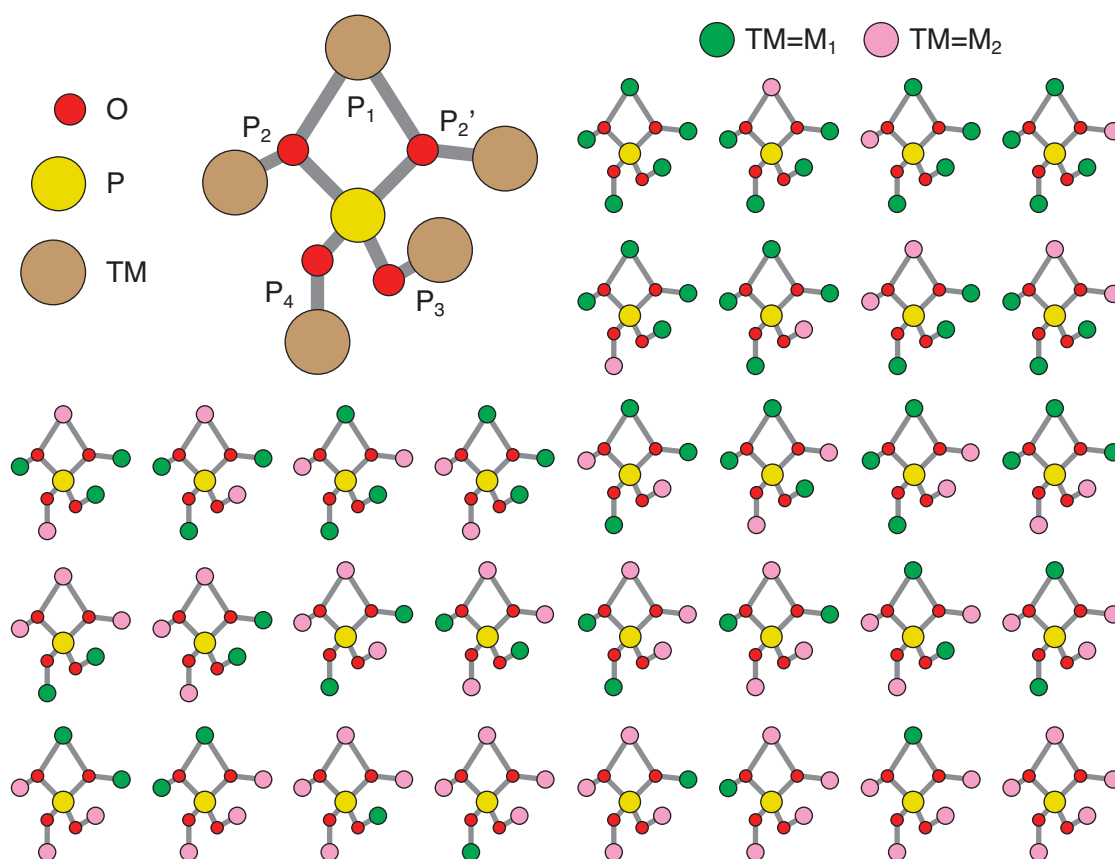


Figure 2.1: The local geometry of the PO_4 group in olivine-type LiMPO_4 phases (top left) with the spin-transfer pathway from each metal site to the P nucleus denoted for each site (P_N). Also provided are all 32 possible arrangements of TMs in binary mixed-phase LiMPO_4 compositions. Adapted with permission from [9]. Copyright 2012 American Chemical Society.

NMR spectra of these materials difficult to acquire and subsequently interpret. This is especially true for the case of ^{31}P NMR due to substantial effects resulting from through-bond interactions in olivine-type LiMPO_4 . Paramagnetic TMs induce isotropic shifts on the order of 10–1000 ppm and shift anisotropies of the order of 100–10000 ppm. Combine with this the fact that additional inhomogeneous broadening is added to the NMR line shapes by temperature gradients within the MAS rotor and potentially by anisotropic bulk magnetic susceptibility (ABMS) effects, and that in the mixed phase there are 32 possible configurations of TMs around the PO_4 (Figure 2.1), we may expect the 1D ^{31}P spectra of these compounds to be quite complex and unresolved using conventional MAS rotation rates and magnetic fields. See Figure 2.2 for an example of the combination of these effects. Indeed, prior investigations of mixed-phase LTMP compositions [9, 12] have relied on complex two-dimensional (2D) techniques [9, 105] to separate the isotropic and anisotropic components of the NMR shift in order to simplify analysis by the removal of the spinning sidebands in one dimension.

The first systematic combined experimental and theoretical NMR study of a mixed-phase LiMPO_4 was given by Clément *et al.* in 2012 on the $\text{LiFe}_x\text{Mn}_{1-x}\text{PO}_4$ ($x = 0, 0.25, 0.5, 0.75, 1$) cathode phases [9], which was carried out in part to determine the contributions of Fe^{2+} and Mn^{2+} to the measured ^{31}P shift, and also to study if substitution of Mn^{2+} for Fe^{2+} would cause

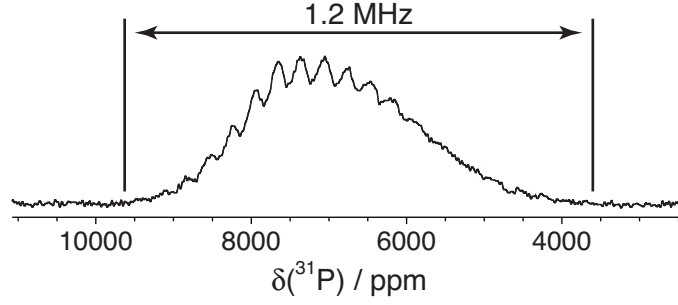


Figure 2.2: The 1D ^{31}P MAS spectra of $\text{LiFe}_{0.25}\text{Mn}_{0.75}\text{PO}_4$ acquired at $B_0 = 11.7$ T (500 MHz) and 60 kHz MAS. The combination of large isotropic contact interactions and shift anisotropies unique to each of the 32 possible arrangements of TMs in $\text{LiFe}_{0.25}\text{Mn}_{0.75}\text{PO}_4$ leads to considerable spectral overlap, resulting in a spectrum which is impossible to interpret using 1D NMR techniques at this combination of external magnetic field strength and MAS rotation rate. Adapted with permission from [9]. Copyright 2012 American Chemical Society.

observable local distortions in the PO_4 local geometry. In order to carry this out, the authors took advantage of the well-known fact from the literature that the total Fermi-contact shift of nuclei in olivine-type LiMPO_4 phases can be approximated as the sum total of all possible spin-transfer pathways to the measured nucleus [84], that is, pathways of the type $\text{TM}\cdots\text{P}$ comprising a single bridging oxygen, *i.e.* $\text{TM}-\text{O}-\text{P}$, which are labeled P_1 - P_4 in Figure 2.1. This results in a measured shift of:

$$\delta^{\text{FC}} = \sum_{\text{N}} \varepsilon_{\text{N}}. \quad (2.1)$$

where ε_{N} is the contribution from an individual metal ion along each pathway P_{N} in Figure 2.1. However, 1D ^{31}P spectra were far from having sufficient resolution, under the experimental conditions the authors used, to be able to determine the contributions of TMs from these 5 pathways. Figure 2.2 shows a representative example of this lack of observed resolution in the ^{31}P spectrum of $\text{LiFe}_{0.25}\text{Mn}_{0.75}\text{PO}_4$.

In order to achieve isotropic resolution in the ^{31}P spectra of $\text{LiFe}_x\text{Mn}_{1-x}\text{PO}_4$, the authors adapted the magic angle turning (MAT) experiment [63], used for the separation of isotropic and anisotropic interactions, for paramagnetic samples by the incorporation of swept-frequency chirped pulses [5], which was dubbed adiabatic MAT (aMAT). This experiment evolves pure isotropic shift in the indirect dimension, resulting in an isotropic spectrum upon projection along the vertical axis. The resulting isotropic aMAT projections of each of the $\text{LiFe}_x\text{Mn}_{1-x}\text{PO}_4$ compositions ($x = 0.25, 0.50, 0.75$) were then fitted simultaneously to extract the *relative* contributions, $\Delta\varepsilon_{\text{N}} = \varepsilon_{\text{N}}(\text{Mn}^{2+}) - \varepsilon_{\text{N}}(\text{Fe}^{2+})$, to each spin-transfer pathway upon substitution of Mn for Fe. A similar analysis was carried out by Strobridge *et al.* in 2014 on the mixed-phase $\text{LiFe}_x\text{Co}_{1-x}\text{PO}_4$ ($x = 0, 0.25, 0.5, 0.75, 1$) LIB cathode phases using the MATPASS experiment [105] to extract the relative contributions, $\Delta\varepsilon_{\text{N}} = \varepsilon_{\text{N}}(\text{Fe}^{2+}) - \varepsilon_{\text{N}}(\text{Co}^{2+})$, to each spin-transfer pathway upon substitution of Co for Fe. A study using DFT methods by Middlemiss *et al.* in 2013 [95] predicted the contribution to each spin-transfer pathway for Mn^{2+} , Fe^{2+} , and Co^{2+}

	LiMnPO ₄		LiFePO ₄		LiCoPO ₄	
	H20	H35	H20	H35	H20	H35
ε_1	671	544	230	201	-436	-412
$\varepsilon_2=\varepsilon_2'$	2245	1903	1925	1629	1344*	1142*
ε_3	1504	1219	34	-72	657	517
ε_4	1996	1667	271	130	858	679

Table 2.1: A summary of the DFT-calculated values of ε_N for LiMnPO₄, LiFePO₄, and LiCoPO₄ [95], where H20 and H35 correspond to DFT methods utilizing the B3LYP functional incorporating both 20% and 35% Hartree-Fock exchange, respectively. *For LiCoPO₄, first-principles calculations at 0 K revealed a lack of degeneracy between the P₂ and P'₂ pathways. An average of these two pathways is expected at room temperature [12], which is the value given.

	LiFe _x Mn _{1-x} PO ₄			LiFe _x Co _{1-x} PO ₄		
	H20	H35	Exp (err)	H20	H35	Exp (err)
$\Delta\varepsilon_1$	441 ^{c,d} - 587 ^{b,e}	343 ^{c,d} - 453 ^{b,e}	461 (4)	666 ^{c,g} - 1129 ^{f,h}	595 ^{c,h} - 989 ^{f,g}	539
$\Delta\varepsilon_2=\Delta\varepsilon_2'$	320 ^{c,d} - 1373 ^{b,e}	274 ^{c,d} - 1169 ^{b,e}	644 (40)	581 ^{c,g} - 657 ^{f,h}	487 ^{c,g} - 532 ^{f,h}	422
$\Delta\varepsilon_3$	1316 ^{b,d} - 1665 ^{c,e}	1142 ^{b,d} - 1442 ^{c,e}	1201 (5)	-623 ^{c,g} - 193 ^{f,h}	-589 ^{c,g} - 118 ^{f,h}	-479
$\Delta\varepsilon_4$	1725 ^{c,d} - 2077 ^{b,e}	1537 ^{c,d} - 1821 ^{b,e}	1350 (2)	-587 ^{c,g} - 243 ^{f,h}	-549 ^{c,g} - 185 ^{f,h}	-294

Table 2.2: A comparison of the DFT-calculated (H20 and H35) values [9, 12, 95] with experimental values of $\Delta\varepsilon_N$ for LiFe_xMn_{1-x}PO₄ [9] and LiFe_xCo_{1-x}PO₄ [12] for each of the four distinct pathways^a in the first coordination shell of PO₄. ^aThe ranges in relative pathway contributions correspond to extremal values resulting from the substitution of Fe²⁺ and Mn²⁺ in to both fixed LFP and LMP structures, or Fe²⁺ and Co²⁺ in to both fixed LFP and LCP structures, with the specific combinations denoted by superscripts: ^bFe@LMP. ^cFe@LFP. ^dMn@LMP. ^eMn@LFP. ^fFe@LCP. ^gCo@LCP. ^hCo@LFP. All values are given in ppm.

for each respective local geometry, denoted hereafter as LMP, LFP, and LCP, respectively. The results of this study are shown in Table 2.1 for two different DFT methods using the B3LYP functional incorporating both 20% and 35% Hartree-Fock exchange, denoted hereafter as H20 and H35, respectively. H20 has been shown in previous studies to provide good performance for the calculation of band gaps and for properties of TM compounds [106, 107], while H35 has been shown provide magnetic coupling constants that agree well with experimental values [108–110]. These two methods effectively form bounds for the expected experimental chemical shifts [9, 95]. These DFT values, together with values for metal sites in non-native geometries (*i.e.* Mn²⁺ in the LFP structure, denoted as Mn@LFP) from references [9, 12], were used to calculate the expected relative contributions, $\Delta\varepsilon_N$, to each of the four distinct spin-transfer pathways in the mixed-phase LiMPO₄ phases studied by Clément *et al.* and Strobridge *et al.*, which are compared in Table 2.2. The range of DFT-calculated values predicts the effect of structural 'distortions' that may be induced by cationic substitution into a non-native local structure environment, and where the experimental value lies in this distribution can be an indication of the effect of this substitution.

As the overall LIB performance may be affected by substitutions of TMs in olivine-type LiMPO₄, it would therefore be crucial to be able to uniquely determine the absolute effect of the

substitution of Mn or Co for Fe in order to better understand the effect each of these substitutions may have not only on the local electronic structure of PO_4 in mixed-phase LiMPO_4 cathode phases, but also on the local geometry by structural distortions induced. In this work we set out to do just this, by examining uniquely the effect of Mn-substitution on the ^{31}P isotropic shift on the mixed-phase composition $\text{LiMg}_x\text{Mn}_{1-x}\text{PO}_4$, which contains the diamagnetic Mg metal, using 1D MAS NMR spectra acquired at low field and ultrafast MAS rotation rates. The motivation for developing the aMAT experiment by Clément *et al.* was that the combination of ultrafast MAS (60 kHz) and low field (100-300 MHz ^1H Larmor frequency) would render 1D NMR experiments to be too insensitive to perform a routine analysis of ^{31}P shifts in mixed-phase LiMPO_4 despite the fact that the spinning sidebands in such spectra would be largely suppressed at especially low fields (~ 100 MHz). As such, the use of higher fields would not only increase sensitivity in ^{31}P NMR, but would be beneficial for the study of the quadrupolar ^7Li nucleus in LIBs.

These 2D sideband-separation experiments do not come without drawbacks, though. The 2D MATPASS experiment relies on non-selective $\frac{\pi}{2}$ pulses and as such suffers from sensitivity issues due to the exclusion of the majority of signal components and accumulated effects of RF inhomogeneity during this pulse train. The 2D aMAT experiment suffers from significant intensity biasing resulting from substantial T_2' decay during extremely long pulse sequences (often longer than the ^{31}P T_2'), long experiment times (1-2 days for LTMP compositions usually), and the tendency to introduce, unpredictably, intensity in the $\pm\frac{\nu_R}{2}$ and $\pm\nu_R$ sidebands if the shaped pulses are poorly optimized, shown clearly in recent work by Perras *et al.* [111]. In the case of the study by Clément *et al.* on the $\text{LiFe}_x\text{Mn}_{1-x}\text{PO}_4$ phases, the use of 2D aMAT resulted in isotropic ^{31}P spectra with considerable biasing in the intensity of the 32 different sites due to differential T_2' relaxation times, and potentially with line shape distortions due to small reintroductions of sideband intensity.

In the present study, we aim to show that the use of lower external magnetic field strength ($B_0 = 7.05$ T, 300 MHz ^1H Larmor frequency) coupled with the higher rotation capabilities of the recently-developed 0.7 mm MAS probe (up to 111 kHz) provide spectra with similar resolution as those resulting from 2D sideband-separation experiments in a fraction of the time. We show that simplifying the experimental methods by using lower magnetic fields and faster MAS rotation results not only in significantly shorter experiment times but without significant spectral biasing. We illustrate the effectiveness of this approach on the composition $\text{LiFe}_{0.25}\text{Mn}_{0.75}\text{PO}_4$ and compare the results to those previously published [9]. Then, we apply these methods to the $\text{LiMg}_x\text{Mn}_{1-x}\text{PO}_4$ composition to determine the effect of Mn^{2+} substitution in LiMPO_4 .

2.2 ^{31}P NMR of $\text{LiFe}_{0.25}\text{Mn}_{0.75}\text{PO}_4$ at 7.05 T and 111 kHz MAS - a proof of concept

We begin by comparing the relative effects of external magnetic field strength and MAS rotation rate on the ^{31}P spectrum of $\text{LiFe}_{0.25}\text{Mn}_{0.75}\text{PO}_4$, with the aim to compare these results with those previously published [9]. In order to do this, 1D ^{31}P spectra were acquired at external magnetic

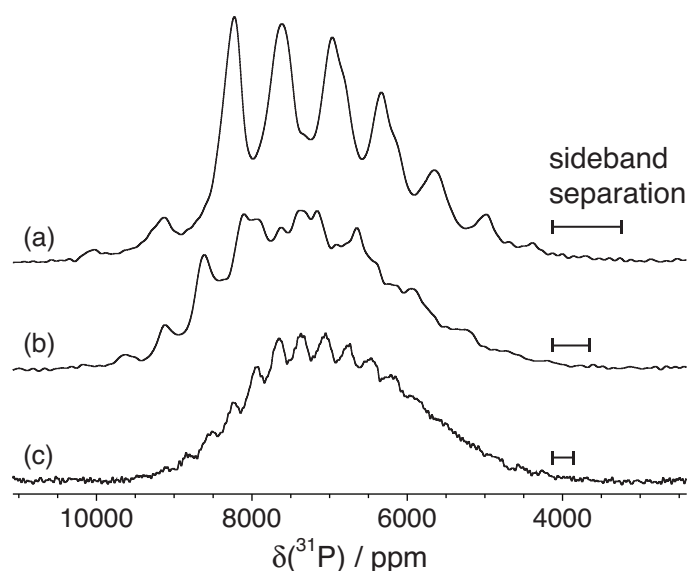


Figure 2.3: The 1D ^{31}P MAS spectra of $\text{LiFe}_{0.25}\text{Mn}_{0.75}\text{PO}_4$ acquired at (a) $B_0=7.05$ T (300 MHz) and 111 kHz MAS, (b) $B_0=7.05$ T (300 MHz) and 60 kHz MAS, and (c) $B_0=11.7$ T (500 MHz) and 60 kHz MAS [9], with the sideband separation at each combination of external magnetic field and MAS rotation rate noted to the right of each spectrum. The spectra in (a) and (b) were collected in 3.8 hours with 1 M scans and a recycle delay of 10 ms, whereas the spectrum in (c) was collected in 0.9 hours with 32k scans and a recycle delay of 100 ms. The spectrum in (c) is adapted with permission from [9]. Copyright 2012 American Chemical Society.

field strengths of 11.74 T (500 MHz ^1H) and 7.05 T (300 MHz ^1H) and MAS rotation rates of 60 kHz and 111 kHz. The resulting spectra are given in Figure 2.3, which shows very clearly (and as expected) that the most significant improvement in resolution is achieved by a combination of low magnetic field and, in particular, high MAS rotation rate. The resolution of the resulting spectrum (Figure 2.3(a)) is significantly improved due to the decreased intensity and increased separation of spinning sidebands, resulting in a spectrum nearly completely composed of isotropic bands, which was collected in less than 4 hours.

In order to fit the new 1D spectrum of $\text{LiFe}_{0.25}\text{Mn}_{0.75}\text{PO}_4$ and extract the relative contributions of Fe and Mn to the spin-transfer pathways shown in Figure 2.1, we utilize a fitting routine similar to that published already [9, 12]. The method used by Clément *et al.* assumes:

1. That the total integrated area of each of the 32 sites in $\text{LiFe}_x\text{Mn}_{1-x}\text{PO}_4$ are constrained assuming a statistically random distribution of metal ions around PO_4 , *i.e.*, the integrated area of each peak follows the distribution $x^m(1-x)^n$ for a configuration with m Fe^{2+} ions and n Mn^{2+} ions. This is justified by the results of previous studies [112–116] which have shown that various LFMP compositions are solid solutions of LFP and LMP.
2. That the intensities of each of the 32 peaks are further weighted by the expected T'_2 relaxation losses during the pulse sequence, assuming that the ^{31}P T'_2 is dominated by local PRE effects from the 5 metal centers coordinating PO_4 . The T'_2 coherence lifetimes were measured to be 131.9 μs for LiMnPO_4 and 333.9 μs for LiFePO_4 . As such the relaxation rate, R'_2 , for each ^{31}P site is modeled to vary linearly from $R'_2(\text{LiFePO}_4)$ to $R'_2(\text{LiMnPO}_4)$ as

the number of Mn^{2+} in the first coordination sphere of PO_4 increases from 0 to 5. The *relaxation time* is then taken as the reciprocal of R_2' for each site.

3. That the line width is uniform for all sites as the dominant line broadening mechanism is expected to be due to anisotropic bulk magnetic susceptibility effects, and was fixed for the fit to the line width of the 5-Fe ($m = 5$) resonance in the ^{31}P spectrum of $\text{LiFe}_{0.75}\text{Mn}_{0.25}\text{PO}_4$, which was well-resolved from the other peaks.
4. That the spin-transfer contributions from the 5 spin-transfer pathways P_N accurately determine the ^{31}P shift, resulting effectively in 32 isotropic ^{31}P environments, and
5. That the ^{31}P shift of the 5-Fe ($m = 5$) site is equal to the shift measured in LiFePO_4 .

As the ^{31}P spectrum of $\text{LiFe}_{0.25}\text{Mn}_{0.75}\text{PO}_4$ in Figure 2.3(a) was acquired under different conditions than the results of Clément *et al.*, and thus providing different results, it is necessary to modify this fitting routine with the following changes and assumptions:

6. That despite the use of lower field and higher MAS rotation rates, there is nonetheless a small contribution to the line shape by spinning sidebands, especially first-order (± 1) sidebands. As such we include first order sidebands for each of the 32 sites with intensity fixed at 17% of the intensity of the centerband, assuming that both sidebands of each line have equal intensities. This is justified by observing the aMAT spectrum of $\text{LiFe}_{0.25}\text{Mn}_{0.75}\text{PO}_4$ shown in Figure 2.4 and the cross section provided therein, which was acquired at 7.05 T and 111 kHz MAS. In this case the cross sections of the MAS dimension show that the majority of the intensity of each site is located in the centerband, and that the sideband pattern is symmetric with sideband intensities $\approx 17\%$ that of the centerband. This is true for all sites in this spectrum.
7. That because the spectrum of LiFePO_4 was not acquired under these experimental conditions (111 kHz MAS, 7.05 T), the shift of the 5-Fe site is allowed to vary to allow for any shift differences due to temperature effects, and
8. That the line width, while being held uniform for all sites, is allowed to vary for the same reason, in order to account for line broadening due to homogeneous and inhomogeneous contributions to the line width.

The combination of these assumptions results in a 7-parameter fit (the 5 P_N values, the shift of the 5-Fe peak, and the line width), which produces a very high-quality fit of the experimental ^{31}P MAS spectrum of $\text{LiFe}_{0.25}\text{Mn}_{0.75}\text{PO}_4$, shown in Figure 2.5. As was seen in previous studies [9, 12], the values of P_2 and P_2' were observed to be the same within error, and henceforth are treated as equal quantities. The extracted relative contributions to the spin-transfer pathways ($\Delta\varepsilon_N$) are summarized in Table 2.3. Overall the resulting shift of the 5-Fe site and the relative spin-transfer contributions of each of the four pathways (Table 2.3 column 1) were higher those in reference

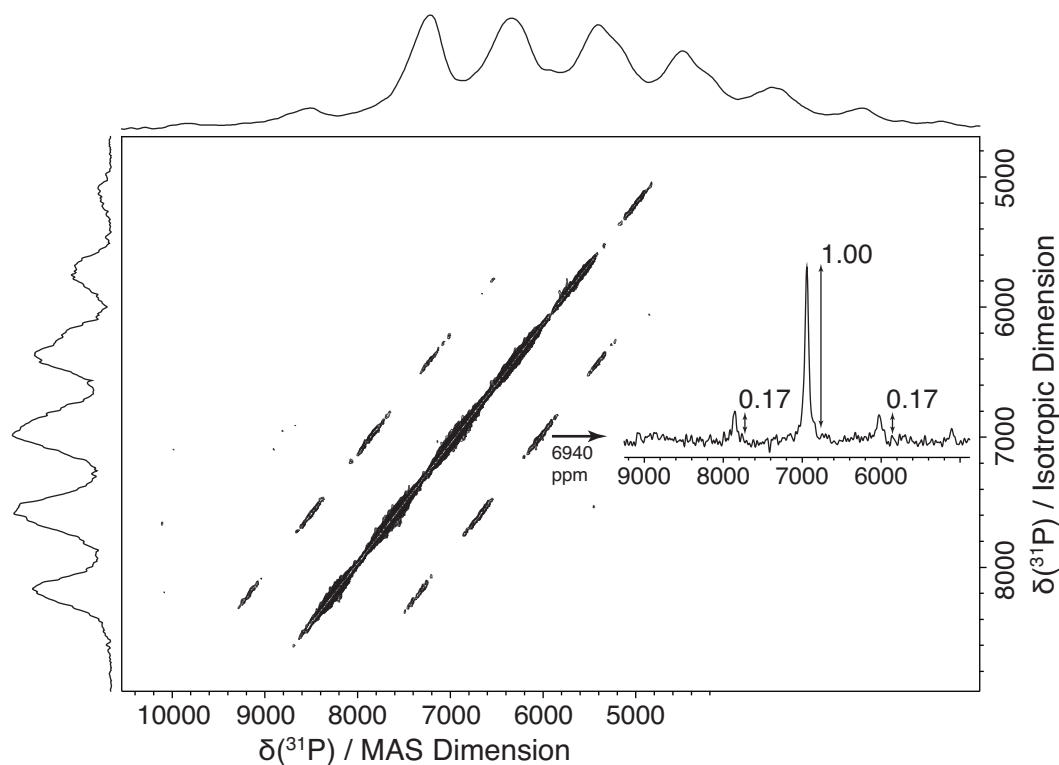


Figure 2.4: The 2D aMAT spectrum of $\text{LiFe}_{0.25}\text{Mn}_{0.75}\text{PO}_4$ acquired at an external magnetic field strength of 7.05 T and with an MAS rotation rate of 111.111 kHz. The spectrum indicates that the 1D MAS spectrum is largely composed of resonances corresponding to the isotropic shifts of the 32 sites present in the material, with small but non-negligible intensity in the first-order sidebands of each resonance. The cross section from 6940 ppm was used to constrain the sideband intensity at 17% of the centerband intensity in the fitting routine. Adapted with permission from [9]. Copyright 2012 American Chemical Society.

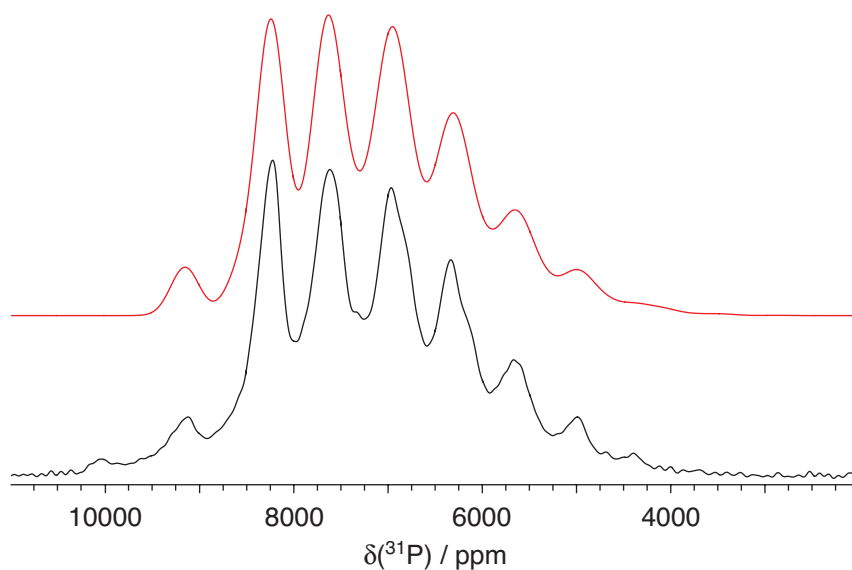


Figure 2.5: Overlay of the 1D ^{31}P experimental MAS spectrum of $\text{LiFe}_{0.25}\text{Mn}_{0.75}\text{PO}_4$ (black) acquired at 7.05 T and 111.111 kHz MAS, and the results of the fit of this spectrum (red). This result, together with the data in Table 2.3, confirms that 1D NMR methodology with 111 kHz MAS rotation rates can be used to accurately reproduce results previously only attainable with challenging 2D methods.

	This work	This work (T-corrected)	Clément <i>et al.</i> [9]
$\delta(5-Fe)$	3781	3641	3631
$\Delta\varepsilon_1$	529	509	461
$\Delta\varepsilon_2=\Delta\varepsilon_{2'}$	647	623	644
$\Delta\varepsilon_3$	1251	1205	1201
$\Delta\varepsilon_4$	1385	1334	1350

Table 2.3: A summary of the results from fitting the 1D ^{31}P spectrum (column 1), the temperature-corrected values (column 2), and the values previously published (column 3). All values given in ppm.

[9] (Table 2.3 column 3) which is presumably due to a difference in experimental temperatures, as the Fermi contact interaction is proportional to temperature via the Curie-Weiss law:

$$\delta^{FC} \propto \frac{1}{T - \Theta}, \quad (2.2)$$

where T is the absolute temperature and Θ is the Weiss constant. As such, the values resulting from the fit (Figure 2.5) can be temperature-corrected with the assumption that the temperature reported by Clément *et al.*, 320 K, was accurate, and that the Weiss constant is equal to that of a weighted average of the Weiss constants of $LiFePO_4$ ($\Theta = -72.5$ K [117]) and $LiMnPO_4$ ($\Theta = -58$ K [118]) for each site depending on the metals occupying each site. By then comparing the resulting fitted value for the 5-Mn ($n = 5$) peak for both sets of fitted values and applying these assumptions, the experimental temperature of our data was determined to be approximately 306 K, and this result was subsequently used to scale down the fitted results to a temperature of 320 K (Table 2.3 column 2). The relatively good agreement between the present values and those published by Clément *et al.* establishes that one-dimensional experimental methodology with 111 kHz MAS rotation rates can reliably be used to measure the contribution of different TMs to the five spin-transfer pathways of local PO_4 groups in olivine-type $LiMPO_4$.

2.3 The contribution of Mn^{2+} to the ^{31}P shift in olivine-type $LiMg_xMn_{1-x}PO_4$

In order to determine the unique contribution of Mn^{2+} to the ^{31}P NMR shift in $LiTMPO_4$, it is necessary to study a mixed-phase olivine-type $LiMPO_4$ containing one diamagnetic metal (and thus not significantly contributing to the overall ^{31}P shift), and Mn^{2+} , which will dominate the ^{31}P shift. To determine uniquely the contribution of Mn^{2+} to the spin-transfer pathways in $LiMPO_4$ we therefore decided to study the composition $LiMg_xMn_{1-x}PO_4$. This composition exhibits a ^{31}P shift range spanning ≈ 9000 ppm (≈ 1.2 MHz on a 7.05 T instrument or ≈ 2 MHz on a 11.74 T instrument) arising from the large disparity of spin-transfer pathway contributions, ε_N , caused by Mn^{2+} [95]. For this reason these compositions would be very difficult to study at relatively high magnetic field strengths without extensive effort, and as such it is much simpler to perform experiments at lower field strengths. Figure 2.6 shows a comparison of ^{31}P MAS

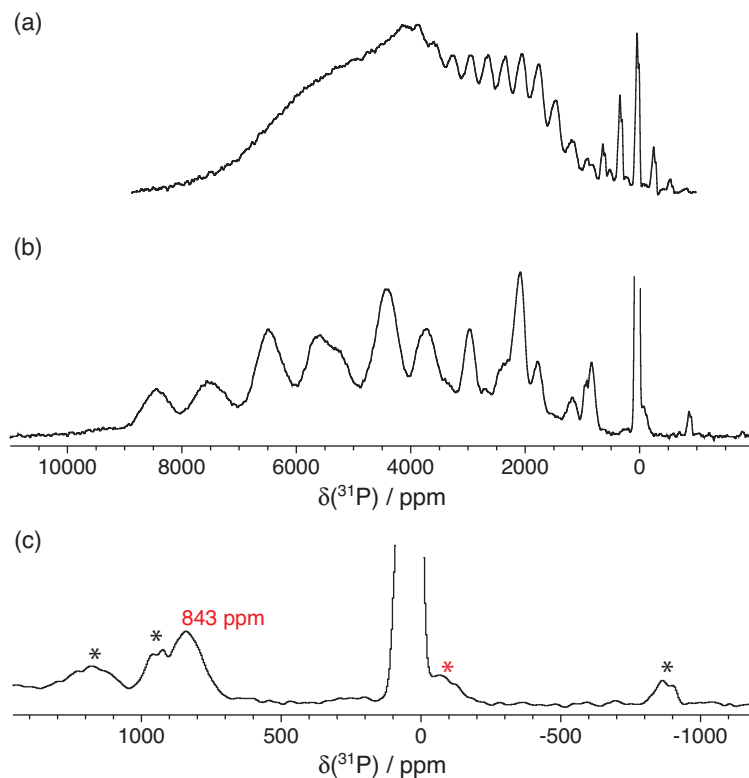


Figure 2.6: The 1D ^{31}P MAS spectra of $\text{LiMg}_{0.5}\text{Mn}_{0.5}\text{PO}_4$ acquired at (a) $B_0 = 11.7$ T (500 MHz) and 60 kHz MAS, and (b) $B_0 = 7.05$ T (300 MHz) and 111.111 kHz MAS using Tanh/Tan refocusing pulses with pulse parameters of $\Delta\nu_{\text{RF}} = 5$ MHz and $t_p = 50$ μs for (a) and $\Delta\nu_{\text{RF}} = 10$ MHz and $t_p = 18$ μs for (b), each with a maximum RF field strength of $\nu_{1,\text{max}} \approx 400$ kHz. Each experiment utilized $\frac{\pi}{2}$ excitation pulses with an RF field strength of approximately 400 kHz. Immediately we see that as a result of decreasing the external magnetic field, the effective excitation bandwidth in (b) is increased compared to (a), and as such the peaks at ~ 7500 and ~ 8500 ppm are now present. The most striking difference, though, is the remarkable increase in resolution in (b) due to the near-complete absence of spinning sidebands as a result of increasing the MAS rate and utilizing a smaller external magnetic field strength.

spectra of $\text{LiMg}_{0.5}\text{Mn}_{0.5}\text{PO}_4$ at: (a) an external magnetic field strength of 11.74 T and with a MAS rotation rate of 60 kHz, and (b) an external magnetic field strength of 7.05 T and with a MAS rotation rate of 111 kHz. This figure highlights the necessity to combine low field and the maximum possible MAS rate for the study of $\text{LiMg}_x\text{Mn}_{1-x}\text{PO}_4$, as the spectrum in Figure 2.6(a) has very little resolution and, perhaps more importantly, is incomplete due to the inability to excite the totality of the resonances, whereas the entire spectrum is collected in Figure 2.6(b) at lower external magnetic field strength with dramatically increased resolution.

As the Weiss constant of $\text{LiMg}_x\text{Mn}_{1-x}\text{PO}_4$ is expected to increase from $\Theta = -58$ K (the Weiss constant of LiMnPO_4) to 0 as x increases from 0 to 1, it is therefore impossible to perform the simultaneous fitting routines as used in the analyses by Clément *et al.* and Strobridge *et al.*, as the shifts of each of the 32 peaks will be increasing with increasing values of x . Therefore, in order to simplify the overall analysis, we have decided to determine the individual spin-transfer pathway elements of Mn^{2+} from the spectrum of $\text{LiMg}_{0.2}\text{Mn}_{0.8}\text{PO}_4$ shown in Figure 2.7. This spectrum primarily exhibits resonances resulting from PO_4 groups coordinated by two or more

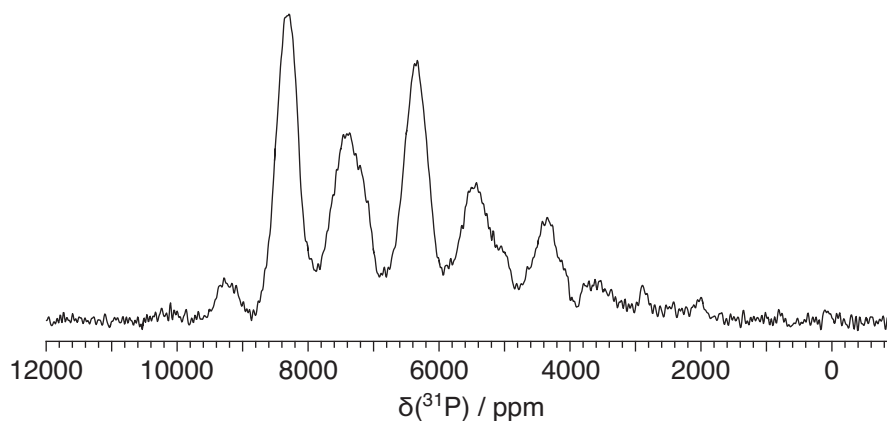


Figure 2.7: The 1D MAS spectrum of $LiMg_{0.2}Mn_{0.8}PO_4$ acquired at an external magnetic field strength of 7.05 T, using a MAS rotation rate of 111.111 kHz. This spectrum was acquired using 266240 scans using a recycle delay of 10 ms. The total experiment time was 49 minutes.

Mn^{2+} atoms, and importantly, contains a very intense peak at ≈ 8300 ppm, corresponding to the 5-Mn site, which forms a natural constraint on the fitting routine, forcing all five spin-transfer pathways to sum to the shift of the 5-Mn peak. A major difference from the ^{31}P spectra of $LiFe_xMn_{1-x}PO_4$ is that the linewidth is not uniform for all sites, as can be obviously seen in Figure 2.6 (b). Therefore the fitting routine was modified to permit varying line widths as the number of Mn^{2+} atoms coordinating PO_4 increases. We must therefore determine what the possible sources to line broadening mechanism are, which are:

1. Broadening due to ABMS effects, which is expected to be zero, unlike prior results on $LiFe_xMn_{1-x}PO_4$, as the magnetic susceptibility tensor of Mn^{2+} is expected to be isotropic.
2. PRE broadening from local metals, which is expected to vary linearly with increasing Mn content.
3. Broadening due to a distribution of shifts arising from Fermi contact shifts from Mn^{2+} atoms in distant coordination shells, which is expected to be uniform for all sites in a solid solution and to produce a Gaussian distribution of shifts. This effect can be measured by measuring the linewidth of the 5-Mg peak in Figure 2.6 (b), and is approximately 50 ppm.
4. Broadening from temperature gradients within the NMR rotor, which is expected to produce spectra with broadened "tails" as seen in the ^{31}P 2D aMAT spectrum of LMP in Reference [9], and
5. Broadening from structural distortions arising from the substitution of Mg^{2+} in the $LiMnPO_4$ structure. This effect is difficult to model without extensive computer simulations, but is expected to roughly increase linearly with increasing Mn content.

The routine used to fit the spectrum is very similar to that used previously, with a modification to allow for varying linewidths, but for completeness is listed below with the following assumptions:

1. That the intensities of each of the 32 sites in $\text{LiMg}_{0.2}\text{Mn}_{0.8}\text{PO}_4$ are constrained assuming a statistically random distribution of metal ions around PO_4 , *i.e.*, the integrated area of each peak follows the distribution $0.2^m(0.8)^n$ for a configuration with m Mg^{2+} ions and n Mn^{2+} ions.
2. That the intensities are further weighted by the expected T_2' relaxation losses during the pulse sequence, assuming that the ^{31}P T_2' is dominated by local PRE effects from the 5 metal centers coordinating PO_4 . The T_2' coherence lifetime of LiMnPO_4 was measured to be 131.9 μs . As such the *relaxation rate*, R_2' , for each ^{31}P site is modeled to vary linearly from $\frac{1}{5}R_2'(\text{LiMnPO}_4)$ to $R_2'(\text{LiMnPO}_4)$ as the number of Mn^{2+} coordination PO_4 increases from 1 to 5. The T_2' of each site is then calculated from the reciprocal of R_2' . The intensity of the peak corresponding to the 5-Mg site is subsequently allowed to vary as its T_2' does not follow this trend.
3. That the line width for each site increases linearly with increasing Mn^{2+} content, starting from a value of 166 ppm (FWHM), which is the linewidth measured for the peak at 843 in the ^{31}P spectrum of $\text{LiMg}_{0.5}\text{Mn}_{0.5}\text{PO}_4$, shown in Figure 2.6 (c), and increasing to a variable value for the all-Mn site.
4. That the spin-transfer contributions from the 5 spin-transfer pathways P_N accurately determine the ^{31}P shift, resulting effectively in 32 isotropic ^{31}P environments.
5. That despite the use of lower field and higher MAS rotation rates, spinning sidebands intensity must be accounted for, especially first-order (± 1) sidebands. As such we include first order sidebands for each of the 32 sites with intensity fixed at 15% of the intensity of the centerband, assuming that the both sidebands of each line have equal intensities. This value was chosen by iteratively fitting the spectrum with varying sideband intensity until the intensity of the +1 order sideband of the all-Mn site at ≈ 8300 ppm was well-represented. This represents a disadvantage of this method compared to the 2D sideband-separation methods employed by others [9, 12], although in our opinions the ease of implementation of the experimental methods and high sensitivity of the 1D method is fair compensation.
6. That the spin-transfer pathway of the Mn^{2+} atom contributing to the P_1 pathway is constrained to 803 ppm, after scaling the value of the well-resolved peak at 843 ppm in Figure 2.6(c) to account for the different Weiss constant of this stoichiometry. This is a reasonable constraint, albeit not general, since the values calculated by Middlemiss *et al.*, shown in Table 2.1 show that there is only one spin-transfer pathway contributing a one-metal shift in this range.
7. That the 5-Mg peak, albeit weak, can be fit with a single Gaussian peak of variable width and position, which was constrained to be less 100 ppm.

The culmination of these constraints produces in a 7-parameter fit (the four P_N pathways, not including P_1 , sideband intensity, line width of the 5-Mn peak, and shift of the 5-Mg peak), and

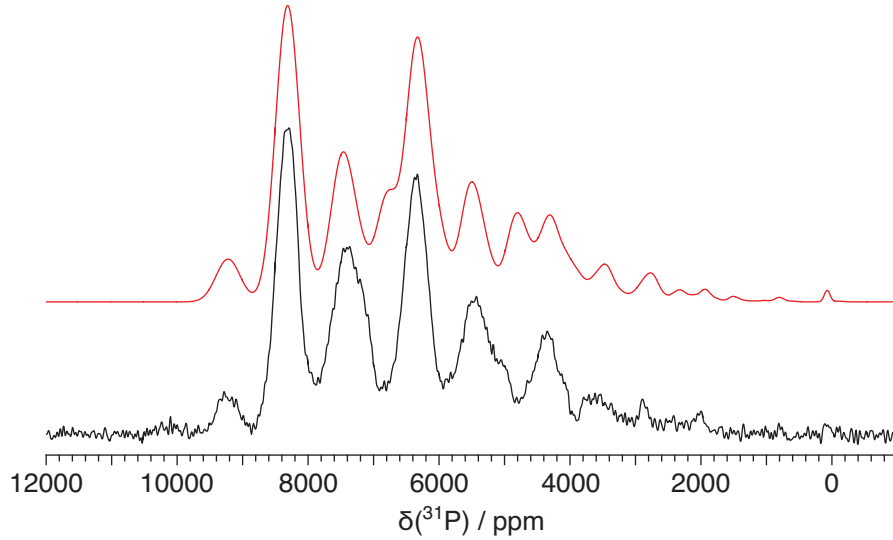


Figure 2.8: Overlay of the 1D ^{31}P experimental MAS spectrum of $LiMg_{0.2}Mn_{0.8}PO_4$ (black) and the results of the fitting routine used to model this spectrum (red).

	DFT-calculated [95]		Experimental	
	H20	H35	As fitted	Θ -corrected
ε_1	671	544	803*	778*
$\varepsilon_2 = \varepsilon_2'$	2245	1903	1941	1881
ε_3	1504	1219	1514	1468
ε_4	1996	1667	2107	2042

Table 2.4: A summary of the DFT-calculated values for the spin-transfer pathways in $LiMnPO_4$ by Middlemess *et al.*, compared to the values extracted by fitting the spectrum of $LiMg_{0.2}Mg_{0.8}PO_4$ using the fitting routine given in the text. The experimental data were corrected for an expected difference in Weiss constants between pure-phase $LiMnPO_4$ and the mixed-phase $LiMg_{0.2}Mg_{0.8}PO_4$, given in the fourth column of the table. All values given in ppm. *Constrained to 803 ppm as discussed in the text.

the results of this fitting routine are given in Figure 2.8, with the extracted spin-transfer pathway contributions of Mn^{2+} compared against the DFT-calculated values in Table 2.4. In order to make a more meaningful comparison to the DFT-calculated values, the experimental values must be scaled according to the Weiss constant in the material. Recalling Equation 7.111 from Pell *et al.* [25], reprinted below in Equation 2.3, the Weiss constant in Ferro/Anti-Ferromagnetic describing the bulk materials can be calculated by summing over all Heisenberg exchange coupling constants, $\mathcal{J}^{(AB)}$:

$$\Theta = \frac{2S(S+1)}{3k_B} \sum_{\beta \neq \alpha} \mathcal{J}^{(AB)}. \quad (2.3)$$

In the case of $LiMg_{0.2}Mg_{0.8}PO_4$, this would produce unique local "Weiss constants" for each of the 32 possible structures. The determination of these constants without DFT calculations is difficult, and therefore we have decided to model the Weiss constant of the bulk material as scaling linearly with Mn^{2+} content; for $LiMg_{0.2}Mg_{0.8}PO_4$, this results in an effective Weiss constant of $\Theta = -46.4$ K. The values in column 3 of Table 2.4 are scaled to what would be

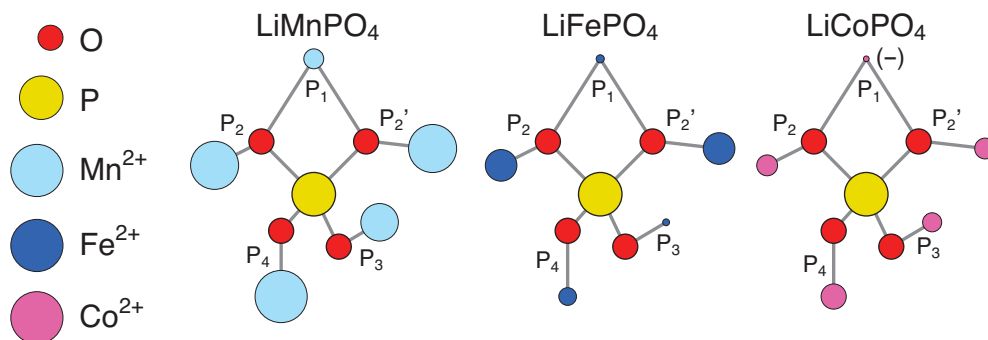


Figure 2.9: A comparison between the absolute pathway contributions, ε_N , of Mn^{2+} , Fe^{2+} , and Co^{2+} in mixed-phase olivine-type LiMPO₄ cathode phases, where the width of each circle corresponds to the magnitude of the contribution to the overall measured contact shift for each pathway P_N . All values are positive with the exception of ε_1 in LCP, which is denoted by a negative sign.

expected for pure-phase LiMnPO₄ in column 4. Overall the agreement between the results is impressive with all values falling near to those calculated, although there was an overestimate of the DFT-calculated value for ε_1 and a corresponding slight underestimate of the DFT-calculated value of ε_4 .

As discussed previously, prior results gave only relative contributions of metals to the spin-transfer pathways: $\Delta\varepsilon_N = \varepsilon_N(\text{Mn}^{2+}) - \varepsilon_N(\text{Fe}^{2+})$ for $\text{LiFe}_x\text{Mn}_{1-x}\text{PO}_4$ and $\Delta\varepsilon_N = \varepsilon_N(\text{Fe}^{2+}) - \varepsilon_N(\text{Co}^{2+})$ for $\text{LiFe}_x\text{Co}_{1-x}\text{PO}_4$. As such, the absolute spin-transfer pathways contributions of Mn^{2+} resulting from this fit can be used to extract the absolute contributions to the spin-transfer pathways in LiMPO₄ of both Fe^{2+} and Co^{2+} . These values, together with the DFT-calculated values, are summarized in Table 2.5. In order to better visualize these results, Figure 2.9 depicts the relative contributions of each metal to the spin-transfer pathways ε_N , where the width of the circle denoting each TM is proportional to the magnitude of ε_N , with the sign of each being positive with the exception of ε_1 in LCP.

The values for the unique spin-transfer pathway contributions, ε_N , for Mn^{2+} , Fe^{2+} , and Co^{2+} given in rows 1-4 of Table 2.5 represent the first experimental determination of the effect these metals have on the paramagnetic ³¹P shift in mixed-phase olivine-type LiMPO₄ phases. The values for ε_N were summed ($\varepsilon_1 + 2 \times \varepsilon_2 + \varepsilon_3 + \varepsilon_4$) in order to compare to previously-reported values for ³¹P shifts in pure-phase olivine-type LiMPO₄ [9, 12], given in the fifth row of Table 2.5. Comparing the shifts, Mn^{2+} contributes most to the spin-transfer pathways. This is not unexpected by any means, as it is clear that the five singly-occupied 3d orbitals in Mn^{2+} (d^5) can contribute spin density, whereas Fe^{2+} (d^6) has only four singly-occupied orbitals, and Co^{2+} (d^7) only three. This is expected to be a particular strong effect for P_3 and P_4 , as the orbital which is singly-occupied in the case of Mn^{2+} has a nearly coplanar orientation relative to P_3 and P_4 , while it is more orthogonal to P_1 and P_2 [9]. Figure 2.10 gives plots of the isosurface of the spin density difference between Mn@LFP and Fe@LFP for this orbital, in the case of (a) the distorted MO₆ octahedron and (b) the TM–O–P pathways around a PO₄ tetrahedron. Following this logic, we should expect to see even smaller shifts caused by Co^{2+} compared to Fe^{2+} . While this is true for ε_2 , this trend is lost for the other pathways.

	Mn^{2+}		Fe^{2+}		Co^{2+}				
	exp (err)	H20	H35	exp (err)	H20	H35			
ϵ_1	778* (-)	671 ^d -767 ^e	544 ^d -612 ^e	317 (4)	180 ^b -230 ^c 230 ^c -666 ^f	159 ^b -201 ^c 201 ^c -577 ^f	-222 (-)	-463 ^h -436 ^g	-394 ^h -412 ^g
$\epsilon_2=\epsilon_2'$	1881 (18)	2245 ^d -2875 ^e	1903 ^d -2437 ^e	1237 (44)	1502 ^b -1925 ^c 1925 ^c -1944 ^f	1268 ^b -1629 ^c 1629 ^c -1640 ^f	815 (-)	1287 ^h -1344 ^g	1108 ^h -1142 ^g
ϵ_3	1468 (9)	1504 ^d -1699 ^e	1219 ^d -1370 ^e	267 (10)	34 ^c -187 ^b 34 ^c -404 ^f	-72 ^c -77 ^b -72 ^c -245 ^f	746 (-)	211 ^h -657 ^g	127 ^h -517 ^g
ϵ_4	2042 (6)	1996 ^d -2335 ^e	1667 ^d -1948 ^e	692 (6)	258 ^b -271 ^c 271 ^c -828 ^f	127 ^b -130 ^c 130 ^c -627 ^f	986 (-)	585 ^h -858 ^g	442 ^h -679 ^g
sum	8050 (21)			3750 (46)			3122 (-)		
lit.	7931 (41) [9]			3631 (3) [9]			2945 [12]		

Table 2.5: The experimental (exp) spin-transfer pathway contributions for Mn^{2+} , Fe^{2+} , and Co^{2+} compared against DFT-calculated values [9, 12, 95], for each of the four distinct pathways^a in the first coordination shell of PO_4 . ^aThe ranges in relative pathway contributions correspond to extremal values resulting from the substitution of each metal in to the fixed crystal structures of LMP, LFP, or LCP, with the specific combinations denoted by superscripts. For consistency, the subscripts follow the same notation in Table 2.2: ^bFe@LMP. ^cFe@LFP. ^dMn@LMP. ^eMn@LFP. ^fFe@LCP. ^gCo@LCP. ^hCo@LFP. The standard error of each experimental value is given in parenthesis next to the corresponding value, which were estimated by performing the fitting routine 10,000 times with a Monte Carlo variation of the experimental intensities within the noise level of the experimental spectrum. Standard errors were not reported in [12]. The summation of the values ($\epsilon_1 + 2*\epsilon_2 + \epsilon_3 + \epsilon_4$) given in the fifth row (labeled "sum") correspond well to the previously-reported ^{31}P shifts in pure-phase LMPs given in the sixth row (labeled "lit.") especially when considering that temperature differences between experiments may be as much as 20-30 K. All values given in ppm.

One obvious explanation of this deviation from expected trends would be small changes in the local geometry around each metal center, notably the bond angles, M–O–P. These angles are given in Table 2.6. For ε_1 , a negative contribution from Co^{2+} was observed, whereas a small albeit positive shift is expected by electronic configuration considerations only. The M–O–P bond angles for each of the three compositions are similar, with variations of only about 0.4° from the average value, though it is worth noting that the angle becomes more acute as the ionic radius decreases. It was proposed by Strobridge *et al.* that a second competing mechanism contributing to the ^{31}P shift may come in to play, which comes as a result of the different bonding environments around TMs in these materials. A linear relationship between DFT-calculated values of ε_1 and the ionic radii was observed, leading to negative shifts when the size of the ion is <90 pm, suggesting that a second spin-transfer mechanism resulting from differences in the covalency of the M–O bond becomes important, and is stronger with shorter (more covalent) M–O bonds from small ions. These calculated values are given in Table 2.7. For ε_3 and ε_4 , the contributions from Co^{2+} are considerably higher than the contributions of Fe^{2+} , and notably, much more similar to the DFT-calculated values for Co@LCP than Co@LFP shown in Table 2.5. As such this must be a structural effect. Indeed, the M–O–P bond angles for all three pure-phase compositions given in Table 2.6 show that the $\text{M}_3\text{–O–P}$ and $\text{M}_4\text{–O–P}$ bond angles are more obtuse in LCP than in LFP, each by more than 2.5° . As a result of these structural differences it cannot be blindly assumed that Co^{2+} will be a more innocent paramagnetic center than Fe^{2+} from arguments based on the electronic configuration of each metal. The fact that the DFT reflects this geometric difference in the calculated hyperfine shifts supports the conclusion that Co^{2+} adopts a more native LCP-like local geometry rather than being adopting a LFP-like local geometry in mixed phase $\text{LiFe}_x\text{Co}_{1-x}\text{PO}_4$.

An additional purpose of this study has been not only to determine the unique contribution of Mn^{II} to the ^{31}P paramagnetic shift, but perhaps more importantly, to examine if this information would provide any insight in to the effect of cationic substitution on the local environment surrounding the metals, *i.e.*, whether metals tend to adopt native local structures as given by their pure-phase compositions. Prior work by Clément *et al.* and Strobridge *et al.* came to the conclusion that significant geometric distortions are not observed in these mixed-phase materials. The present results, however, pose a question to this conclusion. Table 2.5 also gives DFT-calculated values for Mn^{II} in the LMP and LFP structures, Fe^{II} in the LMP, LFP, and LCP structures, and Co^{II} in the LFP and LCP structures. There is no obvious trend in the data; for example, the values of ε_3 and ε_4 for Co^{II} seem to agree the best with the DFT-calculated values for Co^{II} in the LCP structure. At the same time, ε_2 for Fe^{II} agrees best for Fe^{II} in the LMP structure, while ε_4 agrees best with Fe^{II} in the LCP structure, and ε_1 seemingly agrees well with the LFP structure. The experimental values of ε_{N} for Mn^{II} agree well with Mn^{II} in the LMP structure, which perhaps should be expected considering these values come from the analysis of a material rich in Mn^{II} . Although we cannot draw meaningful conclusions from these data at the present moment, it is plausible that the results suggest that local geometric distortions may in fact be present in mixed-phase LiTMPO_4 compositions.

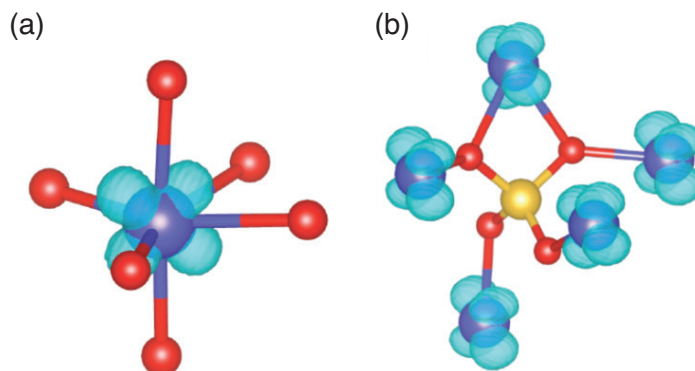


Figure 2.10: Isosurface of the spin density difference, $\rho^{\alpha-\beta}(Mn@LFP) - \rho^{\alpha-\beta}(Fe@LFP)$, illustrating the d orbitals that is singly occupied in Mn^{2+} (d^5) and doubly-occupied in Fe^{2+} (d^6) shown relative to (a) the distorted MO_6 octahedron and (b) TM–O–P pathways. Reprinted with permission from [9]. Copyright 2012 American Chemical Society.

	LiMgPO ₄	LiMnPO ₄	LiFePO ₄	LiCoPO ₄
P ₁	94.09	94.682	94.272	93.892
P ₂	126.68	128.090	128.057	127.47
P ₃	124.74	122.045	120.349	122.87
P ₄	129.60	123.461	123.650	126.22

Table 2.6: Comparison of the M–O–P bond angles in LMP, LFP, and LCP.

Material	Ion	Valence Shell	Size / pm	H20 / ppm	H35 / ppm
LiMnPO ₄	Mn ²⁺	d ⁵	97	671	544
LiFePO ₄	Fe ²⁺	d ⁶	92	240	20
LiCoPO ₄	Co ²⁺	d ⁷	88.5	−436	−412
MnPO ₄	Mn ³⁺	d ⁴	78.5	−494	−500
FePO ₄	Fe ³⁺	d ⁵	78.5	−752	−785
CoPO ₄	Co ³⁺	d ⁶	68.5	−1911	−1935

Table 2.7: The Fermi contact shift for P₁ in six olivine materials calculated with H20 (column 5) and H35 (column 6). The shift steadily decreases as the size of the ion decreases. All metals are in a high-spin octahedral electron configuration.

2.4 Conclusions and Perspectives

In this section we have shown that one-dimensional NMR methods can be applied to the study of the local geometries and electronic structures around ^{31}P sites in mixed-phase LTMP compositions using a combination of low magnetic field strength (7.05 T) and the newly-attainable magic-angle spinning rate of 111 kHz. These experimental conditions combine to produce ^{31}P MAS spectra of these LTMP compositions which are composed mostly of isotropic lines, and result in a resolution similar to that observed in prior studies using 2D sideband-separation methods. Furthermore, we have shown that 1D methods using low fields and ultrafast MAS rates in small rotors, in contrast to claims made in the literature, have quite good sensitivity and therefore short experiment times. The 1D ^{31}P spectrum of $\text{LiMg}_{0.2}\text{Mn}_{0.8}\text{PO}_4$ was collected in only 49 minutes, whereas a comparable spectrum using 2D aMAT or MATPASS would take ≈ 2 days to acquire using a 1.3 mm MAS probe and a magnetic field of 11.7 T. Moreover, we have shown that the intensities in ^{31}P spectra are not significantly biased using 1D methods, whereas this effect is considerable using 2D methods.

The fact that these 1D methods accurately reproduce the spin-transfer pathway contribution differences in $\text{LiFe}_{0.25}\text{Mn}_{0.75}\text{PO}_4$ validates the power of these methods for the analysis of electronic structure around PO_4 environments in these mixed-phase materials. This approach was then applied to the more challenging $\text{LiMg}_x\text{Mn}_{1-x}\text{PO}_4$ phases, which, due to the introduction of the diamagnetic Mg^{2+} ion, exhibit ^{31}P isotropic shifts spanning ≈ 8000 ppm. The contribution of Mn^{2+} to the spin transfer pathways in $\text{LiMg}_{0.2}\text{Mn}_{0.8}\text{PO}_4$ was determined using 1D methods and a simplistic 7-parameter model. These values were then used to determine the unique contribution of both Fe^{2+} and Co^{2+} to the ^{31}P shift in mixed-phase materials by comparison to spin-transfer pathway contribution differences published previously [9, 12], and suggest that prior conclusions, that geometric distortions are not significantly present in these mixed-phase materials, may in fact be incorrect.

These 1D methods and subsequent spectral analysis do not come without drawbacks, though. Due to the necessity of introducing a simplistic model to account for first-order sideband intensities in the 1D ^{31}P spectra, we expect that comparable results could still be attained using 2D methods at higher fields, although the problem of uniformly exciting the ^{31}P shifts remains in this case. The problem with sideband intensities could be solved simply by moving to lower fields, although this carries with it a decreased sensitivity due to the lower ^{31}P polarization at lower field. A better approach would be to simply rotate faster using a smaller rotor and remain at relatively higher fields. A MAS probe capable of rotation rates of around 200 kHz would alleviate the issue of sideband overlap in ^{31}P spectra of these materials, and such a probe with its smaller coil would still provide high sensitivity and would provide higher maximum RF fields strengths, thereby providing even more uniform excitation across the range of ^{31}P shifts in these materials. We anticipate that the never-ending quest for higher MAS rates by members of our field will result in better experimental conditions for the study of these mixed-phase LTMP materials, resulting not only in higher resolution in ^{31}P spectra, but with high throughput as well, permitting systematic studies of these materials.

Chapter 3

Low-power broadband NMR under fast MAS conditions

3.1 Introduction

In general, NMR studies suffer from low sensitivity due primarily to the inherently low nuclear spin polarization. This effect is particularly troublesome for nuclei with low gyromagnetic ratio and low natural abundance, such as ${}^6\text{Li}$, ${}^{13}\text{C}$, ${}^{15}\text{N}$, or ${}^{29}\text{Si}$, as the sensitivity scales with the electromotive force induced in the NMR coil, $\mathcal{E}(t)$, which itself is proportional to γ^3 :

$$\mathcal{E}(t) \propto \gamma^3 N_s, \quad (3.1)$$

where γ is the gyromagnetic ratio and N_s is the number of spins in the system. Before taking into account the number of spins present, this means that the sensitivity relative to ${}^1\text{H}$ for ${}^7\text{Li}$ is $\sim 5.9\%$, and only a miniscule $\sim 0.3\%$ for ${}^6\text{Li}$! Add to this the low natural abundance of ${}^6\text{Li}$ (7.59%) and considering that the signal-to-noise ratio grows only by the square root of the number of co-added transients, we see that it is obviously crucial to maximize the strength of the signal in each scan in order to collect a spectrum in a reasonable amount of time for low-abundance, low-gamma nuclei.

The acquisition of MAS spectra of nuclei exhibiting very broad anisotropic spinning sideband patterns is inherently challenging due primarily to limitations in the the bandwidth of the pulse used and the detection bandwidth of the probe. A spin echo experiment, $\frac{\pi}{2}-\tau_{\text{echo}}-\pi$, must typically be used to acquire a flat baseline, however, conventional RF π pulses often have bandwidths limited to around 100 kHz using typical maximum pulse powers available in MAS probes. It is possible to overcome bandwidth issues by using a shorter refocusing pulse, for instance a $\frac{\pi}{2}$ or even a $\frac{\pi}{4}$ pulse, but this approach results in severe sensitivity losses as $\frac{\pi}{2}$ or $\frac{\pi}{4}$ pulses do not efficiently refocus coherences. Another approach to solve this issue could be the use of frequency stepping [119–122] to collect multiple spectra at different frequency offsets and sum them to yield a spectrum without truncation due to pulse imperfections or limited probe bandwidth. This technique is suitable for highly abundant and sensitive spins such as ${}^1\text{H}$ and ${}^{31}\text{P}$, however in practice it is time consuming for sensitive studies of low- γ , low-abundant nuclei.

A more sensitive alternative is to use broadband swept-frequency pulses for refocusing coherences exhibiting broad anisotropic spinning sideband manifolds. Many pulse shapes have been introduced to solve this problem, such as the hyperbolic secant pulse [51], the Wide, Uniform-Rate Smooth-Truncation (WURST) pulse [53], and the tanh/tan pulse [52]. These broadband pulses have many uses in a variety of magnetic resonance applications and in the case of solid-state studies, WURST pulses have been used to great effect in ultra-wideline spectroscopy [123] of static powders [124–126], and have also been used in broadband adiabatic inversion cross polarization (BRAIN-CP) experiments of static powders [127, 128].

Broadband swept-frequency pulses were not robustly applied to fast MAS ($\nu_R > 30$ kHz) studies of samples with very large shift anisotropies until the introduction of short high-powered adiabatic pulses (SHAPs) [5], as outlined in Chapter 1. It must be stressed that SHAPs demand very high RF fields, ν_1 , falling in the so-called high-power regime, $\nu_1 \gg \nu_R$, and this relationship between MAS rate and the required RF field seems to grow at a rate that is more than linear [13]. This is due to the fact that the increased rate of modulation of the anisotropic shift during higher MAS rates necessarily cause SHAPs to require increasing RF field strengths at increasing MAS rates to maintain the adiabatic condition, and thus keep the magnetization sufficiently locked to the effective field [5]. The use of SHAPs are therefore limited to studies where suitably high RF fields can be achieved [13].

On the other hand, low-power pulses have been long used for a variety of applications, notably selective saturation [57, 129]. In order to achieve excitation, inversion, or refocusing of broad spinning sideband manifolds with low RF fields, one approach is to use DANTE pulse trains [130]; however, although this method can be used to excite broad spinning sideband manifolds, one must sacrifice bandwidth over the isotropic range of frequencies [13]. Spectra containing multiple isotropic environments are incompletely excited as a result, but it is nevertheless useful to accurately measure SA tensor information for isotropically resolved sites [130]. An alternative type of pulse that falls in the low-power regime, $\nu_1 \ll \nu_R$, and which suffers significantly less than DANTE with respect to limited isotropic bandwidth, was recently proposed for MAS measurements of spectra with broad sideband manifolds and was dubbed the single-sideband-selective adiabatic pulse (S^3AP) [6]. S^3AP s sweep slowly through only a single sideband (*i.e.* $\Delta\nu_{RF} \sim \nu_R$, Figure 3.1 right panel) and rely on rotary resonance to invert or refocus the entire spinning sideband manifold during a long pulse ($\tau_p \gg \tau_R$). This means that over the course of the pulse the instantaneous resonance frequency of the magnetization vector of each crystallite sweeps through the excitation window multiple times, eventually leading to inversion if the adiabatic condition is met. In this way S^3AP s have very low RF field requirements, and indeed have been shown *in silico* to demand *decreasing* RF fields at increasing MAS rates [13]. Using a similar principle, hyperbolic secant pulses and WURST pulses have been used to increase sensitivity for half-integer spin quadrupolar nuclei [131–133]. S^3AP s have been used recently in BRAIN-CP measurements under MAS conditions for integer spin [134] and half-integer spin quadrupolar nuclei [135], and were also recently used to achieve efficient population inversion of the ^{14}N resonances with large quadrupolar couplings in glycine at an MAS rate of 111 kHz

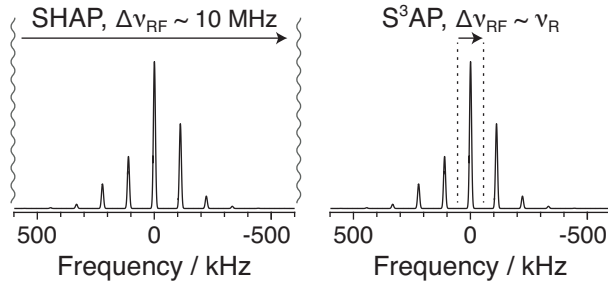


Figure 3.1: A comparison between the different frequency sweep profiles a high-power SHAP and a low-power S³AP applied to a spin with shift anisotropy parameters $\zeta_\delta = 250$ kHz, and $\eta = 0.5$ at 111 kHz MAS. Reprinted from reference [14].

[56].

In this chapter we explore the advantages of using high-power tanh/tan SHAPs versus low-power WURST S³APs for population inversion in broadband NMR experiments for the case of the paramagnetic lithium ion battery cathode material $\text{LiFe}_{0.25}\text{Mn}_{0.75}\text{PO}_4$ [100]. This material exhibits a large SA due to coupling between ^{6,7}Li spins and unpaired electrons in the Fe^{II} and Mn^{II} metal centers. We use both the ⁶Li ($\gamma_{\text{Li}} = 6.27$ MHz/T) and ⁷Li ($\gamma_{\text{Li}} = 16.55$ MHz/T) nuclei in order to examine the effect of γ on the pulse performance at MAS rates ranging from 40 kHz to 111 kHz.

3.2 Inversion pulses in the high-power and low-power limits

We start by discussing the use of high-power SHAPs and low-power S³APs for population inversion. We note in passing that despite the fact that swept-frequency pulses are most routinely used as refocusing pulses (in magnetic resonance imaging, solution-state NMR, and static solid-state NMR studies in particular), the pulse performance under MAS conditions is much more readily examined in the case of inversion. Therefore the remainder of this manuscript will focus solely on the inversion performance of SHAPs and S³APs, though we note that S³APs may be used for refocusing in the same way that SHAPs have been implemented previously [5, 13, 56]. Two general conclusions can be drawn from prior work [6, 13, 56] in the case of S³APs: (1) In general, the maximum available MAS rate should be used, and (2) Generally the frequency sweep should be swept through the most intense sideband. These conclusions come as a result of the fact that the low-power condition must necessarily be met. Therefore at low-to-moderate MAS rates the available RF field strengths are limited and therefore the low-power condition is often violated, whereas under ultrafast MAS the maximum permitted RF field is higher. Prior results have shown S³APs to outperform SHAP pulses under ultrafast ($\nu_{\text{R}} \geq 60$ kHz) MAS rates, but this has been hitherto unconfirmed experimentally.

The performance of SHAPs and S³APs under moderate MAS (40 kHz) and ultrafast MAS (111 kHz) are shown in Figure 3.2 (a) and (b), respectively, which shows the optimal inversion results for each condition and highlights the ability of SHAP pulses to perform comparably better

than S³AP pulses under moderate MAS conditions. The complete RF inversion results for ⁶Li are shown in Figure 3.2 (c) and (d) for SHAPs and S³APs respectively, as a function of RF field strength. They show quite nice agreement between experimental values (filled shapes) and simulated values (solid or dashed lines) for MAS rotation frequencies of 40, 62.5, and 111 kHz. However, sufficiently high RF fields for low- γ nuclei are extremely difficult to generate in order for SHAPs to be efficient. For example, in a 0.7 mm probe a maximum RF field strength of 182 kHz was achieved for ⁶Li with 100 W input power, and this problem is exacerbated with larger coils. Therefore, the S³AP clearly outperforms the SHAP at 111 kHz MAS, shown in Figure 3.2(b). To the best of our knowledge, this is the first such time that a low power pulse has outperformed a high-power counterpart for broadband inversion of an entire spinning sideband manifold.

The same results were not observed in the study of ⁷Li NMR at 111 kHz MAS, the results of which are shown in Figure 3.3, with full simulation results for ⁶Li and ⁷Li given in Figure 3.4. Due to the higher γ of ⁷Li, the probe was able to provide a sufficiently high RF field of 520 kHz, thereby permitting near perfect inversion by SHAP pulses. Surprisingly, the S³AP pulse performs significantly worse than was expected from simulation results, and we expect that this results from a combination of deterring effects. First, due to paramagnetic relaxation enhancement from Mn^{II} and Fe^{II} the ⁷Li relaxation times are quite short, and as a result the T_1 of ⁷Li was measured to be 1.49 ms. As such, relaxation losses during a long inversion pulse may be non-negligible, and assuming pure T_1 relaxation, would be about 17% for a 270 μ s S³AP, compared to about 1% for a 18 μ s SHAP. As the magnetization during the pulse spends a non-negligible time in the transverse plane there will also be additional relaxation losses due to T_2 relaxation, but these losses are difficult to quantify without extensive modeling and simulations, which are outside the scope of this work. An additional and important effect arises from the inability of the S³AP to uniformly excite each crystallite in a microcrystalline powder at low RF field strengths.

In microcrystalline powders there exist different carousels [39] of crystallites, that is, sets of crystallites with the same Euler angles α and β but different values of γ (*i.e.* occupying the same orientation but at different times during sample rotation) that each produce distinct sideband patterns. A feature of S³APs is that these pulses inherently perform differently for each carousel, as can be explained by recalling equation 17 from Pell et al. [6], which gives the first-order average Hamiltonian of a swept-frequency pulse in the low-power limit:

$$\overline{\hat{\mathcal{H}}} = \nu_1(t) A_n \hat{R}_z(\phi(t) - \phi_n) \hat{I}_x \hat{R}_z(\phi(t) - \phi_n)^{-1}, \quad (3.2)$$

where $\nu_1(t)$ is the time-dependent amplitude of the pulse, A_n is the amplitude of the n^{th} -order sideband through which the pulse sweeps, $\hat{R}_z(\theta)$ is a rotation operator representing a spin rotation by an angle θ about the z -axis, $\phi(t)$ is the time-dependent phase of the pulse, and ϕ_n is the phase of the sideband through which the pulse sweeps. We see immediately from this that the effective magnetic field of the pulse is scaled by the sideband intensity, A_n , through which the pulse is swept. This has the important effect for samples with anisotropies much larger than the

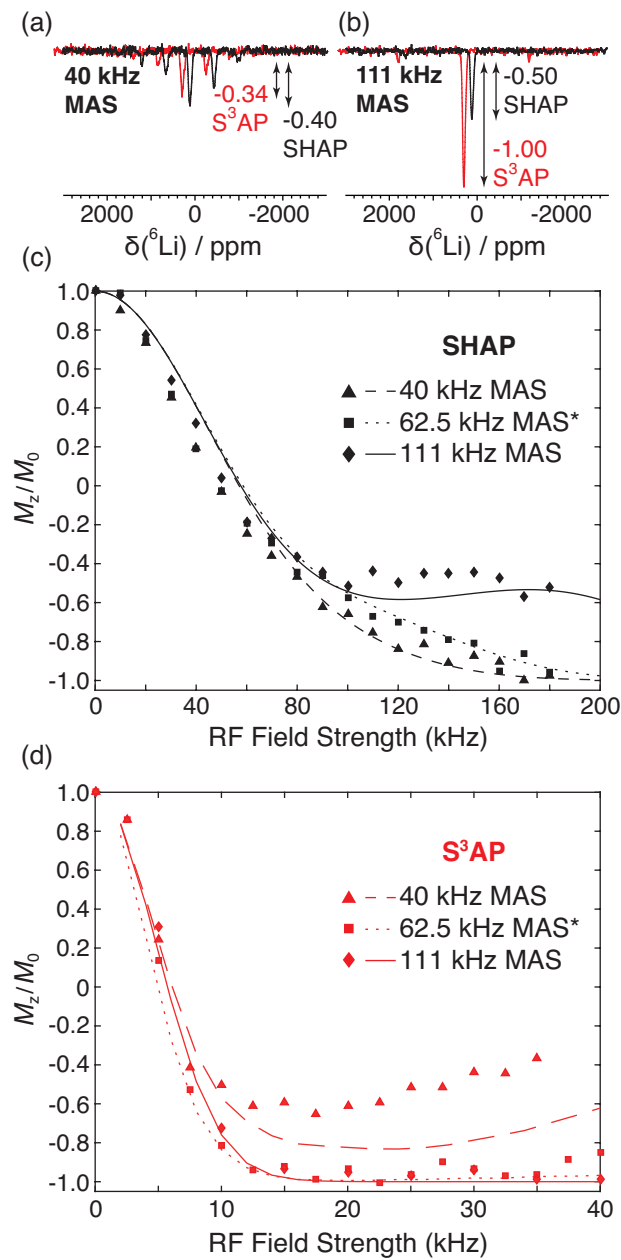


Figure 3.2: Comparison of inversion efficiencies under an MAS rate of (a) 40 kHz, and (b) 111 kHz for a SHAP ($\Delta\nu_{\text{RF}} = 10$ MHz, black) and S³AP ($\Delta\nu_{\text{RF}} = \nu_{\text{R}}$, red) on the ⁶Li nucleus, normalized in intensity to the S³AP-inverted spectrum in (b). The results show the clear difference in performance of SHAPs and S³APs depending on the spinning frequency and thus the RF field requirements. Full RF inversion profiles were determined at 40, 62.5, and 111 kHz MAS for SHAP pulses (c) and S³AP pulses (d) as a function of the RF field strength, where the filled shapes represent experimental values and solid or dashed lines are vertical cross sections from the simulations shown in Figure 3.4 (further simulation details given in the caption). The inverted spectra in (a) and (b) are taken from the optimum points in (c) and (d), corresponding to an RF field strength of 17.5 kHz for the S³AP and 180 kHz for the SHAP in (a), and RF field strengths of 40.0 kHz for the S³AP and 180 kHz for the SHAP in (b). *The simulated inversion profile is an interpolation between simulated inversion profiles with MAS rates of 62 and 63 kHz. Reprinted from reference [14].

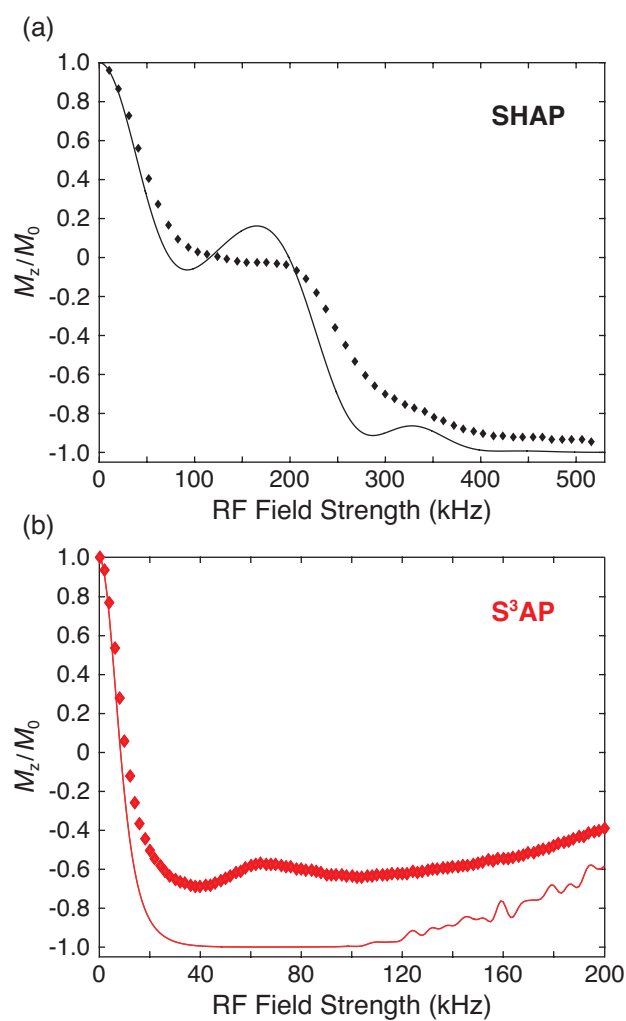


Figure 3.3: Experimental (diamonds) and simulated (lines) RF inversion profiles for SHAPs ($\Delta\nu_{\text{RF}} = 10$ MHz, black) and S³APs ($\Delta\nu_{\text{RF}} = \nu_{\text{R}} = 111$ kHz, red) on the ⁷Li nucleus at a MAS rate of 111 kHz, with simulated values calculated for a spin with equivalent anisotropic to the fitted experimental values, $\zeta_{\delta} = 245$ kHz and $\eta = 0.65$. Reprinted from reference [14].

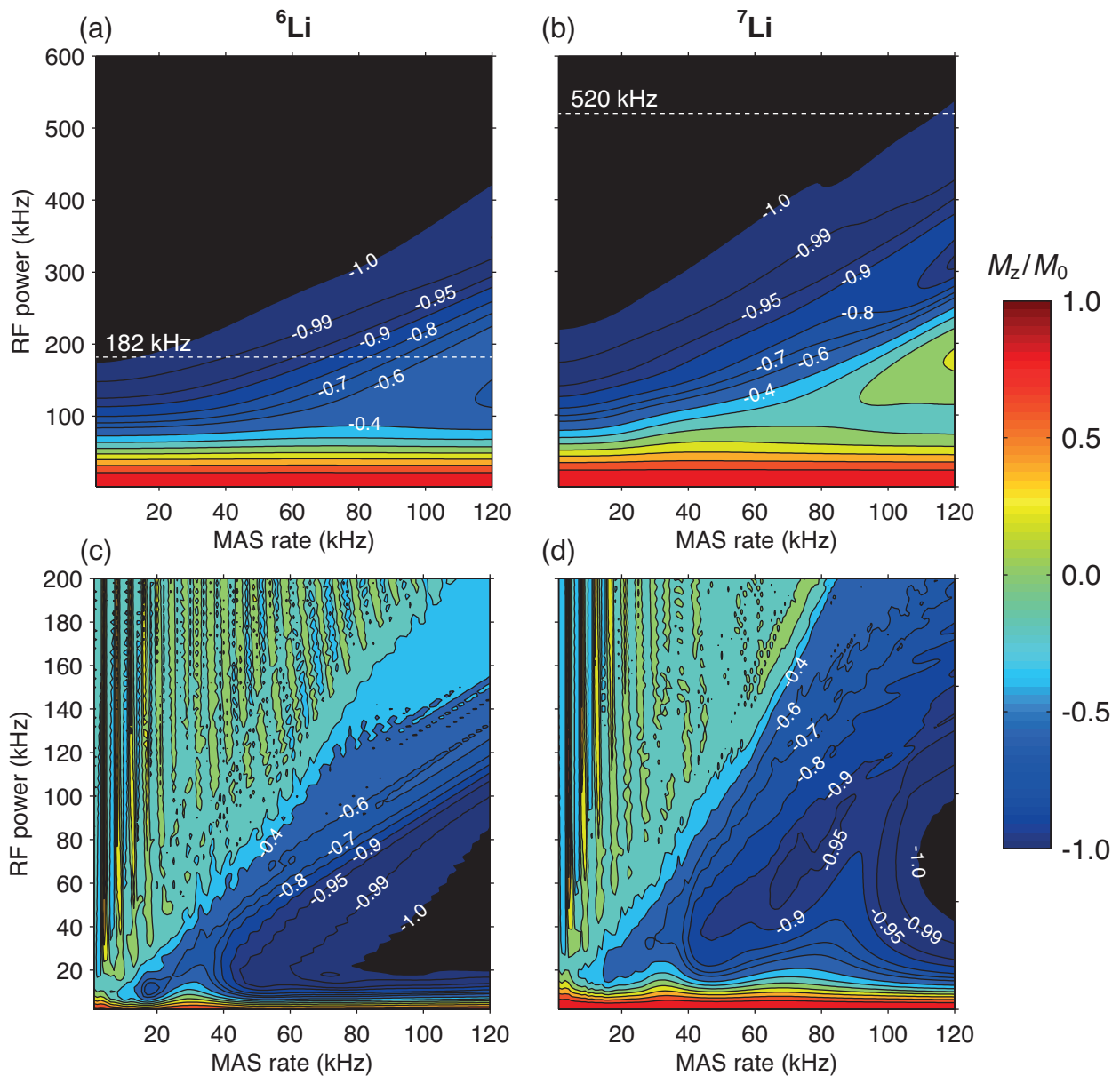


Figure 3.4: Simulated inversion profile contour plots for a SHAP ($\Delta\nu_{\text{RF}} = 10$ MHz) ((a) and (b)) and for a S³AP ($\Delta\nu_{\text{RF}} = \nu_{\text{R}}$) ((c) and (d)) as a function of MAS rate and RF field strength, where the white dashed lines denote the maximum available RF field strength for each Li isotope. The experimental CSA values for ⁶Li and ⁷Li were the same and correspond to the fitted experimental values from the ⁷Li spectrum: $\zeta_{\delta} = 245$ kHz and $\eta = 0.65$ with $\delta = 0$ for convenience. It is clear that as the MAS rate and CSA become larger, the RF field requirements for SHAP pulses increase, and in the case of ⁶Li, to an unobtainable practical limit, while the S³AP pulse can achieve perfect inversion at RF field strengths well below the MAS rotation rate in both cases. Reprinted from reference [14].

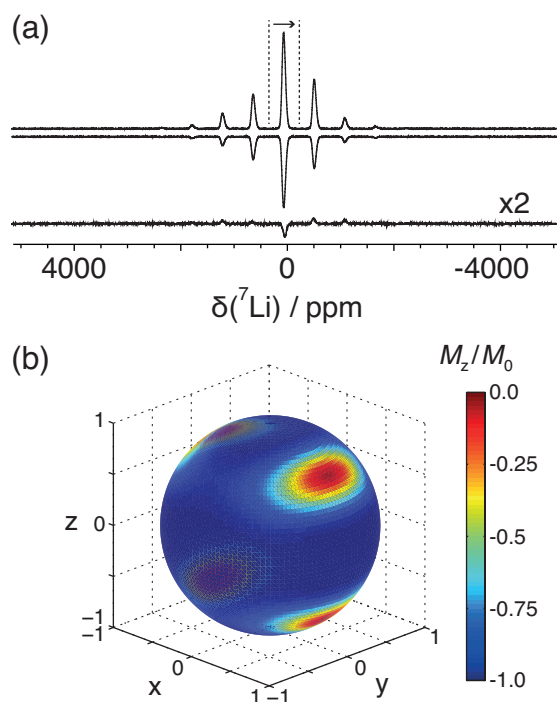


Figure 3.5: (a) ^7Li MAS control spectrum (above), and inverted spectrum (below) using a S^3AP pulse ($\Delta\nu_{\text{RF}} = \nu_{\text{R}} = 111$ kHz) applied to the centerband. The scaled residuals (black, bottom) show a clear biasing of the centerband as a result of the effects discussed in the text. (b) Simulated orientation-dependent inversion profile of a S^3AP pulse with $\nu_{1,\text{max}} = 20$ kHz as a function of the crystallite orientation. Each point on the surface of the sphere corresponds to a unique set of Euler angles (α, β) and the axis labels (x, y, z) are the Cartesian coordinates for the crystallite orientations after transformation from spherical polar frame to the Cartesian frame. The color of each point corresponds to the size of the \hat{I}_z magnetization after the inversion pulse. The results show a clear omission of certain crystallites with small intensity of the centerband, leading to the biasing observed in the residuals in (a). Reprinted from reference [14].

MAS rate that the pulse will not be effective for any carousel of crystallites whose MAS pattern has small or zero intensity in the band over which the pulse is swept. In this case, the optimal RF field for the powder will not be large enough for a carousel with small A_n , resulting in a biasing of the intensities of the resulting sideband pattern by incompletely inverting or omitting some carousels of crystallites. This effect can be appreciated in Figure 3.5(a), which shows the S³AP-inverted spectrum of ⁷Li at 111 kHz MAS, where the pulse was swept over the centerband. The residuals show a clear bias due to exclusion of carousels with little intensity in the centerband. A simulation of the orientation-dependent inversion profiles of a S³AP pulse with $\nu_{1,\max} = 20$ kHz was completed by calculating the inversion efficiency as a function of the Euler angles (α, β) of a uniformly-sampled set of crystallites, the results of which are shown in Figure 3.5(b). The results clearly show that certain sets of crystallites with low intensity in the centerband are poorly inverted at low RF field strengths, leading to the biasing observed in Figure 3.5(a).

3.3 Simultaneous irradiation over multiple sidebands

A possible solution to this problem could be to sweep over multiple sidebands simultaneously. The concept of simultaneous irradiation is itself not new [136] but has not yet been applied to spin inversion using broadband sweeps. We begin by recalling the form of a constant amplitude, constant phase pulse:

$$\vec{\nu}_1 = \nu_1 [\cos(\phi_p)_x + \sin(\phi_p)_y], \quad (3.3)$$

where ν_1 is the RF field strength and ϕ_p is the phase of the RF pulse. This equation can be readily adapted for time-dependent amplitudes and phases:

$$\vec{\nu}_1(t) = \nu_1(t) [\cos(\phi_p(t))_x + \sin(\phi_p(t))_y], \quad (3.4)$$

From here, the equation can be modified to permit simultaneous irradiation over two bands. To build a pulse sweeping simultaneously across two bands we will assume that each of the two constituent pulses have the same amplitudes and phase profiles. As such, this new pulse will be described mathematically as the sum of two pulses at with phase offsets O_1 and O_2 :

$$\vec{\nu}_1(t) = \nu_1(t) \left[\begin{array}{c} \left[\frac{1}{2} \cos(\phi_p(t) + O_1 t) + \frac{1}{2} \cos(\phi_p(t) + O_2 t) \right]_x \\ + \left[\frac{1}{2} \sin(\phi_p(t) + O_1 t) + \frac{1}{2} \sin(\phi_p(t) + O_2 t) \right]_y \end{array} \right]. \quad (3.5)$$

This can then be expanded using trigonometric identities:

$$\begin{aligned} \vec{\nu}_1(t) = \frac{1}{2}\nu_1(t) & \left[\left[\cos(\phi_p(t)) \cos(O_1t) - \sin(\phi_p(t)) \sin(O_1t) \right. \right. \\ & \left. \left. + \cos(\phi_p(t)) \cos(O_2t) - \sin(\phi_p(t)) \sin(O_2t) \right]_{\mathbf{x}} \right. \\ & \left. + \left[\sin(\phi_p(t)) \cos(O_1t) + \cos(\phi_p(t)) \sin(O_1t) \right. \right. \\ & \left. \left. + \sin(\phi_p(t)) \cos(O_2t) + \cos(\phi_p(t)) \sin(O_2t) \right]_{\mathbf{y}} \right]. \end{aligned} \quad (3.6)$$

If we assume that the pulse is symmetric about zero such at $O_2 = -O_1$, this can be re-written as

$$\begin{aligned} \vec{\nu}_1(t) = \frac{1}{2}\nu_1(t) & \left[\left[2 \cos(\phi_p(t)) \cos(O_1t) \right]_{\mathbf{x}} \right. \\ & \left. + \left[2 \sin(\phi_p(t)) \cos(O_1t) \right]_{\mathbf{y}} \right], \end{aligned} \quad (3.7)$$

and now the term $\cos(O_1t)$ can be factored, yielding the general equation

$$\vec{\nu}_1(t) = \nu_1(t) \cos(O_1t) [\cos(\phi_p(t))_{\mathbf{x}} + \sin(\phi_p(t))_{\mathbf{y}}], \quad (3.8)$$

so we see that this is an equation of the same form as a normal RF pulse but with the term $\cos(O_1t)$ superimposed on the amplitude. This results in a pulse that sweeps simultaneously over two bands with equal RF field strength. It is worth stressing that this result produces simultaneous sweeps *in the same direction*, as compared to “diverging” or “converging” sweeps (in opposite directions) [137] produced by a simple cosine modulation.

For measurements where the desired pulse spacing is a multiple of the rotor frequency, ν_R , this formalism can be rewritten as

$$\vec{\nu}_1(t) = \nu_1(t) \cos\left(\frac{2\pi\Delta n\nu_R t}{2}\right) [\cos(\phi_p(t))_{\mathbf{x}} + \sin(\phi_p(t))_{\mathbf{y}}], \quad (3.9)$$

where Δn corresponds to the separation of the irradiated bands in terms of sideband order, noting that the transmitter should be always placed directly between the two desired sidebands. In practice when the amplitude becomes negative, 180° is added to the phase of the pulse.

Type	ν_{tx}/ν_R (ssb)	$\nu_{1,\max}$ / kHz	M_z/M_0
$\mathbf{P1}_{\nu_R}$	-2 (-2)	82	-0.52
	-1 (-1)	50	-0.68
	0 (0)	40	-0.69
	1 (+1)	74	-0.75
	2 (+2)	112	-0.77
$\mathbf{P2}_{\nu_R}^1$	-1.5 (-2,-1)	92	-0.67
	-0.5 (-1,0)	64	-0.71
	0.5 (0,+1)	74	-0.71
	1.5 (+1,+2)	128	-0.73
$\mathbf{P2}_{\nu_R}^2$	-1 (-2,0)	72	-0.71
	0 (-1,+1)	170	-0.63
	1 (0,+2)	76	-0.71
$\mathbf{P3}_{\nu_R}^1$	-1 (-2,-1,0)	90	-0.64
	0 (-1,0,+1)	88	-0.76
	1 (0,+1,+2)	112	-0.67

Table 3.1: Full experimentally optimized parameters for multiple band-swept pulses at 111 kHz as a function of sweep type (column 1), transmitter offset (ν_{tx} , column 2), and RF field strength (column 3). The resulting inversion is given in column 4 with the best performing conditions highlighted with bold text. In all cases the offset was varied in order to include the ± 2 sidebands as the extremities, and the RF field was varied from 0 to 200 kHz in steps of 2 kHz. Optimum conditions were chosen on the basis of experimental integrated areas and not intensities in order to examine the effect of biasing. For simplicity $\nu_{tx} = 0$ corresponds to the frequency of the centerband.

Pulsing on three or more bands

Now that we have worked through the case of two simultaneous sweeps, it is trivial to set up cases with three or more simultaneous frequency sweeps. In the case of three simultaneous sweeps across three adjacent sidebands we can assume that the offsets O_1 , O_2 , and O_3 are set such that $O_1 = -O_3 = 2\pi\nu_R$ and $O_2 = 0$. Therefore we can construct the amplitude modulation by considering the pulse to be composed of one normal S³AP pulse centered about zero, and a pulse simultaneously sweeping over two bands also centered at zero with a band separation $\Delta n = 2$. As such the pulse has the form:

$$\vec{\nu}_1(t) = \frac{1}{3}\nu_1(t)[1 + 2\cos(2\pi\nu_R t)] [\cos(\phi_p(t))_{\mathbf{x}} + \sin(\phi_p(t))_{\mathbf{y}}], \quad (3.10)$$

which results in a simultaneous frequency sweep across three adjacent sidebands. This logic could be extended further to sweep simultaneously across four or more bands but this extension is not detailed here.

In order to be able to describe any multiple-band-swept pulse precisely and concisely, we introduce a general notation to describe each pulse: $\mathbf{P}N_{\Delta\nu_{RF}}^{\Delta n}$, where \mathbf{P} simply denotes that an RF pulse is used, N denotes the number of bands over which the pulse sweeps, Δn is the spacing of the bands in terms of sideband order (*i.e.* $\Delta n = 1$ would denote a pulse with adjacent irradiated

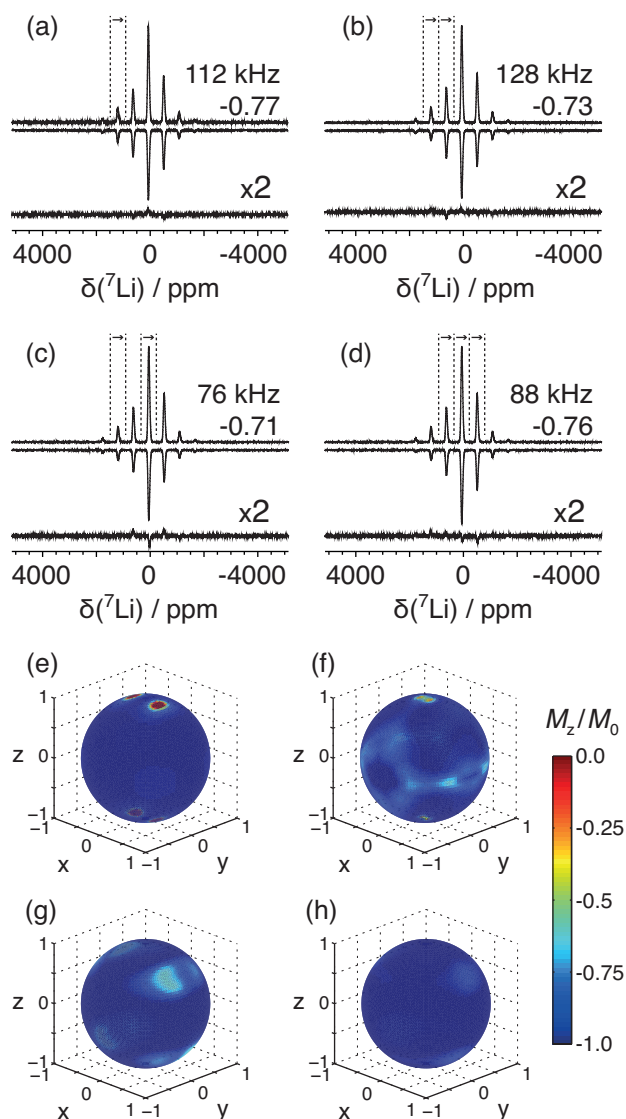


Figure 3.6: Optimized experimental inversion efficiency and optimized RF field strength for (a) $\text{P}1_{\nu_R}$ (S^3AP), (b) $\text{P}2^1_{\nu_R}$, (c) $\text{P}2^2_{\nu_R}$, and (d) $\text{P}3^1_{\nu_R}$ pulses. The upper spectrum in each panel corresponds to the shifted second echo control spectrum, while the experimental inversion spectrum is below. The residuals for each case are given at the bottom in each panel. The arrows indicate the sidebands over which each experimentally-optimized pulse was swept. Shown below the experimental spectra are simulated orientation-dependent inversion profiles of (e) $\text{P}1_{\nu_R}$ (S^3AP), (f) $\text{P}2^1_{\nu_R}$, (g) $\text{P}2^2_{\nu_R}$, and (h) $\text{P}3^1_{\nu_R}$ pulses using the experimentally-optimized RF field strength and offset in each case. Each point on the surface of the sphere corresponds to a unique set of Euler angles (α, β) and the axis labels (x, y, z) are the Cartesian coordinates for the crystallite orientations after transformation from spherical frame to the Cartesian frame. The color of each point corresponds to the size of the \hat{I}_z magnetization after the inversion pulse and follow the coloring scheme shown at the right of the simulated data. The results in (e) show that even in the optimized case for $\text{P}1_{\nu_R}$ pulses, there are sets of crystallite orientations that are excluded from the resulting inverted spectra as a result of these crystallites having spinning sideband patterns with no intensity in the +2 order sideband. On the other hand, the results in (h) demonstrate that sweeping simultaneously over three adjacent sidebands produces much more uniform inversion and therefore a more accurate sideband pattern of the powder after inversion. Reprinted from reference [14].

sidebands), and $\Delta\nu_{\text{RF}}$ is the RF sweep width of each band. With this notation, it is thus necessary to only specify the type of swept-frequency pulse used and the transmitter offset. It should be noted that for $\text{P}N_{\Delta\nu_{\text{RF}}}^{\Delta n}$ pulses with $N > 1$, the effective RF field strength applied to each band is the nominal RF field scaled by N . For simplicity we report only the nominal RF field (*i.e.* the frequency measured in a nutation experiment) in all subsequent figures.

The optimal experimental inversion performance of all tested $\text{P}N_{\Delta\nu_{\text{RF}}}^{\Delta n}$ pulses is shown in Figure 3.6 (a-d) with the optimal sweeps indicated by arrows and the optimized RF field strengths and inversion efficiency given in text with each panel. Each pulse was optimized experimentally as a function of both transmitter offset and RF field strength with the optimal conditions giving the maximum integrated area. The full results of this optimization are provided in Table 3.1. Contrary to what may be expected, the $\text{P}1_{\nu_{\text{R}}}$ (S^3AP) results shown in Figure 3.6 (a) provided an optimum inversion when sweeping over the +2 order sideband. This may be explained by considering that more crystallites could have non-negligible intensity, albeit small, in the +2 order sideband thereby permitting more crystallites to be inverted. This observation would also explain the relatively high optimal RF field strength when sweeping over the +2 order sideband, as higher amplitude RF irradiation must necessarily be applied to compensate for small sideband intensity as previously discussed. A similar result is observed in Figure 3.6 (b), where a $\text{P}2_{\nu_{\text{R}}}^1$ pulse was optimized to sweep over the +1 and +2 order sidebands, again resulting in a very high optimal RF field. In both these cases we observe residuals free of any significant biasing. Sweeping over the 0 and +2 order sidebands with a $\text{P}2_{\nu_{\text{R}}}^2$ pulse unsurprisingly resulted in lower optimal RF field requirements, shown in Figure 3.6 (c), due to the high intensity of the centerband, however we observe biasing in the residuals, which could have come as a result of incomplete inversion of crystallites being inverted by pulsing over the +2 band, as the optimized RF field is lower. Finally, sweeping over the -1, 0, and +1 order sidebands with a $\text{P}3_{\nu_{\text{R}}}^1$ pulse (Figure 3.6(d)) resulted in similar inversion efficiency to the $\text{P}1_{\nu_{\text{R}}}$ pulse but at lower RF field and with small biasing in the residuals, representing a possible compromise between RF field strength and sideband intensity biasing.

In an effort to bolster the conclusions about sideband biasing, orientation-dependent inversion profiles of each $\text{P}N_{\Delta\nu_{\text{RF}}}^{\Delta n}$ pulse were completed by calculating the inversion efficiency as a function of the Euler angles (α, β) for the experimentally-optimized RF field strength and transmitter offset. The results of these simulations are shown in Figure 3.6 (e-h). In the case of the $\text{P}1_{\nu_{\text{R}}}$ (S^3AP) pulse, the results in Figure 3.6 (e) show that the inversion is largely uniform, with the exception of a small set of crystallites that have zero intensity in the +2 order sideband. For these crystallites almost no inversion was observed, with an inversion efficiency of $M_z/M_0 = 0.93$ in the worst case, resulting in the small biasing observed in the residuals of Figure 3.6 (a). This effect decreases as the number of sweeps is increased (Figure 3.6 (f) and (g)), with the best results being given in Figure 3.6 (h) for the $\text{P}3_{\nu_{\text{R}}}^1$ pulse, showing that sweeping over three adjacent sidebands simultaneously yields nearly perfectly uniform inversion. In this case, the worst inversion efficiency was observed for crystallites with low intensity in the centerband, yielding an inversion efficiency of $M_z/M_0 = -0.87$ in the worst case. For all pulses the crystallites with

the highest degree of inversion yielded inversion efficiencies of $M_z/M_0 = -1$. In all cases the simulated results do not account for relaxation, and as such small differences may be observed between the simulated and experimental results.

The simulated inversion results for all $\text{PN}_{\Delta\nu_{\text{RF}}}^{\Delta n}$ pulses on a simulated powder is given in Figure 3.7 as a function of RF field strength and transmitter offset, with powder averaging achieved by simulating 109 (α, β) pairs according to the Lebedev octant scheme [138]. The optimum values for RF field strength and offset were chosen on the basis of maximum integrated area after the inversion pulse, and are denoted with dashed white lines in the first column of Figure 3.7, with the corresponding cross sections given in the second and third column of Figure 3.7 for the RF field strength and offset, respectively. The optimized values for RF field strength and offset differ slightly from the experimentally-optimized values in the case of the $\text{P}1_{\nu_{\text{R}}}$ and $\text{P}2^1_{\nu_{\text{R}}}$ pulses, and this may be explained due to the fact that the simulation does not account for relaxation during the pulse. Although only the optimal condition is denoted in Figure 3.7, we note that there exist many good combinations of RF field strength and transmitter offset for each pulse, which are given in the deep blue regions of panels (a,d,g,j) of Figure 3.7. As such, we observe that in the case of the $\text{P}1_{\nu_{\text{R}}}$ pulse, efficient inversion can be achieved when sweeping across the +2 order sideband using an RF field strength of about 100 kHz; likewise, efficient inversion can be achieved using the $\text{P}2^1_{\nu_{\text{R}}}$ pulse when sweeping over the +1 and +2 order sidebands with an RF field strength of about 120 kHz. Both of these results closely match the experimentally-optimized values as given in Figure 3.6.

3.4 Low-power broadband NMR of ^{14}N

In order to examine nitrogen sites in biomolecules and molecular complexes by NMR, the ^{14}N nucleus may seem, at first glance, the obvious choice due to its high natural abundance of 99.6%. This is not the case, however, due to the fact that ^{14}N is quadrupolar and has an integer nuclear spin, $I = 1$, with typically large quadrupolar couplings on the order of 1 MHz. This results in MAS spectra featuring a broad collection of spinning sidebands and very low sensitivity due to the extremely low gyromagnetic ratio of ^{14}N , which is $\gamma = 3.077 \text{ MHz/T}$, corresponding to a Larmor frequency of $\approx 36 \text{ MHz}$ on a 11.74 T magnet. Furthermore, these spectra are typically very hard to excite and manipulate using the relatively low RF fields achievable due to this low Larmor frequency, to the point that it is typically impossible to efficiently excite ^{14}N spectra using conventional RF pulses. Recently, Vitzthum *et al.* proposed the use of DANTE pulses [139] to excite the broad spinning sideband manifolds of ^{14}N . While an efficient approach, DANTE pulses have the distinct disadvantage of being able to excite very small bandwidths for isotropic sites, limited to only a few kHz in the best cases [13]. A more efficient approach may be to use swept-frequency adiabatic pulses. As before, SHAPs are not an attractive option due to the impracticably high RF fields required for good efficiency; however, S^3APs may be expected to be comparatively efficient due to their low RF field requirements during ultrafast MAS [13]. In this work we show that, indeed, that S^3APs can be used efficiently for the inversion of ^{14}N

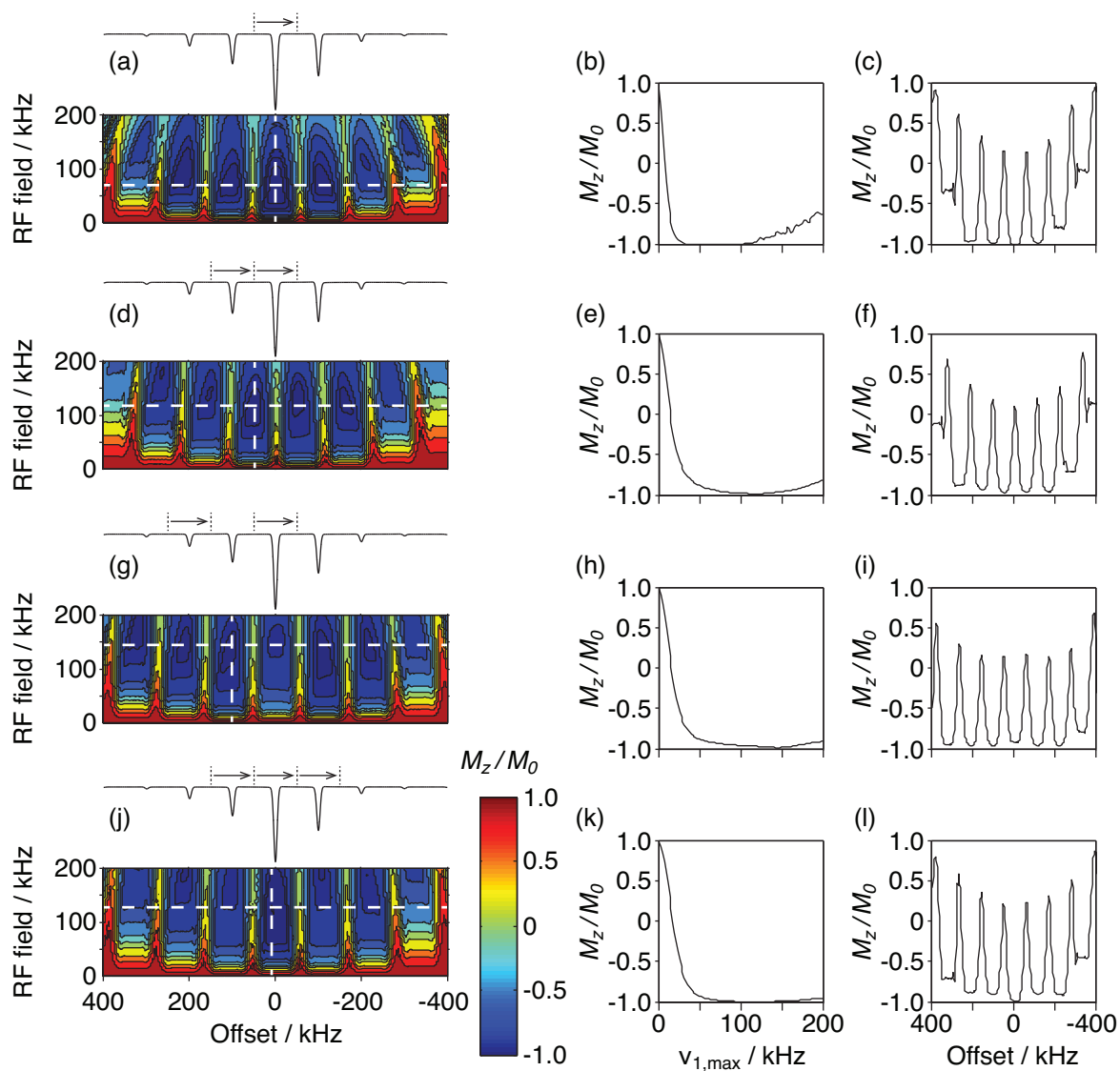


Figure 3.7: Simulated inversion profiles of a spin with CSA parameters $\zeta_\delta = 245$ kHz, $\nu = 0.65$, of a $\mathbf{P}1_{\nu_R}$ (S^3AP) pulse (a-c), $\mathbf{P}2_{\nu_R}^1$ pulse (d-f), $\mathbf{P}2_{\nu_R}^2$ pulse (g-i), and a $\mathbf{P}3_{\nu_R}^1$ pulse (j-i) as a function of offset and RF field strength. The optimal offset and RF conditions are denoted by dashed white lines in (a,d,g,j) with the corresponding frequency sweeps shown above each panel, with corresponding vertical (b,e,h,k) and horizontal (c,f,i,l) cross sections provided. Reprinted from reference [14].

spinning sideband manifolds in the case of (1) $(\text{NH}_4)_2\text{C}_2\text{O}_4$ using a moderate MAS rate of 20 kHz, and (2) glycine using an ultrafast MAS rate of 111.111 kHz.

The simulated RF inversion profiles, following irradiation of different sidebands, of the ^{14}N site of $(\text{NH}_4)_2\text{C}_2\text{O}_4$ with a MAS rate of 20 kHz are given in Figure 3.8 (a). The simulated S^3AP had a WURST-20 shape [53], a length of 5 ms, and a sweep width of 20 kHz. Nearly 100% inversion is predicted for RF field amplitudes between 6 and 15 kHz by irradiating sidebands comprising -2 and +2 orders. This range of RF fields spans 30-75% of the MAS frequency, representing a large optimal window, which shows that the pulse is very tolerant to a mis-set of the RF field strength as might be expected due to *e.g.* RF field inhomogeneities and amplifier imperfections. For comparison, the experimental inversion values are given in Figure 3.8 (b). These experimental values were calculated from the integrals of the spectra over all observed spinning sidebands, and normalized to a spectrum of $(\text{NH}_4)_2\text{C}_2\text{O}_4$ without inversion, shown in Figure 3.8 (c). The agreement between simulated and experimental values is remarkable and shows that the predicted tolerance to RF field mis-set is also realized in practice. Unlike what was observed before in the case of paramagnetic ^7Li sites in $\text{LiFe}_{0.25}\text{Mn}_{0.75}\text{PO}_4$, where the disagreement between simulated and experimental inversion profiles were postulated to be due to PRE effects, the long relaxation times of ^{14}N in $(\text{NH}_4)_2\text{C}_2\text{O}_4$ permit 100% agreement between simulation and experiment. In this case, 100% inversion was observed following irradiation of the +1 order sideband using an RF field strength of 7.1 kHz, with the corresponding spectrum given in Figure 3.8 (d). An important note from these results is that inversion by a S^3AP does not distort the sideband intensities, indicating that the pulse uniformly excites all crystallite orientations uniformly.

The application of a S^3AP inversion pulse to glycine represents a considerably higher challenge due to the much larger quadrupolar interaction relative to $(\text{NH}_4)_2\text{C}_2\text{O}_4$ (C_Q of 1.19 MHz, $\eta_Q = 0.52$ for glycine versus C_Q of 93.4 kHz $\eta_Q = 0.42$ for $(\text{NH}_4)_2\text{C}_2\text{O}_4$). The use of faster MAS rates allows the use of higher RF field strengths while remaining in the low power limit, and in turn, permits the use of shorter S^3AP s with increased sweep widths. This shorter pulse results in smaller signal losses due to relaxation, and the larger sweep widths results in the pulse having a wider range of possible isotropic shifts over which the pulse is efficient for inversion. This combination leads to impressive inversion efficiencies of up to 80%, as shown in Figure 3.9 (a), which shows simulated and experimental inversion profiles for S^3AP s applied to the ^{14}N spectrum of glycine. The experimental results were acquired using a WURST-20 S^3AP of length 1 ms which was irradiated on the centerband, with a sweep width equal to the MAS rate of 111.111 kHz. Five experimental points were acquired using RF field strengths linearly varying between 40-80 kHz, with a maximum inversion efficiency of 80% using 70 kHz of maximum RF field strength for the S^3AP . The deviations from the simulated inversion profile are expected to arise from the faster T_1 relaxation and T_2' dephasing observed for glycine compared to $(\text{NH}_4)_2\text{C}_2\text{O}_4$. These results are very impressive considering the control spectrum, shown in Figure 3.9 (b) has a broad spinning sideband manifold with a width of approximately 2 MHz. The optimum inverted spectrum is shown in Figure 3.9 (c).

These results show that the S^3AP is capable of ^{14}N population inversion with efficiencies of

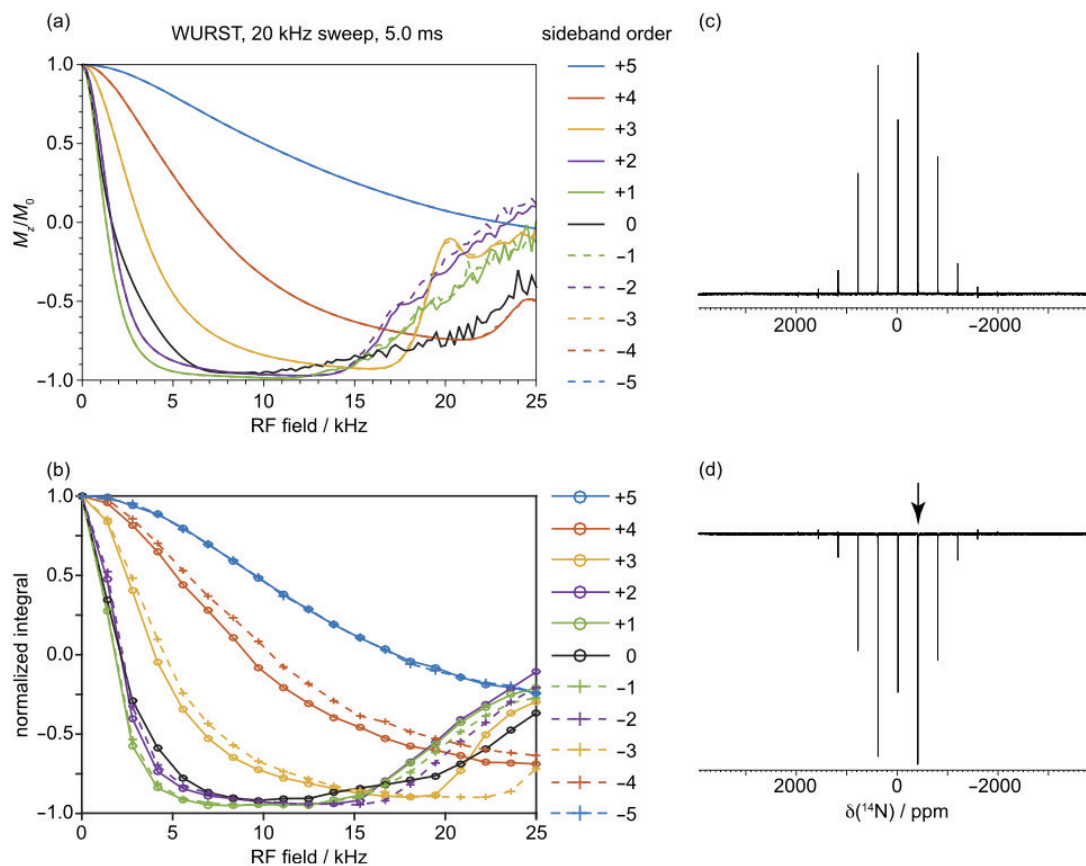


Figure 3.8: Evaluation of the inversion performance of a WURST-20 S^3 AP acting on a spinning microcrystalline powder sample of $(\text{NH}_4)_2\text{C}_2\text{O}_4$. The simulated RF inversion profiles are shown in (a), and the corresponding experimental profiles are shown in (b). In the latter the data points are computed from the integral over the whole spinning-sideband manifold, and normalizing the values relative to the spectrum acquired following an S^3 AP RF field amplitude of zero. In both cases the RF profiles have been determined for irradiation of all the sidebands between orders 5 and +5. The experimental MAS NMR spectra in (c) and (d) were acquired to illustrate the optimum inversion conditions. The reference spectrum is shown in (c). The spectrum following irradiation with a WURST-20 S^3 AP is shown in (d), and shows 100% inversion with an optimum RF field amplitude of 7.1 kHz, as determined from the RF inversion profiles shown in (b). The irradiated sideband is indicated with the arrow in (d). The MAS frequency is 20 kHz, and the WURST-20 S^3 AP has length 5 ms and sweep width 20 kHz. The simulated profiles were calculated with a C_Q of 93.4 kHz ($\omega_Q/2\pi = 70.05$ kHz) and $\eta_Q = 0.42$, corresponding to the parameters for $(\text{NH}_4)_2\text{C}_2\text{O}_4$. The powder averaging was performed with 538 ZCW angles. Reprinted from [56] with the permission of AIP Publishing.

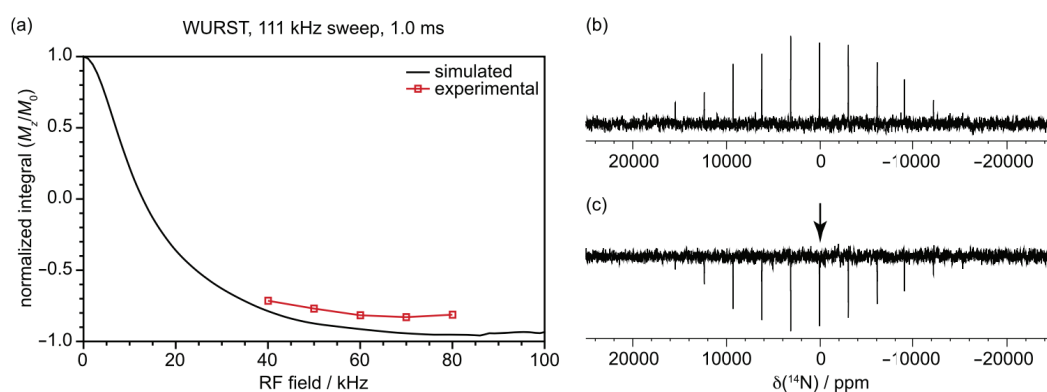


Figure 3.9: Evaluation of the inversion performance of a WURST-20 S^3 AP acting on a spinning microcrystalline powder sample of glycine. The simulated and experimental RF profiles shown in (a) show the effect of irradiation of the centerband. In the latter the data points are computed from the integral over the whole spinning-sideband manifold, and normalizing the values relative to the a control spectrum acquired following an S^3 AP inversion pulse with an RF field amplitude of zero. The MAS frequency was 111.111 kHz, and the WURST-20 S^3 AP has a length of 1 ms and a sweep width of 111.111 kHz. The experimental ^{14}N MAS NMR spectra of glycine are also shown. The reference spectrum at 111.111 kHz MAS is shown in (b). The spectrum following irradiation with a WURST-20 S^3 AP is shown in (c), and shows 80% inversion with an optimum RF field amplitude of 70 kHz, as determined by experimental optimization in (a). The irradiated sideband was the centerband, as indicated by the arrow in (c). The simulated profiles were calculated with a C_Q of 1.19 MHz ($\omega_Q/2\pi = 892.5$ kHz) and $\eta_Q = 0.52$, corresponding to the parameters for glycine. The powder averaging was performed with 538 ZCW angles. Reprinted from [56] with the permission of AIP Publishing.

up to 100% in the best cases, using RF field strengths of only 30-70% of the MAS frequency. Such a result is totally unprecedented and cannot be routinely obtained using conventional high-power RF pulses. From these results we can make a few general comments about the use of S³APs to spin $I = 1$ quadrupolar nuclei in powder samples:

- The S³AP can be used to completely invert a spinning sideband manifold that is 1-2 orders of magnitude more broad than the applied RF field amplitude.
- Higher MAS rates improves the performance of the pulse, permitting higher RF fields and broader sweep widths to be used, which improves the range of isotropic shifts which can be inverted by the pulse.
- The sweep width of the pulse should always be set to equal to the MAS rate.
- In general, longer pulses result in lower optimal RF field strengths, whereas shorter pulses minimize sensitivity losses due to relaxation. The choice of pulse length is a compromise between these two considerations.
- A full parameter optimization of the pulse is relatively straight-forward, requiring only an optimization on the applied RF field and the transmitter offset (irradiated sideband).
- However if time does not permit a full optimization of these values, it is sufficient to irradiate the most intense sideband and optimize only the RF field amplitude up to a value that is equal to the MAS frequency, keeping in mind that the optimal value is typically observed between 30-70% of the MAS frequency.

3.5 Conclusions

We have examined the benefits and limitations of both high-power SHAPs and low-power S³APs and their application to broadband MAS studies of spectra exhibiting broad spinning sideband manifolds due to large anisotropic contributions to the shift. On the LiB cathode material LiFe_{0.25}Mn_{0.75}PO₄, when using a MAS rotation rate of 111.111 kHz, we found that for ⁶Li, where the anisotropy is large but γ is low, the high-power SHAP performs poorly due primarily to sufficiently large RF fields being unavailable, whereas the low-power S³AP provided the maximum achieved sensitivity of all ⁶Li experiments owing to the fact that only 40 kHz of RF field strength was required for 100% inversion. This is the first time that a low-power pulse has been observed to outperform a high-power alternative for an inversion of a broad spinning sideband manifold. This result was not observed for inversion of the high- γ ⁷Li nucleus where sufficiently high RF fields were available to make SHAPs efficient, while S³APs suffered sensitivity losses due to relaxation during the pulse and non-uniform inversion of crystallites within the powder. Moreover, it was shown that S³APs can be easily and efficiently applied to the inversion of ¹⁴N spectra of (NH₄)₂C₂O₄ and glycine, with inversion efficiencies of 100% using a MAS rate of 20 kHz in the best case for (NH₄)₂C₂O₄, which exhibits a relatively small quadrupolar coupling, and

up to 80% using a MAS rate of 111 kHz for glycine, which exhibits a relatively large quadrupolar coupling. These inversion efficiencies are unprecedented, and greatly outperform conventional RF pulses. In both cases, optimization of the S³AP is very straight-forward.

As a potential way to decrease or even eliminate biasing of sideband intensities caused by S³APs, we have examined a class of S³AP-like pulses which sweep simultaneously over multiple bands and can fall comfortably in the low-power regime, and have introduced a notation to describe them. We have found that contrary to what may be expected, S³APs could indeed invert ⁷Li spectra well, but when sweeping not over the centerband. This result comes at the cost of comparatively high RF field requirements, thereby violating the low-power approximation. We can achieve a similar result - while still falling within the low-power limit - by pulsing over three adjacent sidebands simultaneously. This represents the possibility of easily implementing low power pulses without extensive experimental optimization, permitting accurate determination of shift anisotropy parameters when efficient high-power pulses are not available due to hardware limitations. We anticipate that this approach to invert spins will be of particular importance for the study of ^{6/7}Li sites in LiB materials, for studies of ¹⁴N sites in powdered crystalline solids or even biomolecules, and more generally, for the study of paramagnetic systems containing low-gamma nuclei.

Chapter 4

Solid-state NMR applications to heterogeneous catalytic systems

4.1 Introduction

Catalysts play a critical role in modern society, as the production of synthetic reagents, fuel, and polymers (to name but a few examples) rely on catalysts to enable chemical reactions to occur. Heterogeneous catalysts, that is, catalysts which exist in a different phase than reactants, are especially crucial for chemical industries due to the easy separation of catalysts from reaction products, applications to continuous flow processes, and their recyclability [140]. Typically heterogeneous catalysts are solids, with the reactants being liquids or gases. These catalysts typically consist of a metal site or complex bound to a surface, often silica [140], alumina [141], or an aluminosilicate [142]. The Phillips catalyst [143] is based on silica-supported chromium oxide, and is responsible for the production of a large fraction of the high-density polyethylene worldwide. The Ziegler-Natta family of heterogeneous catalysts, meanwhile, are composed of a MgCl_2 support with a Titanium (III/IV) chloride catalyst bound to the surface [144, 145]. These catalysts are responsible for the production of nearly half of the 300 million tons of plastic produced each year by the production of polyolefins like polyethylene and polypropylene [146]. Despite their numerous technical advantages and vast applications in modern life, heterogeneous catalysts have several drawbacks compared to homogeneous catalysts; in particular, the active site of heterogeneous catalysts is not well defined, and thus rational design of new catalysts is a challenge. As such, the structure and activity of active sites are a matter of intense debate in modern chemistry.

Due to its inherent specificity of local order and electronic structure, solid-state NMR can have emerged as an invaluable tool to study local structures in heterogeneous catalytic systems [147–149]. However, due to its low innate polarization, NMR studies of surface-supported species suffer from extremely low sensitivity, especially when attempting to study species containing carbon or nitrogen sites in ligands (1.11% and 0.36% natural abundance for ^{13}C and ^{15}N , respectively), or while attempting to measure interactions with silicon (4.67% natural abundance of ^{29}Si). One possible solution to this problem is to isotopically label the sample, however this can be incredibly costly. Another approach is by the use of dynamic nuclear polarization surface

enhanced spectroscopy (DNP-SENS) [150, 151], which has been shown to increase nuclear polarization by factors upwards of 200 [149]. This technique has incredible promise, and has been recently used to determine a well-defined geometry in a silica-supported platinum species by conventional 2D NMR methods [149]. DNP-SENS has a serious drawback, though, as it cannot be employed across the board for the study of surface-supported heterogeneous catalysts: the DNP effect is quenched in the presence of paramagnetic metals. Therefore in the case of paramagnetic surface-supported catalysts, NMR studies are limited to more conventional techniques. To some degree the enhanced nuclear relaxation by PRE addresses this issue by allowing the acquisition of more scans per unit time, thereby decreasing experiment times, but peak intensities are decreased by the increased anisotropies and line widths resulting from the hyperfine coupling between the metal center and ligands bound to it.

One approach to bridge this gap is to study molecular model complexes which in some ways mimic the effect of binding a metal complex to a surface, which is the focus of this chapter. To begin, I will present a preliminary study carried out by our group and others [15], which focused on a series of diamagnetic organolanthanum complexes of the composition $\text{Lu}[\text{CH}(\text{SiMe}_3)_2]_{3-x}[\text{O}-2,6\text{-}t\text{Bu}_2\text{-C}_6\text{H}_3]_x$ (where $x = 0, 1, 2$). This complex exhibits interesting secondary bonding interactions between the ligand and the lanthanide metal center, and is an interesting case to examine the electrophilicity of the metal center. By substituting the alkyl $\text{CH}(\text{SiMe}_3)_2$ for the oxygen-containing $\text{O}-2,6\text{-}t\text{Bu}_2\text{-C}_6\text{H}_3$ ligand, the structure of the molecule and the electrophilicity of the metal center are made more like the expected surface structure. The results of the study of the surface structure by complementary techniques are then rationalized in light of the results on the molecular complexes. The second section discusses the isostructural complex $\text{Yb}[\text{CH}(\text{SiMe}_3)_2]_3$. Although the molecular structure is expected to be the same, significant paramagnetic effects arising from the $\text{Yb}^{\text{(III)}}$ center present a considerable challenge for the acquisition and interpretation of the NMR spectra described therein. This chapter will focus on the development and implementation of paramagnetic methods and the resulting structural model deduced therefrom. The final section introduces some preliminary studies about using molecular models to study the electronic environment around $\text{Ti}^{\text{(III)}}$ paramagnetic centers, which may have implications for the study of Titanium-based Ziegler-Natta polyolefin polymerization catalysts. While these studies are fresh and relatively undeveloped, the perspectives introduced may be of particular importance to examine the electronic environment around $\text{Ti}^{\text{(III)}}$.

4.2 Secondary Interactions in organometallic lanthanide complexes

Secondary interactions between a metal and its ligands are often suggested as playing an important role in stabilizing ground states and transition states in a catalytic reaction. These interactions imply that the electrons of a specific bond in a ligand are in close contact with an electrophilic metal site. This type of interaction is often present in 3-center-2-electron (3c-2e) bond interactions between an empty orbital on the metal with a pair of electrons in a $\sigma\text{-C-H}$ bond, and are

called agostic C–H interactions[152–154]. The presence of α -, β -, and/or γ -C–H agostic interactions is often postulated in the transition states for insertion of olefins [155–158]. As a very brief overview, the α -C–H agostic interaction found in the transition state in metal-catalyzed polymerization of polypropylene is thought to direct the stereoselectivity in the polymer products. The insertion of an olefin into an early metal–alkyl bond can generate a γ -C–H agostic interaction, which are proposed intermediates in metal-catalyzed olefin polymerization reactions. β -C–H agostic interactions are intermediates in late transition-metal olefin polymerization catalysts that undergo chain-walking to form hyper-branched polyolefins.

In complexes exhibiting β -C–H agostic interactions, there are several important structural features: In general, the C–H bond is elongated, the M \cdots HC distance is shortened, and the M \cdots CC angles become more acute than what would be expected for a sp^3 -hybridized carbon without such an interaction. One of the first complexes exhibiting such an interaction to be fully structurally characterized was (dmpe)Ti(Et)Cl₃ (dmpe = 1,2-bis(dimethylphosphino)ethane), which has bond angles and distances summarized in Figure 4.1(a) [159, 160]. In addition to bond angle and length changes, there are spectroscopic observables that are typical of complexes exhibiting agostic interactions: the ¹H chemical shift in diamagnetic systems tends to shift upfield compared to a comparable alkane, and the ¹J_{CH} coupling constant becomes substantially lower than the typical ~ 125 Hz coupling constant observed in sp^3 C–H bonds. In low-coordinate tris-bis(trimethylsilyl)-methyl lanthanide complexes, Ln[CH(SiMe₃)₂]₃, there are unusually short distances between the metal and one –SiMe₃ group of the pendant alkyl as determined by X-ray crystallography, which is a signature of the electrophilicity of the lanthanide. As such, the secondary interactions exhibited by molecular Ln[CH(SiMe₃)₂]₃ complexes would be interesting in order to evaluate the electrophilicity in silica-supported (\equiv Si)OLn-[CH(SiMe₃)₂]₂.

The following two sections demonstrate an effort to do this one two challenging systems. First, the nature of secondary interactions in the diamagnetic molecular Lu[CH(SiMe₃)₂]_{3-x}[O-2,6-*t*Bu₂-C₆H₃]_x complexes and the silica-supported surface species of Lu[CH(SiMe₃)₂]₃, (\equiv Si)OLu-[CH(SiMe₃)₂]₂, are discussed. The monomeric, three coordinate molecules have short Lu \cdots C γ distances in the solid-state crystal structure from X-ray diffraction, the nature of which is described by solution-state and solid-state NMR spectroscopies as a 3c-2e Lu \cdots C γ Si β interaction. Moreover, the Lu \cdots C γ distance was found to decrease as the alkyl CH(SiMe₃)₂ ligand is substituted by the aryloxy O-2,6-*t*Bu₂-C₆H₃ ligand, which in some ways mimics the effects expected on the silica surface. The resulting model is then used to rationalize the structure of the supported species (\equiv Si)OLu-[CH(SiMe₃)₂]₂, obtained by EXAFS spectroscopy and solid-state NMR. This section represents work published by colleagues, with very minor contributions by me, in the Journal of the American Chemical Society [15]. This thorough discussion is important, as it sets the stage for my investigation of the nature of the secondary interactions in the paramagnetic isostructural molecular complex Yb[CH(SiMe₃)₂]₃ using NMR spectroscopy, where the conclusions drawn therein are discussed in light of the conclusions drawn from Lu[CH(SiMe₃)₂]₃ previously. The solid-state low-temperature crystal structure of Yb[CH(SiMe₃)₂]₃ determined by XRD exhibits the same short Yb \cdots C γ distance as was observed

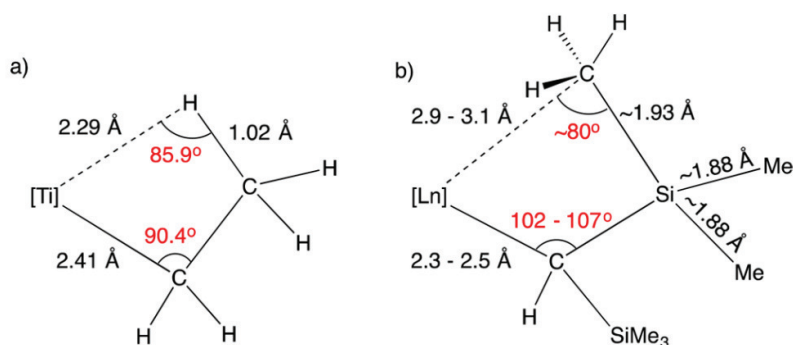


Figure 4.1: (a) The β -C-H agostic interaction in $(dmpe)Ti(Et)Cl_3$ and (b) the secondary interactions in the $Ln[CH(SiMe_3)_2]_3$ family of complexes, which is interpreted as a $Lu \cdots C\gamma-Si\beta$ agostic interaction.

in the case of the $Lu[CH(SiMe_3)_2]_3$; however, because Yb^{III} is paramagnetic, the same NMR methodology used to confirm the structure of $Lu[CH(SiMe_3)_2]_3$ in the solid state is no longer accessible, which presented a considerable experimental challenge due to extremely broad line-shapes and short relaxation times. Paramagnetic constraints, namely pseudocontact shifts (PCS), were eventually acquired and resolved, which revealed the same $3c-2e$ $Yb \cdots C\gamma Si\beta$ secondary interaction as seen in the case of $Lu[CH(SiMe_3)_2]_3$. This work is in preparation for publication [161].

4.2.1 $Lu[CH(SiMe_3)_2]_{3-x}[O-2,6-tBu_2-C_6H_3]_x$ molecular complexes

The crystal structures of the $Lu[CH(SiMe_3)_2]_{3-x}[O-2,6-tBu_2-C_6H_3]_x$ complexes, where $x = 0, 1, 2$, were determined at low temperature (100 K) by X-ray crystallography, with relevant bond lengths and angles summarized in Table 4.1. The ORTEP of $Lu[CH(SiMe_3)_2]_3$ is given in Figure 4.2 (a), with important bond lengths and angles summarized for a single $CH(SiMe_3)_2$ ligand in Figure 4.2 (b). $Lu[CH(SiMe_3)_2]_3$ crystallizes in the $P31c$ space group, and adopts a pyramidal geometry with lutetium laying outside of the plane defined by the C_1 atoms by 0.89 Å. The molecule has C_3 symmetry, since the $-SiMe_3$ groups are oriented like the blades of a propeller. The structure features a relatively short $Lu \cdots C_2$ distance of 2.937(4) Å, and as a result of the C_2-Si_2 distance is elongated to 1.907(3) Å, whereas the other $C\gamma-Si\beta$ bonds have an average length of 1.871 ± 0.005 Å. The observation of asymmetry in the bond lengths and angles in lutetium alkyl-related compounds is generally attributed to an agostic $M \cdots H-C\gamma$ or a $M \cdots C\gamma-Si\beta$ interaction [162]. For $Lu[CH(SiMe_3)_2]_3$, it is possible to distinguish between these two interactions by analyzing the orientation of hydrogen atoms on the C_2 methyl (*i.e.* whether the hydrogens point toward or away from the metal in the crystal structure), and/or by analyzing the $^1J_{CH}$ values in a ^{13}C NMR spectrum. As can be seen in the Newman projection down the C_2-Si_2 bond, shown in Figure 4.2 (c), the orientation of the $C_2-H(2a,2b,2c)$ bonds in $Lu[CH(SiMe_3)_2]_3$ are oriented away from Lu. Moreover, the $Lu-C_1-C_2-H(2a,2b,2c)$ torsion angles ($66(4)^\circ$, $43(4)^\circ$, $176(7)^\circ$, respectively) are inconsistent with those expected for an agostic $M \cdots H-C\gamma$ interaction, though may be consistent with a $3c-2e$ $M \cdots C\gamma-Si\beta$ interaction [163]. This assertion is supported

by solution-state, and importantly, solid-state NMR spectra of Lu[CH(SiMe₃)₂]₃, as described in the following sections.

The crystal structures of Lu[CH(SiMe₃)₂]₂[O-2,6-*t*Bu₂-C₆H₃] and Lu[CH(SiMe₃)₂][O-2,6-*t*Bu₂-C₆H₃]₂ are quite similar to each other, but considerably different from Lu[CH(SiMe₃)₂]₃, as Lu lies in the plane defined by the carbon and oxygen atoms, rather than adopting a pyramidal structure as is seen in Lu[CH(SiMe₃)₂]₃. ORTEPs of both molecules are shown in Figure 4.2 (d) and (e), respectively. Both of the molecules crystallize with two independent molecules in the unit cell, with only one being shown in Figure 4.2. Additionally, one of the Lu-CH(SiMe₃)₂ fragments in only one of the independent molecules of Lu[CH(SiMe₃)₂]₂[O-2,6-*t*Bu₂-C₆H₃] was found to be disordered and was refined in two positions. For Lu[CH(SiMe₃)₂]₂[O-2,6-*t*Bu₂-C₆H₃], one C_γ was found to be in a preferential configuration around Lu, leading to a disparity in the Lu...C_γ distances for each CH(SiMe₃)₂ ligand in each molecule, shown in Table 4.1. A few interesting trends can be observed in Table 4.1, notably that the Lu-C_α distance remains largely uniform as O-2,6-*t*Bu₂-C₆H₃ is substituted for CH(SiMe₃)₂, whereas there is a dramatic decrease in the Lu...C_γ distance upon the first substitution of O-2,6-*t*Bu₂-C₆H₃ for CH(SiMe₃)₂. There is another decrease, albeit less dramatic, upon the second substitution. This result will be explored in later sections when the discussion moves to the silica-supported system, (≡Si)OLu[CH(SiMe₃)₂]₂ in terms of the electrophilicity of Lu.

	M-C _α	M...C _γ	M...Siβ ^a	Siβ-C _γ	M-C _α -Siβ	C _α -Siβ-C _γ
Lu[CH(SiMe ₃) ₂] ₃	2.319(3)	2.937(3)	3.242(1)	1.908(2) ^b 1.871±0.004 ^c	101.9(1) 125.7(4)	106.7(1)
Lu[CH(SiMe ₃) ₂] ₂ [O-2,6- <i>t</i> Bu ₂ -C ₆ H ₃]						
molecule 1	2.29(6)	2.67(1)	3.095(4)	1.89(1) ^b	96.8(7) 139.3(8)	106.9(5)
	2.32(1)	2.74(1)	3.111(4)	1.88(2) ^c 1.87±0.04 ^c	96.3(5) 133.0(6)	106.0(6)
molecule 2 ^d	2.31(2)	2.71(4)	3.13(3)	2.01(3) ^b	99(1) 124(1)	98(1)
	2.33(2)	2.64(5)	3.07(1)	1.87(2) ^b	89(1) 138(1)	103(1)
	2.35(1)	2.69(1)	3.107(4)	1.93(1) ^b 1.86±0.03 ^c	94.6(6) 135.4(7)	107.4(6)
Lu[CH(SiMe ₃) ₂][O-2,6- <i>t</i> Bu ₂ -C ₆ H ₃] ₂						
molecule 1	2.317(7)	2.595(7)	3.042(7)	1.917(7) ^b 1.860±0.008 ^c	93.0(3) 123.1(3)	107.8(3)
molecule 2	2.331(7)	2.601(8)	3.054(2)	1.917(7) ^b 1.867±0.007 ^c	93.3(9) 123.5(3)	106.9(3)

Table 4.1: Selected bond lengths (Å) and angles (°) for Lu[CH(SiMe₃)₂]₃, Lu[CH(SiMe₃)₂]₂[O-2,6-*t*Bu₂-C₆H₃], and Lu[CH(SiMe₃)₂][O-2,6-*t*Bu₂-C₆H₃]₂. ^aDistance from Lu to the proximal Siβ. ^bSiβ-C_γ proximal to the Lu atom. ^cAverage of all non-interacting Siβ-C_γ. ^dOne -CH(SiMe₃)₂ group was refined in two positions.

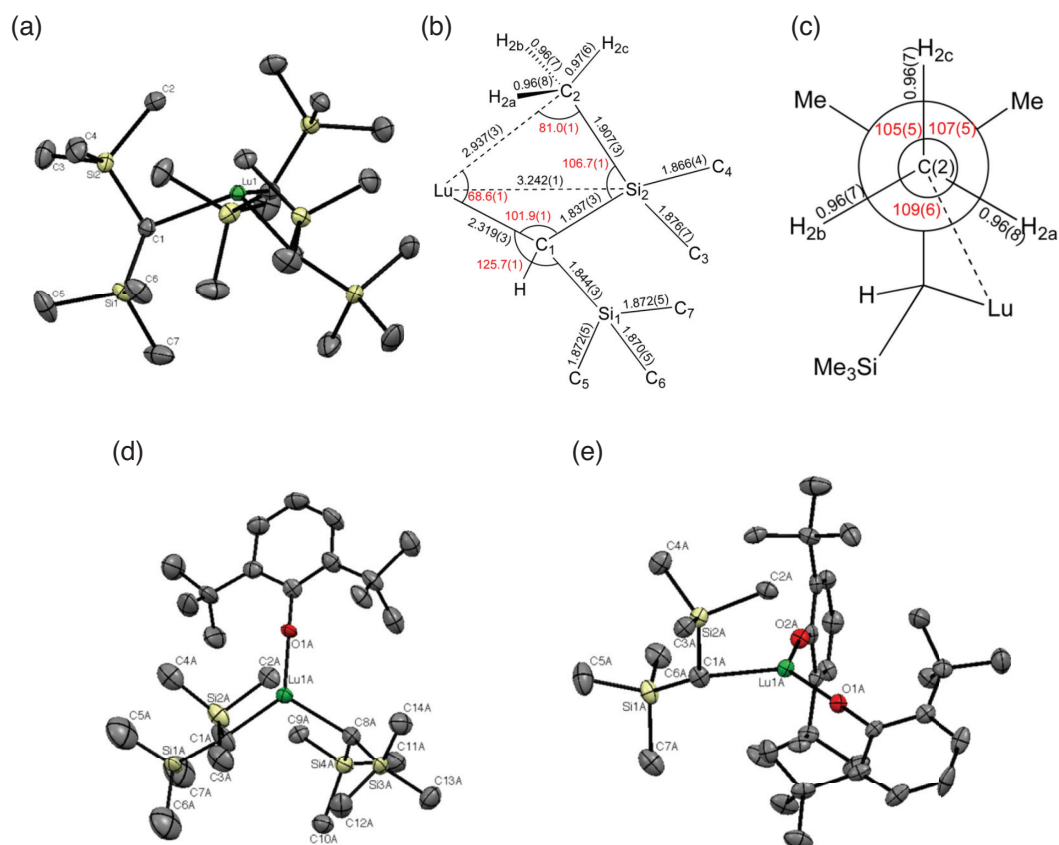


Figure 4.2: (a) ORTEP of $\text{Lu}[\text{CH}(\text{SiMe}_3)_2]_3$ with thermal ellipsoids plotted at 50% probability, omitting hydrogens for clarity. (b) Schematic illustration of the bond lengths and angles for a single $\text{CH}(\text{SiMe}_3)_2$ ligand in $\text{Lu}[\text{CH}(\text{SiMe}_3)_2]_3$. (c) The Newman projection down the $\text{C}_2\text{-Si}_2$ bond in $\text{Lu}[\text{CH}(\text{SiMe}_3)_2]_3$. (d) ORTEP of $\text{Lu}[\text{CH}(\text{SiMe}_3)_2]_2[\text{O}-2,6\text{-}t\text{Bu}_2\text{-C}_6\text{H}_3]$ with thermal ellipsoids plotted at 50% probability. (e) ORTEP of $\text{Lu}[\text{CH}(\text{SiMe}_3)_2][\text{O}-2,6\text{-}t\text{Bu}_2\text{-C}_6\text{H}_3]_2$ with thermal ellipsoids plotted at 50% probability.

Solution-state NMR properties of Lu[CH(SiMe₃)₂]₃

Due to the 3c-2e M...C γ -Si β interactions present in Lu[CH(SiMe₃)₂]₃, the signals in a ¹H NMR spectrum arising from the inequivalent -SiMe₃ groups should appear in a 3:3:3:9 ratio, resulting from the lack of rotation around the Lu-C₁ and C₁-Si₂ bonds. However, the ¹H solution NMR spectrum of Lu[CH(SiMe₃)₂]₃ at 20 °C in methylcyclohexane-*d*₁₄ contains only a single sharp resonance for the -SiMe₃ groups at 0.36 ppm, while the ²⁹Si spectrum exhibits a single resonance at -8.6 ppm. The ¹³C spectrum shows two resonances: one at 59.8 ppm (¹J_{CH} = 91 Hz) and at 5.6 ppm (¹J_{CH} = 118 Hz) for the Lu-C α and the -SiMe₃ groups, respectively. These results seem to indicate that the -SiMe₃ groups undergo fast exchange at this temperature. Figure 4.3(a) shows the variable temperature solution ¹H NMR spectra of Lu[CH(SiMe₃)₂]₃ down to a temperature of -140 °C. Minimal line broadening is observed down to -100 °C; at -125 °C the signal decoalesces and at -140 °C two signals of equal area are observed, with the downfield resonance more broad than the upfield resonance. These results suggest that at this low of a temperature, the dynamics in solution are not completely quenched. The presence of two sites indicates that rotation about the Lu-C₁ bond has been halted, though rapid rotation about the C₁-Si β remains. The linewidth of the downfield resonance does seem to suggest that this peak can be assigned to Si₂Me₃ resonances, and that the rotation about the C₁-Si₂ bond is slowed relative to the C₁-Si₁ bond. The variable temperature ¹³C{¹H} spectra in Figure 4.3(b) are qualitatively similar to the ¹H spectra, with the single peak of the -SiMe₃ resonances at higher temperatures splitting in to two signals at lower temperature, and with the upfield resonance being broader than the upfield one. Figure 4.3(c) shows the non-¹H decoupled ¹³C spectra, which shows two peaks with roughly equal values for the ¹J_{CH} coupling constants, suggesting that for each peak the H-C bond lengths are the same.

Solid-state NMR of Lu[CH(SiMe₃)₂]₃

Although the site exchange between -SiMe₃ groups is quenched at low temperature in solution, rotation about the Si β -C γ bond remains rapid even at a temperature as low as -140 °C. As such, the Lu...C γ structural feature observed in the crystal structure is not preserved in solution. Solid-state NMR provides the definitive answer, and reveals that the Lu...C γ interaction observed in the low-temperature (100 K) crystal structure is present also at room temperature. The first piece of evidence is shown in Figure 4.4 (a), which shows the ²⁹Si CPMAS spectrum with a MAS rate of 5 kHz. The spectrum contains two sharp signals at -5.3 and -11.7 ppm, which indicates that the silicon atoms are inequivalent, and that the rotation about the Lu...C₁ is slow in the solid state. Furthermore, the ²⁹Si spectrum with a MAS rate of 1.5 kHz in Figure 4.4 (b) reveals that the two sites have considerably different CSA tensor parameters, summarized in Table 4.2. The change in magnitude and notably, of the sign of the anisotropy parameter $\Delta\delta$ for each sites indicates that there is a significant structural difference between the two Si nuclei (*i.e.* different bond lengths and angles around each ²⁹Si nucleus) – an indication of a Lu...C γ interaction.

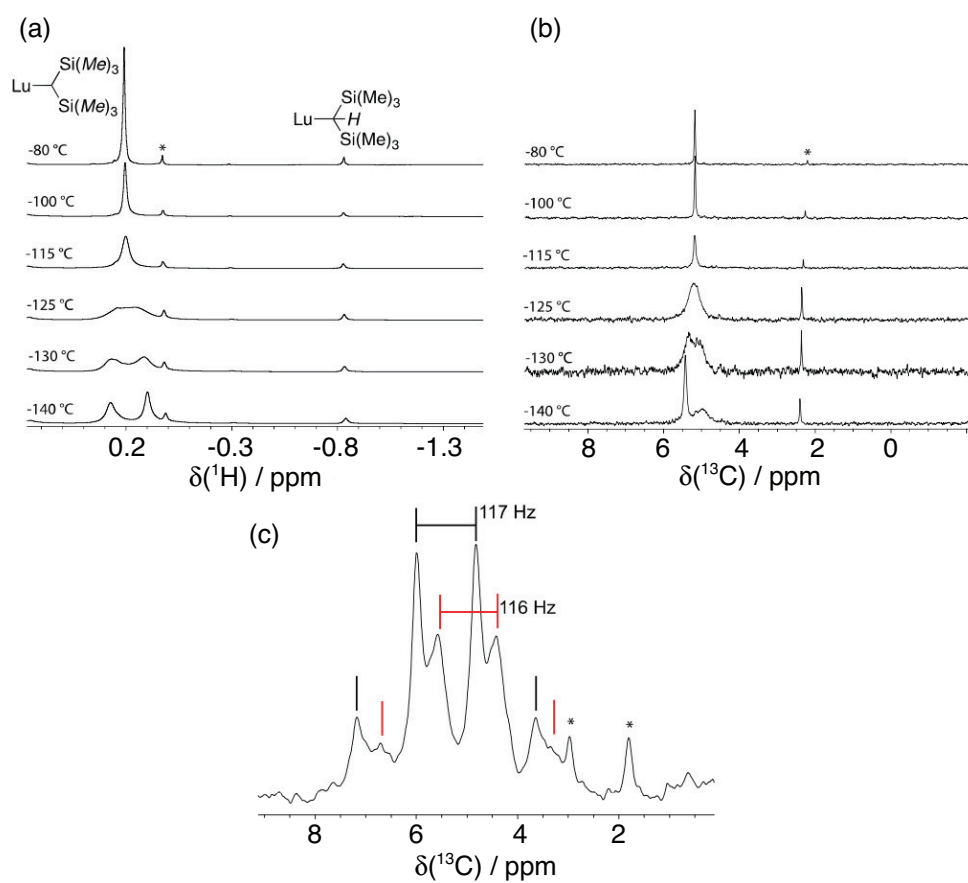


Figure 4.3: (a) Variable temperature ^1H solution NMR spectra with the temperatures indicated. (b) Variable temperature ^1H -decoupled ^{13}C solution NMR spectra. (c) ^{13}C solution NMR spectrum with relevant $^1J_{\text{CH}}$ coupling constants given. Asterisks (*) correspond to residual $\text{CH}_2(\text{SiMe}_3)_2$ from the synthesis.

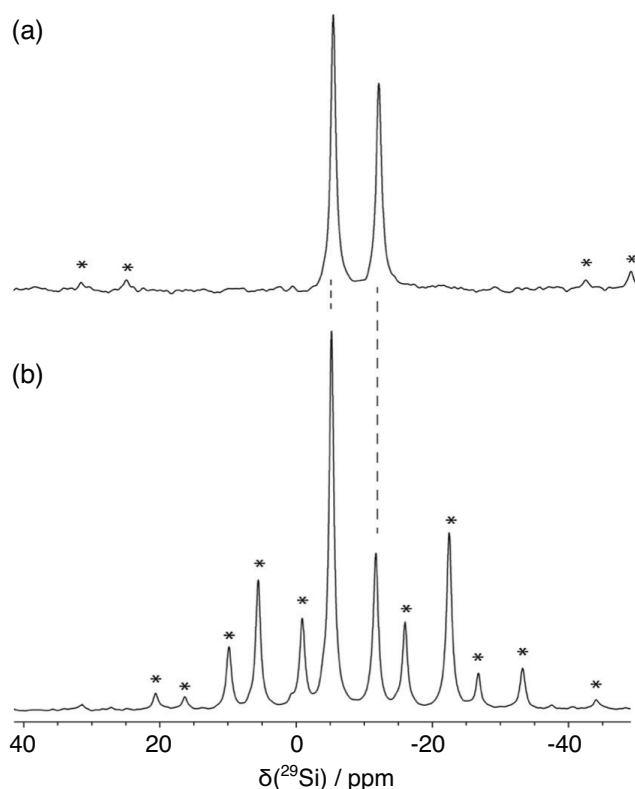


Figure 4.4: (a) CPMAS ^{29}Si spectrum collected with a rotation rate of 5 kHz MAS, and (b) the same with a rotation rate of 1.5 kHz. Asterisk (*) indicate spinning sidebands of each site.

$\delta_{\text{iso}} / \text{ppm}$	$\Delta\delta / \text{ppm}$	η
-5.2	-19.8	0.06
-11.7	31.1	0.01

Table 4.2: ^{29}Si CSA tensor parameters for $\text{Lu}[\text{CH}(\text{SiMe}_3)_2]_3$, determined at a MAS rotation rate of 1.5 kHz.

The ^{13}C MAS spectrum in Figure 4.5 (a), acquired with a rotation rate of 12.5 kHz, shows four unique ^{13}C resonances, one at 57.7 ppm corresponding to the C_α , and three peaks corresponding to SiMe_3 resonances at 4.5, 4.7, and 5.4 ppm, in a 1:1:4 area ratio. This ratio may be rationalized with the assumption that the chemical shift of one of the $\text{C}_2\text{-Me}$ groups is equal to that of the Si_1Me_3 methyl groups. This is confirmed by the $^1\text{H}\text{-}^{13}\text{C}$ HETCOR spectrum shown in Figure 4.5 (f), which shows in the inset that there are four inequivalent $^1\text{H}\text{-}^{13}\text{C}$ pairs in the $-\text{SiMe}_3$ region of the spectrum, two which are overlapped in the ^{13}C dimension but resolved in the ^1H dimension. These results clearly indicate that the $\text{Si}_2\text{-Me}$ groups are inequivalent, and confirms that rotation about the $\text{C}_1\text{-Si}_2$ bond is slow in the solid state.

The final piece of evidence that the secondary interactions between Lu and the $-\text{SiMe}$ group is a 3c-2e $\text{Lu}\cdots\text{C}_\gamma\text{-Si}\beta$ interaction is shown in Figure 4.5 (b)-(e), which shows the J -resolved ^{13}C spectrum of $\text{Lu}[\text{CH}(\text{SiMe}_3)_2]_3$ in (b), with relevant cross sections provided in (c)-(e). This result shows that nearly identical $^1J_{\text{CH}}$ values of $\approx 117 \pm 3$ Hz are observed for each carbon resonance, unequivocally showing that agostic $\text{Lu}\cdots\text{H-C}_\gamma$ interactions are not present in neither solution nor

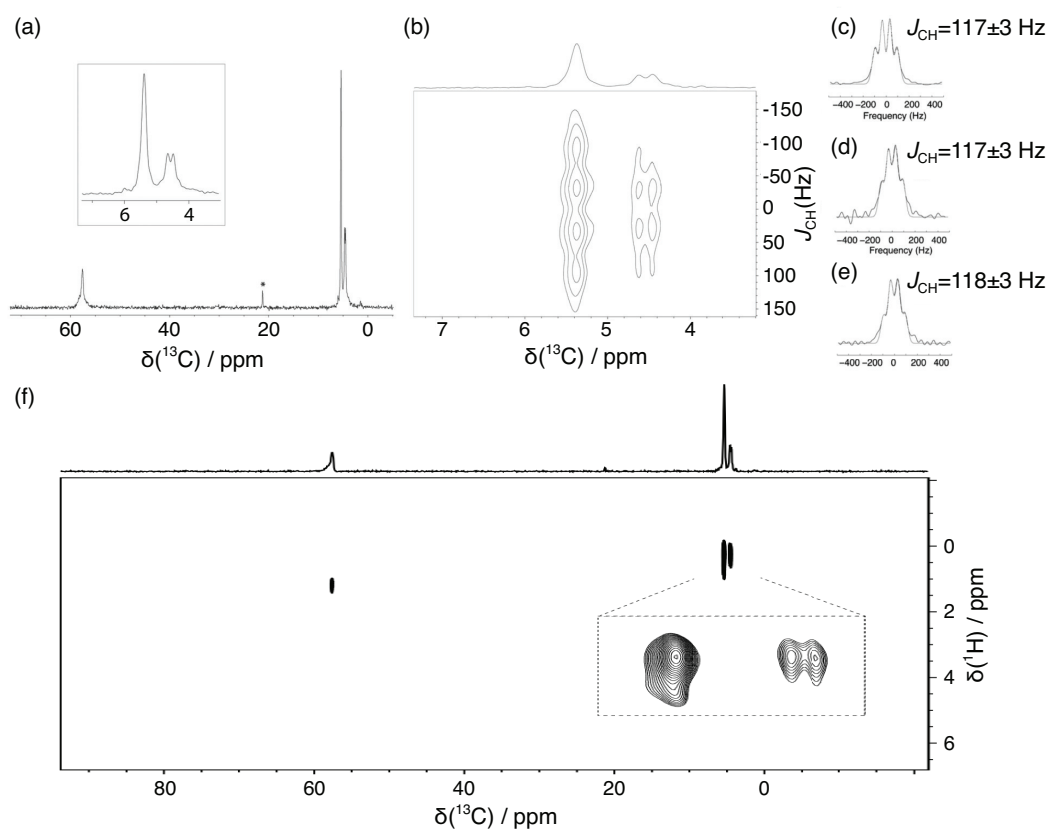


Figure 4.5: (a) The ¹³C CPMAS spectrum of Lu[CH(SiMe₃)₂]₃ collected at a rotation rate of 12.5 kHz, with an inset showing an expansion of the spectrum from 3-7 ppm, * = toluene. (b) 2D *J*-resolved spectrum of Lu[CH(SiMe₃)₂]₃ at 12.5 kHz MAS, shown from 3-7 ppm. (c-e) 1D traces extracted from the spectrum with the corresponding ¹J_{CH} coupling constants given for each trace, where the signal in (c) comes from the ¹³C signal at 5.4 ppm, (d) from 4.7 ppm, and (e) from 4.5 ppm. (f) 2D ¹H-¹³C correlation spectrum, with an inset showing the four signals resulting from H_γ-C_γ pairs.

	Lu[CH(SiMe ₃) ₂] ₃	Lu[CH(SiMe ₃) ₂] ₂ [O-2,6- <i>t</i> Bu ₂ -C ₆ H ₃]	Lu[CH(SiMe ₃) ₂][O-2,6- <i>t</i> Bu ₂ -C ₆ H ₃] ₂
Lu	1.32	1.37	1.50
C α	-1.81	-1.80	-1.80
O	—	-0.86	-0.87
C γ^a	-1.11	-1.14	-1.15
C γ^b	-1.12	-1.12	-1.12
Si β^a	1.81	1.80	1.79
Si β^b	1.80	1.80	1.79
H γ^c	0.25	0.27	0.26

Table 4.3: Trends in the DFT-calculated NBO charges. ^aProximal to Lu. ^bAverage of all other values. ^cHydrogens located on the proximal C γ .

in the solid state. The results clearly indicate that this is a 3c-2e Lu \cdots C γ -Si β interaction.

Computational studies of Lu[CH(SiMe₃)₂]_{3-x}[O-2,6-*t*Bu₂-C₆H₃]_x ($x = 0, 1, 2$)

The geometry of each complex was optimized at the DFT level using the B3PW91-GD3BJ functional, and the geometries are in good agreement with the X-ray structures. This exercise was carried out primarily to investigate the effect of ligand substitution on the natural bond order (NBO) charges of each atom, in order to better understand the electrophilicity of Lu as a function of substitution of the alkyl ligand (CH(SiMe₃)₂) for the aryloxide ligand (O-2,6-*t*Bu₂-C₆H₃), which is used to model the expected effects upon grafting of Lu[CH(SiMe₃)₂]₃ on a silica surface. The results in Table 4.3 point to the fact that there is always a partial positive charge on the Lu atom, with a corresponding partial negative charge on C γ , and partial positive charges on H γ and Si β . These observations support the deduction that Lu \cdots C γ -Si β is a 3c-2e interactions rather than a Lu \cdots H-C γ 3c-2e interaction. As each -CH(SiMe₃)₂ moiety is replaced by -O-2,6-*t*Bu₂-C₆H₃, the trends in the charges are remarkable stable for all atoms, with the exception of Lu, which exhibits an increase upon the first substitution, and a somewhat larger increase with the second substitution. There is also a corresponding slight increase in the negative charge on the proximal C γ atoms. These data are consistent with an increasing electrophilicity of the metal sites, and show how the ligands can modulate the relative charges in a metal-ligand bond following the Pauling electroneutrality principle.

4.2.2 Grafting Lu[CH(SiMe₃)₂]₃ on to partially dehydroxylated silica

The reaction of silica which has been partially dehydroxylated at 700 °C (Sylapol-948, 0.35 mmol OH \cdot g⁻¹) with benzene solutions of Lu[CH(SiMe₃)₂]₃ yields 1.0 equivalent of CH₂(SiMe₃)₂ per surface silanol, with the proposed surface structure given in Figure 4.6 (a). The resulting material, (\equiv Si)OLn-[CH(SiMe₃)₂]₂, lacks a characteristic -OH vibration in the infrared spectrum shown in Figure 4.6 (b), which indicates that Lu[CH(SiMe₃)₂]₃ grafts quantitatively on the surface. Per elemental analysis, the material contains 6.07% Lu, corresponding to 0.347 mmol g⁻¹, and has a C/Lu ratio of 14 \pm 1, supporting the proposed structure in Figure 4.6 (a). The ²⁹Si CPMAS spectrum shown in Figure 4.6 (c) exhibits typical resonances around -100– -120 ppm

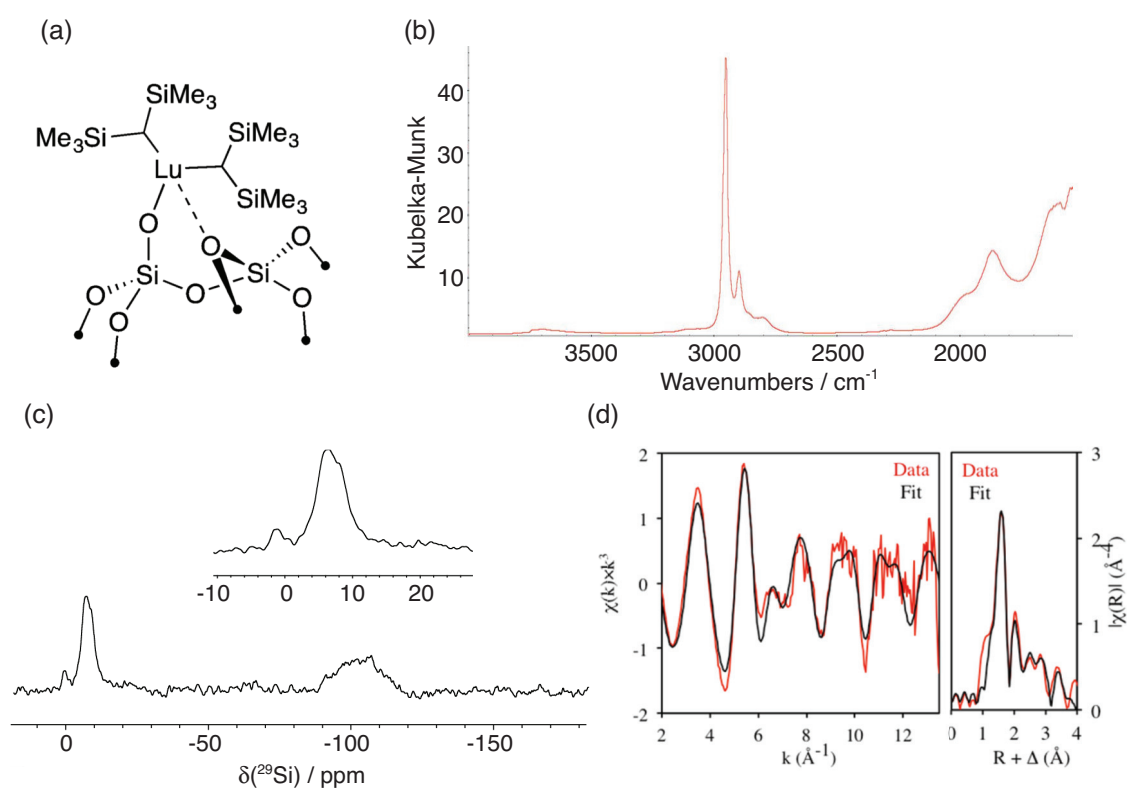


Figure 4.6: (a) Proposed surface structures of $(\equiv\text{Si})\text{OLn}-[\text{CH}(\text{SiMe}_3)_2]_2$. (b) IR spectrum of $(\equiv\text{Si})\text{OLn}-[\text{CH}(\text{SiMe}_3)_2]_2$, which does not exhibit the broad OH vibration expected if intact surface silanol groups were present. (c) ^{29}Si CPMAS NMR spectrum of $(\equiv\text{Si})\text{OLn}-[\text{CH}(\text{SiMe}_3)_2]_2$, indicating the presence of two inequivalent ^{29}Si resonances in $(\equiv\text{Si})\text{OLn}-[\text{CH}(\text{SiMe}_3)_2]_2$. (d) Lu L_3 -edge EXAFS spectrum (black) and the resulting fit (red) of $(\equiv\text{Si})\text{OLn}-[\text{CH}(\text{SiMe}_3)_2]_2$.

element	no. of atoms	distance (Å)	σ^2 (Å ²)	p
O	1	2.038(7)	0.0040(6)	<0.001
C	2	2.32(1)	0.011(2)	<0.001
C	1	2.80(2)	0.006(2)	0.003
O	1	3.23(2)	0.004(1)	0.002
C	1	3.87(2)	0.002(2)	0.061

Table 4.4: EXAFS parameters for $(\equiv\text{SiO})[\text{CH}(\text{SiMe}_3)_2]_2$

corresponding to $Q^{(4)}$ and to a lesser extent $Q^{(3)}$ sites in bulk silica, whereas the resonances from $(\equiv\text{Si})\text{OLn}-[\text{CH}(\text{SiMe}_3)_2]_2$ have shifts of -6 and -8 ppm, displayed in the inset of Figure 4.6 (c). This indication of two inequivalent ^{29}Si sites further corroborates the proposed surface structure of $(\equiv\text{Si})\text{OLn}-[\text{CH}(\text{SiMe}_3)_2]_2$.

The extended X-ray absorption fine structure (EXAFS) spectrum shown in Figure 4.6 (d, black), together with the fit in red, gives a definitive answer for the structure of $(\equiv\text{Si})\text{OLn}-[\text{CH}(\text{SiMe}_3)_2]_2$. The results of the fit are summarized in Table 4.4. The short Lu–O distance of ~ 2.04 Å can be assigned to a surface siloxy group. This distance is comparable to Lu–O bond distances for alkoxide complexes [164, 165] and for $\text{Lu}[\text{CH}(\text{SiMe}_3)_2]_2[\text{O}-2,6-t\text{Bu}_2-\text{C}_6\text{H}_3]$ (~ 2.03 Å). The two carbon scatters at 2.32 Å are assigned to the Lu–C α carbons. The next scattering shell contains longer-range Lu–O and Lu–C scatters at 3.23 and 3.87 Å, respectively. Interestingly, one carbon atom at 2.80 Å must be included in the fit, which is attributed to a secondary Lu \cdots C γ interaction. This value lies in between the Lu \cdots C γ distances observed for $\text{Lu}[\text{CH}(\text{SiMe}_3)_2]_3$ (~ 2.94 Å) and $\text{Lu}[\text{CH}(\text{SiMe}_3)_2]_2[\text{O}-2,6-t\text{Bu}_2-\text{C}_6\text{H}_3]$ (~ 2.7 Å). This observation, together with the observation of the Lu–O scatter at 3.23 Å (attributed to a bridging oxygen, Si–O–Si, on the surface) seems to indicate that the electrophilicity of lutetium increases upon grafting on to silica.

Discussion of results

The structural characterization of $(\equiv\text{SiO})[\text{CH}(\text{SiMe}_3)_2]_2$ revealed the presence of one short intramolecular Lu \cdots C γ distance of 2.80(2) Å, which is significantly longer than the direct Lu–C α bond distance of 2.32(1) Å, and is classified as a secondary interaction. In order to better understand the root nature of this secondary interaction in the grafted compound, the surface structure is compared with the molecular Lu complexes $\text{Lu}[\text{CH}(\text{SiMe}_3)_2]_3$, $\text{Lu}[\text{CH}(\text{SiMe}_3)_2]_2[\text{O}-2,6-t\text{Bu}_2-\text{C}_6\text{H}_3]$, and $\text{Lu}[\text{CH}(\text{SiMe}_3)_2][\text{O}-2,6-t\text{Bu}_2-\text{C}_6\text{H}_3]_2$ which have been studied by X-ray crystallography, solution and solid-state NMR spectroscopies, and DFT calculations. The solid-state structure of $\text{Lu}[\text{CH}(\text{SiMe}_3)_2]_3$ shows that the complex adopts a pyramidal geometry with Lu lying outside the plane defined by the three C α atoms. This results in three methyl groups with short Lu \cdots C γ distances, referred to as proximal methyl groups, and 15 other methyl groups called distal methyl groups. The Lu \cdots C γ distances are about 0.38 Å longer than the Lu–C α bonds, and are referred to as secondary bond distances. The root nature of this interaction, whether mediated by protons (*i.e.* a Lu \cdots H γ –C γ agostic interaction) or by

carbons (*i.e.* a Lu...C γ -Si β secondary interaction interaction) remains unproven by x-ray crystallography, or by low-temperature solution-state NMR due to fluxionality of the proximal and distal SiMe₃ groups in solution. The solid-state ¹³C CPMAS NMR and ¹H-¹³C HETCOR spectra of Lu[CH(SiMe₃)₂]₃ provide definitive evidence that dynamics about the Lu-C α and C α -Si β bonds are quenched in the solid state, with the observation of four pairs of resonances resulting from methyl groups in a 1:1:1:3 ratio. Moreover, the observation of equal ¹J_{CH} couplings for all H-C pairs in the methyl groups suggests that all H-C bond lengths are equal. The DFT-calculated NBO charges give some final pieces of evidence to determine the nature of secondary interactions in the organolutetium complexes studied here. First, the NBO charges on the silicon atoms in -SiMe₃ groups are large and positive, and those on the hydrogen atoms are also positive but smaller. The NBO charges on C α and C γ are large and negative, with the value for C γ being approximately 40% that of C α , and therefore allows us to classify the former as a secondary bonding interaction whereas the latter is a primary one. Furthermore, the relative charges on all atoms clearly indicate that the Lu-C α and Lu...C γ are attractive interactions, whereas Lu...Si β and Lu...H γ are repulsive.

These results combine to form the inescapable conclusion that the nature of the short Lu...C γ distance in Lu[CH(SiMe₃)₂]₃ is not due to a Lu...H-C γ agostic interaction, but rather to a Lu...C γ -Si β interaction in which the methyl group bridges the lutetium and silicon atoms [166, 167]. Furthermore, the Lu-C γ distance in molecular complexes decreases as the number of oxygen-containing ligands increase. These results mimic the interatomic distances in (≡SiO)[CH(SiMe₃)₂]₂ measured by EXAFS, where the Lu-C γ distance lies between Lu[CH(SiMe₃)₂]₃ and Lu[CH(SiMe₃)₂]₂[O-2,6-*t*Bu₂-C₆H₃]. This interaction between Lu and O atoms is associated with an increased positive charge on Lu with increasing oxygen-containing ligands, and therefore with the increased electrophilicity at the metal site. This interaction is particularly favorable in the complexes studied here, as Lu is three-coordinate and therefore unsaturated in the absence of secondary bonding interactions. The nature of the Lu-C γ interaction also allows us to probe the effects caused by the surface siloxy ligand in the coordination sphere of a low-coordinate metal site, and shows how silica can affect the electrophilicity of surface metal sites, making them better Lewis acids and is therefore of particular interest for the field of heterogeneous catalysis.

4.3 Molecular organoytterbium complexes

Following the results from our study of organolutetium complexes and the conclusions drawn about the electrophilicity of the metal site thereof, our focus shifted to the Yb[CH(SiMe₃)₂]₃ complex, which is isostructural to Lu[CH(SiMe₃)₂]₃ in the low-temperature crystal structure. A schematic illustration of the bond lengths and angles for a single CH(SiMe₃)₂ ligand in Yb[CH(SiMe₃)₂]₃ is given in Figure 4.7, with selected bond lengths and angles for both Yb and Lu complexes given in Table 4.5. Yb[CH(SiMe₃)₂]₃ exhibits catalytic activity, with 4.8 mg Yb[CH(SiMe₃)₂]₃ giving 140 mg of polyethylene in 20 minutes with a partial pressure of

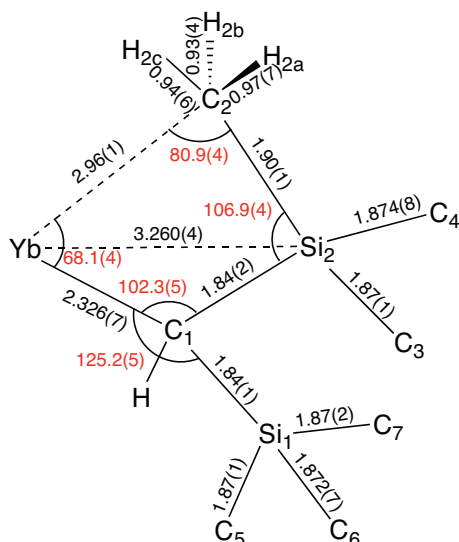


Figure 4.7: Schematic illustration of the bond lengths and angles for a single $\text{CH}(\text{SiMe}_3)_2$ ligand in $\text{Yb}[\text{CH}(\text{SiMe}_3)_2]_3$.

	M–C α	M...C γ	M...Si β	Si β –C γ	M–C α –Si β	C α –Si β –C γ
$\text{Yb}[\text{CH}(\text{SiMe}_3)_2]_3$	2.326(7)	2.96(1)	3.260(4)	1.907(4)	102.3(5)	106.9(4)
$\text{Lu}[\text{CH}(\text{SiMe}_3)_2]_3$	2.319(3)	2.937(3)	3.242(1)	1.908(2)	101.9(1)	106.7(1)

Table 4.5: Comparison of bond lengths (Å) and angles (°) in the low-temperature crystal structures of $\text{Yb}[\text{CH}(\text{SiMe}_3)_2]_3$ and $\text{Lu}[\text{CH}(\text{SiMe}_3)_2]_3$. The values listed for C γ and Si β are for the proximal atoms in the ligand.

ethylene of 10 bar, at a temperature of 340 K. As such, it is critical to understand the nature of secondary $\text{Yb}\cdots\text{C}\gamma$ interactions in $\text{Yb}[\text{CH}(\text{SiMe}_3)_2]_3$ in order to better understand the catalytic activity of the molecular complex, as well as to gain a deeper understanding of the electrophilicity of the metal and how that may change upon grafting to a silica surface.

However, whereas Lu(III) has an electronic configuration of $4f^{14}5d^0$, the electronic configuration for Yb(III) is $4f^{13}5d^0$ and is therefore paramagnetic. As discussed in previous chapters, the presence of unpaired electrons in a molecular complex induces effects which are potentially deleterious, while at the same time providing valuable information about the coordination geometry and electronic structure around a paramagnetic center. Paramagnetic lanthanide ions, in particular, pose a considerable experimental challenge due to considerable PRE effects and line broadening due to anisotropic bulk magnetic susceptibility effects [16, 25, 168]. Moreover, the anisotropic component of the magnetic susceptibility tensor, $\Delta\chi$, is expected to be large, giving rise to large pseudocontact shifts, δ^{PC} . The increased relaxation rates and line widths caused by the paramagnetism of the sample therefore render utterly useless the NMR methods used to determine the nature of the secondary interactions in $\text{Lu}[\text{CH}(\text{SiMe}_3)_2]_3$, and do not permit $^1J_{\text{CH}}$ couplings to be measured. I will show in the subsequent sections, though, that paramagnetic constraints, namely the pseudocontact shift induced by the Yb(III) center, can be used to determine the nature of the $\text{Yb}\cdots\text{C}\gamma$ secondary bonding interactions in $\text{Yb}[\text{CH}(\text{SiMe}_3)_2]_3$.

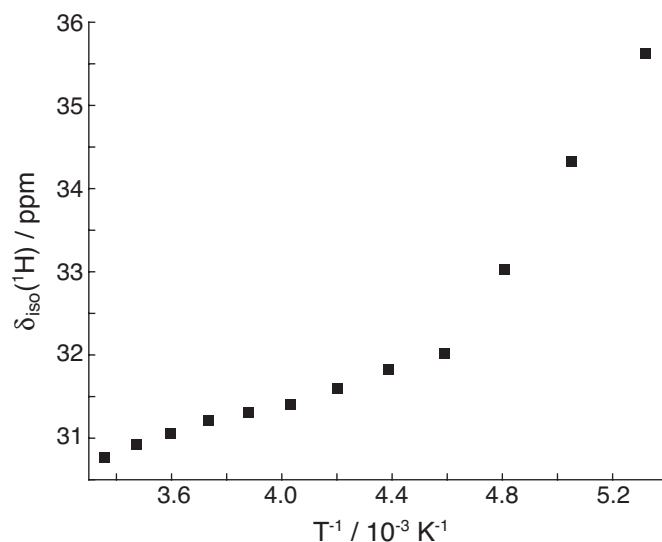


Figure 4.8: Variable temperature ^1H solution-state NMR results for $\text{Yb}[\text{CH}(\text{SiMe}_3)_2]_3$ in perdeuterated isopentane, with the chemical shift of the sole resolved peak plotted against T^{-1} .

4.3.1 Solution-state NMR of $\text{Yb}[\text{CH}(\text{SiMe}_3)_2]_3$

The solution state ^1H NMR spectrum of $\text{Yb}[\text{CH}(\text{SiMe}_3)_2]_3$ at 20°C consists of a single, broad peak at 29.4 ppm with a halfwidth of $\nu_{1/2}=1290$ Hz, in addition to weak and narrow resonances from residual $\text{CH}_2(\text{SiMe}_3)_2$ at 0.01 and -0.42 ppm, for resonances from SiMe_3 and CH_2 , respectively. As the SiMe_3 group fluxionality was removed in the diamagnetic Lu complex at temperatures below -130° , variable temperature NMR spectra were carried out as well on $\text{Yb}[\text{CH}(\text{SiMe}_3)_2]_3$ dissolved in perdeuterated isopentane. The resonance at approximately 30 ppm begins to slowly shift downfield and broaden as the temperature is decreased to $T = 220$ K, at which point the shift and linewidth abruptly increase, and is completely lost below $T=190$ K. This sudden change in the rate of change of the shift likely comes as a result of slowed dynamics of the $\text{CH}(\text{SiMe}_3)_2$ ligands. If there is a transient interaction between methyl groups and the Yb center, contact coupling will begin not only contributing more significantly to the shift, but indeed due to its Curie behavior would increase in strength with decreased temperature. The loss of the signal due to broadening can be explained in the same way, as contact coupling can cause efficient PRE by the Bloembergen mechanism. Add to this that the electron relaxation times are expected to increase with decreasing temperature, it should not come as a surprise that the signal is lost at low temperature.

4.3.2 Solid-state NMR of $\text{Yb}[\text{CH}(\text{SiMe}_3)_2]_3$

While the solution state NMR results on $\text{Yb}[\text{CH}(\text{SiMe}_3)_2]_3$ were inconclusive, solid-state NMR methods, as was seen before in the case of $\text{Lu}[\text{CH}(\text{SiMe}_3)_2]_3$, provide insightful results to the nature of $\text{Yb}\cdots\text{C}\gamma$ secondary bonding interactions in $\text{Yb}[\text{CH}(\text{SiMe}_3)_2]_3$. The ^{29}Si 1D MAS spectrum given in Figure 4.9 (a) provides the first clue that the secondary interactions observed in $\text{Lu}[\text{CH}(\text{SiMe}_3)_2]_3$ are preserved in $\text{Yb}[\text{CH}(\text{SiMe}_3)_2]_3$. This spectrum exhibits two resolved ^{29}Si

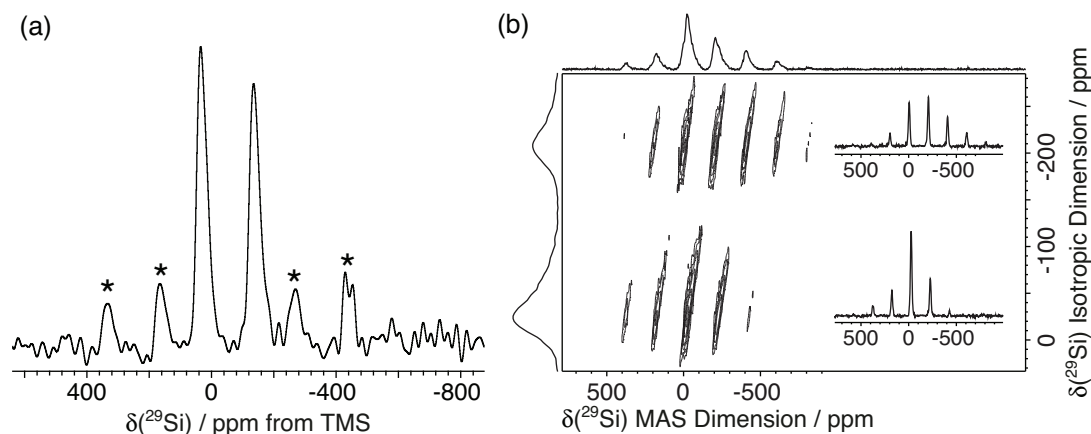


Figure 4.9: (a) The 1D ^{29}Si double spin echo spectrum of $\text{Yb}[\text{CH}(\text{SiMe}_3)_2]_3$ acquired with a MAS rate of 30 kHz, showing two sites with isotropic shifts of $\delta_{\text{iso}} = -21.5$ ppm for site 1 and $\delta_{\text{iso}} = -207.0$ ppm for site 2. (b) The 2D ^{29}Si aMAT spectrum of $\text{Yb}[\text{CH}(\text{SiMe}_3)_2]_3$ acquired with an MAS rate of 20 kHz with CSA values of $\delta_{\text{iso}} = -21.5$ ppm, $\Delta = 410$ ppm, and $\eta = 0.5$ for site 1, and $\delta_{\text{iso}} = -207.0$ ppm, $\Delta = -528$ ppm, and $\eta = 0.7$ for site 2.

resonances with isotropic shifts of $\delta_{\text{iso}} = -21.5$ ppm for site 1 and $\delta_{\text{iso}} = -207.0$ ppm for site 2. The large negative shifts of each site, especially that of site 2, indicates that each nucleus experiences paramagnetic contributions to the isotropic chemical shift due to direct contact coupling between Yb and the two Si atoms, as well as from PCS. Additionally, the width of each peak is considerable, with a FWHM of about 70 ppm for both ^{29}Si environments which can be attributed to ABMS effects from the Yb(III) center. The 2D ^{29}Si aMAT spectrum in Figure 4.9 (b) reveals that each site has large anisotropic contributions to each respective chemical shift tensor, with CSA tensor values of $\delta_{\text{iso}} = -21.5$ ppm, $\Delta = 410$ ppm, and $\eta = 0.5$ for site 1, and $\delta_{\text{iso}} = -207.0$ ppm, $\Delta = -528$ ppm, and $\eta = 0.7$ for site 2. The difference in size and sign of the anisotropy parameter Δ for each site is a particularly interesting observation, and indicates that each site experiences large and competing contributions to the anisotropy of the chemical shift tensor, such as anisotropic contributions from spin-dipolar coupling (through space), and contact coupling (through bond).

The 1D ^1H MAS spectrum shown in Figure 4.10 (a, black) at first glance appeared to be too poorly resolved for use, as it is expected to be composed of at least four signals, each with a unique spinning sideband pattern and with large line widths similar to ^{29}Si . The 2D ^1H aMAT spectrum in Figure 4.10 (b) reveals that isotropic ^1H resonances arise in two domains, centered at approximately -25 and 40 ppm. The 1D ^{13}C MAS spectra in Figure 4.11 (a) and (b) show a similar lack of resolution, with a single grouping of resonances around 35 ppm. Resolution of each of the four expected H–C pairs is finally achieved with the acquisition of a 2D H–C TEDOR heteronuclear correlation experiment, shown in Figure 4.12. This spectrum shows clear evidence of the existence of four peaks, attributable to the resonance pairs $\text{H}_2\text{--C}_2$, $\text{H}_3\text{--C}_3$, $\text{H}_4\text{--C}_4$, and $\text{H}_{5-7}\text{--C}_{5-7}$. The resonance for the $\text{H}_1\text{--C}_1$ pair is not expected to be acquired, owing to the fact that these two nuclei are expected to experience considerable PREs. Even if it were possible to acquire these resonances, extremely large contact shifts would exclude them from this acquisition window. The constraints acquired in the 2D TEDOR spectrum resulted in the deconvolutions shown in Figures 4.10 (a) and 4.11 (b). The experimental isotropic shifts, $\delta_{\text{iso}}^{\text{exp}}$, of

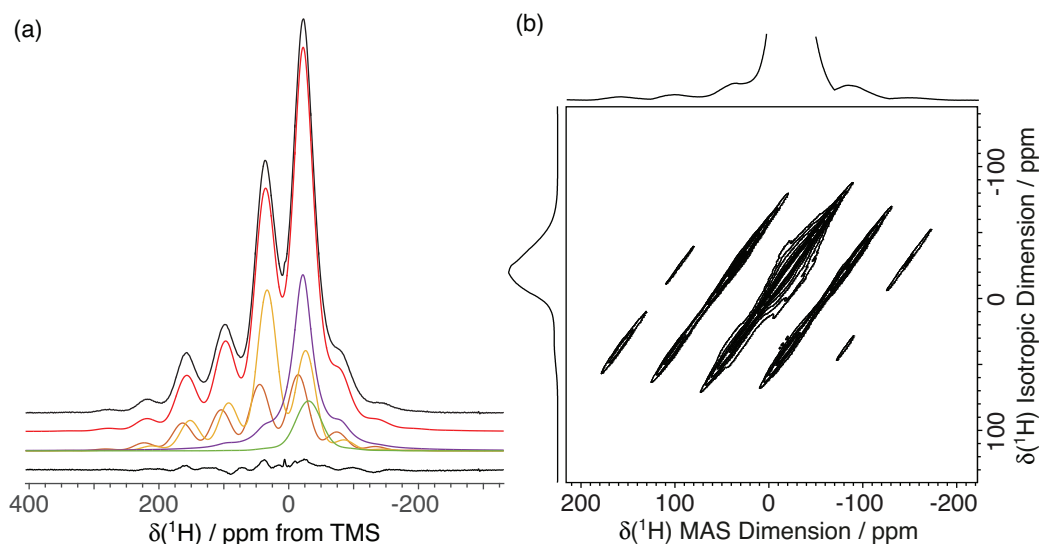


Figure 4.10: (a) The 1D ^1H double spin echo spectrum (black, top) of $\text{Yb}[\text{CH}(\text{SiMe}_3)_2]_3$ acquired with an MAS rate of 30 kHz and the resulting deconvolution (red). The individual deconvoluted line shapes are given below the total deconvolution spectrum, with isotropic shifts of: $\delta_{\text{iso}} = -30.4$ ppm for $\text{H}_5\text{-H}_7$ (green), $\delta_{\text{iso}} = -21.7$ ppm for H_2 (purple), $\delta_{\text{iso}} = 33.4$ ppm for H_4 (yellow), and $\delta_{\text{iso}} = 44.9$ ppm for H_3 (orange). The residuals of the fit are given below in black. (b) the 2D aMAT spectrum of $\text{Yb}[\text{CH}(\text{SiMe}_3)_2]_3$ acquired with a MAS rate of 30 kHz, yielding two isotropic domains in the indirect dimension with centers of mass for each domain given at approximately -25 and 40 ppm.

every resolved site are given in the second column of Table 4.6.

4.3.3 Point-dipole model of the isotropic shifts

In order to confirm the room temperature solid state structure of $\text{Yb}[\text{CH}(\text{SiMe}_3)_2]_3$, it would be necessary to model the paramagnetic isotropic shifts of ^1H and ^{13}C , and ^{29}Si . However, as quantum chemical methods are not yet sufficiently developed to be able to routinely predict the EPR property tensors of lanthanides [169], we are limited to modeling the experimental paramagnetic shifts of the ^1H and ^{13}C sites as arising from solely from PCS contributions to the paramagnetic shift using a point-dipole model. The paramagnetic shifts are determined using the relation

$$\delta_{\text{iso}}^{\text{para}} = \delta_{\text{iso}}^{\text{exp}} - \delta_{\text{iso}}^{\text{dia}}, \quad (4.1)$$

where $\delta_{\text{iso}}^{\text{dia}}$ are the chemical shifts from the ^1H , ^{13}C , and ^{29}Si MAS spectra of the isostructural $\text{Lu}[\text{CH}(\text{SiMe}_3)_2]_3$ complex, and $\delta_{\text{iso}}^{\text{exp}}$ are the experimental isotropic shifts of the nuclei in $\text{Yb}[\text{CH}(\text{SiMe}_3)_2]_3$ determined from the deconvolution of the ^1H , ^{13}C , and ^{29}Si MAS spectra. These values are summarized in column 3 of Table 4.6. We necessarily start with the assumption that the room temperature structure of $\text{Yb}[\text{CH}(\text{SiMe}_3)_2]_3$ is the same as the low temperature crystal structure. Using the atomic positions determined by x-ray crystallography, we can model the isotropic shift of each site as arising from the pseudocontact interactions between the metal center and atoms in the ligands:

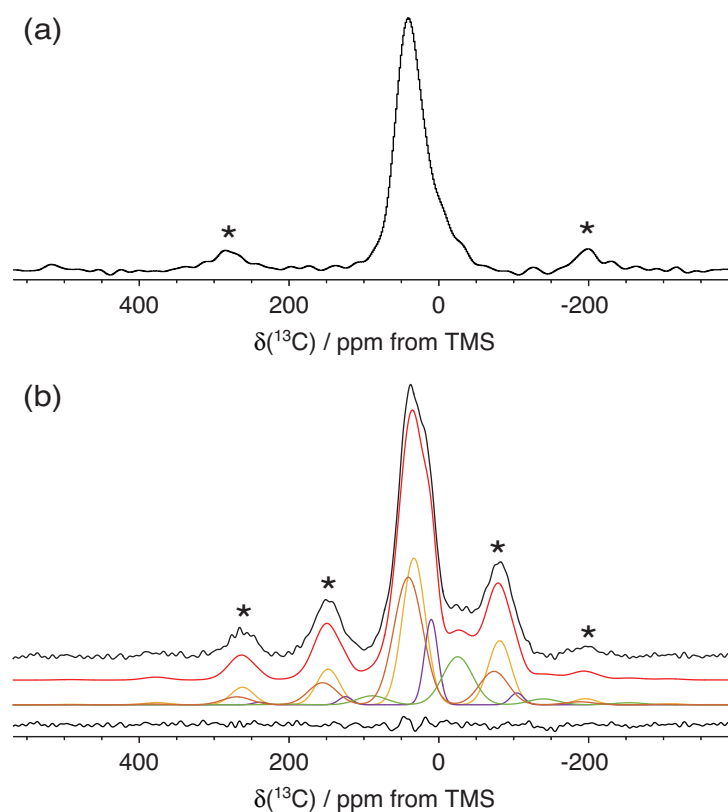


Figure 4.11: (a) The 1D ^{13}C double spin echo spectrum of $\text{Yb}[\text{CH}(\text{SiMe}_3)_2]_3$ acquired with an MAS rate of 30 kHz, showing a single isotropic domain consisting of overlapping resonances for all four observed ^{13}C sites. (b) The 1D ^{13}C double spin echo spectrum of $\text{Yb}[\text{CH}(\text{SiMe}_3)_2]_3$ acquired with an MAS rate of 14.286 kHz (black, top) and the resulting deconvolution (red). The individual deconvoluted line shapes are given below the total deconvolution spectrum, with isotropic shifts of: $\delta_{\text{iso}} = -22.7$ ppm for $\text{C}_5\text{-C}_7$ (green), $\delta_{\text{iso}} = 2.8$ ppm for C_2 (purple), $\delta_{\text{iso}} = 31.4$ ppm for C_4 (yellow), and $\delta_{\text{iso}} = 41.7$ ppm for C_3 (orange). The residuals of the fit are given below in black.

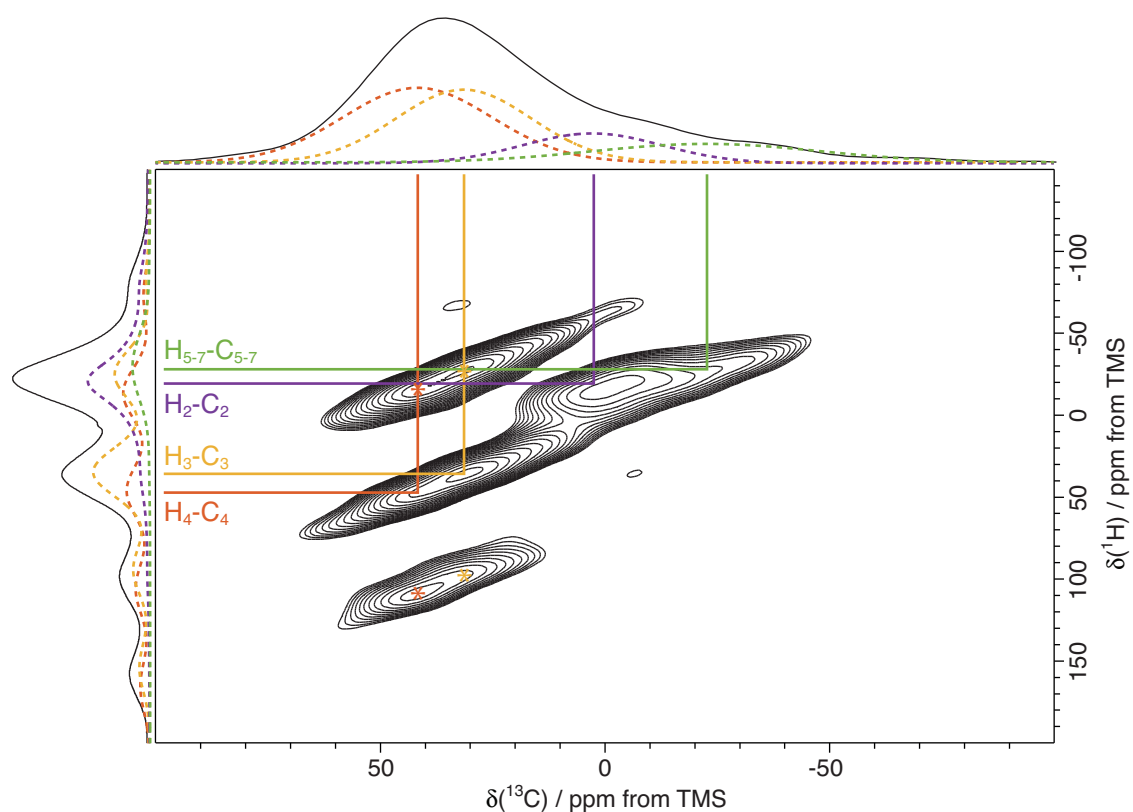


Figure 4.12: The 2D ^1H - ^{13}C heteronuclear correlation TEDOR spectrum of $\text{Yb}[\text{CH}(\text{SiMe}_3)_2]_3$ acquired with 30 kHz spinning, with the corresponding 1D spectra and deconvolutions for each dimension provided. Colored lines for each site indicate the isotropic positions for each nucleus in each site, with the assignments given to the left. Rotational sidebands in the ^1H dimension are denoted with asterisks for H_3 and H_4 .

$$\delta_j^{\text{pc}} = \sum_j \frac{1}{12\pi r^3} \left[\Delta\chi_{\text{ax}}^j (3 \cos \theta_i - 1) + \frac{3}{2} \Delta\chi_{\text{rh}}^j \sin^2 \theta_i \cos 2\phi_i \right]. \quad (4.2)$$

where r is the distance from Yb to the nucleus i , and where θ_i and ϕ_i are the Euler angles defining the position of the nucleus i relative to the principle axis of the χ . As Yb[CH(SiMe₃)₂]₃ has natural C_3 rotational symmetry, the principle axis of χ is normal to the plane defined by the three C α atoms of each CH(SiMe₃)₂ ligand, and as such the rhombic component of the magnetic susceptibility tensor, $\Delta\chi_{\text{rh}}$ is zero. Thus the expression for the PCS can be simplified to the following expression:

$$\delta_j^{\text{pc}} = \sum_j \frac{1}{12\pi r^3} \left[\Delta\chi_{\text{ax}}^j (3 \cos \theta_i - 1) \right]. \quad (4.3)$$

This expression can be further simplified by collecting terms:

$$\delta_j^{\text{pc}} = \sum_j \kappa \Delta\chi_{\text{ax}}^j, \quad (4.4)$$

where κ is defined as

$$\kappa = \frac{3 \cos \theta_i - 1}{12\pi r^3}. \quad (4.5)$$

Thus as κ can be calculated for each atomic position, it is possible to perform a single-variable linear fit of $\delta_{\text{iso}}^{\text{para}}$ against κ to extract the value of $\Delta\chi_{\text{ax}}$.

As the PCS is a long-range, through-space effect, it is not sufficient to simply model a single molecule with the assumption that the local metal is the sole contributor to the experimental PCS. Nearby metal ions must be therefore taken into account, which is achieved by summing the effects of all Yb centers in a 19x19x19 supercell, at which point the effects from distant Yb centers have no considerable effect and any larger supercells do not improve the results. To account for rotation of the methyl groups, the PCSs arising from two equally-spaced orientations were averaged by rotating about each Si-C bond by 180° starting from the crystal structure orientation, assuming a rigid body. To account for rotation about the C₁-Si₁ bond, the PCSs arising from ten equally-spaced orientations were averaged by rotating about the C₁-Si₁ bond in 36° increments starting from the crystal structure orientation. Using this protocol, the value of κ for each site was calculated, and the experimental paramagnetic shifts of each site were plotted against their respective values for κ , shown in Figure 4.13 (a). Only the atoms three or more bonds from Yb, and therefore expected to have a very small contact contribution to the isotropic shift, were included in the fit of $\Delta\chi_{\text{ax}}$, which gave a value of $\Delta\chi_{\text{ax}} = -16.5 \times 10^{-32} \text{ m}^3$. This value for $\Delta\chi_{\text{ax}}$ is in good agreement with previously measured values for Yb(III) in a protein matrix [170]. Moreover, the resulting PCS calculated for each site using $\Delta\chi_{\text{ax}} = -16.5 \times 10^{-32} \text{ m}^3$ results in good agreement between the experimental paramagnetic shifts, shown in Figure 4.13 (b). The calculated values of the PCS for each site, $\delta^{\text{pc, calc}}$, are given in column 4 of Table 4.6.

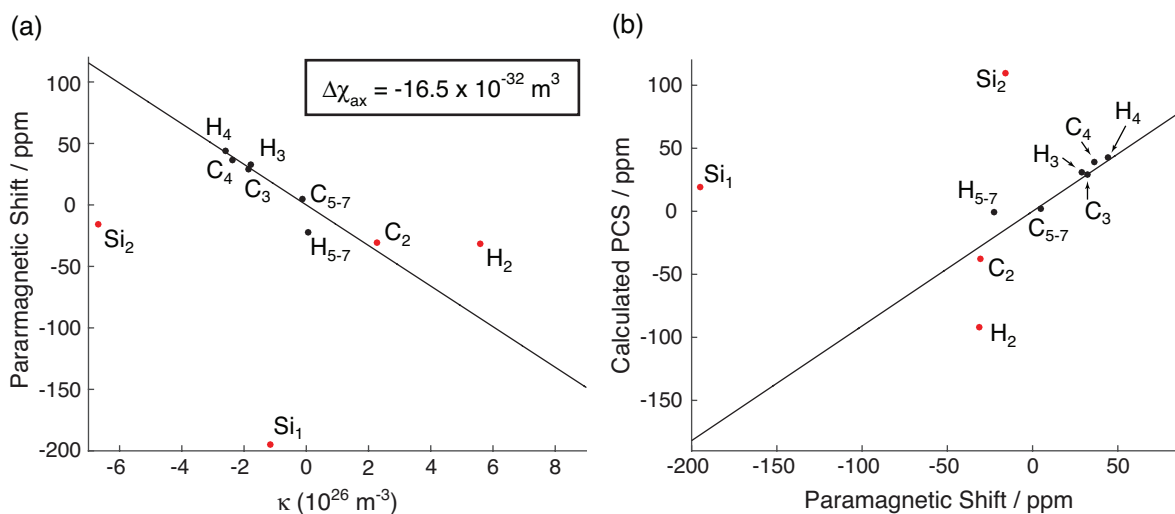


Figure 4.13: (a) The result of fitting the experimental paramagnetic shift against κ using a point-dipole coupling between Yb and each individual nucleus. Only the points given in black were used for the fit, which correspond to the nuclei most distant from the Yb center, thereby experiencing the weakest contact shifts. The linear regression, which was forced through zero, yielded a value for the axial component of the anisotropic magnetic susceptibility tensor of $\Delta\chi_{\text{ax}} = -16.5 \times 10^{-32} \text{ m}^3$. (b) A plot of the calculated PCS using $\Delta\chi_{\text{ax}} = -16.5 \times 10^{-32} \text{ m}^3$ against the experimental paramagnetic shift.

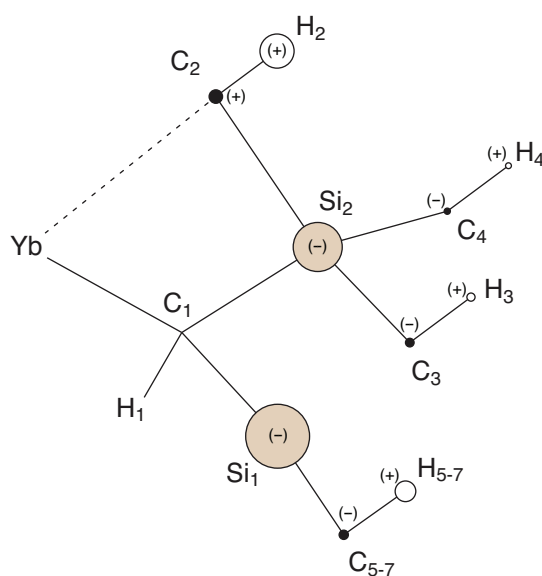


Figure 4.14: Depiction of the size (area of circles) and sign (positive or negative, given within or next to the circles) of the contact shift experienced by each observed nucleus, given in column 5 of Table 4.6. For simplicity, only one of the equivalent carbon and proton sites are shown for each unique site.

	$\delta_{\text{iso}}^{\text{exp}}$	$\delta_{\text{iso}}^{\text{para, exp}}$	$\delta^{\text{pc, calc}}$	$\delta^{\text{con, calc}}$
Si ₁	-207.0	-195.3	19.1	-214.4
Si ₂	-21.5	-16.2	110.1	-126.3
H ₂	-21.7	-30.9	-92.1	61.2
H ₃	44.9	32.9	29.4	3.5
H ₄	33.4	44.4	42.6	1.8
H ₅ -H ₇	-30.4	-23.1	-0.7	-22.4
C ₂	2.8	-28.1	-37.6	9.5
C ₃	41.7	26.8	30.7	-3.9
C ₄	31.4	37.1	39.1	-2.0
C ₅ -C ₇	-22.7	-2.6	1.9	-4.5

Table 4.6: The experimental isotropic shifts (column 2), experimental paramagnetic shifts (column 3), calculated PCS (column 4) and estimated contact shift (column 5) for each nucleus in Yb[CH(SiMe₃)₂]₃. All values are given in ppm.

With the calculated PCS values for each site, it is possible to estimate the contact contribution to the experimental isotropic shift for each site using the relation:

$$\delta_{\text{iso}}^{\text{para}} = \delta^{\text{con}} + \delta^{\text{pc}}, \quad (4.6)$$

which, in terms of the variables used in Table 4.6, can be re-expressed as

$$\delta^{\text{con, calc}} = \delta_{\text{iso}}^{\text{para, exp}} - \delta^{\text{pc, calc}}. \quad (4.7)$$

The resulting values are given in column 5 of Table 4.6, and summarized graphically in Figure 4.14. Unsurprisingly, the two ²⁹Si nuclei in each CH(SiMe₃)₂ ligand experience relatively large contact shifts, owing to the fact that only two covalent bonds separate these atoms from the Yb center. When considering the size of the contact shift for each site, it is worth stressing that it cannot be assumed that Si₁ and Si₂ experience the same contact shift due to the asymmetry of the ligand resulting from the secondary Yb...C γ bonding interaction. Of particular interest is the fact that H₂ and C₂ experience relatively large contact shifts relative to the other proton and carbon sites in the complex, indicating that there is orbital overlap with the Yb³⁺ center, further supporting the notion that there exists a 3c-2e Yb...C γ -Si β secondary bonding interaction in Yb[CH(SiMe₃)₂]₃.

Following the prior results on Lu[CH(SiMe₃)₂]₃, it is absolutely clear from the present results on Yb[CH(SiMe₃)₂]₃ that these two molecules are geometrically equivalent. The observation of two sites in the ²⁹Si MAS spectrum, along with the observation of four sites in the ¹H and ¹³C spectra are completely in line with the structural model developed for Lu[CH(SiMe₃)₂]₃. Moreover, as the experimental paramagnetic shifts of the peaks for H₃-H₇ and C₃-C₇ fit well to a point-dipole model of PCS with a believable value of $\Delta\chi_{\text{ax}}$, the room temperature solid-state structure of Yb[CH(SiMe₃)₂]₃ is confirmed to match the low temperature x-ray structure. Finally, as the estimated contact shift of H₂ and C₂ are comparatively large relative to the other proton and carbon sites, there must be an additional spin-transfer pathway to these sites due to

an additional bonding interaction with the Yb^(III) center. All these results combined form the inescapable conclusion that the nature of this bond is a 3c-2e Yb...C γ -Si β secondary bonding interaction, just as was seen before in the case of Lu[CH(SiMe₃)₂]₃.

4.4 Molecular Ti³⁺ complexes as a model for surface-supported Ti catalysts

As previously mentioned, the Ziegler-Natta family of catalysts (ZNCs) [144, 145] are of particular importance in the modern world; the discovery of ZNCs paved the way for the takeover of plastics in every day life. As of 2015, polyolefins like polyethylene and polypropylene represent nearly half of the 300 million tons of plastic produced each year [146]. The latest generation of Ziegler-Natta heterogeneous catalysts are composed of four main components: (1) the support (most commonly MgCl₂, (2) the catalyst, usually TiCl₄, which is grafted on the MgCl₂ surface, (3) the cocatalyst, which is nearly exclusively alkylaluminum compounds, commonly triethylaluminum, and (4) a Lewis base, commonly ethanol or tetrahydrofuran (THF). Despite the fact that these catalysts are used in such abundance, the precise mechanism of polymerization remains a mystery, owing to the fact that the surface structure of these catalysts is not well defined. Numerous experimental [147, 171–177] and computational [178–183] studies have been carried out in order to gain insight in to the surface structure of MgCl₂-TiCl₄-based ZNCs. Of the available experimental methods, solid-state NMR has emerged as a particularly powerful tool for the study of the surface characteristics in ZNCs [147, 148, 174–177] due to its inherent specificity of local variations in structure.

Paramagnetic NMR methods in particular can be a valuable tool for the study of interactions between Lewis bases and the surface Ti^(III) metal sites, and in the case of direct bonding interactions, the coordination geometry around Ti^(III) may be able to be probed directly by the paramagnetic effects induced on such ligands. In order to probe these paramagnetic effects induced by Ti^(III), we have chosen to study molecular Ti^(III) complexes of the composition Ti[OSi(O*t*Bu)₃]₃L₂, where the ligand L was pyridine (pyr) and THF. The molecules adopt a trigonal bipyramidal geometry, with L occupying the axial positions. These structures are depicted in Figure 4.15 (a) and (b). These ligands can be used to probe the electronic environment and local electronic structure of the complexes as a result of the fact that large chemical shift dispersions are expected in the ¹H and ¹³C spectra for each complex, which arise from strong contact interactions between the Ti^(III) metal center and the ligand. In the case of L=THF, comparatively large contact shifts are expected for the C β resonance, as this position is only two bonds from Ti^(III). For L=pyr, the conjugated network in the ligand permits spin delocalization across the ligand, and the sign of the contact shift should alternate between β , γ , and δ carbon positions following well-known rules [184].

The 1D ¹H and ¹³C MAS NMR spectra of Ti[OSi(O*t*Bu)₃]₃(THF)₂ shown in Figure 4.16 (a) and (b), respectively, were acquired using a MAS rate of 30 kHz, yielding spectra containing only isotropic resonances in both spectra. The lines in each spectra are quite narrow, owing to

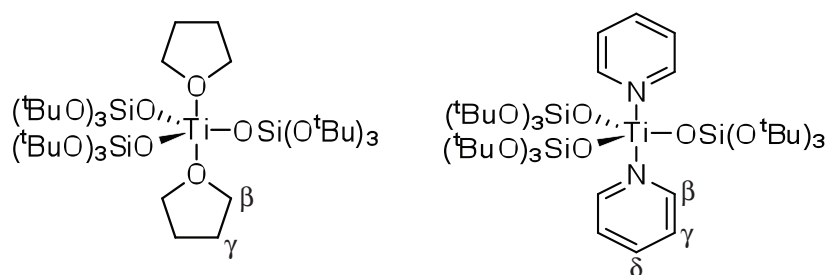


Figure 4.15: Schematic illustrations of the two $Ti^{(III)}$ molecular complexes of the composition $Ti[OSi(OtBu)_3]_3L_2$ used in this study, where $L=THF$ (left), and $L=pyr$ (right), with the β , γ , and δ positions marked on each ligand for reference.

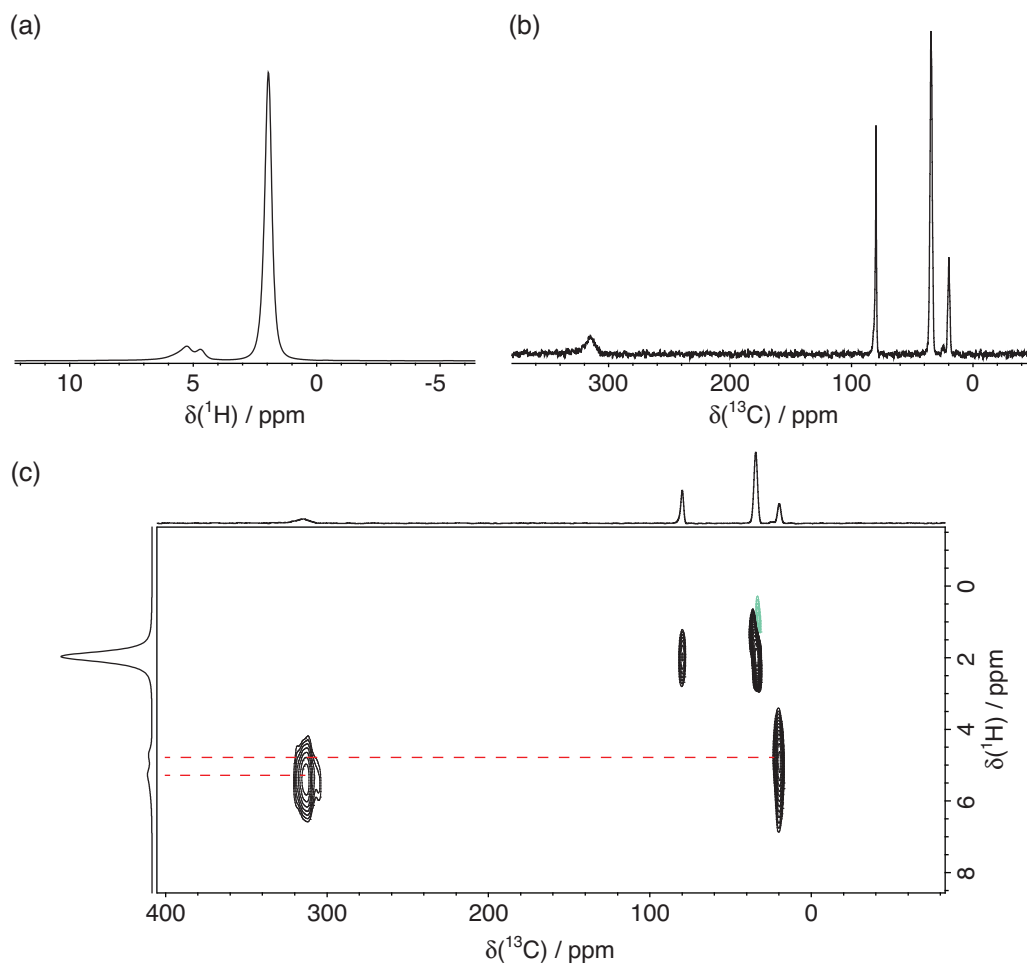


Figure 4.16: (a) 1D 1H MAS NMR spectrum of $Ti[OSi(OtBu)_3]_3(THF)_2$. Three sites are resolved, with chemical shifts of 1.96, 4.71, and 5.28 ppm. (b) 1D ^{13}C MAS NMR spectrum of $Ti[OSi(OtBu)_3]_3(THF)_2$ with four resolved sites exhibiting chemical shifts of 19.8, 34.6, 79.8, and 315 ppm. (c) 2D 1H - ^{13}C TEDOR correlation spectrum, yielding four observed correlations. This permits assignment of the 1H spectrum, where the signals at 1.96, 4.71, and 5.28 ppm are assigned to the methyl resonances, H_γ , and H_β , respectively. The ^{13}C spectrum is also accordingly assigned, where the signals with chemical shifts of 19.8, 34.6, 79.8, and 315 ppm are assigned to C_γ , methyl resonances, tBu resonances, and C_β , respectively.

the fact that $\text{Ti}^{(\text{III})}$ is not expected to contribute large PRE broadening or ABMS effects, as its electronic configuration is d^1 and has a short electron relaxation time. Due to the intensity of the lines in the ^1H spectra, the resonance at 1.96 ppm can be readily assigned to the methyl groups in the OtBu_3 ligands. The other two lines at 4.71 and 5.28 ppm have similar intensity, and must therefore come from the $\text{H}\beta$ and $\text{H}\gamma$ sites of the THF ligand. The ^{13}C spectrum exhibits four signals with isotropic shifts of 19.8, 34.6, 79.8, and 315 ppm. The large shift and line width of the peak at 315 ppm suggests that this site experiences large contact coupling to the $\text{Ti}^{(\text{III})}$ center, and can be immediately assigned to the $\text{C}\beta$ resonances of the THF ligands. The 2D ^1H - ^{13}C heteronuclear correlation TEDOR spectrum in Figure 4.16 (c) provides complete assignment of the observed ^1H and ^{13}C resonances. As the $\text{OSi}(\text{OtBu})_3$ ligand ^1H and ^{13}C sites are not expected to experience large contact couplings to the $\text{Ti}^{(\text{III})}$ center, the carbon resonances at 34.6 and 79.8 ppm can be immediately assigned to the methyl and tertiary butyl groups, respectively. The ^1H resonance at 4.71 ppm and the ^{13}C resonance at 19.8 ppm are assigned to the γ resonances of the THF group, and the remaining ^1H resonance at 5.28 ppm is assigned to the $\text{H}\beta$ resonance.

The 1D ^1H and ^{13}C MAS NMR spectra of $\text{Ti}[\text{OSi}(\text{OtBu})_3]_3(\text{pyr})_2$ shown in Figure 4.17 (a) and (b), respectively, were acquired using a MAS rate of 30 kHz, likewise yielding spectra containing only isotropic resonances in both spectra. The ^1H spectrum exhibits four resonances at -10.8, -10.0, 1.6, and 12.4 ppm. Due to the relative intensity and chemical shift of the peak at 1.6 ppm, this can be readily assigned to the ^1H resonances of the methyl groups of the $\text{OSi}(\text{OtBu})_3$ ligands. Deconvolution of this spectrum yields an integrated area ratio of 2:1:2 for the peaks at -10.8, -10.0, and 12.4 ppm, respectively. As the peaks on the pyridine ligands are expected to experience alternating signs of the contact shift following well-known rules, the peak at 12.4 ppm must come from the $\text{H}\gamma$ sites of the pyr ligand, and the area ratio therefore assigns the peak at -10.8 ppm to the $\text{H}\beta$ sites with the peak at -10.0 ppm arising from $\text{H}\delta$ sites on the pyr ligand. The ^{13}C MAS spectrum exhibits five distinct signals with chemical shifts of 34.1, 43.5, 77.7, 247, and 448 ppm. The relative intensities, narrow line widths, and chemical shifts of the peaks at 34.1 and 77.7 ppm permit the immediate assignment of these resonances to the methyl and tertiary carbon resonances of the $\text{OSi}(\text{OtBu})_3$ ligands, respectively. The remaining sites at 43.5, 247, and 448 ppm are significantly broader, and arise in an area ratio of 2:1:2. Therefore these peaks can be assigned to the $\text{C}\gamma$, $\text{C}\delta$, and $\text{C}\beta$ sites in pyridine, respectively.

Perhaps the most interesting result in this study was the acquisition of ^{15}N MAS spectra of $\text{Ti}[\text{OSi}(\text{OtBu})_3]_3(\text{pyr})_2$ using ^{15}N -labeled pyridine shown in Figure 4.18. Owing to the fact that the ^{15}N atoms are directly contacting the $\text{Ti}^{(\text{III})}$ center, huge contact shifts and PRE effects would be expected for these ^{15}N resonances. Indeed, the observed ^{15}N chemical shift of -1380 ppm at $T = 300\text{ K}$ in the 30 kHz MAS spectrum is consistent with what may be expected for a pyridine ligand contacted to a $\text{Ti}^{(\text{III})}$ metal center. Curiously, the anisotropy of this site seems to be relatively small, as it is unmeasurable at 30 kHz MAS. Decreasing the MAS rotation rate to 10 kHz reveals spinning sidebands up to the ± 2 order, and fitting of the spectrum reveals CSA tensor components of $\delta_{\text{iso}} = -1561\text{ ppm}$, $\Delta = 334\text{ ppm}$, and $\eta = 0.05$. The decreased chemical shift of this site compared to the 30 kHz MAS spectrum is a result of the fact that the

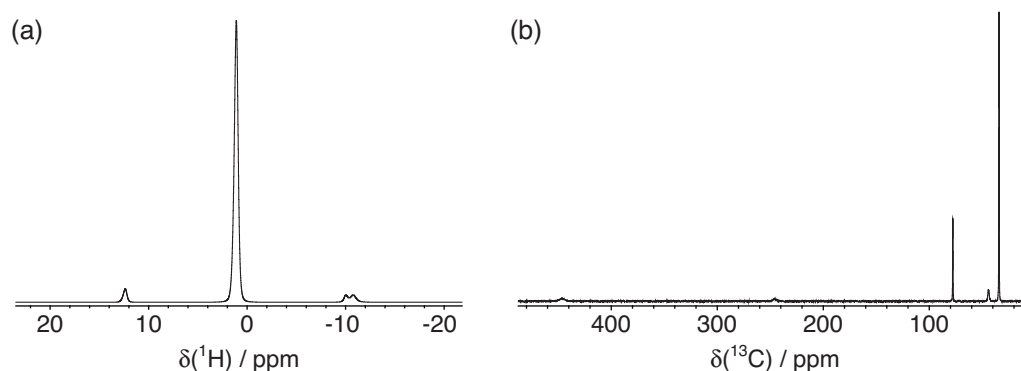


Figure 4.17: (a) 1D 1H MAS NMR spectrum of $Ti[OSi(OtBu)_3]_3(pyr)_2$. Four sites are resolved, with chemical shifts of -10.8, -10.0, 1.6, and 12.4 ppm, which are assigned $H\beta$, $H\delta$, the methyl resonances, and $H\gamma$, respectively. (b) 1D ^{13}C MAS NMR spectrum of $Ti[OSi(OtBu)_3]_3(pyr)_2$ with five resolved sites exhibiting chemical shifts of 34.1, 43.5, 77.7, 247, and 448 ppm, assigned to methyl resonances, $C\gamma$, tBu resonances, $C\delta$, and $C\beta$, respectively.

temperature inside the MAS stator was held constant for each MAS spectrum, but the decreased frictional heating when spinning at 10 kHz compared to 30 kHz resulted in a sample temperature of approximately 260 K. By plotting the isotropic chemical shift versus the inverse temperature, the hyperfine coupling constant may be obtained using the equation below for the experimental chemical shift of a nucleus experiencing only contact coupling:

$$\delta_{iso}^{exp} = \frac{g_e \mu_B A^{FC}}{4\hbar \gamma_I kT} + \delta_{iso}^{orb}, \quad (4.8)$$

which yields a value of $A^{FC} = 4.5 \pm 0.2$ MHz, totally consistent with hyperfine coupling constants expected for nuclei one bond away from a metal center. The uncertainties on temperature (± 5 K) do not permit an accurate determination of the orbital shift. As the $Ti^{(III)}-^{15}N$ contact coupling is expected to be extremely sensitive to the geometry around the $Ti^{(III)}$ center, pyridine may be useful as a tool to "spy" on the electronic environment of surface $Ti^{(III)}$ species in the future. It is worth notifying the reader here that this project is very much in its infancy and that the results listed above represent the current progress by our group. We are particularly interested to see if the use of pyridine as a "spy" can investigate the coordination and oxidative state of surface $Ti^{3+/4+}$ species in Ziegler-Natta polyolefin polymerization catalysts, however, sample preparation and experimental difficulties have so far caused us to not have any presentable results. With the aid of state-of-the-art quantum chemical calculations, we hope in the future to be able to deduce structural models of surface $Ti^{3+/4+}$ sites in activated Ziegler-Natta catalysts, on the basis of ^{15}N chemical shifts from pyridine "spies" and of 1H and ^{13}C shifts from electron donors and alkyl aluminum species interacting with $Ti^{3+/4+}$. Future experiments by our group, in collaboration with the groups of Vincent Monteil (C2P2 Lyon) and Christophe Copéret (ETH Zürich) will attempt to answer these questions.

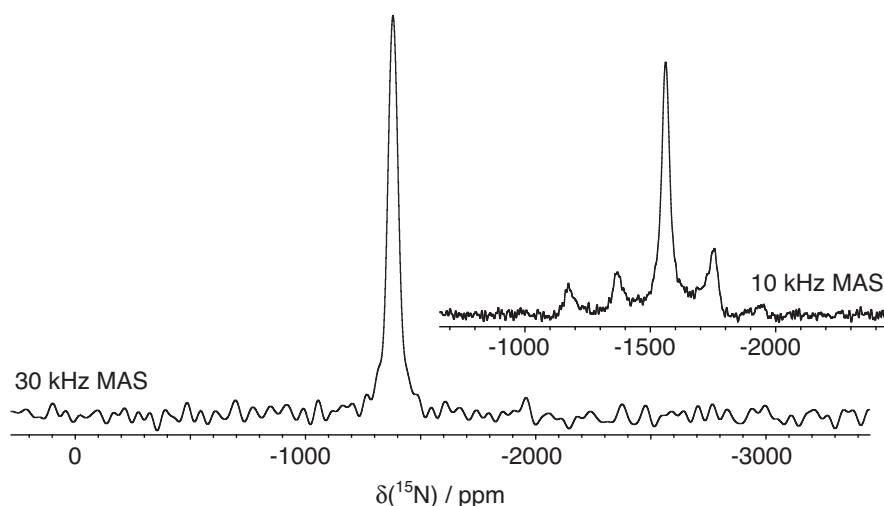


Figure 4.18: 1D ^{15}N MAS NMR spectra of $\text{Ti}[\text{OSi}(\text{O}t\text{Bu})_3]_3(^{15}\text{N}\text{-pyr})_2$ at rotation rates of 30 kHz and 10 kHz, with sample temperatures of 300 K and 260 K, respectively. In the 30 kHz spectrum, the single ^{15}N resonance from the equivalent pyridine ligands appears at -1380 ppm. Due to temperature differences between the spectra, the resonance appears at -1561 ppm in the 10 kHz MAS spectrum, owing to the fact that the Fermi contact interaction has a Curie temperature dependence. Fitting of the spectrum reveals CSA tensor components of $\delta_{\text{iso}} = -1561$ ppm, $\Delta = 334$ ppm, and $\eta = 0.05$.

4.5 Conclusions and perspectives

The primary focus of this work has been exploring the possibilities of (P)NMR techniques to probe the structure of heterogeneous catalysts and molecular models of surface-supported catalysts. In the first two sections, organolanthanide complexes containing (1) the diamagnetic Lu^{III} ion, and (2) the paramagnetic Yb^{III} ion were studied by NMR. Conventional solid-state NMR techniques (one pulse experiments, CP-based HETCOR), as well as more modern high-resolution methods (J -resolved spectroscopy), were used to determine that the $\text{Lu}[\text{CH}(\text{SiMe}_3)_2]_{3-x}[\text{O}-2,6\text{-}t\text{Bu}_2\text{-C}_6\text{H}_3]_x$ series of molecular complexes all exhibit a 3-center-2-electron secondary bonding interaction between methyl groups on the ligands and the Lu^{III} center. This secondary interaction was also found to be present in the silica-grafted $(\equiv\text{SiO})[\text{CH}(\text{SiMe}_3)_2]_2$ complex. We then moved to the paramagnetic $\text{Yb}[\text{CH}(\text{SiMe}_3)_2]_3$ complex, which exhibits extremely broad lineshapes in the 1D spectra of ^1H , ^{13}C , and ^{29}Si due to ABMS broadening from the Yb^{III} , which has a very large anisotropic component of the χ tensor. Heteronuclear ^1H - ^{13}C correlation by the 2D TEDOR experiment permitted the identification of four ^1H and ^{13}C signals each. Following an analysis of the isotropic chemical shifts by a point-dipole model, the same secondary interactions present in $\text{Lu}[\text{CH}(\text{SiMe}_3)_2]_3$ were confirmed to be present in $\text{Yb}[\text{CH}(\text{SiMe}_3)_2]_3$ as well. The fact that isotropic resolution was achievable for the Yb complex is itself notable, considering that Yb in general has a large and anisotropic magnetic susceptibility tensor, which leads to large inhomogeneous broadenings of the NMR signals. We expect that ultrafast magic angle spinning will open the doors to structural studies of complexes containing lanthanides with even larger $\Delta\chi$, such as Tb^{III} and Dy^{III} [168]. We expect that although computational techniques to estimate paramagnetic effects in lanthanide complexes are far from

routine with current technologies [169], in the future these methods will be achievable with the ever-advancing capabilities of modern computers. Finally, the possibility of using small molecules like tetrahydrofuran and pyridine to coordinate Ti centers and act as spies of the metal oxidation state was explored. ^{15}N -labeled pyridine was found to be a particularly attractive choice, as it was possible to acquire the ^{15}N shift despite the fact that it is directly coordinated to the $\text{Ti}^{(\text{III})}$ center. A hyperfine coupling of $A^{\text{FC}} = 4.5 \pm 0.2$ MHz between $\text{Ti}^{(\text{III})}$ and ^{15}N was measured, which is consistent with a one-bond hyperfine coupling. The ^{15}N shift of pyridine coordinated to $\text{Ti}^{(\text{III})}$ is expected to be a particularly sensitive probe for $\text{Ti}^{(\text{III})}$ coordination geometries and oxidation state, with possible applications to the structural study of activated Ziegler-Natta catalysts.

Chapter 5

Structural studies of paramagnetic Fe⁽⁰⁾-based homogeneous catalysts

5.1 Introduction

As alluded to in the previous chapter, homogeneous catalysts carry some advantages over heterogeneous catalysts due to their high selectivities, lower operating temperature, and better chemical definition [140]. Indeed, the well-defined nature of the active sites in homogeneous catalysts makes these materials more amenable for rational design through structure-activity relationships. Our group and coworkers have recently been particularly interested in the synthesis and structural analysis of low-valent Fe⁽⁰⁾-based homogeneous catalysts, with a particular emphasis on the analysis of geometric and electronic structure features of these materials using solid-state NMR methods [18]. This motivation is due to the fact that the interest and development of new low-valent Fe complexes has enjoyed a renaissance of late, leading to the development of new materials with well-defined structures and unprecedented reactivities [185–191]. The pursuit of highly efficient low-valent Fe catalytic complexes has so far mostly been focused on complexes containing nitrogen donor ligands [192], although doubt has been cast on the oxidation state of Fe in these complexes due to the non-innocent character of these ligands [193]. Another branch of the research towards efficient low-valent Fe catalysts has been the use of phosphorus donor ligands, as these ligands are favorable due to the fact that the electronic and steric properties of these ligands are easily tunable, and thus are advantageous to produce stable metal complexes with a low oxidation state. This said, the bulk of the research in this field has been directed towards 18-valence-electron (ve) metal centers, which suffer from relatively limited reactivity due to their coordinatively and electronically saturated nature [194–197]. Therefore the pursuit of more active, coordinatively unsaturated low-valent Fe⁽⁰⁾ complexes, with well-defined geometries, seems to be a logical course to take, however the literature in this field is scarce, even more so low-coordinate 16-ve Fe⁰ centers with alkene with P-donor ligands [198–202], and even then, these materials must be handled at temperatures below 0 °C to avoid decomposition.

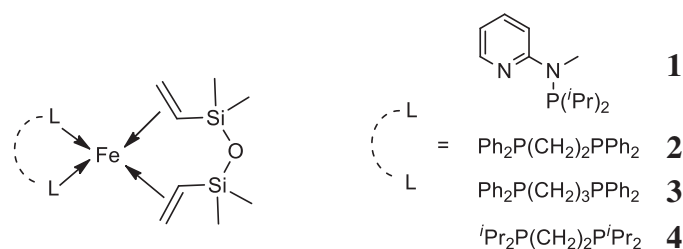


Figure 5.1: Schematic illustration of the four Fe⁰(L-L)(dvtms) complexes **1-4**. Reproduced with permission from reference [18]. Copyright 2017 American Chemical Society.

5.2 Stable 16-ve phosphine-stabilized Fe⁰ olefin complexes

The work in this chapter outlines a project undertaken in collaboration with coworkers towards the synthesis and subsequent characterization of 16-ve phosphine-stabilized Fe⁰ complexes which are highly active alkyne cyclotrimerization catalysts, culminating in a first publication in 2017 [18]. This chapter focuses on just four of the complexes discussed within that publication, each of which have the general formula Fe⁰(L-L)(dvtms), where dvtms = divinyltetramethyldisiloxane and the L-L ligand describes a bidentate ligand where L is a two-electron P or N donor. Throughout the remainder of the text, these four complexes will be referred to as **1**, **2**, **3**, and **4**, where **1** is Fe⁰(pyNMeP(*i*Pr)₂)(dvtms) (pyNMeP(*i*Pr)₂ = *N*-(diisopropylphosphino)-*N*-methylpyridine-2-amine), **2** is Fe⁰(dppe)(dvtms) (dppe = 1,2-bis(diphenylphosphino)ethane), **3** is Fe⁰(dppp)(dvtms) (dppp = 1,2-bis(diphenylphosphino)propane), and **4** is Fe⁰(dipe)(dvtms) (dipe = 1,2-bis(diisopropylphosphino)propane). A cartoon depiction of the structure of each Fe⁰(L-L)(dvtms) complex is given in Figure 5.1. Single crystal X-ray diffraction measurements established the structures of complexes **1-3**, which revealed a η²:η² coordination mode of dvtms (see Figure 5.2). The metal coordination geometries of **2** and **3** are best described as distorted tetrahedral. The structure of **1** is significantly different: the two vinyl moieties are nearly coplanar (torsion angle of 4.22°) and are perpendicular to the plane of the P-N ligand. The P and Fe atoms almost lie in the plane defined by the vinyl fragments, and as such the coordination geometry is best described as trigonal pyramidal. Crystals of suitable quality for X-ray diffraction could not be obtained for **4**; as such, NMR is a powerful candidate for the determination of the structure of **4**. In general the hyperfine coupling between each nucleus on a ligand and the metal center is very sensitive to the coordination geometry and as such, is a powerful probe of the molecular structure if NMR shifts are able to be acquired and properly interpreted.

5.2.1 Cyclotrimerization of alkynes

In order to probe the effect of the structure of the L-L ligand on catalytic activity, the cyclotrimerization of 3-hexyne was used as a model reaction to compare the reactivities of complexes **1-4** (see Table 5.1). Up to 35% conversion was obtained with **2**, and hexaethylbenzene (HEB) was produced exclusively. Increasing the bite angle of the ligand from dppe to dppp (84.75° to 91.37° for **2** and **3**, respectively) disfavors 3-hexyne conversion (12%); in addition, the N,P mixed-donor

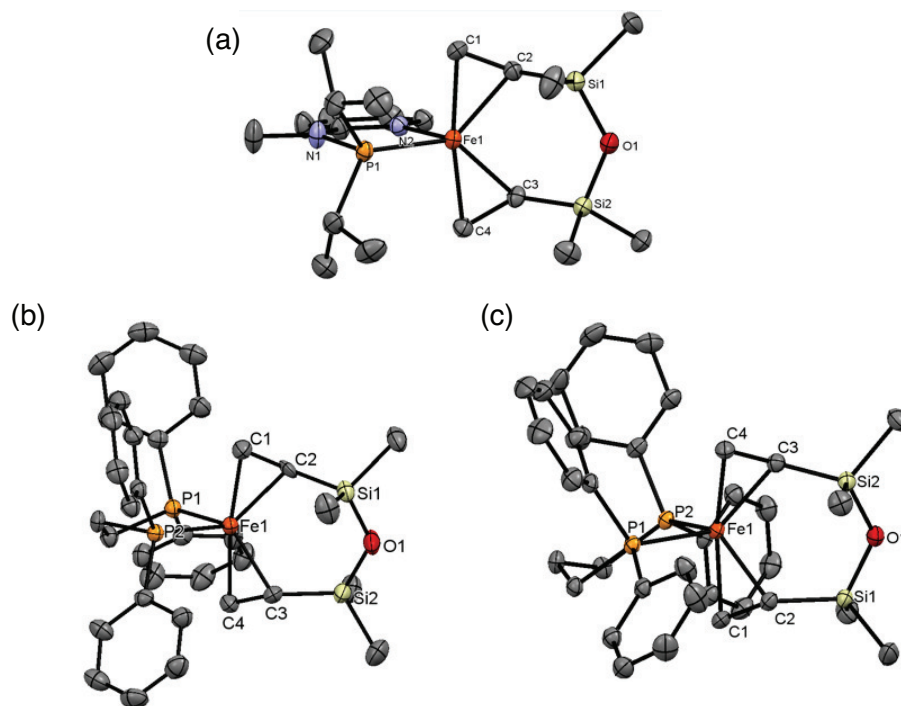
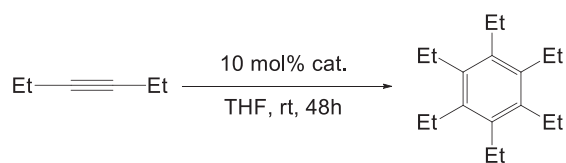


Figure 5.2: Thermal ellipsoid representation (50% probability) of complexes **1-3**. H atoms are not shown for clarity. Selected bond lengths (Å) and angles (°) are given here: For **1**: P1–Fe1–P2 80.77(6); P1–Fe1 2.245(8); P2–Fe1 2.147(2). For **2**: P1–Fe1–P2 84.75(3); P1–Fe1 2.30(1); P2–Fe1 2.32(1). For **3**: P1–Fe1–P2 91.37(2); P1–Fe1 2.291(6); P2–Fe1 2.335(6). Reproduced with permission from reference [18]. Copyright 2017 American Chemical Society.

ligand in **1** does not lead to efficient 3-hexyne conversion (only 11% to HEB). The conversion of 3-hexyne was considerably more efficient with **4** (49% compared to 35% with **2**), however cyclic and linear C12 products were produced in addition to HEB. Considering a metallacyclic reaction mechanism (see Figure 5.3) the lower selectivity by **4** may come as a result of steric hindrance brought about by the isopropyl P substituents that hampers coordination of a third molecule of 3-hexyne to the 16-ve intermediate **C** and thus the formation of the metallacycle **D** precursor to HEB.

5.3 De novo structure of $\text{Fe}(\text{dipe})_2(\text{dvtms})$

In order to determine the structure of **4**, we constructed a putative model by de novo DFT optimization, shown in Figure 5.4 (b) and confirmed the dipe ligand binding to $\text{Fe}^{(0)}$ by using PNMR quantum chemical calculations [26] and solid-state NMR spectroscopy of a precipitated powder sample whose composition was confirmed by elemental analysis. It has been shown that DFT can provide high-quality structures of high-spin open-shell transition-metal complexes which are in excellent agreement with structures obtained by way of X-ray diffraction [203, 204]. These DFT methodologies necessarily require a proper functional, a sufficiently large atomic basis, and a dispersion correction which properly accounts for van der Waals forces. The method used in this study meets all of these demands. The putative structure of **4** was constructed from **2** by



catalyst	conversion (wt %) ^a (selectivity to HEB, %)
1	11 (100)
2	35 (100)
3	12 (100)
4	49 (48.2)

Table 5.1: Catalyzed cyclotrimerization of 3-hexyne by complexes **1-4**. 0.20 mol of catalyst was reacted with 2.0 mol of 3-hexyne in 5 mL THF. The reactions were carried out at room temperature for 48 h. ^aDetermined by GC-MS.

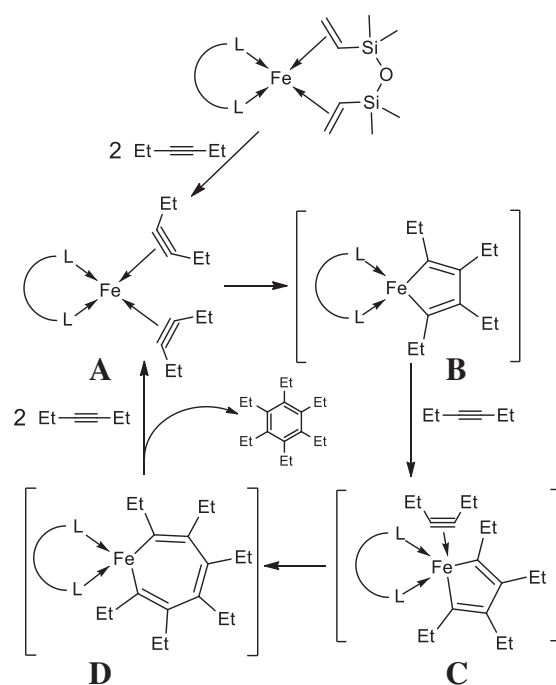


Figure 5.3: Suggested mechanism for alkyne cyclotrimerization by the $Fe^{(0)}(L-L)(dvtms)$ complexes **1-4**

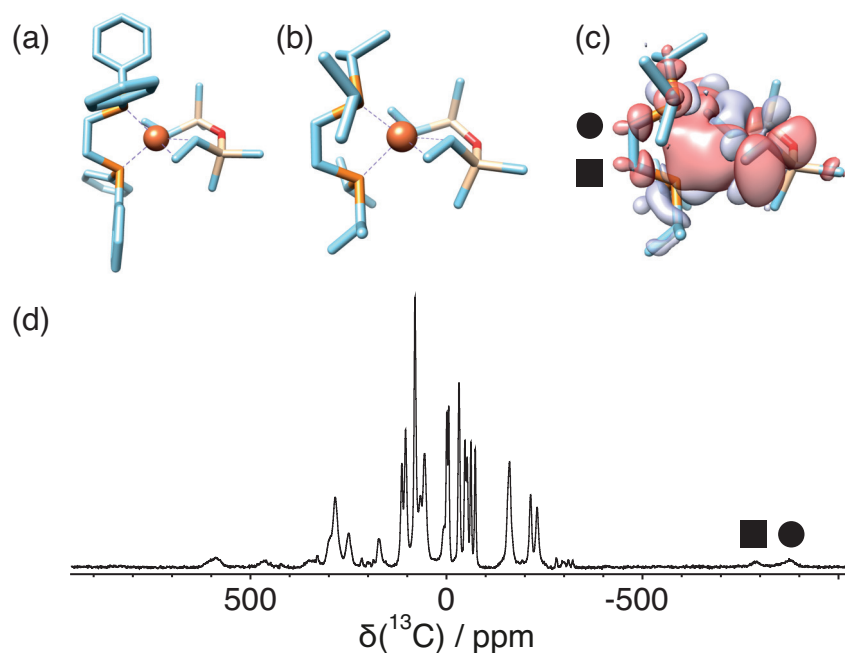


Figure 5.4: (a) X-ray structure of **2** (H atoms not shown for clarity). (b) DFT-optimized de novo structure of **4**. (c) Visualization of positive (blue) and negative (red) isosurfaces of the spin density distribution of **4** (for ± 0.0002 au isovalues). (d) ^{13}C PNMR spectrum of **4** acquired with a MAS rotation rate of 31.25 kHz on a 500 MHz instrument. The two CH_2 "backbone" carbons of the ligand and their signals are labeled with a circle and a square, respectively, in (c) and (d). Reproduced from [18].

substituting ^iPr groups for phenyl groups, and was minimized by DFT. The energy minimum found by DFT structure optimization for **4** very closely resembles the structure of **2**, as shown in Figure 5.4 (a) and (b).

To support this DFT-optimized structure, we measured and calculated ^{13}C PNMR shifts of **4**. As stated in previous chapters, NMR spectra of paramagnetic complexes contain a wealth of structural information, since the unpaired electrons induce large perturbations in the chemical shifts and NMR relaxation properties of surrounding nuclei. These effects depend on the distribution of unpaired electron density ("spin density") on the ligands, which in turn is highly sensitive to the metal binding and the conformation of the ligands [3]. The spin density provides a qualitative insight into this phenomenon, shown in Figure 5.4 (c). Notably, negative unpaired electron density and large negative contact shifts are predicted for the ^{13}C nuclei of the $-(\text{CH}_2)_2-$ bridge. The corresponding experimental ^{13}C MAS NMR spectrum of **4** is shown in Figure 5.4 (d). The magnitude of ^{13}C shifts is often overestimated by DFT calculations (see the Discussion below), but a few assignments can be reliably established in less crowded regions of the NMR spectrum. This is the case around -850 ppm, where two very broad signals are observed, which can be directly assigned to two carbons in the $-(\text{CH}_2)_2-$ bridge of the dipe ligand, denoted by a square and a circle in Figure 5.4 (c) and (d). Without extensive further modeling, a clear assignment could not be made for other resonances in the NMR spectrum of **4**. Nevertheless, the agreement between the experimental and calculated ^{13}C shifts for the $-(\text{CH}_2)_2-$ bridge confirms dipe binding to $\text{Fe}^{(0)}$ and by extension the putative structure of **4**.

structure	g,D	PNMR ^b	δ_C
DFT ^a	—	no SOC	-1017, -1015
DFT ^a	DFT	full	-1047, -1085
exp			-800, -890

Table 5.2: Experimental and calculated ^{13}C NMR shifts (ppm from TMS) of the $-(CH_2)_2-$ bridge of the bidentate dipe ligand in **4**. ^aPBE0-D3 optimized structure. ^bThe level of PNMR theory used, where "no SOC" denotes a doublet-like theory and where "full" denotes Vaara's 2015 theory [26].

5.3.1 Discussion of the PNMR computational protocol

The accuracy of the calculation of PNMR shifts is limited by three main effects: (1) the method for calculating the spin-orbit coupling (SOC)-dependent EPR property tensors g and D , (2) the method for hyperfine coupling (HFC) calculations, and (3) the quality and relevance of the molecular structure for which the PNMR calculations were performed to the experimental conditions in the molecular crystal. Each of these points are addressed in turn below:

1. The calculation of reliable g and D tensors in 3d transition metal complexes requires the use of correlated multireference *ab initio* methods. Performing these calculations for systems comprising ~ 80 atoms is currently at the very limit of standard computation capabilities. Table 5.2 compares the results of ^{13}C PNMR shifts calculated with and without DFT-based SOC property tensors. We see that upon inclusion of the SOC-dependent property tensors the shifts decrease by some tens of ppm. Comparable or even slightly larger effects might be expected when calculating g and D with *ab initio* methods.
2. To the best of our knowledge, there is currently no benchmark *ab initio* method for reliable HFC calculations. Pure (generalized gradient approximation Kohn-Sham) DFT is known to overdelocalize spin density from the metal center [205, 206], leading to overestimation of the Fermi contact HFCs and shifts on the metal ligand atoms, which in this case dominate the total HFC and PNMR shifts. Adding an exact exchange admixture in hybrid DFT usually improves the results [207], but this improvement can be nonsystematic and nonuniform across the NMR-active atoms of the molecule. Only qualitative accuracy of the calculated Fermi contact HFCs and shifts may be expected from the PBE0 HFC calculations used here (*i.e.* with 25% Hartree-Fock exchange admixture).
3. Even though there is an overall agreement between the DFT-optimized structure of **4** and the X-ray structure of the closely related **2**, only a qualitative agreement between the PNMR calculations and the experiment can be expected in view of the high sensitivity of the PNMR shifts to the metal coordination geometry. If internal dynamics are in play, which is expected for the ligands in **4**, these geometric fluctuations might render the results of a static PNMR calculation slightly inaccurate. Modeling the dynamic effects on PNMR shifts in **4** using *ab initio* molecular dynamics, albeit potentially worthwhile and relevant

for molecular crystals with flexible groups, is currently on the very edge of computation capabilities.

5.4 PNMR as a tool for structural determination of complexes 1-4

The use of solid-state NMR and quantum chemical calculations for the determination of electronic structure and/or coordination geometries in organometallic complexes has largely been focused on molecules with relatively simple ligands with a variety of paramagnetic metal sites, such as metallocenes [94, 208, 209], amino acids [1, 2] and other small organic molecules [2, 19, 92], to give just a few examples. As of the writing of this document, no publications characterizing Fe⁽⁰⁾-containing molecules by NMR have been given in the literature besides one prior publication from this project [18]. As shown in Chapter 1, Kervern *et al.* [3] studied the Fe^(II)-containing DIAD-Fe^(II) molecule which contains 14 inequivalent carbon sites and 9 inequivalent proton sites, which until now is among the largest organometallic complexes studied in terms of the number of inequivalent sites. The authors in that work showed that the combination of heteronuclear correlation spectroscopy using moderate MAS rates and non-relativistic DFT calculations of paramagnetic shifts can, in favorable cases, give full spectral assignment, and as a result, confirmation of the coordination geometry and determination of the electronic structure of the molecular complex. In many cases, however, such a simple methodology will not provide conclusive results. More advanced experimental methodology, including higher MAS rates, more advanced correlation spectroscopies, and/or more sophisticated computational methods including relativistic effects need to be applied as a result.

5.4.1 Geometry and electronic structure of 1

Complex **1** is the simplest of the four molecules used in this study, and due to the lack of symmetry in this molecule it exhibits 20 inequivalent carbon sites and 21 proton sites over both ligands. Therefore **1** represents a good starting point in order to establish that our solid-state NMR methods and quantum chemical calculations can be used to validate the structure of these complexes. These samples are not isotopically enriched, so we began by using a 2.5 mm MAS system capable of a rotation rate of 31.25 kHz (32 μ s rotor period), as this larger rotor should afford adequate sensitivity for natural-abundance ¹³C measurements while rotating sufficiently fast to provide adequate resolution by minimizing overlap from rotational sidebands. The resulting 1D ¹H and ¹³C MAS spectra of **1** are given in Figure 5.5 (a) and (b), respectively. The 1D ¹H spectrum exhibits a broad spinning sideband manifold due to strong proton-electron dipolar couplings. In order to identify the isotropic resonances, a 2D aMAT spectrum was acquired, the isotropic projection of which is given in the inset of Figure 5.5 (a). The 1D ¹H MAS spectrum does not exhibit adequate resolution to identify the isotropic resonances contained therein. The 1D ¹³C MAS spectrum exhibits 13 intense isotropic peaks but relatively small spinning sidebands, owing to the fact that

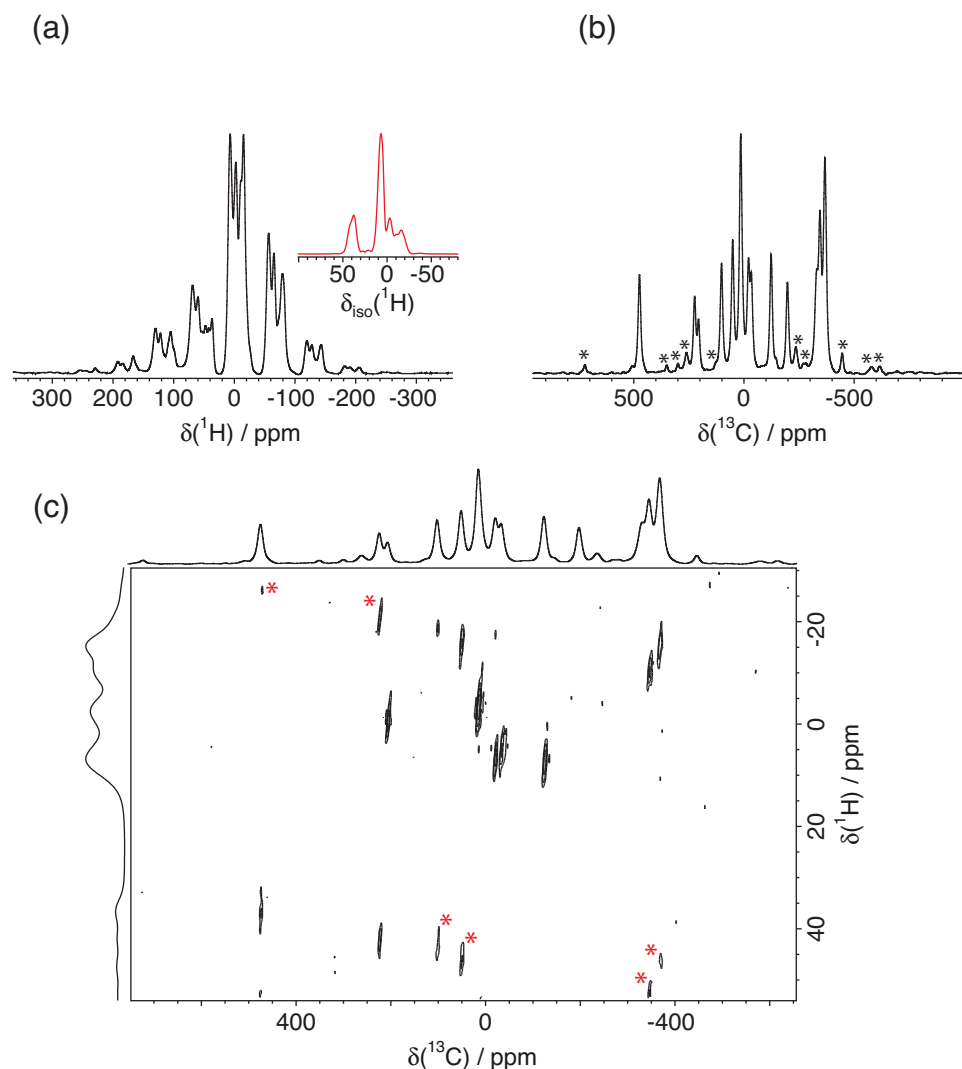


Figure 5.5: (a) 1D 1H MAS spectrum of **1**. The inset represents the isotropic projection from an aMAT experiment, showing that the 1H isotropic shifts span a range from -19 ppm to 42 ppm. (b) 1D ^{13}C MAS spectrum of **1**. In this case, all intense peaks are isotropic, while small peaks are sidebands. The isotropic ^{13}C shifts range from -368 to 474 ppm. Small rotational sidebands are marked by black asterisks. 524,288 scans were collected over 4.8 hours using a recycle delay of 30 ms. (c) the 2D TEDOR 1H - ^{13}C heteronuclear correlation spectrum of **1**. In total 11 correlations were observed (comprising 12 H-C pairs, see Table 5.3 for explanation). 32,768 scans were collected for each of the 64 t_1 increments, giving a total experiment time of 2.6 hours using a recycle delay of 3 ms. Rotational sidebands in the 1H are marked by red asterisks, and were confirmed by repeating the measurement using a different MAS rate. All spectra were acquired with a MAS rotation rate of 31.25 kHz and with an external magnetic field strength of $B_0 = 11.74$ T (500 MHz)

carbon–electron dipolar couplings are much weaker than proton–electron couplings. Considering that resonances close to the Fe⁽⁰⁾ center are not expected to be observed due to a combination of PRE effects and large Fermi contact shifts (*i.e.* atoms in the vinyl moieties and C–H groups in the ⁱPr moieties), we expect to see 14 resonances. A 2D H–C correlation experiment was acquired using the TEDOR sequence, and is shown in Figure 5.5 (c). This spectrum exhibits 11 correlations out of an expected 13, comprising 4 H–C pairs and 1 rotationally-averaged methyl group in the 2-(methylamino)pyridine moiety, 4 H–C pairs from the rotationally-averaged methyl groups of the ⁱPr moieties, and 4 H–C pairs from the rotationally-averaged methyl groups of dtms.

5.4.2 Resonance assignments of ¹H and ¹³C shifts for **1**

To complete the assignment for **1**, two paths can be chosen: (1) more advanced experimental correlation methodologies could be applied, or, (2) a computational path, provided that a reliable methodology is available. When reliable calculations can be performed, a direct agreement between experimental and calculated shifts provides not only resonance assignment, but also confirmation of the structure, quantification of the spin delocalization across ligands, and as a result, determination of the electronic structure of the molecule. This information cannot be extracted by experimental methods alone. Such a reliable methodology has been introduced in Section 5.3.

As stated previously in this thesis, paramagnetic shifts are extremely sensitive to the metal coordination geometry. In the case of **1**, a high-resolution structure is available from XRD. As a first approach, this structure was directly employed in PNMR calculations, with the positions of hydrogen atoms optimized (H-opt). The resulting paramagnetic shifts from this structure were compared with those calculated using a structure fully optimized in vacuo (Full-opt), shown in Figure 5.6. Furthermore, as discussed in Section 5.3, the level of spin density delocalization is highly dependent on the choice of DFT functional, and this effect on hyperfine couplings needs to be tested to estimate the confidence bounds of the calculated shifts. Therefore, we have calculated the hyperfine coupling tensors for each nucleus at the DFT level with a hybrid PBE functional with Hartree-Fock exchange admixture ranging from 10% (PBE10) to 40% (PBE40). The last consideration for accurate PNMR calculations concerns the inclusion of relativistic spin-orbit coupling effects on the calculated shifts. Modern computational methodologies permit the calculation of EPR *g* and *D* tensors at the multi-reference *ab initio* level, and the resulting effects can be included following Vaara’s 2015 theory [26].

To address the question about which structure to use, a comparison of the results is given in Figure 5.6 (a) for the fully-optimized structure, and (b) for the structure with only the ¹H positions optimized. We give therein seven resulting computed values for each ¹H–¹³C correlation (with *A* calculated with PBE10, PBE15, PBE20, PBE25 (commonly called PBE0), PBE30, PBE35, and PBE40 and including SOC effects), which are overlaid with the experimental 2D ¹H–¹³C correlation spectrum. Overall the results for the H-opt structure are in better agreement with the experimental results than those for the Full-opt structure. This is not unexpected for a molecule of this size, as single-crystal XRD of small complexes tends to have quite small errors on the

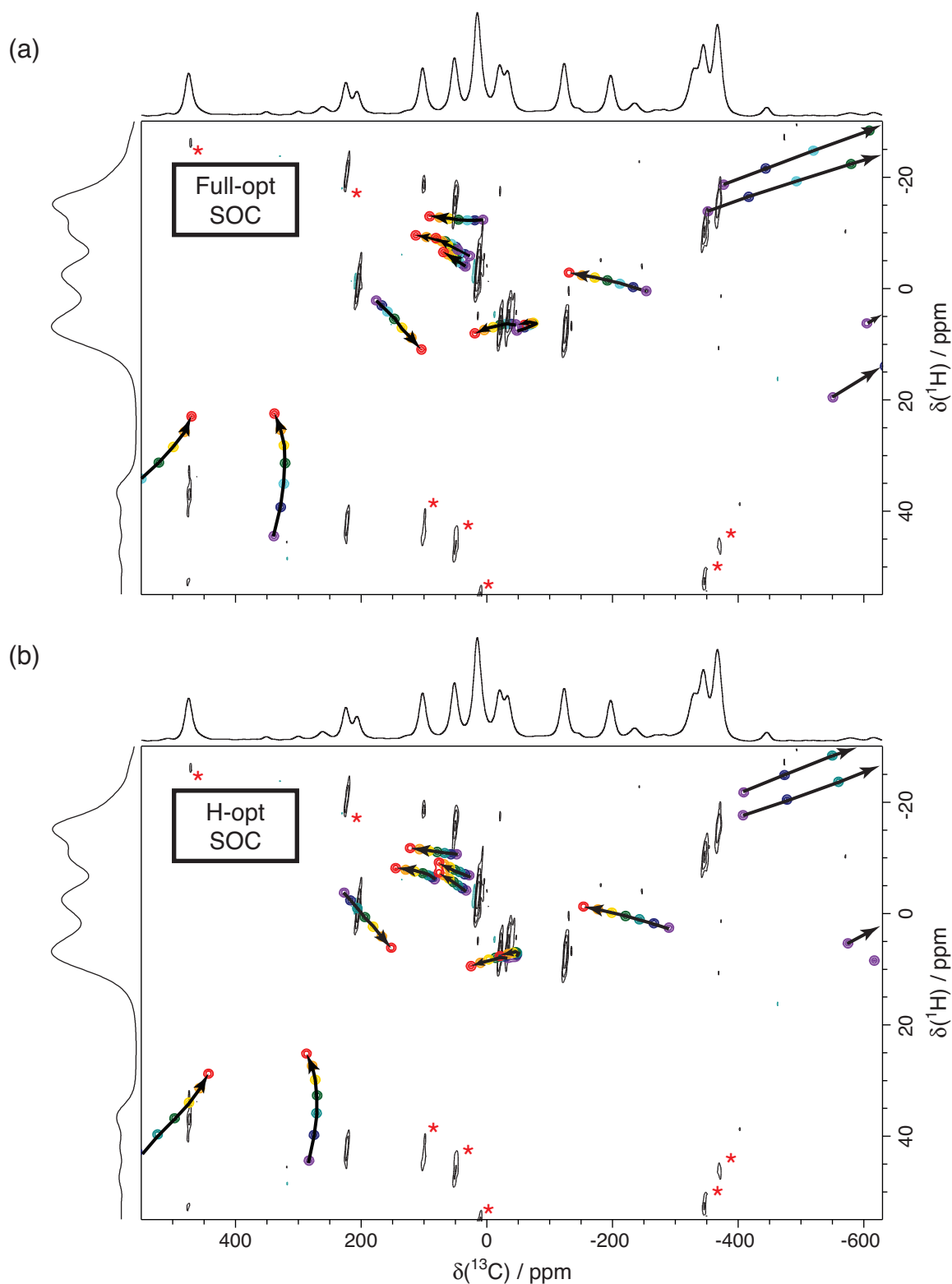


Figure 5.6: A comparison of the effect of geometry on the calculated 1H and ^{13}C chemical shifts with (a) full geometric DFT optimization in vacuo and (b) optimization of the H atoms only. Each figure shows an overlay of the experimental H-C correlation spectrum and calculated values. The calculated values are given by colored circles, with purple representing values using PBE10 in the calculation of the hyperfine couplings, and red representing values using PBE40. The arrows laid over the calculated values indicate the trend of the calculated paramagnetic shift for each H-C pair towards increasing levels of Hartree-Fock exchange admixture. Each calculated H-C correlation was given an arbitrary line width to aid visualization.

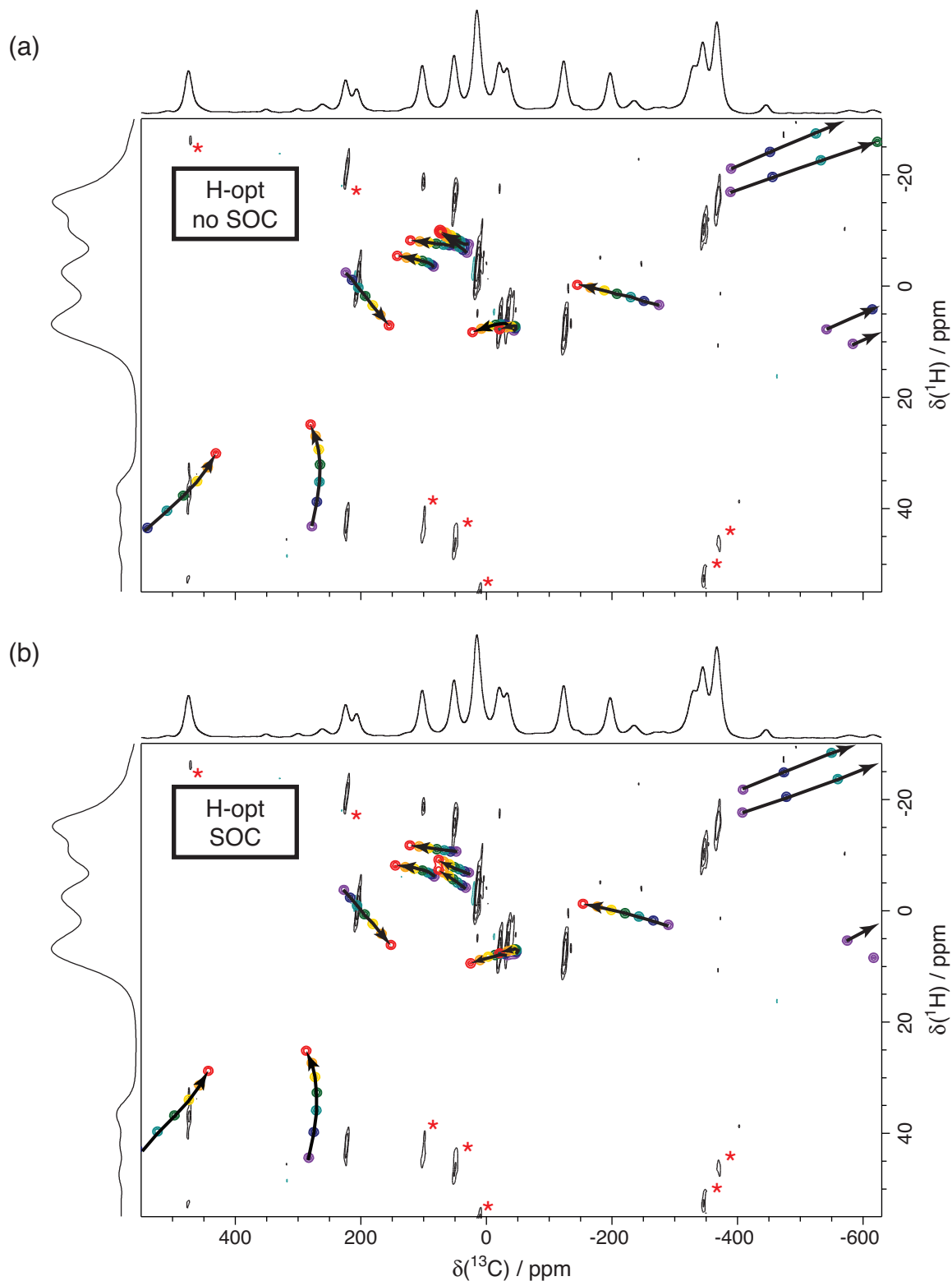


Figure 5.7: A comparison of the effect of the inclusion of SOC effects on the calculated ^1H and ^{13}C chemical shifts with (a) without SOC effects, and (b) with SOC effects. Each figure shows an overlay of the experimental H-C correlation spectrum and calculated values. The calculated values are given by colored circles, with purple representing values using PBE10 in the calculation of the hyperfine couplings, and red representing values using PBE40. The arrows laid over the calculated values indicate the trend of the calculated paramagnetic shift for each H-C pair towards increasing levels of Hartree-Fock exchange admixture. Each calculated H-C correlation was given an arbitrary line width to aid visualization.

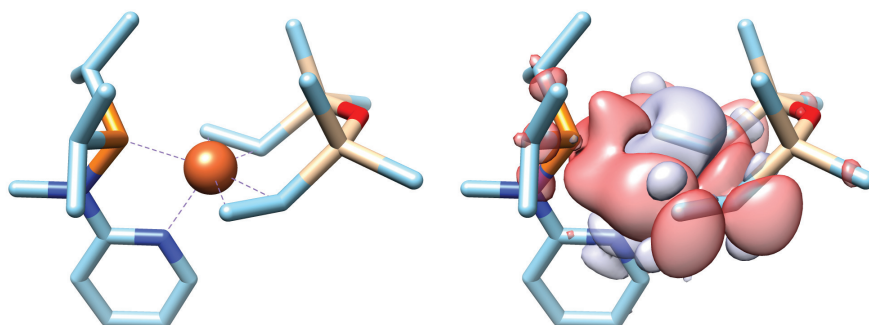
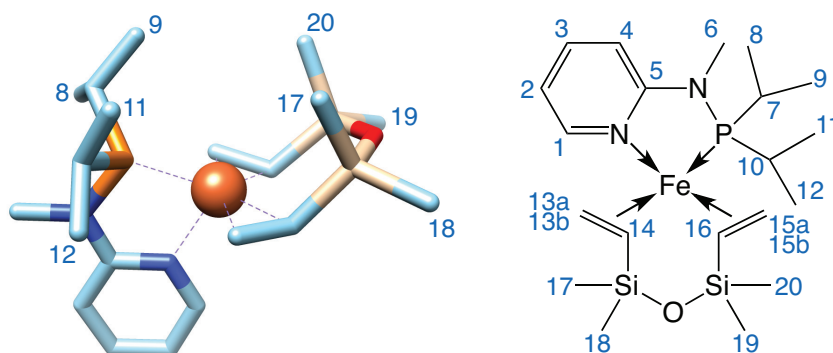


Figure 5.8: (left) X-ray structure of **1** (H atoms not shown for clarity). (right) Visualization of the positive (blue) and negative (red) isosurfaces of the spin density distribution of **1** (for ± 0.0005 au isovalues).

positions of heavy atoms, with a lesser degree of certainty on hydrogens. Therefore, when a high-resolution X-ray structure is available, optimizing only the hydrogen positions is a preferred approach for calculating reliable PNMR shifts. An image of the spin density distribution in complex **1** resulting from these calculations is given in Figure 5.8.

The effects of SOC on the calculated shifts are shown in Figure 5.7 (a) and (b), where SOC effects were not included in (a) and are included in (b). As $\text{Fe}^{(0)}$ has an electron spin $S = 1$, the effects of spin-orbit coupling are not expected to be large relative to the Fermi-contact couplings for each nucleus. Indeed, this is the case, with only minor SOC effects on the calculated shifts; nevertheless, the inclusion of SOC significantly clarified the region around 0-100 ppm in the ^{13}C dimension. The other experimental resonances are sufficiently well resolved to permit assignment already without SOC. Following these findings, for the remainder of this chapter any calculated values of complexes **1-3** will use input structures with the H-positions optimized, and SOC effects will be included. This computational methodology constitutes the current state of the art.

The overall agreement between calculated and experimental shifts permits a full assignment of all observed resonances. A summary of the calculated values and experimental shifts, together with the assignment, is given in Table 5.3 with a cartoon of the structure of **1** with labels for each site. The calculations indicate that all four *i*Pr-Me moieties, sites 8, 9, 11, and 12, are clustered in the same spectral area, between 0 and 100 ppm in the ^{13}C dimension and from -20 to 0 ppm in the ^1H dimension. The peaks at the positions, $[\delta(^1\text{H}), \delta(^{13}\text{C})]$ (in ppm), of $[-18.7, 51.1]$, $[-15.6, 101.7]$, and $[-3.3, 14.3]$ are thus firmly assigned to sites 8, 9, and 11+12. The latter peak clearly contains overlap of two resonances, as the peak has an intensity roughly double that of other peaks in the spectrum. Another interesting feature is the vast disparity of shifts for the methyl groups in *dtm*s. The two methyl groups which are in the plane roughly defined by the *dtm*s backbone (sites 18 and 19) have very large and negative shifts for both protons and carbons, whereas the two methyl groups roughly orthogonal to this plane (sites 17 and 20) have small negative carbon shifts and small positive proton shifts. This suggests that dihedral angles between the vinyl moieties and the methyl groups ($\text{CH}_2\text{-CH-Si-Me}$) are of critical importance for the hyperfine couplings. It should be stressed that although assignments could be made in this



Site	^{13}C / ppm			^1H / ppm		
	Exp	Calc.		Exp	Calc.	
		Min	Max		Min	Max
1	-329.5	-281	-158	—	73.0	111.1
2	473.9	444	596	36.9	28.7	46.7
3	205.5	153	228	-1.2	-3.7	6.2
4	223.6	270	287	41.9	25.1	44.3
5	-197.6	-308	-301	—	—	—
6	-123.8	-291	-155	7.7	-1.2	2.7
7	—	-1059	-619	—	-9.6	8.4
8	51.1	33	76	-18.7	-7.3	-4.1
9	101.7	83	144	-15.6	-8.3	-6.4
10	—	-1079	-574	—	-5.4	5.7
11	14.3*	46	120	-3.3*	-11.5	-10.4
12	14.3*	27	75	-3.3*	-9.0	-6.7
13a	—	-5699	-2170	—	270.9	287.5
13b	—	—	—	—	443.2	456.6
14	—	-3454	-1534	—	679.1	732.2
15a	—	-5302	-2016	—	320.5	339.8
15b	—	—	—	—	394.9	448.0
16	—	-3155	-1412	—	662.7	718.5
17	-34.3	-31	-27	6.6	7.1	8.8
18	-367.7	-962	-409	-15.2	-45.8	-21.6
19	-345.8	-998	-408	-10.1	-38.8	-17.6
20	-20.4	-49	-22	5.1	7.3	8.1

Table 5.3: A comparison of the assigned experimental resonances and calculated ranges (using the H-optimized geometries) of isotropic ^{13}C and ^1H shifts in complex **1** with the labels given by the above right structure of **1**, with the methyl and phenyl moiety labels clarified in the structure on the above left. Sites which were not observed or do not exist in the molecule are denoted by a dash, —. *Two sites are overlapped in both dimensions.

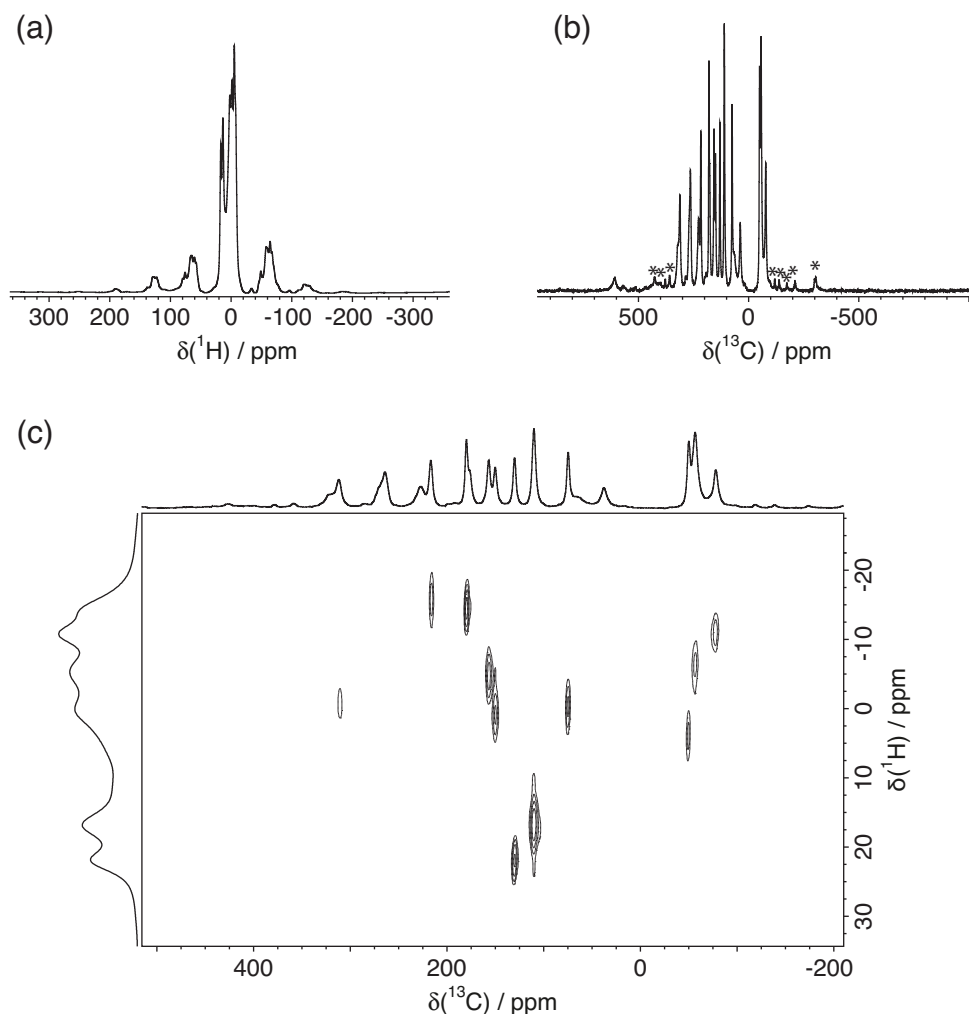


Figure 5.9: (a) 1D 1H MAS spectrum of **2**. (b) 1D ^{13}C MAS spectrum of **2**. In this case, all intense peaks are isotropic, while small peaks are sidebands. The isotropic ^{13}C shifts range from -78 to 608 ppm. 1,064,960 scans were collected over 4.8 hours using a recycle delay of 20 ms. (c) the 2D TEDOR 1H - ^{13}C heteronuclear correlation spectrum of **2**. 65,536 scans were collected for each of the 50 t_1 increments, giving a total experiment time of 7.3 hours using a recycle delay of 5 ms. All spectra were acquired with a MAS rotation rate of 31.25 kHz and with an external magnetic field strength of $B_0 = 11.74$ T (500 MHz)

case, this methodology may not provide resolution sufficient for systems larger than complex **1**.

5.4.3 Quantum chemistry calculation of PNMR shifts of **2** and **3**

Complexes **2** and **3** contain up to 34 or 35 carbon sites, respectively, while complex **1** exhibits only 20 unique carbon sites. Given the limited resolution in the 1H dimension, the increased size of **2** and **3** may complicate the assignment protocol compared to **1**. This is indeed the case, with the 1H and ^{13}C 1D MAS spectra and 2D H-C TEDOR correlation spectra of given in Figures 5.9 and 5.10 (a), (b), and (c), respectively. In each case, the spectra are comparatively more crowded than the spectra of **1**. As before in the case of **1**, computational methods were used in order to aid in the assignment of the spectra. The calculated PNMR shifts are overlaid on the 2D TEDOR spectra of **2** and **3** in Figure 5.11. In both cases, the increased complexity

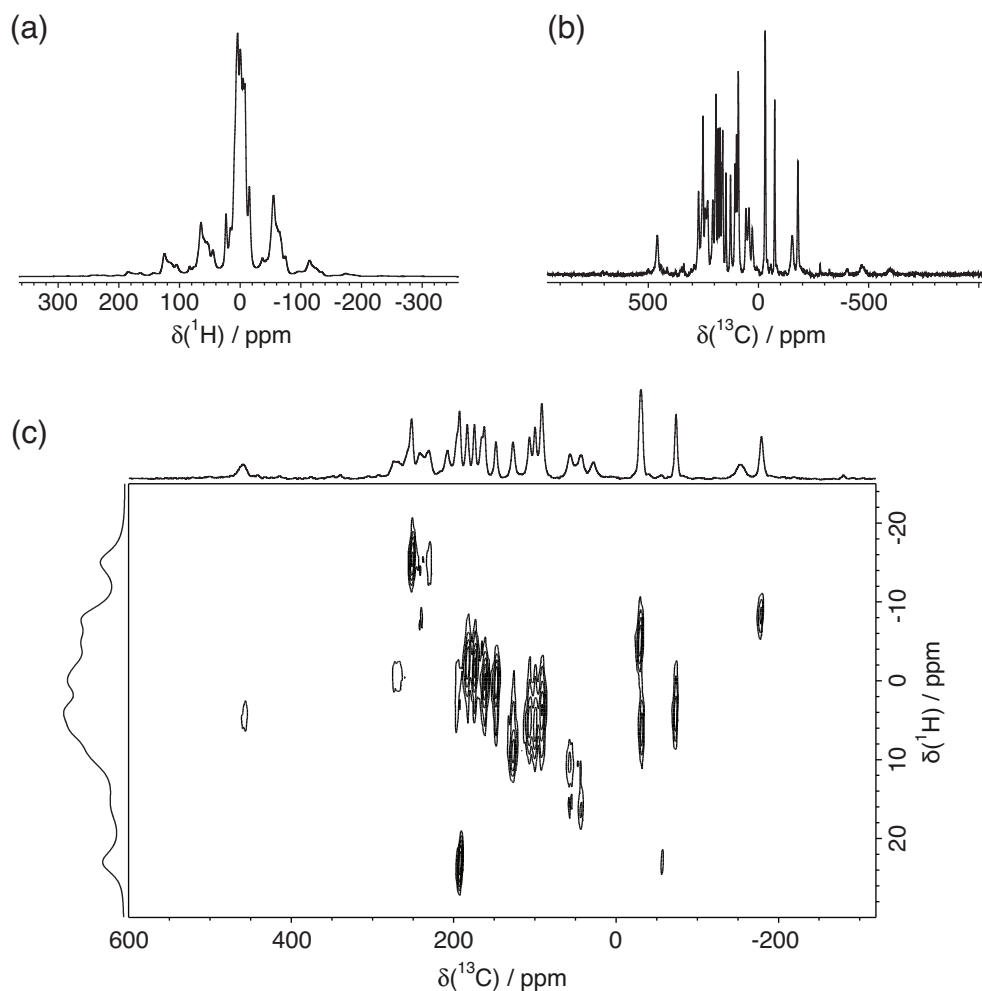


Figure 5.10: (a) 1D ^1H MAS spectrum of **3**. The inset represents the isotropic projection from an aMAT experiment. (b) 1D ^{13}C MAS spectrum of **3**. In this case, all intense peaks are isotropic, while small peaks are sidebands. The isotropic ^{13}C shifts range from -596 to 460 ppm. $614,400$ scans were collected over 3.9 hours using a recycle delay of 30 ms. (c) the 2D TEDOR ^1H - ^{13}C heteronuclear correlation spectrum of **3**. In total all 16 of the 16 expected H-C correlations were observed. $98,304$ scans were collected for each of the 50 t_1 increments, giving a total experiment time of 8.2 hours using a recycle delay of 3 ms. All spectra were acquired with a MAS rotation rate of 31.25 kHz and with an external magnetic field strength of $B_0 = 11.74$ T (500 MHz)

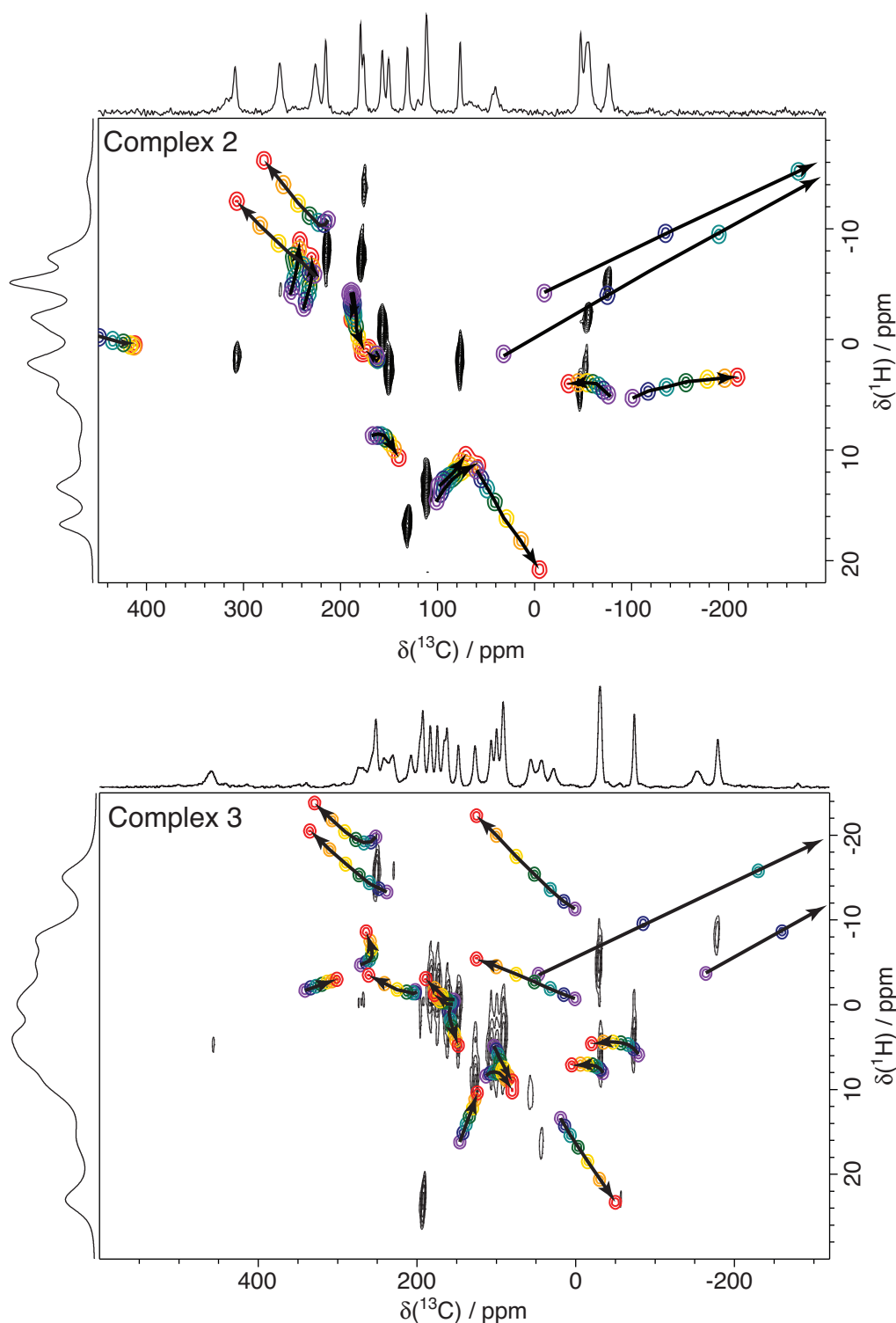


Figure 5.11: Overlays of the experimental H-C TEDOR correlation spectrum of **2** (top) and **3** (bottom) and calculated values using the H-optimized geometry for **2** and the fully-optimized geometry for **3**. The calculated values are given by colored circles, with purple representing values using PBE10 in the calculation of the hyperfine couplings, and red representing values using PBE40. The arrows laid over the calculated values indicate the trajectory of the calculated paramagnetic shift for each H-C pair towards increasing levels of Hartree-Fock exchange admixture. Each calculated H-C correlation was given an arbitrary line width to aid visualization.

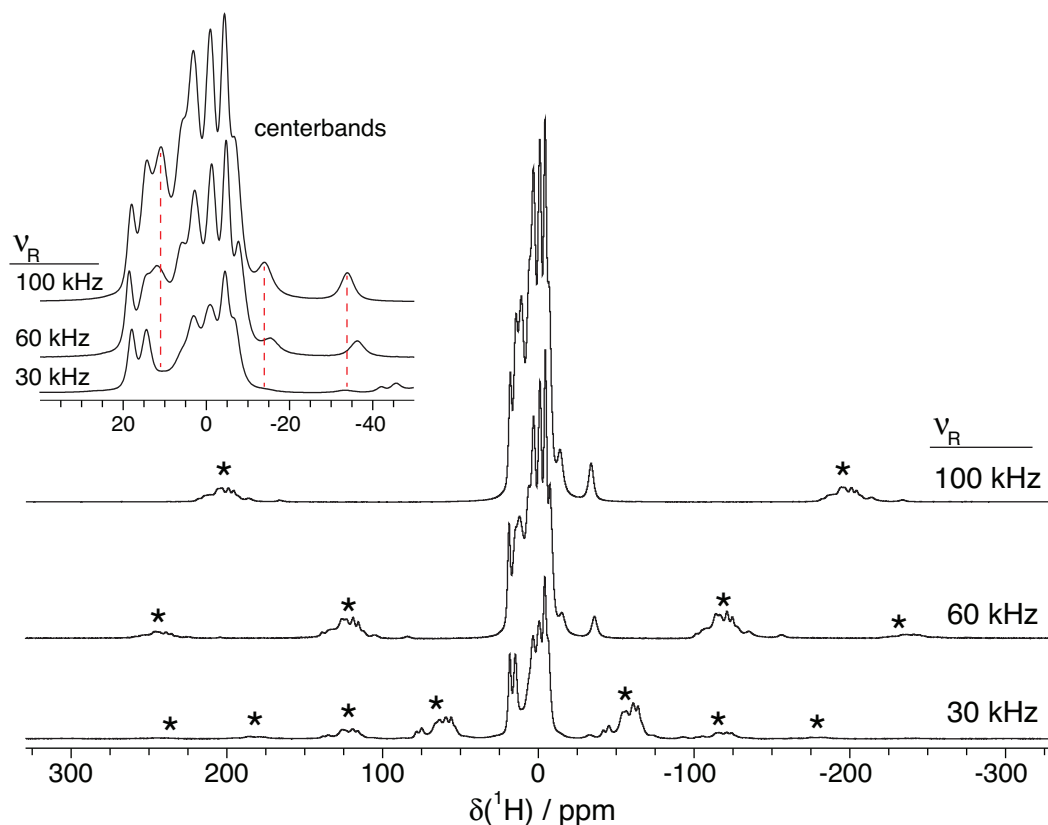
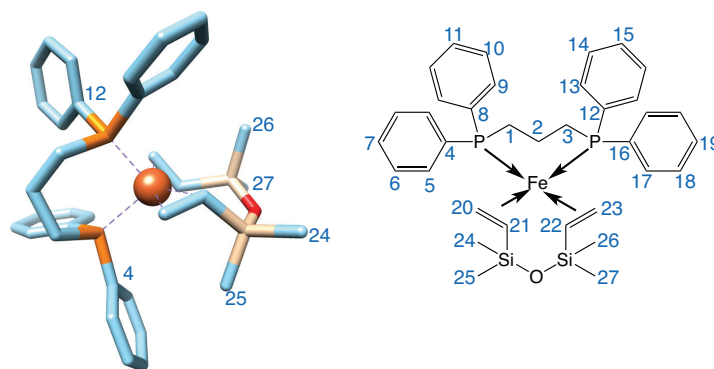


Figure 5.12: Comparison of the effect of MAS rate on the ^1H spectrum of **2**, using the MAS rates given at the right of each spectrum. Beyond the obvious increase in resolution and sensitivity due to the greater separation of spinning sidebands, the resonances marked by the dashed red lines became much stronger by the increase in spinning speed, presumably due to less T_2' dephasing during the double adiabatic echo experiment. SHAP refocusing pulses with a tanh/tan shape in (a) were $66.67 \mu\text{s}$ in length and swept through 10 MHz, resulting in a total pulse sequence length of $266.67 \mu\text{s}$, in (b) the SHAPs were $33.33 \mu\text{s}$ in length and swept through 10 MHz, resulting in a total pulse sequence length of $166.67 \mu\text{s}$, while in (c) the SHAPs were $20 \mu\text{s}$ in length and swept through 10 MHz, resulting in a total pulse sequence length of $80 \mu\text{s}$. All spectra were recording with an external magnetic field strength of $B_0 = 11.74 \text{ T}$ (500 MHz). The slight shift in the peaks denoted by the red dashed lines came as a result of temperature differences between the measurements. Spinning sidebands are denoted by asterisks above each spectrum.

of the ligands and relatively higher spectral overlap compared to **1** prevent direct unambiguous resonance assignment.

The agreement between experiment and calculations for **3** is comparatively better than for **2**, with 4 resonances being assigned directly from the calculations, including all four methyl groups at positions $[\delta(^1\text{H}), \delta(^{13}\text{C})]$ of $[-5.0, -29.7]$, $[6.5, -31.7]$, $[4.2, -73.5]$, and $[-8.3, -178.5]$, sites 24, 27, 25, and 26, respectively (all values in ppm). A summary of the calculated and assigned experimental values is given in Table 5.4. The density of experimental peaks in the center of the TEDOR spectrum of **3** prevents further assignment, but already the fact that the calculations and experiments agree for several peaks validates the structure of **3** and thus supports the electronic structure determined by computational methods. On the other hand, no resonances can be clearly assigned in the TEDOR spectrum of **2** with the calculated values alone besides being able to identify that the four peaks with negative carbon shifts correspond to methyl groups.



Site	^{13}C / ppm			1H / ppm		
	Exp	Calc.		Exp	Calc.	
		Min	Max		Min	Max
1a	—	-1382	-1282	—	-43.0	-30.2
1b	—			—	23.8	26.7
2a	—	1	125	—	-22.3	-11.3
2b	—			—	-5.4	-0.7
3a	—	-1500	-841	—	-15.9	47.1
3b	—			—	27.2	36.0
4	—	-300	-77	—	—	—
5	—	238	335	—	-20.5	-13.3
6	—	-50	19	—	13.4	23.3
7	—	252	329	—	-23.8	-19.1
8	—	-36	1138	—	—	—
9	—	301	341	—	-3.0	-1.7
10	—	124	146	—	10.4	16.2
11	—	148	161	—	0.0	4.8
12	—	-838	-755	—	—	—
13	—	202	261	—	-3.5	-1.4
14	—	80	103	—	4.9	10.3
15	—	153	189	—	-3.1	-0.3
16	—	-858	-509	—	—	—
17	—	257	271	—	-8.6	-4.7
18	—	80	113	—	8.0	9.0
19	—	168	178	—	-1.2	-0.4
20a	—	-4347	-1443	—	298.8	349.8
20b	—			—	18.7	151.6
21	—	-3181	-1068	—	731.2	876.6
22	—	-3646	-1548	—	608.0	678.4
23a	—	-5281	-1879	—	394.6	470.3
23b	—			—	320.8	355.1
24	-29.7	-948	47	-5.0	-44.0	-3.6
25	-73.5	-79	-20	4.2	4.4	5.9
26	-178.5	-34	5	-8.3	7.0	8.0
27	-31.7	-976	-164	6.5	-39.7	-3.7

Table 5.4: A comparison of the assigned experimental and calculated (H-optimized geometries) isotropic 1H and ^{13}C shifts in complex **3** with the labels given by the above right structure of **3**, with the α positions and of each phenyl moiety and methyls of the Si-Me moieties labeled in the above right structure. Sites which were not observed or do not exist in the molecule are denoted by a dash, —.

5.4.4 Experimental assignments for complex **2** using 100 kHz MAS methodologies

As the computational results are wholly inconclusive for **2**, additional experimental constraints are needed for the assignment of the ^1H and ^{13}C signals of **2**. Of particular importance would be ^1H - ^1H correlations to identify sites within each phenyl moiety of dppe, and to identify the methyl groups of dtvms, and possibly even phenyl-methyl contacts. 2D back-to-back (BABA) [62] spectroscopy is an attractive choice to achieve this, as the use of $\pi/2$ pulses in relatively short recoupling periods are beneficial for applications to paramagnetic samples. In order to achieve adequate bandwidth in the indirect dimension of the BABA experiment and to concentrate more signal in the centerbands, the use of the fastest available magic angle spinning rate is necessary. The effect of using faster MAS afforded by the 0.7 mm probe on the ^1H double adiabatic echo spectrum of **2** is given in Figure 5.12. Increasing the MAS rate from 30, to 60, and finally to 100 kHz results in a significant improvement in the sensitivity of the centerbands, as is expected, as well as a very minor decrease in the average line widths by the reduction of homogeneous broadening due to ^1H - ^1H homonuclear dipolar coupling. A perhaps unexpected result is that three peaks with shifts of -33.9 , -14.0 , and 10.9 ppm became considerably more intense upon faster rotation. This may be explained if these three sites experience significant PRE and thus have very short T_2' dephasing times, as the length of the double adiabatic echo pulse sequence was shortened from $266.67 \mu\text{s}$, to $133.33 \mu\text{s}$, and finally to $80 \mu\text{s}$ as the MAS rate was increased from 30 to 60 to 100 kHz, respectively. We expect that these three peaks come from the $-\text{CH}_2-$ moieties of the "backbone" of the dppe, which experience significant hyperfine couplings and are close to the metal center, thus leading to large PRE effects on these nuclei.

A schematic structure of **2** is given in Figure 5.13 (a) with numeric labels given in blue for each carbon site in the molecule. The 2D BABA spectrum of **2**, collected with a MAS rate of 100 kHz, is given in Figure 5.13 (b). Twelve correlations are resolved in total, comprising 7 dppe intra-phenyl correlations, 1 inter-phenyl correlation, 1 dppe CH_2 - CH_2 correlation, 2 dppe CH_2 -phenyl correlations, and 1 dtvms methyl-methyl correlation, all denoted by colored lines in Figure 5.13 (b). The data in the BABA spectrum allow us to identify resonances from three of the four phenyl groups in **2** (groups A-C in the legend), as well as identify all four methyl groups unambiguously, as these resonances should fall on the diagonal due to auto-correlation (denoted by the thin black line in the BABA spectrum). Resonances from the phenyl group D may were not observed, likely due to a lack of resolution for its proton sites. One methyl-methyl correlation was observed, which permits the identification of pairs of methyl groups on each side of the dtvms ligand, *i.e.*, correlations between sites 23-24 and 25-26. One inter-phenyl correlation was observed between phenyls A and B. This indicates spatial proximity between A and B, but care must be taken in assigning this correlation, as it may arise from either an intra-molecular correlation or an inter-molecular correlation in a molecular crystal, *i.e.*, a contact to a neighboring molecule. The one observed CH_2 - CH_2 correlation confirms that the ^1H resonance at 12.9 ppm comes from the $-\text{CH}_2-\text{CH}_2-$ backbone of the dppe ligand, together with the resonances at -13.9 ppm and -33.9 ppm. The broad feature at 11.6 ppm is assigned as the final remaining

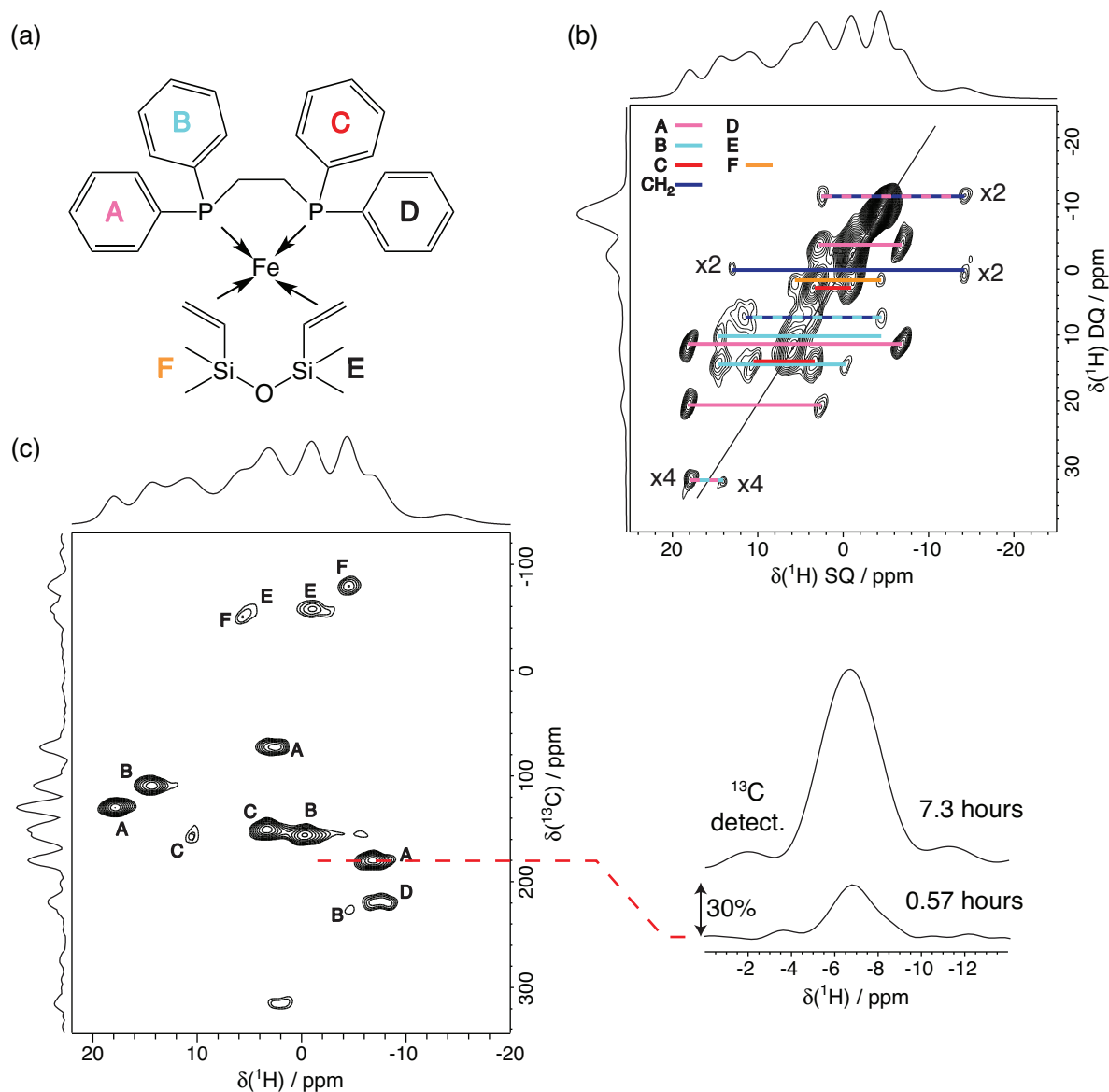


Figure 5.13: (a) Schematic structure of **2** with atomic labels given in blue. (b) The 2D 1H SQ-DQ BABA correlation spectrum of **2**, with correlations marked by colored lines corresponding to (1) dppe intra-phenyl correlations (pink, red, light blue), (2) dvtms methyl group correlations (yellow), (3) dppe CH₂-correlations. Dashed multi-colored lines indicate correlations between different moieties. The thin black diagonal line corresponds to autocorrelation peaks, in this case solely consisting of methyl resonances. The BABA sequence from Figure 1.12 (c) was used. 1024 scans for each of the 200 t_1 increments were collected using a recycle delay of 2 ms. The total experiment time was 15 minutes. (c) The 1H -detected 2D HSQC-TEDOR spectrum of **2** using the sequence in Figure 1.12 (b), with 2560 scans collected for each of the 200 t_1 increments, giving a total experiment time of 34 minutes. The labels next to experimental peaks correspond to the assigned groups given by the legend in the BABA spectrum. Both spectra were collected with a MAS rate of 100 kHz with $B_0 = 11.7$ T (500 MHz). A 1H dimension cross-section from the resonance at $\delta(^{13}C) = 180$ ppm is given to the right of the TEDOR spectrum, over which is given the equivalent cross section from the ^{13}C -detected TEDOR spectrum in Figure 5.9 (c), which was collected using a spinning speed of 31.25 kHz. The relative intensities and experiment times indicate that the sensitivity is equivalent between these two spectra. All experiments were performed with a temperature of approximately 290 K.

CH₂ resonance, which was found to correlate with a resonance from B, indicating that these two protons are close by in space. Additionally, a correlation was observed between the CH₂ resonance at -13.9 ppm and a resonance at 2.6 ppm from A, which likewise indicates that these two protons are near to each other in the molecule.

A ¹H-detected 2D TEDOR ¹H-¹³C correlation spectrum of **2** was reacquired using a MAS rate of 100 kHz, and is given in Figure 5.13 (c). The ¹H-¹H correlations from the BABA spectrum were used to label the experimental resonances in the TEDOR spectrum according to the legend given in the BABA spectrum, *i.e.* groups A-F, corresponding to phenyl resonances (A-D) and methyl resonances (E, F). Correlations between protons and carbons in the CH₂ groups of the backbone of the dppe ligand are not observed due to the large negative ¹³C shifts expected for these resonances. One very important result is that the sensitivity of the ¹H-detected TEDOR experiment is equivalent to the ¹³C-detected experiment in Figure 5.9 (c), contrary to what may be expected by the significant decrease in sample volume in a 0.7 mm rotor compared to a 2.5 mm rotor. This comes as a result of the fact that ¹H is inherently a factor of ≈ 64 times more sensitive than ¹³C, so even though the sample volume is considerably less and there is an additional polarization transfer in the ¹H-detected TEDOR experiment, we are able to achieve equivalent sensitivity. This is a promising result, as it may in the future permit more complex experiments, such as a 3D ¹H-¹H-¹³C correlation experiment, to be acquired in a reasonable amount of time and would, as a result, improve the resolution of the experimental methodology, potentially permitting more extensive experimental assignments of resonances.

5.4.5 Discussion on the structure of **2**

The agreement between experimental and calculated shifts for **2** was significantly worse than what was observed for **1** and **3**. Following the synthesis information given in Appendix C, the samples used in NMR analysis were not all generated in the same manner. Crystals of complexes **1** and **3**, although not X-ray quality, were grown slowly out of solution, which likely resulted in the same coordination geometry as was determined by XRD. On the other hand, the sample of complex **2** received for NMR analysis was triturated from a green oil, resulting in a sticky, perhaps non-crystalline solid. Although it is clear from the NMR spectra of **2** that the local geometry is well-defined (sharp resonances, correct number of peaks), it need not be the same as the X-ray structure used in PNMR calculations. The fact that the agreement between experiment and calculations for **2** is so poor relative to the results obtained for **1** and **3** strongly supports this notion. Moreover, the NMR spectra were measured at 290-300 K, whereas the X-ray structures were determined at 150 K. Thus, the discrepancy between the experimental and calculated results for **2** may come as a result of structural change/relaxation as a function of temperature, or simply that the precipitated solid adopts a unique geometry compared to single crystals which were slowly grown for XRD analysis. This project is ongoing and we are in discussion with our collaborators to determine what may be causing this discrepancy.

On one hand, this is a confusing result, yet on the other hand, it opens the door to a unique opportunity – a computational search for a *de novo* structure of **2** that would provide agreement

with the experimental PNMR shifts. We are currently pursuing this idea.

5.5 Conclusions and outlook

The results in this chapter represent the current state of the art in PNMR spectroscopy applied to transition-metal organometallic complexes. Due to the impossibility of obtaining X-ray quality single crystals of **4**, we showed in the first part of this chapter how broadband NMR spectroscopy and computational techniques permitted the identification of a de novo structure of **4**. Then, we show for complex **1** how the combination of suitable geometry optimization, calculation of the hyperfine coupling tensors by a range of DFT functionals, and calculation of spin-orbit coupling effects calculated at a multi-reference *ab initio* level can be used to achieve full assignment of the experimental PNMR shifts obtained using relatively moderate MAS rates, thus confirming the coordination geometry and determining the electronic structure of complex **1**. Similar results were obtained for **3**, albeit with fewer unambiguous assignments. The applied computational methods represent the state of the art for quantum chemical prediction of PNMR shifts.

The agreement between calculation and experiment was not observed for **2**, though, presumably due to a discrepancy between the X-ray quality single crystal structure and the structure of the precipitated sample used for PNMR analysis. Nevertheless, with the use of 100 kHz MAS, we show how nearly full experimental resonance assignment can be achieved for **2** by employing broadband ¹H-¹H and ¹H-¹³C correlations. Moreover, it was shown that ¹H-detection can be used to achieve well-resolved and sensitive 2D spectra in a matter of minutes, which opens the doors to more advanced methodology, such as 3D correlation experiments. Finally, we demonstrated the power of combining state-of-the-art experimental and computational PNMR methodologies to confirm or exclude a given structural model, making thus the first steps towards de novo PNMR structure determination.

Conclusions and perspectives

The results shown in this thesis have been largely made possible by recent advancements in MAS probe technology, now permitting rotation rates exceeding 100 kHz. At the beginning of the thesis a brief explanation of paramagnetic effects in NMR is given, followed by an outline of the current experimental "toolkit", which is used to achieve (1) broadband excitation, inversion, and refocusing under MAS conditions, (2) broadband homo- and heteronuclear correlations with ultrafast MAS rotation rates, and (3) isotropic resolution in MAS NMR of paramagnetic materials by the removal of spinning sidebands. The combination of carefully-tuned pulse sequences and high MAS rates permits extensive experimental constraints for resonance assignment, a reduction in experiment time, and marked improvements in sensitivity, resolution, and excitation bandwidths of experimental NMR spectra of paramagnetic materials. Indeed, this current age of ultrafast magic-angle spinning has resulted in a dramatic expansion of the experimental capabilities in paramagnetic NMR. Hopefully, the continued development of MAS probes capable of ever higher MAS rates will extend the horizon of experimental capabilities and allow the study of even more complicated systems.

The opportunities afforded by magic-angle spinning NMR were explored in two main directions in this thesis:

(i) **Low-power broadband swept-frequency pulses.** Due to the prohibitively high RF field requirements of SHAPs when MAS rates exceed 60 kHz [13], low-power S³AP pulses [6] were examined for broadband inversions for fast MAS experiments. The results point to the fact that the S³APs are an attractive alternative, especially for studies of low-gamma nuclei like ⁶Li and ¹⁴N when the rotation rate exceeds 60 kHz. It was shown that S³APs have non-uniform orientational efficiency though, which leads to biasing of sideband intensities in the inverted NMR spectrum due to the inclusion or absence of certain sets of crystallites. To improve the orientational selectivity, the possibility of sweeping over multiple bands simultaneously was explored. Through a combined simulated and experimental analysis, it is shown that uniform spatial selectivity can be achieved by sweeping simultaneously over three adjacent sidebands, resulting in only modest increases in the required RF field strength for these pulses [14].

(ii) **Local geometries and electronic structures of challenging paramagnetic systems.** Ultrafast MAS NMR and modern paramagnetic experimental methodologies were used to study principally three new and intriguing classes of paramagnetic materials: mixed-phase olivine-type phosphates for lithium-ion battery cathodes, organolanthanide complexes for heterogeneous catalysis, and low-valent stable Fe⁽⁰⁾ complexes for homogeneous catalysis. The use of MAS rates exceeding 100 kHz delivers unprecedented resolution in 1D ³¹P NMR spectra of the examined cathode materials, which permitted site-specific identification of paramagnetic

shifts and the subsequent conclusion that transition metals tend to adopt native local geometries even in mixed phases. Heteronuclear correlation spectroscopy and a point-dipole model of paramagnetic shifts permitted the identification of a 3-center-2-electron secondary bonding interaction in the organoytterbium Yb[CH(SiMe₃)₂]₃ molecular complex, similar to what was seen previously for the isostructural diamagnetic Lu[CH(SiMe₃)₂]₃ complex [15]. Finally, broadband NMR correlation methods using ultrafast MAS and state-of-the-art computational methods were used to determine coordination geometries and electronic structures of four Fe⁽⁰⁾ complexes. It was found that, in general, the agreement between calculated and experimental values of the paramagnetic shifts is quite good, provided the structure used for the calculations is accurate. When this is not the case, it becomes necessary to search for a de novo structure which results in calculated shifts in good agreement with experiment.

This work has been carried out in an exciting point in time where the field of solid-state NMR is rapidly evolving towards higher and higher MAS rates and external magnetic field strengths. We believe that the methodologies presented herein and their applications to interesting modern materials in chemistry represent a leap forward in the experimental possibilities, and are a reason to be highly optimistic about the prospects of MAS NMR applications to more complex chemical systems in the future.

Solid-state NMR with ultrafast MAS rotation is being used more and more in recent years for the study of paramagnetic complexes and materials with ever-increasing complexity [1, 3, 8–10, 12, 14, 18, 19, 22, 65, 78, 91]. Despite these advances, the analysis of dilute chemical environments, like on surfaces or in defect sites, is a major challenge due to the inherently low sensitivity of NMR. Sensitivity enhancements by dynamic nuclear polarization (DNP) for the study of surface species [150, 151] has in recent years garnered much attention due to the possibility of observing surface sites with high sensitivity, and has been recently used to determine a well-defined ligand geometry on a silica surface together with selective labeling schemes [149]. Due to the relatively slow MAS rates used during DNP measurements, these studies have been primarily focused on the characterization of, and correlation between heteronuclei (*i.e.* atoms other than protons) of ligands of a metal site bound to a surface. Unfortunately DNP is not typically applicable to paramagnetic systems, and due to the low gyromagnetic ratios of nuclei such as ¹³C, ¹⁵N, and ²⁹Si, the methodology used in these prior studies is too insensitive for applications using conventional NMR methodology.

Due to the high gyromagnetic ratio of ¹H, one possible route to overcome the inherently low sensitivity of surface studies by NMR would be to use ¹H-detection combined with ultrafast MAS rotation. There has been a revolution in recent years in the field of structural biology, where ¹H-detected experiments have resulted in unprecedented increases in resolution and sensitivity [210–215]. A similar approach should be possible for paramagnetic samples as well. Indeed it has been recently shown that ¹H-detected 1D and 2D correlation experiments from the paramagnetic NMR "toolkit" applied to the paramagnetic superoxide dismutase metalloprotein have permitted the detection of ¹H, ¹³C, and ¹⁵N signals of the ligands coordinating the active metal site of the protein and a subsequent refinement of the crystal structure at this site [77]. Applied to

metal-ligand complexes on surfaces, we anticipate that the combination of ultrafast MAS rates, and state-of-the-art experimental and computational methodologies will provide unprecedented insight in nuclear chemical environments and as a result, determination of surface structure of these materials.

List of publications

- (1) Sanders, K. J.; Benda, L.; Lejeune, A.; Burcher, B.; Pell, A. J.; Quoineaud, A.-A.; Breuil, P.-A.; Grey, C. P.; Pintacuda, G. 100+ kHz MAS NMR for the determination of electronic structure and local geometry in paramagnetic materials. *In preparation* **2018**.
- (2) Allouche, K.; Sanders, K. J.; Klöse, D.; Ashuiev, A.; Conley, M. P.; Lapadula, G.; Walter, M.; Copéret, C.; Jeschke, G.; Maron, L.; Pintacuda, G.; Andersen, R. A. Defying the Lewis structure of $\text{Yb}(\text{CH}(\text{SiMe}_3)_2)_3$ from 2D solid state EPR and NMR spectroscopies combined with CASSCF calculations. *Manuscript in preparation* **2018**.
- (3) Jardón-Álvarez, D.; Sanders, K. J.; Phyo, P.; Baltisberger, J. H.; Grandinetti, P. J. Cluster formation of network-modifier cations in cesium silicate glasses. *J. Chem. Phys.* **2018**, *148*, 094502.
- (4) Sanders, K. J.; Pell, A. J.; Wegner, S.; Grey, C. P.; Pintacuda, G. Broadband MAS NMR spectroscopy in the low-power limit. *Chem. Phys. Lett.* **2018**, *697*, 29–37.
- (5) Pell, A. J.; Sanders, K. J.; Wegner, S.; Pintacuda, G.; Grey, C. P. Low-power broadband solid-state MAS NMR of ^{14}N . *J. Chem. Phys.* **2017**, *146*, 194202.
- (6) Burcher, B.; Sanders, K. J.; Benda, L.; Pintacuda, G.; Jeanneau, E.; Danopoulos, A. A.; Braunstein, P.; Olivier-Bourbigou, H.; Breuil, P.-A. R. Straightforward Access to Stable, 16-Valence-Electron Phosphine-Stabilized Fe^0 Olefin Complexes and Their Reactivity. *Organometallics* **2017**, *36*, 605–613.
- (7) D'Anna, V.; Norsic, S.; Gajan, D.; Sanders, K.; Pell, A. J.; Lesage, A.; Monteil, V.; Copéret, C.; Pintacuda, G.; Sautet, P. Structural Characterization of the $\text{EtOH-TiCl}_4\text{-MgCl}_2$ Ziegler-Natta Precatalyst. *J. Phys. Chem. C* **2016**, *120*, 18075–18087.
- (8) Baltisberger, J. H.; Florian, P.; Keeler, E. G.; Phyo, P. A.; Sanders, K. J.; Grandinetti, P. J. Modifier cation effects on ^{29}Si nuclear shielding anisotropies in silicate glasses. *J. Magn. Reson.* **2016**, *268*, 95–106.
- (9) Conley, M. P.; Lapadula, G.; Sanders, K.; Gajan, D.; Lesage, A.; del Rosal, I.; Maron, L.; Lukens, W. W.; Copéret, C.; Andersen, R. A. The Nature of Secondary Interactions at Electrophilic Metal Sites of Molecular and Silica-Supported Organolutetium Complexes from Solid-State NMR Spectroscopy. *J. Amer. Chem. Soc.* **2016**, *138*, 3831–3843.
- (10) Baltisberger, J. H.; Walder, B. J.; Keeler, E. G.; Kaseman, D. C.; Sanders, K. J.; Grandinetti, P. J. Communication: Phase incremented echo train acquisition in NMR spectroscopy. *J. Chem. Phys.* **2012**, *136*, 211104.

- (11) Davis, M. C.; Sanders, K. J.; Grandinetti, P. J.; Gaudio, S. J.; Sen, S. Structural Investigations of magnesium silicate glasses by ^{29}Si 2D Magic-Angle Flipping NMR. *J. Non-Cryst. Solids* **2011**, *357*, 2787–2795.
- (12) Davis, M. C.; Kaseman, D. C.; Parvani, S. M.; Sanders, K. J.; Grandinetti, P. J.; Massiot, D.; Florian, P. Q⁽ⁿ⁾ Species Distribution in $K_2O \cdot 2SiO_2$ Glass by ^{29}Si Magic Angle Flipping NMR. *J. Phys. Chem. A* **2010**, *114*, 5503–5508.

List of abbreviations

ABMS	Anisotropic Bulk Magnetic Susceptibility
BABA	Back-to-Back
CP	Cross-Polarization
CPMG	Carr-Purcell-Meiboom-Gill
CSA	Chemical Shift Anisotropy
DFT	Density Functional Theory
dipe	1,2-bis(diisopropylphosphino)propane
dppe	1,2-bis(diphenylphosphino)ethane
dppp	1,2-bis(diphenylphosphino)propane
DQ	Double Quantum
dvtms	divinyltetramethyldisiloxane
EPR	Electron Paramagnetic Resonance
EXAFS	Extended X-ray Absorption Fine Structure
HFC	Hyperfine Coupling
LCP	Lithium Cobalt Phosphate
LFP	Lithium Iron Phosphate
LIB	Lithium-Ion Battery
LMP	Lithium Manganese Phosphate
MAS	Magic Angle Spinning
MAT	Magic Angle Turning
NMR	Nuclear Magnetic Resonance
NR	Non-Relativistic
PAF	Principle Axis Frame
PBE	Perdew-Burke-Ernzerhof
PCS	Pseudocontact Shift
PNMR	Paramagnetic Nuclear Magnetic Resonance
PRE	Paramagnetic Relaxation Enhancement
pyNMeP(ⁱ Pr) ₂	<i>N</i> -(diisopropylphosphino)- <i>N</i> -methylpyridine-2-amine
RF	Radio Frequency
S ³ AP	Single-Sideband-Selective Adiabatic Pulse
SA	Shift Anisotropy
SHAP	Short, High-power Adiabatic Pulse
SOC	Spin-Orbit Coupling
SQ	Single Quantum
ssNMR	solid-state Nuclear Magnetic Resonance
TEDOR	Transferred-Echo Double Resonance
XRD	X-Ray Diffraction
ZFS	Zero Field Splitting
ZNC	Ziegler-Natta Catalyst

Appendix A

Experimental details

A.1 Solid-state NMR studies LiMPO₄ cathode phases (Chapter 2)

The 1D MAS spectra of LiFe_{0.25}Mn_{0.75}PO₄ and of LiMg_xMn_{1-x}PO₄ ($x = 0.2, 0.5$) were collected on a Bruker Avance III spectrometer operating at an external magnetic field strength of 7.05 T (corresponding to a ¹H Larmor frequency of 300 MHz). All spectra, unless otherwise noted, were acquired using a Bruker 0.7 mm widebore MAS probe at spinning speeds of either 60 kHz or 111.111 kHz. Unless noted otherwise, the temperature is estimated to be 320 K for all measurements. The samples were packed in 0.7 mm zirconia rotors and spun to the desired spinning speed with dry nitrogen gas using a Bruker MAS III unit. All 1D spectra were collected using the double adiabatic echo experiment in Figure A.1. $\pi/2$ pulses with a nominal RF field strength of 420 kHz were used for excitation, with refocusing achieved using tanh/tan SHAP pulses (18 μ s in length sweeping through 10 MHz). The ³¹P MAS spectra of LiFe_{0.25}Mn_{0.75}PO₄ and LiMg_{0.2}Mn_{0.8}PO₄ were fit using a home-written MATLAB fitting routine. The initial parameters used for the contributions were the H20 values from Middlemiss *et al.* [95].

A.2 Low-power broadband NMR (Chapter 3)

A.2.1 SHAP, S³AP inversions of ^{6/7}Li

⁶Li and ⁷Li MAS experiments were carried out on the olivine structure lithium-ion battery cathode material LiFe_{0.25}Mn_{0.75}PO₄ using a Bruker Avance III NMR spectrometer operating at an external field strength of 11.74 T corresponding to Larmor frequencies of 73.603 MHz and 194.391 MHz for ⁶Li and ⁷Li, respectively. The sample was packed in a 0.7 mm rotor and spun at the magic angle, 54.736° relative to the external magnetic field. The magic angle was calibrated by measuring the STMAS [216, 217] spectrum of Na₂SO₄ and adjusting the angle until an isotropic line was achieved in the indirect dimension, and was confirmed to have negligible drift ($\approx \pm 0.001^\circ$) over time and after sample ejection/re-insertion. In all cases the sample temperature was approximately 320 K. A recycle delay of 100 ms was used for all ⁶Li experiments while 10 ms was used for ⁷Li experiments. Further experimental details are given in each figure caption. Due to the hyperfine interaction between Li nuclei and the unpaired electrons in

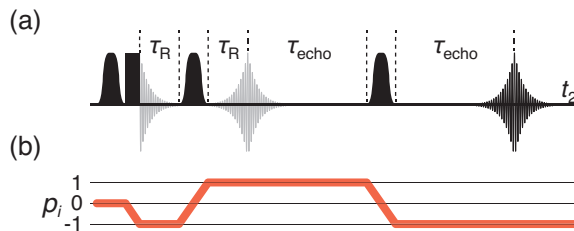


Figure A.1: The inverted shifted second echo (a) experiment used in this study. The coherence transfer pathway is given in (b) which utilized a conventional 64-step phase cycle. The black rectangular pulse represents $\frac{\pi}{2}$ excitation pulses whereas the shaped pulses represent frequency-swept pulses. It is assumed in this sequence that refocusing pulses are rotor-synchronized and likewise that $\tau_{\text{echo}}=N\tau_{\text{R}}$, where N is set to a sufficiently large value to allow acquisition of the entire echo, thereby giving a perfectly flat baseline without truncation artifacts. For ${}^6\text{Li}$ experiments, N was set to 13, 20, and 36 for 40 kHz, 62.5 kHz, and 111.111 kHz MAS experiments, respectively, corresponding to echo shift times of 325 μs , 320 μs , and 324 μs . For ${}^7\text{Li}$ measurements at 111.111 kHz MAS, $N = 22$, corresponding to an echo shift time of 198 μs .

the material, Li nuclei experience a large SA. The ${}^7\text{Li}$ MAS spectrum was fitted using a single anisotropic lineshape, resulting in an experimental chemical shift anisotropy [218], $\zeta_{\delta} = 1260$ ppm, and an asymmetry parameter, $\eta = 0.65$. In terms of frequency, this results in anisotropies of $\zeta_{\delta} = 92.7$ and 245 kHz for ${}^6\text{Li}$ and ${}^7\text{Li}$, respectively.

All swept-frequency pulses used in experiments were constructed using the shape tool in Bruker TopSpin 3.5. Each followed the amplitude, phase, and frequency sweep profiles shown in Table A.1. All S^3APs were WURST-20 [53] waveforms made of 1000 digitized points with length $\tau_{\text{p}} = 270 \mu\text{s}$, and a frequency sweep width, $\Delta\nu = \nu_{\text{R}}$, while all SHAPs were tanh/tan [52] waveforms made of 250 digitized points, with $\xi=10$ and $\tan(\kappa)=20$, $\Delta\nu = 10$ MHz, and $\tau_{\text{p}} = 18\mu\text{s}$. $\text{PN}_{\Delta\nu_{\text{RF}}}^{\Delta n}$ pulses were constructed simply by adding multiple waveforms with suitable offsets, and otherwise had identical parameters as the S^3APs .

The pulses were examined for inversion performance (i) experimentally using the pulse sequence in Figure A.1 (a), and (ii) by spin dynamics simulations using the solid-state simulation program SIMPSON [219] and digitized input pulses constructed by a home-written script in MATLAB. When testing for inversion performance, only the power of the first pulse in Figure A.1 (a) was varied, always starting from 0 kHz, and the resulting integrals were normalized to the integral of the first point. Spin dynamics simulations were carried out at an external field strength corresponding to a ${}^1\text{H}$ Larmor frequency of 500.196 MHz with powder averaging achieved by simulating 109 (α,β) pairs according to the Lebedev octant scheme [138]. The pulses were applied to a single ${}^6\text{Li}$ or ${}^7\text{Li}$ nucleus using chemical shift anisotropy parameters corresponding to the fitted experimental parameters with $\delta_{\text{iso}} = 0$ for convenience.

Pulse scheme	$\omega_1(t)$	$\phi_p(t)$	$\omega_{\text{rf}}(t)$
hyperbolic secant [51]	$\omega_1^{\text{max}} \operatorname{sech}\left(\beta(2t/\tau_p - 1)\right)$	$-\frac{\Delta\omega\tau_p}{4\beta} \left[\ln\left(\operatorname{sech}\left(\beta(2t/\tau_p - 1)\right)\right) \right]$	$\frac{\Delta\omega}{2} \tanh\left(\beta(2t/\tau_p - 1)\right)$
WURST [53]	$\omega_{1,\text{max}} \left(1 - \left \sin\left(\pi\left(\frac{t}{\tau_p} - \frac{1}{2}\right)\right)\right ^n\right)$	$\frac{\Delta\omega}{2} \left(\frac{t^2}{\tau_p} - t + \frac{\tau_p}{4}\right)$	$\frac{\Delta\omega}{2} \left(\frac{2t}{\tau_p} - 1\right)$
tanh/tan [52]	$\omega_{1,\text{max}} \tanh\left(\frac{2\xi t}{\tau_p}\right), \quad 0 < t \leq \tau_p/2$ $\omega_{1,\text{max}} \tanh\left(2\xi\left(1 - \frac{t}{\tau_p}\right)\right), \quad \tau_p/2 \leq t \leq \tau_p$	$-\frac{\Delta\omega\tau_p}{4\kappa\tan\kappa} \ln\left(\cos\left(\kappa\left(1 - \frac{2t}{\tau_p}\right)\right)\right)$	$-\frac{1}{2}\Delta\omega \cot\kappa \tan\left(\kappa\left(1 - \frac{2t}{\tau_p}\right)\right)$

Table A.1: Time-dependent amplitude, phase, and frequency sweep profiles of hyperbolic secant, WURST- n , and tanh/tan pulses. Note that each pulse is symmetric about the point $t = \tau_p/2$.

A.2.2 S³AP inversion of ¹⁴N

Solid-state NMR

Solid-state NMR spectra of (NH₄)₂C₂O₄ were acquired on a Bruker Avance III 700 spectrometer operating at a ¹⁴N Larmor frequency of 50.6 MHz, with a 3.2 mm HXY probe at 20 kHz MAS. The reference spectra were acquired with a solid-echo pulse sequence (90°-τ_r-90°-τ_r-acq.), with an EXORCYCLE phase cycle applied to the second pulse [220]. The 90° pulse length was calibrated at 4.88 μs, corresponding to a nominal RF field amplitude of 51.2 kHz. Inverted spectra were acquired with a solid-echo sequence following a WURST-20 S³AP [13, 53] with a length of 5 ms and a sweep width of 20 kHz. The spectra were acquired with 512 scans and a recycle delay of 2 s.

Solid-state NMR spectra of glycine were acquired on a Bruker Avance III 500 spectrometer operating at a ¹⁴N Larmor frequency of 36.1 MHz, with a 0.7 mm HXY probe at 111.111 kHz MAS. The magic angle was carefully calibrated with a two-dimensional satellite-transition magic-angle spinning (STMAS) spectrum of Na₂SO₄ [216], and it was confirmed that there is a negligible drift (<0.001°) of the angle over time and due to sample ejection/re-insertion. The ¹⁴N reference spectra were acquired with a DANTE solid-echo pulse sequence (DANTE-τ_r-DANTE-τ_r-acq.), with an EXORCYCLE phase cycle applied to the DANTE sequence [220]. The DANTE sequence was a D₁⁴¹ sequence of duration 41 rotor periods (369 μs), each containing a small-flip-angle pulse of length 0.0609 μs with a nominal RF field amplitude of 100 kHz. Inverted spectra were acquired with a DANTE solid-echo sequence following a WURST-20 S³AP [13, 53] with a length of 1 ms and a sweep width of 111.111 kHz. The spectra were acquired with 65,536 scans and a recycle delay of 1 s. All spectra were referenced to solid NH₄Cl.

SpinDynamica simulations

Spin dynamics simulations were performed using Spin-Dynamica 2.13.1 in Mathematica 9.0.1.0. Simulations of inversion in the presence of a first-order quadrupolar interaction were performed either with a C_Q of 93.4 kHz ($\omega_Q/2\pi = 70.05$ kHz) and asymmetry parameter η_Q of 0.42 [221] at 20 kHz MAS, corresponding to (NH₄)₂C₂O₄, or with a C_Q of 1.19 MHz (corresponding to $\omega_Q/2\pi = 892.5$ kHz) and asymmetry parameter η_Q of 0.52 at 111.111 kHz MAS, corresponding to glycine. Simulations of full powders were performed using the Zaremba-Conroy-Wolfsberg (ZCW) scheme with 538 three-angle sets [222–224].

A.3 Solid-state NMR applications to heterogeneous catalytic systems (Chapter 4)

A.3.1 Yb

Natural abundance solid-state ^1H , ^{13}C , and ^{29}Si NMR spectra of $\text{Yb}[\text{CH}(\text{SiMe}_3)_2]_3$ were acquired on a Bruker Avance III spectrometer operating at an external magnetic field strength of 11.74 T (corresponding to a Larmor frequencies of 500.16 MHz, 125.7 MHz, and 99.44 MHz for ^1H , ^{13}C , and ^{29}Si , respectively) using a Bruker HX 2.5 mm wide-bore MAS probe. In all cases the powdered sample was packed in a standard 2.5 mm ZnO_2 rotor in an Argon-filled glovebox, then placed in a sealed glass tube before removal from the glovebox in order to protect the sample from atmosphere. Immediately before measurement, the sealed tube was opened and the rotor was quickly inserted in to the MAS probe, and simultaneously spun up to the desired rotation rate while cooling the stator to a sample temperature of approximately 300 K using a Bruker BCU XTreme cooling unit. Nitrogen gas dried to a dew point of $-80\text{ }^\circ\text{C}$ was used for sample rotation.

The natural abundance ^1H , ^{13}C , and ^{29}Si MAS NMR spectra were acquired using the double spin echo sequence in Figure 1.10 (c). The initial $\pi/2$ excitation pulses had lengths of 1.20 μs , 2.12 μs , and 3.00 μs (with corresponding nominal RF field strengths of 208 kHz, 118 kHz, and 83 kHz) for ^1H , ^{13}C , and ^{29}Si , respectively. The 1D MAS spectrum of ^1H was acquired using a MAS rotation rate of 30 kHz (corresponding to a rotor period of 33.33 μs), and utilized tanh/tan SHAPs of length of 33.33 μs and a RF field strength of 208 kHz for refocusing. The 1D MAS spectrum of ^{13}C was acquired using a MAS rotation rate of 14.286 kHz (corresponding to a rotor period of 70 μs), and utilized tanh/tan SHAPs of length of 70 μs and a RF field strength of 83 kHz for refocusing. The 1D MAS spectrum of ^{29}Si was acquired using a MAS rotation rate of 30 kHz (corresponding to a rotor period of 33.33 μs), and utilized tanh/tan SHAP pulses with a length of 33.33 μs and a RF field strength of 83 kHz.

The adiabatic magic-angle turning (aMAT) spectra of ^1H and ^{29}Si was acquired using the pulse sequence in Figure 1.12 (d). For ^1H , a MAS rotation rate of 30 kHz, was used, and the pulses were identical to those used in the 1D MAS spectra. For ^{29}Si , a MAS rotation rate of 20 kHz was used, the $\pi/2$ excitation pulse was the same as in the case of the 1D MAS spectrum, and 50 μs tanh/tan SHAP pulses were used for refocusing with a RF field strength of 83 kHz.

Heteronuclear correlation (HETCOR) spectroscopy between ^1H and ^{13}C was achieved by using the TEDOR spectrum given in Figure 1.12 (a). The MAS rotation rate was 30 kHz and the ^1H and ^{13}C used RF field strengths of 250 kHz and 111 kHz, respectively.

A.4 Structural studies of paramagnetic $\text{Fe}^{(0)}$ -based homogeneous catalysts (Chapter 5)

All NMR spectra included in this chapter were acquired on a Bruker Avance III spectrometer operating at an external magnetic field strength of 11.7 T (corresponding to Larmor frequencies

of 500.159 MHz and 125.7 MHz for ^1H and ^{13}C , respectively) either using a Bruker HX 2.5 mm wide-bore MAS probe or a Bruker HXY 0.7 mm wide-bore probe. The powder samples were packed in standard 0.7 mm or 2.5 mm ZnO_2 rotors in an argon-filled glovebox and then placed in a sealed in an air-tight container before removal from the glovebox in order to protect the sample from oxygen. Immediately before measurement, the container was opened and the rotor was quickly inserted into the MAS probe and simultaneously spun to the desired MAS rate while the stator was cooled to a sample temperature of approximately 290-300 K using a Bruker BCU XTreme cooling unit. Nitrogen gas dried to a dew point of $-80\text{ }^\circ\text{C}$ was used for sample rotation. Specific details for each complex are given below.

A.4.1 Complex 1

The 1D ^1H NMR spectrum of **1** was acquired with a MAS rate of 31.25 kHz and utilized the double adiabatic echo experiment in Figure 1.10 (c), using a $\pi/2$ excitation pulse with length $1.23\ \mu\text{s}$ (corresponding to an RF field strength of 203 kHz) and SHAPs with a tanh/tan shape and length $32\ \mu\text{s}$, sweeping through 5 MHz using a maximum RF field amplitude of 203 kHz. 4096 scans were acquired using a recycle delay of 10 ms, resulting in a total experiment time of 61 seconds.

The 1D ^{13}C NMR spectrum of **1** was acquired with a MAS rate of 31.25 kHz and utilized the double adiabatic echo experiment, using a $\pi/2$ excitation pulse with length $2.1\ \mu\text{s}$ (corresponding to an RF field strength of 119 kHz) and SHAPs with a tanh/tan shape and length $32\ \mu\text{s}$, sweeping through 5 MHz using a maximum RF field amplitude of 119 kHz. 524288 scans were acquired using a recycle delay of 30 ms, resulting in a total experiment time of 4.8 h.

The 2D TEDOR spectra of **1** were acquired with MAS rates of 25 kHz and 31.25 kHz (with only the 31.25 kHz spectrum shown in the text) and utilized the pulse sequence given in Figure 1.12 (a) without dipolar dephasing pulses. ^1H $\pi/2$ pulses were $2.3\ \mu\text{s}$ in length (108 kHz), while ^{13}C pulses were identical to those given above. 32768 scans were acquired for each of the 64 hypercomplex t_1 steps using a dwell time of $16\ \mu\text{s}$, resulting in a total ^1H evolution time of $512\ \mu\text{s}$. A recycle delay of 3 ms was utilized, resulting in a total experiment time of 2.6 h.

A.4.2 Complex 2

The first 1D ^1H NMR spectrum of **2** was acquired with a MAS rate of 31.25 kHz and utilized the double adiabatic echo experiment, using a $\pi/2$ excitation pulse with length $1.225\ \mu\text{s}$ (corresponding to an RF field strength of 204 kHz) and SHAPs with a tanh/tan shape and length $32\ \mu\text{s}$, sweeping through 5 MHz using a maximum RF field amplitude of 204 kHz. 256 scans were acquired using a recycle delay of 5 ms, resulting in a total experiment time of 2 s.

The 1D ^{13}C NMR spectrum of **2** was acquired with a MAS rate of 31.25 kHz and utilized the double adiabatic echo experiment, using a $\pi/2$ excitation pulse with length $2.05\ \mu\text{s}$ (corresponding to an RF field strength of 122 kHz) and SHAPs with a tanh/tan shape and length 32

μs , sweeping through 5 MHz using a maximum RF field amplitude of 122 kHz. 1,064,960 scans were acquired using a recycle delay of 20 ms, resulting in a total experiment time of 4.8 h.

The 2D ¹³C-detected TEDOR spectrum of **2** was acquired with MAS rates of 31.25 kHz. ¹H $\pi/2$ and ¹³C pulses were identical to those given above. 2048 scans were acquired for each of the 20 hypercomplex t_1 steps using a dwell time of 32 μs , resulting in a total ¹H evolution time of 320 μs . A recycle delay of 5 ms was utilized, resulting in a total experiment time of 5.5 m.

The variable ¹H MAS spectra acquired with rotation rates of 30, 60, and 100 kHz were acquired using the 0.7 mm probe. $\pi/2$ pulses of length 0.85 μs (294 kHz RF field) were used, while SHAPs of length 66.66 μs , 33.33 μs , and 20 μs were used for refocusing for each of the three MAS rates respectively, with sweep widths of 10 MHz and maximum RF fields of 294 kHz in each case. 1024 scans were acquired for all spectra using a recycle delay of 2 ms, resulting in a total experiment time of 4.6 s.

The 2D SQ-DQ BABA spectrum of **2** was acquired at 100 kHz MAS using the pulse sequence in Figure 1.12 (c) with identical pulse parameters as in the 1D spectra, with a recoupling period equal to τ_R . 1024 scans were acquired for each of the 200 hypercomplex t_1 steps using a dwell time of 10 μs , with a recycle delay of 2ms, resulting in a total experiment time of 15.4 m.

The 2D ¹H-detected TEDOR spectrum of **2** was acquired using 100 kHz MAS and the pulse sequence given in Figure 1.12 (b). The ¹H pulse parameters were identical to those before, while the ¹³C $\pi/2$ pulses had a length 0.95 μs (263 kHz RF field). 2560 scans were acquired for each of the 200 hypercomplex t_1 steps using a dwell time of 10 μs , with a recycle delay of 2ms, resulting in a total experiment time of 34.1 m.

A.4.3 Complex 3

The 1D ¹H NMR spectrum of **3** was acquired with a MAS rate of 31.25 kHz and utilized the double adiabatic echo experiment, using a $\pi/2$ excitation pulse with length 1.23 μs (corresponding to an RF field strength of 203 kHz) and SHAPs with a tanh/tan shape and length 32 μs , sweeping through 5 MHz using a maximum RF field amplitude of 203 kHz. 256 scans were acquired using a recycle delay of 50 ms, resulting in a total experiment time of 13.6 s.

The 1D ¹³C NMR spectrum of **3** was acquired with a MAS rate of 31.25 kHz and utilized the double adiabatic echo experiment, using a $\pi/2$ excitation pulse with length 2.05 μs (corresponding to an RF field strength of 122 kHz) and SHAPs with a tanh/tan shape and length 32 μs , sweeping through 5 MHz using a maximum RF field amplitude of 122 kHz. 614,400 scans were acquired using a recycle delay of 20 ms, resulting in a total experiment time of 3.9 h.

The 2D TEDOR spectrum of **3** was acquired with MAS rates of 31.25 kHz. ¹H $\pi/2$ and ¹³C pulses were identical to those given above. 98304 scans were acquired for each of the 50 hypercomplex t_1 steps using a dwell time of 32 μs , resulting in a total ¹H evolution time of 800 μs . A recycle delay of 3 ms was utilized, resulting in a total experiment time of 8.2 h.

A.4.4 Complex 4

The natural abundance solid-state ^{13}C NMR spectrum of complex **4** utilized a $\pi/2$ excitation pulse with length $2.1 \mu\text{s}$ (corresponding to an RF field strength of 119 kHz) at an offset of 270 ppm. Due to the broad span of ^{13}C resonances we employed short, high-powered adiabatic tanh/tan pulses (SHAPs) [5] in the double adiabatic echo sequence (Figure 1.10 (c)) to refocus the chemical shift evolution [8]. The SHAPs were $32 \mu\text{s}$ in length and swept through 5 MHz with an RF field strength of 119 kHz. No ^1H decoupling was used during acquisition. Using a recovery time of 30 ms, 2 M scans were acquired, resulting in a total experiment time of 19.2 h.

Appendix B

Computational details

B.1 DFT calculations of complex 4

Complex **4** and the NMR reference compound tetramethylsilane (TMS) were fully optimized with DFT, employing the hybrid PBE0 functional [225, 226], Grimme's D3 dispersion correction with Becke-Johnson damping [227] and a locally dense Gaussian basis set using def2-TZVP for Fe and def2-SVP for main-group elements [228] as implemented in the Turbomole code [229]. All calculations for the Fe⁽⁰⁾ complex **4** were done in vacuo for a triplet ground state. The initial model for the structure of **4** was built from the coordinates of the framework atoms of the closely related complex **1** obtained crystallographically, substituting the Ph groups of the dppe ligand of **1** with ⁱPr moieties. A frequency calculation confirmed that the optimized structure is a true minimum, finding that all eigenvalues of the mass-weighted Hessian are positive.

The total PNMR *shielding* tensor is a sum of hyperfine and orbital *shielding* terms. The hyperfine shielding calculations were performed with two approaches, allowing us to assess the importance of spin-orbit coupling. The results according to the recent formulation of Kurland-McGarvey PNMR theory [27] in terms of EPR property tensors by Vaara et al. [26] were compared to the "doublet-like" approximation neglecting all SOC effects. The temperature 300 K was used in all PNMR calculations.

The EPR g tensor, zero-field-splitting (ZFS, D) tensor, and hyperfine coupling tensors were calculated in Orca [230] using the PBE0 functional. For both g and D tensors the spin-orbit mean-field approximation [231, 232] was applied to the spin-orbit matrix elements in the Breit-Pauli form. The basis used in the DFT structure optimizations was enhanced with diffuse functions optimized for molecular property calculations [233], thus employing def2-TZVPD and def2-SVPD bases for Fe and main-group elements, respectively. van Wüllen's prefactors for ZFS contributions from different spin channels were utilized [234]. Fermi contact and spin dipolar terms of HFC were calculated using def2-TZVPD and IGLO-III basis sets for Fe and main-group elements, respectively.

The ¹³C orbital shielding tensors of TMS and complex **4** were calculated with gauge-including atomic orbitals [235] using the Gaussian package [236]. The PBE0 functional and the HFC basis defined above were employed. The calculated ¹³C isotropic reference shielding, σ^{ref} , was 185.7 ppm, and the resulting ¹³C isotropic shift δ_K was obtained from the total isotropic PNMR shielding σ_K as

$$\delta_{\mathbf{K}} = \sigma^{\text{ref}} - \sigma_{\mathbf{K}} \quad (\text{B.1})$$

B.2 Calculations of complexes 1–3

Geometry optimizations, hyperfine coupling and orbital shielding calculations of complexes **1–3** were performed with the same methodology described above for complex **4**.

The EPR **g** and **D** tensors were calculated on a correlated multi-reference *ab initio* level with Orca program. The reference wave function was obtained on the state-averaged complete active space self consistent field (SA-CASSCF) level [237, 238], using the active space of eight electrons in five 3d orbitals of Fe⁽⁰⁾. All 10 quartet and 40 doublet roots of CAS(8,5) were involved in the state averaging, all equally weighted. The dynamical electron correlation was treated via the strongly contracted variant of the *N*-electron valence-state perturbation theory of second order (NEVPT2) [239, 240]. The spin-orbit part of the ZFS tensor **D**_{SO} was calculated using quasi-degenerate perturbation theory [241], while the spin-spin part **D**_{SS} was neglected. The **g** tensor was calculated using the effective Hamiltonian approach [242]. The atomic basis employed was the same as in the DFT calculations of the **g** and **D** tensors of complex **4**. The calculated reference ¹H shielding in TMS was 31.59 ppm. The calculated shifts of groups undergoing motion on a timescale much faster than that of NMR experiments (methyls and phenyls) were appropriately averaged.

Appendix C

Synthesis details for complexes 1-4

Unless stated otherwise, all reactions were carried out under an atmosphere of argon using standard Schlenk techniques. All reagents were purchased from commercial suppliers and used without further purification. All yields refer to isolated products. Anhydrous common solvents were purified by a solvent purification system (SPS-M-Braun). NMR spectra were recorded on a Bruker AV 300 MHz instrument. Deuterated solvents were purchased from Sigma-Aldrich or Eurisotop. GC-MS analyses were carried out with an Agilent 6890 N apparatus equipped with a PONA or HP-MS column and an Agilent 5975B inert XL EI/CI MSD mass spectrometer. FT-IR spectra were recorded in the solid state by an ATR Golden Gate (Specac) on a PerkinElmer spectrum one spectrometer. Elemental analyses were determined at London Metropolitan University. Abbreviations used in this section are as follows: dvtms, divinyltetramethyldisiloxane; dipe, 1,2-bis-(diisopropylphosphino)ethane; dppe, 1,2-bis(diphenylphosphino)-ethane; dppp, 1,2-bis(diphenylphosphino)propane; pyNMeP(iPr)₂, N-(diisopropylphosphino)-N-methylpyridin-2-amine.

[Fe(pyNMeP(iPr)₂)(dvtms)] (1) N-(Diisopropylphosphino)-N-methylpyridin-2-amine (0.97 g, 1.95 mmol, 1.05 equiv), [Fe(acac)₃] (0.66 g, 1.86 mmol, 1.00 equiv), and dvtms (1.09 g, 5.84 mmol, 3.14 equiv) were suspended in diethyl ether (30 mL). Diethylaluminum ethoxide (2.00 mL, 13.0 mmol, 7.00 equiv) was added dropwise, and the reaction mixture was stirred overnight. The solution was filtered with a filter cannula, and the solvent was evaporated under reduced pressure. Pentane was added, the solid that formed was washed twice with pentane and then dissolved in the minimum amount of diethyl ether, and the solution was filtered and placed at -20 °C overnight, giving a first crop of brown crystals (0.39 g). A second crop was obtained after cooling the diethyl ether filtrate to -20 °C overnight. By combination of the two crops a total of 0.44 g (48%) of product was isolated. X-ray-quality crystals were obtained by cooling a pentane/toluene solution of the title complex to -34 °C. Anal. Found (calcd) for C₂₀H₃₉FeN₂OPSi₂: C, 51.36 (51.49); H, 8.55 (8.43); N, 5.95 (6.00). Selected IR data (cm⁻¹): 3037 (m), 2952 (m), 2923 (m), 2876 (m), 1598 (s), 1565 (m), 1473 (s), 1330 (m), 1299 (s), 1242 (s), 1188 (s), 967 (vs), 858 (vs), 825 (vs), 776 (vs), 569 (s), 472 (vs).

[Fe(dppe)(dvtms)] (2) 1,2-Bis(diphenylphosphino)ethane (0.60 g, 1.51 mmol, 1.03 equiv), [Fe(acac)₃] (0.50 g, 1.46 mmol, 1.00 equiv), and dvtms (0.79 g, 4.25 mmol, 2.90 equiv) were suspended in diethyl ether (40 mL). Diethylaluminum ethoxide (1.50 mL, 10.0 mmol, 6.85 equiv) was added dropwise. After it was stirred for 30 min, the solution became dark green.

The reaction mixture was further stirred for 5 h. Diethyl ether was evaporated under reduced pressure, leaving a green oil which was triturated with pentane to form a green solid that was washed three times with pentane (3×5 mL). The solid was dried under reduced pressure, affording 0.77 g (81%) of a green solid. X-ray-quality crystals were obtained by cooling a saturated toluene solution of the title complex to -20 °C. Anal. Found (calcd) for $C_{34}H_{42}FeOP_2Si_2$: C, 58.12 (63.74); H, 6.17 (6.61). Inconsistencies observed in the elemental analysis might be due to partial sample decomposition during workup.

[Fe(dppp)(dvtms)] (3) 1,2-Bis(diphenylphosphino)propane (1.30 g, 3.15 mmol, 1.07 equiv), $[Fe(acac)_3]$ (1.04 g, 2.94 mmol, 1.00 equiv), and dvtms (1.17 g, 6.28 mmol, 2.14 equiv) were suspended in diethyl ether (30 mL). Diethylaluminum ethoxide (3.10 mL, 20.7 mmol, 7.04 equiv) was added dropwise. The reaction mixture was stirred overnight. Diethyl ether was evaporated under reduced pressure, leaving a dark green oil which was dissolved in pentane (10 mL), and the solution was cooled to -80 °C for 2 h. The solid that formed was isolated by decantation and dried under reduced pressure at -80 °C, affording 1.15 g of a green powder. A second crop was obtained after cooling the pentane filtrate to -20 °C overnight. Combined crops yielded 1.37 g (71%) of product. X-ray-quality crystals were obtained by cooling to room temperature a filtered saturated diethyl ether solution of the title product. Selected IR data (cm^{-1}): 3057 (w), 3016 (w), 2950 (w), 2905 (w), 2859 (w), 1481 (m), 1431 (s), 1290 (s), 1242 (s), 1180 (m), 964 (s), 820 (s), 771 (s), 739 (vs), 693 (vs), 499 (vs). Elemental analyses (C, H) of this compound were attempted four times on four different crystalline samples. The closest agreement between experimental and theoretical values was as follows. Anal. Found (calcd) for $C_{35}H_{44}FeOP_2Si_2$: C, 62.31 (64.21); H, 6.86 (6.77).

[Fe(dipe)(dvtms)] (4) 1,2-Bis(diisopropylphosphino)ethane (0.82 g, 2.97 mmol, 1.05 equiv), $[Fe(acac)_3]$ (1.00 g, 2.82 mmol, 1.00 equiv), and dvtms (1.58 g, 8.49 mmol, 3.01 equiv) were suspended in diethyl ether (30 mL). Diethylaluminum ethoxide (3.00 mL, 20.0 mmol, 7.09 equiv) was added dropwise, and the reaction mixture was stirred overnight. Diethyl ether was evaporated under reduced pressure, leaving a blue oil which was triturated with pentane to form a blue solid that was washed twice (2×5 mL) with pentane and dried under vacuum, affording 0.80 g of product. The combined blue extracts were cooled to -20 °C, and the solid that formed was isolated and dissolved in the minimum amount of ether. The solution was cooled to -20 °C, giving 0.35 g of blue crystals. A total of 1.15 g (81%) of product was isolated. Anal. Found (calcd) for $C_{22}H_{50}FeOP_2Si_2$: C, 52.14 (52.37); H, 9.93 (9.99). Selected IR data (cm^{-1}): 2953 (s), 2894 (m), 2870 (m), 1601 (w), 1532 (w), 1458 (m), 1287 (s), 1238 (s), 1186 (s), 964 (s), 859 (s), 824 (vs), 769 (vs), 718 (s), 707 (s), 686 (s), 667 (s), 642 (s), 621 (s), 600 (s), 578 (s).

Bibliography

- (1) Ishii, Y.; Wickramasinghe, N. P.; Chimon, S. A New Approach in 1D and 2D ^{13}C High-Resolution Solid-State NMR Spectroscopy of Paramagnetic Organometallic Complexes by Very Fast Magic-Angle Spinning. *J. Amer. Chem. Soc.* **2003**, *125*, 3438–3439.
- (2) Wickramasinghe, N. P.; Shaibat, M.; Ishii, Y. Enhanced Sensitivity and Resolution in ^1H Solid-State NMR Spectroscopy of Paramagnetic Complexes under Very Fast Magic Angle Spinning. *J. Amer. Chem. Soc.* **2005**, *127*, 5796–5797.
- (3) Kervern, G.; Pintacuda, G.; Zhang, Y.; Oldfield, E.; Roukoss, C.; Kuntz, E.; Herdtweck, E.; Basset, J.-M.; Cadars, S.; Lesage, A.; Copéret, C.; Emsley, L. Solid-State NMR of a Paramagnetic DIAD- Fe^{II} Catalyst: Sensitivity, Resolution Enhancement, and Structure-Based Assignments. *J. Amer. Chem. Soc.* **2006**, *128*, 13545–13552.
- (4) Knight, M. J.; Felli, I. C.; Pierattelli, R.; Emsley, L.; Pintacuda, G. Magic Angle Spinning NMR of Paramagnetic Proteins. *Accounts Chem. Res.* **2013**, *46*, 2108–2116.
- (5) Kervern, G.; Pintacuda, G.; Emsley, L. Fast adiabatic pulses for solid-state NMR of paramagnetic systems. *Chem. Phys. Lett.* **2007**, *435*, 157–162.
- (6) Pell, A. J.; Kervern, G.; Emsley, L.; Deschamps, M.; Massiot, D.; Grandinetti, P. J.; Pintacuda, G. Broadband inversion for MAS NMR with single-sideband-selective adiabatic pulses. *J. Chem. Phys.* **2011**, *134* 024117.
- (7) Pell, A. J.; Pintacuda, G.; Emsley, L. Single crystal nuclear magnetic resonance in spinning powders. *J. Chem. Phys.* **2011**, *135*, 144201.
- (8) Kervern, G.; D'Aléo, A.; Toupet, L.; Maury, O.; Emsley, L.; Pintacuda, G. Crystal-Structure Determination of Powdered Paramagnetic Lanthanide Complexes by Proton NMR Spectroscopy. *Angew. Chem. Int. Edit.* **2009**, *48*, 3082–3086.
- (9) Clément, R. J.; Pell, A. J.; Middlemiss, D. S.; Strobridge, F. C.; Miller, J. K.; Whittingham, M. S.; Emsley, L.; Grey, C. P.; Pintacuda, G. Spin-Transfer Pathways in Paramagnetic Lithium Transition-Metal Phosphates from Combined Broadband Isotropic Solid-State MAS NMR Spectroscopy and DFT Calculations. *J. Amer. Chem. Soc.* **2012**, *134*, 17178–17185.
- (10) George, N. C.; Pell, A. J.; Dantelle, G.; Page, K.; Llobet, A.; Balasubramanian, M.; Pintacuda, G.; Chmelka, B. F.; Seshadri, R. Local Environments of Dilute Activator Ions in the Solid-State Lighting Phosphor $\text{Y}_{3-x}\text{Ce}_x\text{Al}_5\text{O}_{12}$. *Chem. Mater.* **2013**, *25*, 3979–3995.

- (11) Estephane, J.; Groppo, E.; Vitillo, J. G.; Damin, A.; Gianolio, D.; Lamberti, C.; Bordiga, S.; Quadrelli, E. A.; Basset, J. M.; Kervern, G.; Emsley, L.; Pintacuda, G.; Zecchina, A. A Multitechnique Approach to Spin-Flips for $\text{Cp}_2\text{Cr(II)}$ Chemistry in Confined State. *J. Phys. Chem. C* **2010**, *114*, 4451–4458.
- (12) Strobridge, F. C.; Middlemiss, D. S.; Pell, A. J.; Leskes, M.; Clement, R. J.; Pourpoint, F.; Lu, Z.; Hanna, J. V.; Pintacuda, G.; Emsley, L.; Samoson, A.; Grey, C. P. Characterising local environments in high energy density Li-ion battery cathodes: a combined NMR and first principles study of $\text{LiFe}_x\text{Co}_{1-x}\text{PO}_4$. *J. Mater. Chem. A* **2014**, *2*, 11948–11957.
- (13) Pell, A. J.; Pintacuda, G. Broadband solid-state MAS NMR of paramagnetic systems. *Prog. Nucl. Mag. Res. Sp.* **2015**, *84-85*, 33–72.
- (14) Sanders, K. J.; Pell, A. J.; Wegner, S.; Grey, C. P.; Pintacuda, G. Broadband MAS NMR spectroscopy in the low-power limit. *Chem. Phys. Lett.* **2018**, *697*, 29–37.
- (15) Conley, M. P.; Lapadula, G.; Sanders, K.; Gajan, D.; Lesage, A.; del Rosal, I.; Maron, L.; Lukens, W. W.; Copéret, C.; Andersen, R. A. The Nature of Secondary Interactions at Electrophilic Metal Sites of Molecular and Silica-Supported Organolutetium Complexes from Solid-State NMR Spectroscopy. *J. Amer. Chem. Soc.* **2016**, *138*, 3831–3843.
- (16) Bertini, I.; Luchinat, C.; Parigi, G.; Ravera, E., *NMR of Paramagnetic Molecules (Second Edition)*, 2nd; Elsevier: 2017.
- (17) Wickramasinghe, N. P.; Shaibat, M. A.; Jones, C. R.; Casabianca, L. B.; de Dios, A. C.; Harwood, J. S.; Ishii, Y. Progress in ^{13}C and ^1H solid-state nuclear magnetic resonance for paramagnetic systems under very fast magic angle spinning. *J. Chem. Phys.* **2008**, *128*, 052210.
- (18) Burcher, B.; Sanders, K. J.; Benda, L.; Pintacuda, G.; Jeanneau, E.; Danopoulos, A. A.; Braunstein, P.; Olivier-Bourbigou, H.; Breuil, P.-A. R. Straightforward Access to Stable, 16-Valence-Electron Phosphine-Stabilized Fe^0 Olefin Complexes and Their Reactivity. *Organometallics* **2017**, *36*, 605–613.
- (19) Rouf, S. A.; Jakobsen, V. B.; Mareš, J.; Jensen, N. D.; McKenzie, C. J.; Vaara, J.; Nielsen, U. G. Assignment of solid-state ^{13}C and ^1H NMR spectra of paramagnetic Ni(II) acetylacetonate complexes aided by first-principles computations. *Solid State Nucl. Mag.* **2017**, *87*, 29–37.
- (20) Andrew, E. R.; Bradbury, A.; Eades, R. G. Nuclear Magnetic Resonance Spectra from a Crystal rotated at High Speed. *Nature* **1958**, *182*, 1659–1659.
- (21) Lowe, I. J. Free Induction Decays of Rotating Solids. *Phys. Rev. Lett.* **1959**, *2*, 285–287.
- (22) Pigliapochi, R.; Seymour, I. D.; Merlet, C.; Pell, A. J.; Murphy, D. T.; Schmid, S.; Grey, C. P. Structural Characterization of the Li-Ion Battery Cathode Materials $\text{LiTi}_x\text{Mn}_{2-x}\text{O}_4$ ($0.2 \leq x \leq 1.5$): A Combined Experimental ^7Li NMR and First-Principles Study. *Chem. Mater.* **2018**, *30*, 817–829.
- (23) Ramsey, N. F. Magnetic Shielding of Nuclei in Molecules. *Phys. Rev.* **1950**, *78*, 699–703.

- (24) Mehring, M., *Principles of High Resolution NMR in Solids*, 2nd; Springer-Verlag: 1983.
- (25) Pell, A. J.; Pintacuda, G.; Grey, C. P. Paramagnetic NMR in solution and the solid state. *Prog. Nucl. Mag. Res. Sp.* **2018**.
- (26) Vaara, J.; Rouf, S. A.; Mareš, J. Magnetic Couplings in the Chemical Shift of Paramagnetic NMR. *J. Chem. Theory Comput.* **2015**, *11*, PMID: 26574272, 4840–4849.
- (27) Kurland, R. J.; McGarvey, B. R. Isotropic NMR shifts in transition metal complexes: The calculation of the fermi contact and pseudocontact terms. *J. Magn. Reson.* **1970**, *2*, 286–301.
- (28) Bloembergen, N.; Purcell, E. M.; Pound, R. V. Relaxation Effects in Nuclear Magnetic Resonance Absorption. *Phys. Rev.* **1948**, *73*, 679–712.
- (29) Alla, M.; Lippmaa, E. Resolution limits in magic-angle rotation NMR spectra of polycrystalline solids. *Chem. Phys. Lett.* **1982**, *87*, 30–33.
- (30) Schwerk, U.; Michel, D.; Pruski, M. Local Magnetic Field Distribution in a Polycrystalline Sample Exposed to a Strong Magnetic Field. *J. Magn. Reson., Ser. A* **1996**, *119*, 157–164.
- (31) Kubo, A.; Spaniol, T. P.; Terao, T. The Effect of Bulk Magnetic Susceptibility on Solid State NMR Spectra of Paramagnetic Compounds. *J. Magn. Reson.* **1998**, *133*, 330–340.
- (32) Kervern, G. High-resolution solid-state NMR of paramagnetic molecules., Ph.D. Thesis, École Normale Supérieure de Lyon, Oct. 2008.
- (33) Bloembergen, N.; Dickinson, W. C. On the Shift of the Nuclear Magnetic Resonance in Paramagnetic Solutions. *Phys. Rev.* **1950**, *79*, 179–180.
- (34) McConnell, H. M.; Chesnut, D. B. Theory of Isotropic Hyperfine Interactions in π -Electron Radicals. *J. Chem. Phys.* **1958**, *28*, 107–117.
- (35) McConnell, H. M.; Robertson, R. E. Isotropic Nuclear Resonance Shifts. *J. Chem. Phys.* **1958**, *29*, 1361–1365.
- (36) La Mar, G. N.; Horrocks, W. D.; Holm, R. H., *NMR of Paramagnetic Molecules*, First Edition; La Mar, G. N., Horrocks, W. D., Holm, R. H., Eds.; Elsevier: Boston, 1973.
- (37) Bertini, I.; Turano, P.; Vila, A. J. Nuclear magnetic resonance of paramagnetic metalloproteins. *Chem. Rev.* **1993**, *93*, 2833–2932.
- (38) Maricq, M.; Waugh, J. S. NMR in rotating solids. *J. Chem. Phys.* **1979**, *70*, 3300–3316.
- (39) Levitt, M. H. Why do spinning sidebands have the same phase? *J. Magn. Reson. (1969)* **1989**, *82*, 427–433.
- (40) Kervern, G.; Steuernagel, S.; Engelke, F.; Pintacuda, G.; Emsley, L. Absence of Curie Relaxation in Paramagnetic Solids Yields Long ^1H Coherence Lifetimes. *J. Amer. Chem. Soc.* **2007**, *129*, 14118–14119.

- (41) Chacko, V. P.; Ganapathy, S.; Bryant, R. G. Carbon-13 CP-MAS NMR spectra of paramagnetic solids. *J. Amer. Chem. Soc.* **1983**, *105*, 5491–5492.
- (42) Cheetham, A. K.; Dobson, C. M.; Grey, C. P.; Jakeman, R. J. B. Paramagnetic shift probes in high-resolution solid-state NMR. *Nature* **1987**, *328*, 706–707.
- (43) Grey, C. P.; Dobson, C. M.; Cheetham, A. K.; Jakeman, R. J. B. Studies of Rare-Earth Stannates by ^{119}Sn MAS NMR. The Use of Paramagnetic Shift Probes in the Solid State. *J. Amer. Chem. Soc.* **1989**, *111*, 505–511.
- (44) Grey, C. P.; Smith, M. E.; Cheetham, A. K.; Dobson, C. M.; Dupree, R. ^{89}Yb MAS NMR Study of Rare-Earth Pyrochlores: Paramagnetic Shifts in the Solid State. *J. Amer. Chem. Soc.* **1990**, *112*, 4670–4675.
- (45) Pines, A.; Gibby, M. G.; Waugh, J. S. Proton-enhanced NMR of dilute spins in solids. *J. Chem. Phys.* **1973**, *59*, 569–590.
- (46) Hodgkinson, P. Heteronuclear decoupling in the NMR of solids. *Prog. Nucl. Mag. Res. Sp.* **2005**, *46*, 197–222.
- (47) Hahn, E. L. Spin Echoes. *Phys. Rev.* **1950**, *80*, 580–594.
- (48) Hing, A. W.; Vega, S.; Schaefer, J. Transferred-echo double-resonance NMR. *J. Magn. Reson. (1969)* **1992**, *96*, 205–209.
- (49) Ernst, R. R.; Bodenhausen, G.; Wokaun, A., *Principles of Nuclear Magnetic Resonance in One and Two Dimensions*; Oxford: 1987.
- (50) Levitt, M. H. Symmetrical composite pulse sequences for NMR population inversion. II. Compensation of resonance offset. *J. Magn. Reson.* **1982**, *50*, 95–110.
- (51) Baum, J.; Tycko, R.; Pines, A. Broadband and adiabatic inversion of a two-level system by phase-modulated pulses. *Phys. Rev. A* **1985**, *32*, 3435–3447.
- (52) Hwang, T.-L.; van Zijl, P. C.; Garwood, M. Fast Broadband Inversion by Adiabatic Pulses. *J. Magn. Reson.* **1998**, *133*, 200–203.
- (53) Kupce, E.; Freeman, R. Adiabatic Pulses for Wideband Inversion and Broadband Decoupling. *J. Magn. Reson. A* **1995**, *115*, 273–276.
- (54) Deschamps, M.; Kervern, G.; Massiot, D.; Pintacuda, G.; Emsley, L.; Grandinetti, P. J. Superadiabaticity in magnetic resonance. *J. Chem. Phys.* **2008**, *129*, 204110.
- (55) Garwood, M.; DelaBarre, L. The Return of the Frequency Sweep: Designing Adiabatic Pulses for Contemporary NMR. *J. Magn. Reson.* **2001**, *153*, 155–177.
- (56) Pell, A. J.; Sanders, K. J.; Wegner, S.; Pintacuda, G.; Grey, C. P. Low-power broadband solid-state MAS NMR of ^{14}N . *J. Chem. Phys.* **2017**, *146*, 194202.
- (57) Caravatti, P.; Bodenhausen, G.; Ernst, R. Selective pulse experiments in high-resolution solid state NMR. *J. Magn. Reson. (1969)* **1983**, *55*, 88–103.

- (58) Haeberlen, U.; Waugh, J. S. Coherent Averaging Effects in Magnetic Resonance. *Phys. Rev.* **1968**, *175*, 453–467.
- (59) Maricq, M. M. Application of average Hamiltonian theory to the NMR of solids. *Phys. Rev. B* **1982**, *25*, 6622–6632.
- (60) Goldman, M.; Grandinetti, P. J.; Llor, A.; Olejniczak, Z.; Sachleben, J. R.; Zwanziger, J. W. Theoretical aspects of higher-order truncations in solid-state nuclear magnetic resonance. *J. Chem. Phys.* **1992**, *97*, 8947–8960.
- (61) Leskes, M.; Madhu, P.; Vega, S. Floquet theory in solid-state nuclear magnetic resonance. *Prog. Nucl. Mag. Res. Sp.* **2010**, *57*, 345–380.
- (62) Feike, M.; Demco, D.; Graf, R.; Gottwald, J.; Hafner, S.; Spiess, H. Broadband Multiple-Quantum NMR Spectroscopy. *J. Magn. Reson. Ser. A* **1996**, *122*, 214–221.
- (63) Hu, J.; Alderman, D.; Ye, C.; Pugmire, R.; Grant, D. An Isotropic Chemical Shift-Chemical Shift Anisotropy Magic-Angle Slow-Spinning 2D NMR Experiment. *J. Magn. Reson., Ser. A* **1993**, *105*, 82–87.
- (64) Wickramasinghe, N. P.; Ishii, Y. Sensitivity enhancement, assignment, and distance measurement in ^{13}C solid-state NMR spectroscopy for paramagnetic systems under fast magic angle spinning. *J. Magn. Reson.* **2006**, *181*, 233–243.
- (65) Kumara Swamy, S. K.; Karczmarzka, A.; Makowska-Janusik, M.; Kassiba, A.; Dittmer, J. Solid-State NMR Correlation Experiments and Distance Measurements in Paramagnetic Metalorganics Exemplified by Cu-Cyclam. *ChemPhysChem* **2013**, *14*, 1864–1870.
- (66) Bennett, A. E.; Griffin, R. G.; Ok, J. H.; Vega, S. Chemical shift correlation spectroscopy in rotating solids: Radio frequency-driven dipolar recoupling and longitudinal exchange. *J. Chem. Phys.* **1992**, *96*, 8624–8627.
- (67) Dixon, W. T. Spinning-sideband-free and spinning-sideband-only NMR spectra in spinning samples. *J. Chem. Phys.* **1982**, *77*, 1800–1809.
- (68) Nadaud, P. S.; Helmus, J. J.; Höfer, N.; Jaroniec, C. P. Long-Range Structural Restraints in Spin-Labeled Proteins Probed by Solid-State Nuclear Magnetic Resonance Spectroscopy. *J. Amer. Chem. Soc.* **2007**, *129*, 7502–7503.
- (69) Nadaud, P. S.; Helmus, J. J.; Kall, S. L.; Jaroniec, C. P. Paramagnetic Ions Enable Tuning of Nuclear Relaxation Rates and Provide Long-Range Structural Restraints in Solid-State NMR of Proteins. *J. Amer. Chem. Soc.* **2009**, *131*, 8108–8120.
- (70) Bertini, I.; Emsley, L.; Lelli, M.; Luchinat, C.; Mao, J.; Pintacuda, G. Ultrafast MAS Solid-State NMR Permits Extensive ^{13}C and ^1H Detection in Paramagnetic Metalloproteins. *J. Amer. Chem. Soc.* **2010**, *132*, 5558–5559.
- (71) Jaroniec, C. P. Solid-state nuclear magnetic resonance structural studies of proteins using paramagnetic probes. *Solid State Nucl. Mag.* **2012**, *43-44*, 1–13.

- (72) Sengupta, I.; Nadaud, P. S.; Helmus, J. J.; Schwieters, C. D.; Jaroniec, C. P. Protein fold determined by paramagnetic magic-angle spinning solid-state NMR spectroscopy. *Nat. Chem.* **2012**, *4*, 410.
- (73) Parthasarathy, S.; Nishiyama, Y.; Ishii, Y. Sensitivity and Resolution Enhanced Solid-State NMR for Paramagnetic Systems and Biomolecules under Very Fast Magic Angle Spinning. *Accounts Chem. Res.* **2013**, *46*, 2127–2135.
- (74) Bertarello, A.; Schubeis, T.; Fuccio, C.; Ravera, E.; Fragai, M.; Parigi, G.; Emsley, L.; Pintacuda, G.; Luchinat, C. Paramagnetic Properties of a Crystalline Iron-Sulfur Protein by Magic-Angle Spinning NMR Spectroscopy. *Inorg. Chem.* **2017**, *56*, PMID: 28537393, 6624–6629.
- (75) Knight, M. J.; Pell, A. J.; Bertini, I.; Felli, I. C.; Gonnelli, L.; Pierattelli, R.; Herrmann, T.; Emsley, L.; Pintacuda, G. Structure and backbone dynamics of a microcrystalline metalloprotein by solid-state NMR. *P. Natl. Acad. Sci. USA* **2012**, *109*, 11095–11100.
- (76) Knight, M. J.; Felli, I. C.; Pierattelli, R.; Bertini, I.; Emsley, L.; Herrmann, T.; Pintacuda, G. Rapid Measurement of Pseudocontact Shifts in Metalloproteins by Proton-Detected Solid-State NMR Spectroscopy. *J. Amer. Chem. Soc.* **2012**, *134*, 14730–14733.
- (77) Bertarello, A.; Benda, L.; Sanders, K. J.; Pell, A. J.; Pelmeshnikov, V.; Felli, I. C.; Kaupp, M.; Emsley, L.; Pieratelli, R.; Pintacuda, G. Paramagnetic NMR crystallography: theory and experiment meet at the catalytic center of a metalloprotein. *Manuscript in preparation*.
- (78) Wickramasinghe, N. P.; Shaibat, M. A.; Ishii, Y. Elucidating Connectivity and Metal-Binding Structures of Unlabeled Paramagnetic Complexes by ^{13}C and ^1H Solid-State NMR under Fast Magic Angle Spinning. *J. Phys. Chem. B* **2007**, *111*, 9693–9696.
- (79) Gul-E-Noor, F.; Jee, B.; Poppl, A.; Hartmann, M.; Himsl, D.; Bertmer, M. Effects of varying water adsorption on a $\text{Cu}_3(\text{BTC})_2$ metal-organic framework (MOF) as studied by ^1H and ^{13}C solid-state NMR spectroscopy. *Phys. Chem. Chem. Phys.* **2011**, *13*, 7783–7788.
- (80) Flambard, A.; Köhler, F. H.; Lescouëzec, R.; Revel, B. Probing Spin Density and Local Structure in the Prussian Blue Analogues $\text{CsCd}[\text{Fe}/\text{Co}(\text{CN})_6] \cdot 0.5 \text{H}_2\text{O}$ and $\text{Cd}_3[\text{Fe}/\text{Co}(\text{CN})_6]_2 \cdot 15 \text{H}_2\text{O}$ with Solid-State MAS NMR Spectroscopy. *Chem. - Eur. J.* **2011**, *17*, 11567–11575.
- (81) Szalontai, G.; Sabolović, J.; Marković, M.; Szabolcs, B. Solid-State NMR Characterization of Paramagnetic Bis(L-valinato)copper(II) Stereoisomers – Effect of Conformational Disorder and Molecular Mobility on ^{13}C and ^2H Fast Magic-Angle Spinning Spectra. *Eur. J. Inorg. Chem.* **2014**, 3330–3340.
- (82) Deschamps, M. In Webb, G. A., Ed.; Annual Reports on NMR Spectroscopy, Vol. 81; Academic Press: 2014, pp 109–144.

- (83) Toma, O.; Leroux, M.; Mercier, N.; Allain, M.; Kassiba, A. H.; Kumara Swamy, S. K.; Dittmer, J. Bipyridinium-bis(carboxylate) Radical Based Materials: X-ray, EPR and Paramagnetic Solid-State NMR Investigations. *Eur. J. Inorg. Chem.* **2016**, 1036–1043.
- (84) Grey, C. P.; Dupré, N. NMR Studies of Cathode Materials for Lithium-Ion Rechargeable Batteries. *Chem. Rev.* **2004**, *104*, 4493–4512.
- (85) Sideris, P. J.; Nielsen, U. G.; Gan, Z.; Grey, C. P. Mg/Al Ordering in Layered Double Hydroxides Revealed by Multinuclear NMR Spectroscopy. *Science* **2008**, *321*, 113–117.
- (86) Bini, M.; Ferrari, S.; Ferrara, C.; Mozzati, M. C.; Capsoni, D.; Pell, A. J.; Pintacuda, G.; Canton, P.; Mustarelli, P. Polymorphism and magnetic properties of Li_2MSiO_4 (M = Fe, Mn) cathode materials. *Sci. Rep-UK* **2013**, *3*, 3452.
- (87) Xu, J.; Lee, D. H.; Clément, R. J.; Yu, X.; Leskes, M.; Pell, A. J.; Pintacuda, G.; Yang, X.-Q.; Grey, C. P.; Meng, Y. S. Identifying the Critical Role of Li Substitution in $\text{P2-Na}_x[\text{Li}_y\text{Ni}_z\text{Mn}_{1-y-z}]\text{O}_2$ ($0 < x, y, z < 1$) Intercalation Cathode Materials for High-Energy Na-Ion Batteries. *Chem. Mater.* **2014**, *26*, 1260–1269.
- (88) Mondal, A.; Kaupp, M. Quantum-Chemical Approach to NMR Chemical Shifts in Paramagnetic Solids Applied to LiFePO_4 and LiCoPO_4 . *J. Phys. Chem. Lett.* **2018**, *9*, 1480–1484.
- (89) Luchinat, C.; Parigi, G.; Ravera, E.; Rinaldelli, M. Solid-State NMR Crystallography through Paramagnetic Restraints. *J. Amer. Chem. Soc.* **2012**, *134*, 5006–5009.
- (90) Bhaumik, A.; Luchinat, C.; Parigi, G.; Ravera, E.; Rinaldelli, M. NMR crystallography on paramagnetic systems: solved and open issues. *CrystEngComm* **2013**, *15*, 8639–8656.
- (91) Schlagnitweit, J.; Tang, M.; Baias, M.; Richardson, S.; Schantz, S.; Emsley, L. Nanostructure of Materials Determined by Relayed Paramagnetic Relaxation Enhancement. *J. Amer. Chem. Soc.* **2015**, *137*, 12482–12485.
- (92) Shaibat, M. A.; Casabianca, L. B.; Wickramasinghe, N. P.; Guggenheim, S.; de Dios, A. C.; Ishii, Y. Characterization of Polymorphs and Solid-State Reactions for Paramagnetic Systems by ^{13}C Solid-State NMR and ab Initio Calculations. *J. Amer. Chem. Soc.* **2007**, *129*, 10968–10969.
- (93) Zhang, Y.; Oldfield, E. NMR Hyperfine Shifts in Blue Copper Proteins: A Quantum Chemical Investigation. *J. Amer. Chem. Soc.* **2008**, *130*, 3814–3823.
- (94) Kaupp, M.; Köhler, F. H. Combining NMR spectroscopy and quantum chemistry as tools to quantify spin density distributions in molecular magnetic compounds. *Coord. Chem. Rev.* **2009**, *253*, Deutsche Forschungsgemeinschaft Molecular Magnetism Research Report, 2376–2386.
- (95) Middlemiss, D. S.; Ilott, A. J.; Clément, R. J.; Strobridge, F. C.; Grey, C. P. Density Functional Theory-Based Bond Pathway Decompositions of Hyperfine Shifts: Equipping Solid-State NMR to Characterize Atomic Environments in Paramagnetic Materials. *Chem. Mater.* **2013**, *25*, 1723–1734.

- (96) Kong, X.; Terskikh, V. V.; Khade, R. L.; Yang, L.; Rorick, A.; Zhang, Y.; He, P.; Huang, Y.; Wu, G. Solid-State ^{17}O NMR Spectroscopy of Paramagnetic Coordination Compounds. *Angew. Chem. Intl. Ed.* **127**, 4835–4839.
- (97) Dawson, D. M.; Ke, Z.; Mack, F. M.; Doyle, R. A.; Bignami, G. P. M.; Smellie, I. A.; Bühl, M.; Ashbrook, S. E. Calculation and experimental measurement of paramagnetic NMR parameters of phenolic oximate Cu(II) complexes. *Chem. Commun.* **2017**, *53*, 10512–10515.
- (98) Mizushima, K.; Jones, P.; Wiseman, P.; Goodenough, J. Li_xCoO_2 ($0 < x < 1$): A new cathode material for batteries of high energy density. *Mater. Res. Bull.* **1980**, *15*, 783–789.
- (99) Reimers, J. N.; Dahn, J. R. Electrochemical and *In Situ* X-Ray Diffraction Studies of Lithium Intercalation in Li_xCoO_2 . *J. Electrochem. Soc.* **1992**, *139*, 2091–2097.
- (100) Padhi, A.; Nanjundaswamy, K.; Goodenough, J. Phospho-olivines as positive-electrode materials for rechargeable lithium batteries. *J. Electrochem. Soc.* **1997**, *144*, 1188–1194.
- (101) Amine, K.; Yasuda, H.; Yamachi, M. Olivine LiCoPO_4 as 4.8 V Electrode Material for Lithium Batteries. *Electrochem. Solid St.* **2000**, *3*, 178–179.
- (102) Okada, S.; Sawa, S.; Egashira, M.; Ichi Yamaki, J.; Tabuchi, M.; Kageyama, H.; Konishi, T.; Yoshino, A. Cathode properties of phospho-olivine LiMPO_4 for lithium secondary batteries. *J. Power Sources* **2001**, *97-98*, Proceedings of the 10th International Meeting on Lithium Batteries, 430–432.
- (103) Zhou, F.; Cococcioni, M.; Kang, K.; Ceder, G. The Li intercalation potential of LiMPO_4 and LiMSiO_4 olivines with $M = \text{Fe, Mn, Co, Ni}$. *Electrochem. Commun.* **2004**, *6*, 1144–1148.
- (104) Yang, J.; Xu, J. J. Synthesis and Characterization of Carbon-Coated Lithium Transition Metal Phosphates LiMPO_4 ($M = \text{Fe, Mn, Co, Ni}$) Prepared via a Nonaqueous Sol-Gel Route. *J. Electrochem. Soc.* **2006**, *153*, A716–A723.
- (105) Hung, I.; Zhou, L.; Pourpoint, F.; Grey, C. P.; Gan, Z. Isotropic High Field NMR Spectra of Li-Ion Battery Materials with Anisotropy > 1 MHz. *J. Amer. Chem. Soc.* **2012**, *134*, 1898–1901.
- (106) Muscat, J.; Wander, A.; Harrison, N. On the prediction of band gaps from hybrid functional theory. *Chem. Phys. Lett.* **2001**, *342*, 397–401.
- (107) Corà, F.; Alfredsson, M.; Mallia, G.; Middlemiss, D. S.; Mackrodt, W. C.; Dovesi, R.; Orlando, R. In *Principles and Applications of Density Functional Theory in Inorg. Chem. II*; Springer Berlin Heidelberg: Berlin, Heidelberg, 2004, pp 171–232.
- (108) Feng, X.; Harrison, N. M. Magnetic coupling constants from a hybrid density functional with 35% Hartree-Fock exchange. *Phys. Rev. B* **2004**, *70*, 092402.
- (109) Middlemiss, D. S.; Lawton, L. M.; Wilson, C. C. A solid-state hybrid density functional theory study of Prussian blue analogues and related chlorides at pressure. *J. Phys. Condens. Mat.* **2008**, *20*, 335231.

- (110) De P. R. Moreira, I.; Illas, F.; Martin, R. L. Effect of Fock exchange on the electronic structure and magnetic coupling in NiO. *Phys. Rev. B* **2002**, *65*, 155102.
- (111) Perras, F. A.; Venkatesh, A.; Hanrahan, M. P.; Goh, T. W.; Huang, W.; Rossini, A. J.; Pruski, M. Indirect detection of infinite-speed MAS solid-state NMR spectra. *J. Magn. Reson.* **2017**, *276*, 95–102.
- (112) Chen, Y.-C.; Chen, J.-M.; Hsu, C.-H.; Yeh, J.-W.; Shih, H. C.; Chang, Y.-S.; Sheu, H.-S. Structure studies on $\text{LiMn}_{0.25}\text{Fe}_{0.75}\text{PO}_4$ by in-situ synchrotron X-ray diffraction analysis. *J. Power Sources* **2009**, *189*, 790–793.
- (113) Hong, J.; Wang, F.; Wang, X.; Graetz, J. $\text{LiFe}_x\text{Mn}_{1-x}\text{PO}_4$: A cathode for lithium-ion batteries. *J. Power Sources* **2011**, *196*, 3659–3663.
- (114) Kim, J.; Park, K.-Y.; Park, I.; Yoo, J.-K.; Hong, J.; Kang, K. Thermal stability of Fe-Mn binary olivine cathodes for Li rechargeable batteries. *J. Mater. Chem.* **2012**, *22*, 11964–11970.
- (115) Yamada, A.; Chung, S.-C. Crystal Chemistry of the Olivine-Type $\text{Li}(\text{Mn}_y\text{Fe}_{1-y})\text{PO}_4$ and $(\text{Mn}_y\text{Fe}_{1-y})\text{PO}_4$ as Possible 4 V Cathode Materials for Lithium Batteries. *J. Electrochem. Soc.* **2001**, *148*, A960–A967.
- (116) Yao, J.; Bewlay, S.; Konstantinov, K.; Drozd, V.; Liu, R.; Wang, X.; Liu, H.; Wang, G. Characterisation of olivine-type $\text{LiMn}_x\text{Fe}_{1-x}\text{PO}_4$ cathode materials. *J. Alloy. Compd.* **2006**, *425*, 362–366.
- (117) Chernova, N. A.; Nolis, G. M.; Omenya, F. O.; Zhou, H.; Li, Z.; Whittingham, M. S. What can we learn about battery materials from their magnetic properties? *J. Mater. Chem.* **2011**, *21*, 9865–9875.
- (118) Tucker, M. C.; Doeff, M. M.; Richardson, T. J.; Fiñones, R.; Cairns, E. J.; Reimer, J. A. Hyperfine Fields at the Li Site in LiFePO_4 -Type Olivine Materials for Lithium Rechargeable Batteries: A ^7Li MAS NMR and SQUID Study. *J. Amer. Chem. Soc.* **2002**, *124*, 3832–3833.
- (119) Sananes, M.; Tuel, A.; Volta, J. A Study by ^{31}P NMR Spin-Echo Mapping of VPO Catalysts. *J. Catal.* **1994**, *145*, 251–255.
- (120) Schurko, R. W.; Wi, S.; Frydman, L. Dynamic Effects on the Powder Line Shapes of Half-Integer Quadrupolar Nuclei: A Solid-State NMR Study of XO_4^- Groups. *J. Phys. Chem. A* **2002**, *106*, 51–62.
- (121) Ash, J. T.; Grandinetti, P. J. Solid-state NMR characterization of ^{69}Ga and ^{71}Ga in crystalline solids. *Magn. Reson. Chem.* **2006**, *44*, 823–831.
- (122) Pell, A. J.; Clément, R. J.; Grey, C. P.; Emsley, L.; Pintacuda, G. Frequency-stepped acquisition in nuclear magnetic resonance spectroscopy under magic angle spinning. *J. Chem. Phys.* **2013**, *138*, 114201.
- (123) Schurko, R. W. Ultra-Wideline Solid-State NMR Spectroscopy. *Accounts Chem. Res.* **2013**, *46*, 1985–1995.

- (124) Larsen, F. H.; Jakobsen, H. J.; Ellis, P. D.; Nielsen, N. C. Sensitivity-Enhanced Quadrupolar-Echo NMR of Half-Integer Quadrupolar Nuclei. Magnitudes and Relative Orientation of Chemical Shielding and Quadrupolar Coupling Tensors. *J. Phys. Chem. A* **1997**, *101*, 8597–8606.
- (125) O-Dell, L. A.; Schurko, R. W. QCPMG using adiabatic pulses for faster acquisition of ultra-wideline NMR spectra. *Chem. Phys. Lett.* **2008**, *464*, 97–102.
- (126) O-Dell, L. A.; Rossini, A. J.; Schurko, R. W. Acquisition of ultra-wideline NMR spectra from quadrupolar nuclei by frequency stepped WURST-QCPMG. *Chem. Phys. Lett.* **2009**, *468*, 330–335.
- (127) Harris, K. J.; Lupulescu, A.; Lucier, B. E.; Frydman, L.; Schurko, R. W. Broadband adiabatic inversion pulses for cross polarization in wideline solid-state NMR spectroscopy. *J. Magn. Reson.* **2012**, *224*, 38–47.
- (128) Harris, K. J.; Veinberg, S. L.; Mireault, C. R.; Lupulescu, A.; Frydman, L.; Schurko, R. W. Rapid Acquisition of ^{14}N Solid-State NMR Spectra with Broadband Cross Polarization. *Chem. Eur. J.* **2013**, *19*, 16469–16475.
- (129) Shen, M.; Trébosc, J.; Lafon, O.; Gan, Z.; Pourpoint, F.; Hu, B.; Chen, Q.; Amoureux, J.-P. Solid-state NMR indirect detection of nuclei experiencing large anisotropic interactions using spinning sideband-selective pulses. *Solid State Nucl. Mag.* **2015**, *72*, Honor Issue for Jake Schaefer, 104–117.
- (130) Carnevale, D.; Vitzthum, V.; Lafon, O.; Trébosc, J.; Amoureux, J.-P.; Bodenhausen, G. Broadband excitation in solid-state NMR of paramagnetic samples using Delays Alternating with Nutation for Tailored Excitation (Para-DANTE). *Chem. Phys. Lett.* **2012**, *553*, 68–76.
- (131) Siegel, R.; Nakashima, T. T.; Wasylishen, R. E. Sensitivity enhancement of NMR spectra of half-integer spin quadrupolar nuclei in solids using hyperbolic secant pulses. *J. Magn. Reson.* **2007**, *184*, 85–100.
- (132) Nakashima, T. T.; Wasylishen, R. E.; Siegel, R.; Ooms, K. J. Sensitivity enhancement of solid-state NMR spectra of half-integer spin quadrupolar nuclei: Double- or single-frequency sweeps: Insights from the hyperbolic secant experiment. *Chem. Phys. Lett.* **2008**, *450*, 417–421.
- (133) Dey, K. K.; Prasad, S.; Ash, J. T.; Deschamps, M.; Grandinetti, P. J. Spectral editing in solid-state MAS NMR of quadrupolar nuclei using selective satellite inversion. *J. Magn. Reson.* **2007**, *185*, 326–330.
- (134) Wi, S.; Schurko, R.; Frydman, L. ^1H - ^2H cross-polarization NMR in fast spinning solids by adiabatic sweeps. *J. Chem. Phys.* **2017**, *146*, 104201.
- (135) Wi, S.; Kim, C.; Schurko, R.; Frydman, L. Adiabatic sweep cross-polarization magic-angle-spinning NMR of half-integer quadrupolar spins. *J. Magn. Reson.* **2017**, *277*, 131–142.

- (136) Kentgens, A.; Verhagen, R. Advantages of double frequency sweeps in static, MAS and MQMAS NMR of spin $I=3/2$ nuclei. *Chem. Phys. Lett.* **1999**, *300*, 435–443.
- (137) Schäfer, H.; Iuga, D.; Verhagen, R.; Kentgens, A. P. M. Population and coherence transfer in half-integer quadrupolar spin systems induced by simultaneous rapid passages of the satellite transitions: A static and spinning single crystal nuclear magnetic resonance study. *J. Chem. Phys.* **2001**, *114*, 3073–3091.
- (138) Edén, M.; Levitt, M. H. Computation of Orientational Averages in Solid-State NMR by Gaussian Spherical Quadrature. *J. Magn. Reson.* **1998**, *132*, 220–239.
- (139) Vitzthum, V.; Caporini, M. A.; Ulzega, S.; Bodenhausen, G. Broadband excitation and indirect detection of nitrogen-14 in rotating solids using Delays Alternating with Nutation (DANTE). *J. Magn. Reson.* **2011**, *212*, 234–239.
- (140) Copéret, C.; Comas-Vives, A.; Conley, M. P.; Estes, D. P.; Fedorov, A.; Mougél, V.; Nagae, H.; Núñez Zarur, F.; Zhizhko, P. A. Surface Organometallic and Coordination Chemistry toward Single-Site Heterogeneous Catalysts: Strategies, Methods, Structures, and Activities. *Chem. Rev.* **2016**, *116*, 323–421.
- (141) Monica, T.; P., T. S. γ -Alumina as a Support for Catalysts: A Review of Fundamental Aspects. *Eur. J. Inorg. Chem.* **2005**, 3393–3403.
- (142) Machado, G. S.; de Freitas Castro, K. A. D.; de Lima, O. J.; Nassar, E. J.; Ciuffi, K. J.; Nakagaki, S. Aluminosilicate obtained by sol-gel process as support for an anionic iron porphyrin: Development of a selective and reusable catalyst for oxidation reactions. *Colloid. Surface. A.* **2009**, *349*, 162–169.
- (143) Hogan, J. P.; Banks, R. L. Polymers and production thereof. Patent, US 2825721A, Mar. 1958.
- (144) Ziegler, K.; Holzkamp, E.; Breil, H.; Martin, H. Polymerisation von Äthylen und anderen Olefinen. *Angew. Chem. Ger. Edit.* **67**, 426–426.
- (145) Natta, G. Macromolecular Chemistry: From the Stereospecific Polymerization to the Asymmetric Autocatalytic Synthesis of Macromolecules. *Science* **1965**, *147*, 261–272.
- (146) Stürzel, M.; Mihan, S.; Mülhaupt, R. From Multisite Polymerization Catalysis to Sustainable Materials and All-Polyolefin Composites. *Chem. Rev.* **2016**, *116*, 1398–1433.
- (147) Grau, E.; Lesage, A.; Norsic, S.; Copéret, C.; Monteil, V.; Sautet, P. Tetrahydrofuran in $\text{TiCl}_4/\text{THF}/\text{MgCl}_2$: a Non-Innocent Ligand for Supported Ziegler-Natta Polymerization Catalysts. *ACS Catalysis* **2013**, *3*, 52–56.
- (148) Copéret, C.; Liao, W.-C.; Gordon, C. P.; Ong, T.-C. Active Sites in Supported Single-Site Catalysts: An NMR Perspective. *J. Amer. Chem. Soc.* **2017**, *139*, 10588–10596.
- (149) Berruyer, P.; Lelli, M.; Conley, M. P.; Silverio, D. L.; Widdifield, C. M.; Siddiqi, G.; Gajan, D.; Lesage, A.; Copéret, C.; Emsley, L. Three-Dimensional Structure Determination of Surface Sites. *J. Amer. Chem. Soc.* **2017**, *139*, 849–855.

- (150) Lesage, A.; Lelli, M.; Gajan, D.; Caporini, M. A.; Vitzthum, V.; Miéville, P.; Alauzun, J.; Roussey, A.; Thieuleux, C.; Mehdi, A.; Bodenhausen, G.; Copéret, C.; Emsley, L. Surface Enhanced NMR Spectroscopy by Dynamic Nuclear Polarization. *J. Amer. Chem. Soc.* **2010**, *132*, 15459–15461.
- (151) Rossini, A. J.; Zagdoun, A.; Lelli, M.; Lesage, A.; Copéret, C.; Emsley, L. Dynamic Nuclear Polarization Surface Enhanced NMR Spectroscopy. *Accounts Chem. Res.* **2013**, *46*, 1942–1951.
- (152) Brookhart, M.; Green, M. L. Carbon-hydrogen-transition metal bonds. *J. Organomet. Chem.* **1983**, *250*, 395–408.
- (153) Maurice, B.; H., G. M. L.; Luet-Lok, W. In *Prog. Inorg. Chem.* Wiley-Blackwell: 2007, pp 1–124.
- (154) Brookhart, M.; Green, M. L. H.; Parkin, G. Agostic interactions in transition metal compounds. *P. Natl. Acad. Sci. USA* **2007**, *104*, 6908–6914.
- (155) Coates, G. W. Precise Control of Polyolefin Stereochemistry Using Single-Site Metal Catalysts. *Chem. Rev.* **2000**, *100*, 1223–1252.
- (156) Grubbs, R. H.; Coates, G. W. α -Agostic Interactions and Olefin Insertion in Metallocene Polymerization Catalysts. *Accounts Chem. Res.* **1996**, *29*, 85–93.
- (157) Brintzinger, H. H.; Fischer, D.; Mülhaupt, R.; Rieger, B.; Waymouth, R. M. Stereospecific Olefin Polymerization with Chiral Metallocene Catalysts. *Angew. Chem. Int. Edit.* **1995**, *34*, 1143–1170.
- (158) Ittel, S. D.; Johnson, L. K.; Brookhart, M. Late-Metal Catalysts for Ethylene Homo- and Copolymerization. *Chem. Rev.* **2000**, *100*, 1169–1204.
- (159) Dawoodi, Z.; Green, M. L. H.; Mtetwa, V. S. B.; Prout, K. Evidence for a direct bonding interaction between titanium and a [small beta]-C-H moiety in a titanium-ethyl compound; X-ray crystal structure of $[\text{Ti}(\text{Me}_2\text{PCH}_2\text{CH}_2\text{PMe}_2)\text{EtCl}_3]$. *J. Chem. Soc., Chem. Commun.* **1982**, 802–803.
- (160) Dawoodi, Z.; Green, M. L. H.; Mtetwa, V. S. B.; Prout, K.; Schultz, A. J.; Williams, J. M.; Koetzle, T. F. Evidence for carbon-hydrogen-titanium interactions: synthesis and crystal structures of the agostic alkyls $[\text{TiCl}_3(\text{Me}_2\text{PCH}_2\text{CH}_2\text{PMe}_2)\text{R}](\text{R} = \text{Et or Me})$. *J. Chem. Soc., Dalton Trans.* **1986**, 1629–1637.
- (161) Allouche, K.; Sanders, K. J.; Klöse, D.; Ashuiev, A.; Conley, M. P.; Lapadula, G.; Walter, M.; Copéret, C.; Jeschke, G.; Maron, L.; Pintacuda, G.; Andersen, R. A. Defying the Lewis structure of $\text{Yb}(\text{CH}(\text{SiMe}_3)_2)_3$ from 2D solid state EPR and NMR spectroscopies combined with CASSCF calculations. *Manuscript in preparation* **2018**.
- (162) Scherer, W.; McGrady, G. S. Agostic Interactions in d^0 Metal Alkyl Complexes. *Angew. Chem. Int. Edit.* *43*, 1782–1806.

- (163) Koga, N.; Morokuma, K. SiC Agostic Interaction with Ti: Origin of Alkenyl Group Distortion in $\text{Ti}[\text{C}(\text{SiH}_2\text{CH}_3)=\text{CH}_2]\text{X}_2^+$. An ab initio MO Study. *J. Amer. Chem. Soc.* **1988**, *110*, 108–112.
- (164) Giesbrecht, G. R.; Gordon, J. C.; Clark, D. L.; Scott, B. L. Auto-ionization in Lutetium Iodide Complexes: Effect of the Ionic Radius on Lanthanide–Iodide Binding. *Inorg. Chem.* **2004**, *43*, 1065–1070.
- (165) Konkol, M.; Spaniol, T. P.; Kondracka, M.; Okuda, J. Lutetium alkyl and hydride complexes in a non-cyclopentadienyl coordination environment. *Dalton Trans.* **2007**, 4095–4102.
- (166) Tilley, T. D.; Andersen, R. A.; Zalkin, A. Tertiary phosphine complexes of the f-block metals. Crystal structure of $\text{Yb}[\text{N}(\text{SiMe}_3)_2]_2[\text{Me}_2\text{PCH}_2\text{CH}_2\text{PMe}_2]$: evidence for a ytterbium- γ -carbon interaction. *J. Amer. Chem. Soc.* **1982**, *104*, 3725–3727.
- (167) Rozenel, S. S.; Andersen, R. A. A new X-ray crystal structure (100K) of $\text{Yb}[\text{N}(\text{SiMe}_3)_2]_2[\text{Me}_2\text{PCH}_2\text{CH}_2\text{PMe}_2]$. *Inorg. Chim. Acta* **2014**, *422*, Special issue: Dedicated to Don Tilley, 202–205.
- (168) Pintacuda, G.; John, M.; Su, X.-C.; Otting, G. NMR Structure Determination of Protein-Ligand Complexes by Lanthanide Labeling. *Accounts Chem. Res.* **2007**, *40*, 206–212.
- (169) Gowda, V. Experimental and computational magnetic resonance studies of selected rare earth and bismuth complexes., Ph.D. Thesis, Luleå University of Technology, Oct. 2017.
- (170) Bertini, I.; Janik, M. B. L.; Lee, Y.-M.; Luchinat, C.; Rosato, A. Magnetic Susceptibility Tensor Anisotropies for a Lanthanide Ion Series in a Fixed Protein Matrix. *J. Amer. Chem. Soc.* **2001**, *123*, 4181–4188.
- (171) Fregonese, D.; Glisenti, A.; Mortara, S.; Rizzi, G. A.; Tondello, E.; Bresadola, S. $\text{MgCl}_2/\text{TiCl}_4/\text{AlEt}_3$ catalytic system for olefin polymerisation: a XPS study. *J. Mol. Catal. A. Chem.* **2002**, *178*, 115–123.
- (172) Groppo, E.; Seenivasan, K.; Barzan, C. The potential of spectroscopic methods applied to heterogeneous catalysts for olefin polymerization. *Catal. Sci. Technol.* **2013**, *3*, 858–878.
- (173) Elena, M.; Elio, G.; Sabine, V.; Giuseppe, A.; Maddalena, D.; Vincenzo, B.; Mario, C. Probing the Coordinative Unsaturation and Local Environment of Ti^{3+} -Sites in an Activated High-Yield Ziegler-Natta Catalyst. *Angew. Chem. Int. Edit.* *54*, 4857–4860.
- (174) Tijssen, K. C.; Blaakmeer, E. M.; Kentgens, A. P. Solid-state NMR studies of Ziegler-Natta and metallocene catalysts. *Solid State Nucl. Mag.* **2015**, *68-69*, 37–56.
- (175) Blaakmeer, E. M.; Franssen, W. M.; Kentgens, A. P. Quadrupolar nutation NMR to discriminate central and satellite transitions: Spectral assignments for a Ziegler-Natta catalyst. *J. Magn. Reson.* **2017**, *281*, 199–208.

- (176) Blaakmeer, E. S. M.; Antinucci, G.; Correa, A.; Busico, V.; van Eck, E. R. H.; Kentgens, A. P. M. Structural Characterization of Electron Donors in Ziegler-Natta Catalysts. *J. Phys. Chem. C* **2018**, *122*, 5525–5536.
- (177) Blaakmeer, E. S. M.; van Eck, E. R. H.; Kentgens, A. P. M. The coordinative state of aluminium alkyls in Ziegler-Natta catalysts. *Phys. Chem. Chem. Phys.* **2018**, *20*, 7974–7988.
- (178) Seth, M.; Ziegler, T. Theoretical Study of the Copolymerization of Ethylene and Propylene by a Heterogeneous Ziegler-Natta Catalyst. *Macromolecules* **2004**, *37*, 9191–9200.
- (179) Cavallo, L.; Guerra, G.; Corradini, P. Mechanisms of Propagation and Termination Reactions in Classical Heterogeneous Ziegler-Natta Catalytic Systems: A Nonlocal Density Functional Study. *J. Amer. Chem. Soc.* **1998**, *120*, 2428–2436.
- (180) Vanka, K.; Singh, G.; Iyer, D.; Gupta, V. K. DFT Study of Lewis Base Interactions with the MgCl₂ Surface in the Ziegler-Natta Catalytic System: Expanding the Role of the Donors. *J. Phys. Chem. C* **2010**, *114*, 15771–15781.
- (181) Boero, M.; Parrinello, M.; Terakura, K. First Principles Molecular Dynamics Study of Ziegler-Natta Heterogeneous Catalysis. *J. Amer. Chem. Soc.* **1998**, *120*, 2746–2752.
- (182) Kuklin, M. S.; Bazhenov, A. S.; Denifl, P.; Leinonen, T.; Linnolahti, M.; Pakkanen, T. A. Stabilization of magnesium dichloride surface defects by mono- and bidentate donors. *Surf. Sci.* **2015**, *635*, 5–10.
- (183) Breuza, E.; Antinucci, G.; Budzelaar, P. H. M.; Busico, V.; Correa, A.; Ehm, C. MgCl₂-Supported Ziegler-Natta Catalysts: a DFT-D "Flexible-Cluster" Approach to Internal Donor Adducts. *J. Phys. Chem. C* **2018**, *122*, 9046–9053.
- (184) Eaton, D. R.; Josey, A. D.; Phillips, W. D.; Benson, R. E. Spin-Density Distributions in Conjugated Ligands of Paramagnetic Chelates from NMR Contact Interaction Shifts. *J. Chem. Phys.* **1962**, *37*, 347–360.
- (185) Lavallo, V.; El-Batta, A.; Bertrand, G.; Grubbs, R. H. Insights Into the Carbene-Initiated Aggregation of [Fe(cot)₂]. *Angew. Chem. Int. Edit.* **2011**, *50*, 268–271.
- (186) Zadrozny, J. M.; Xiao, D. J.; Atanasov, M.; Long, G. J.; Granjean, F.; Neese, F.; R., L. J. Magnetic blocking in a linear iron(I) complex. *Nat. Chem.* **2013**, *5*, 577–581.
- (187) Danopoulos, A. A.; Braunstein, P.; Monakhov, K. Y.; van Leusen, J.; Kögerler, P.; Clémancey, M.; Latour, J.-M.; Benayad, A.; Tromp, M.; Rezabal, E.; Frison, G. Heteroleptic, two-coordinate [M(NHC)N(SiMe₃)₂] (M = Co, Fe) complexes: synthesis, reactivity and magnetism rationalized by an unexpected metal oxidation state. *Dalton Trans.* **2017**, *46*, 1163–1171.
- (188) Hoyt, J. M.; Schmidt, V. A.; Tondreau, A. M.; Chirik, P. J. Iron-catalyzed intermolecular [2+2] cycloadditions of unactivated alkenes. *Science* **2015**, *349*, 960–963.
- (189) Anderson, J. S.; Rittle, J.; Peters, J. C. Catalytic conversion of nitrogen to ammonia by an iron model complex. *Nature* **2013**, *501*, 84–87.

- (190) Fürstner, A.; Majima, K.; Martín, R.; Krause, H.; Kattnig, E.; Goddard, R.; Lehmann, C. W. A Cheap Metal for a Noble Task: Preparative and Mechanistic Aspects of Cycloisomerization and Cycloaddition Reactions Catalyzed by Low-Valent Iron Complexes. *J. Amer. Chem. Soc.* **2008**, *130*, 1992–2004.
- (191) Bart, S. C.; Lobkovsky, E.; Chirik, P. J. Preparation and Molecular and Electronic Structures of Iron(0) Dinitrogen and Silane Complexes and Their Application to Catalytic Hydrogenation and Hydrosilation. *J. Amer. Chem. Soc.* **2004**, *126*, 13794–13807.
- (192) McNeill, E.; Ritter, T. 1,4-Functionalization of 1,3-Dienes With Low-Valent Iron Catalysts. *Accounts Chem. Res.* **2015**, *48*, 2330–2343.
- (193) Khusnutdinova, J. R.; Milstein, D. Metal-Ligand Cooperation. *Angew. Chem. Int. Edit.* **54**, 12236–12273.
- (194) Rathke, J. W.; Muetterties, E. L. Phosphine chemistry of iron(0) and -(II). *J. Amer. Chem. Soc.* **1975**, *97*, 3272–3273.
- (195) Tolman, C. A.; Ittel, S. D.; English, A. D.; Jesson, J. P. The chemistry of 2-naphthyl bis[bis(dimethylphosphino)ethane] hydride complexes of iron, ruthenium, and osmium. 1. Characterization and reactions with hydrogen and Lewis base ligands. *J. Amer. Chem. Soc.* **1978**, *100*, 4080–4089.
- (196) Baker, M. V.; Field, L. D. Reaction of sp^2 C-H Bonds in Unactivated Alkenes with Bis(diphosphine) Complexes of Iron. *J. Amer. Chem. Soc.* **1986**, *108*, 7433–7434.
- (197) Gilbert-Wilson, R.; Field, L. D.; Colbran, S. B.; Bhadbhade, M. M. Low Oxidation State Iron(0), Iron(I), and Ruthenium(0) Dinitrogen Complexes with a Very Bulky Neutral Phosphine Ligand. *Inorg. Chem.* **2013**, *52*, 3043–3053.
- (198) Bleeke, J. R.; Wittenbrink, R. J. Pentadienyl-metal-phosphine chemistry: XXI. Synthesis and characterization of electron-rich (pentadienyl)iron[1,2-bis(diethylphosphino)ethane] complexes. *J. Organomet. Chem.* **1991**, *405*, 121–132.
- (199) Bart, S. C.; Hawrelak, E. J.; Lobkovsky, E.; Chirik, P. J. Low-Valent α -Diimine Iron Complexes for Catalytic Olefin Hydrogenation. *Organometallics* **2005**, *24*, 5518–5527.
- (200) Zhang, H.; Ouyang, Z.; Liu, Y.; Zhang, Q.; Wang, L.; Deng, L. (Aminocarbene) (Divinyltetramethyldisiloxane)Iron(0) Compounds: A Class of Low-Coordinate Iron(0) Reagents. *Angew. Chem. Int. Edit.* **2014**, *53*, 8432–8436.
- (201) Casitas, A.; Krause, H.; Goddard, R.; Fürstner, A. Elementary Steps of Iron Catalysis: Exploring the Links between Iron Alkyl and Iron Olefin Complexes for their Relevance in C-H Activation and C-C Bond Formation. *Angew. Chem. Int. Edit.* **2015**, *54*, 1521–1526.
- (202) Casitas, A.; Krause, H.; Lutz, S.; Goddard, R.; Bill, E.; Fürstner, A. Ligand Exchange on and Allylic C-H Activation by Iron(0) Fragments: π -Complexes, Allyliron Species, and Metallacycles. *Organometallics* **2018**, *37*, 729–739.

- (203) Bühl, M.; Kabrede, H. Geometries of Transition-Metal Complexes from Density-Functional Theory. *J. Chem. Theory Comput.* **2006**, *2*, 1282–1290.
- (204) Minenkov, Y.; Singstad, A.; Occhipinti, G.; Jensen, V. R. The accuracy of DFT-optimized geometries of functional transition metal compounds: a validation study of catalysts for olefin metathesis and other reactions in the homogeneous phase. *Dalton Trans.* **2012**, *41*, 5526–5541.
- (205) Remenyi, C.; Reviakine, R.; Kaupp, M. Density Functional Study of Electron Paramagnetic Resonance Parameters and Spin Density Distributions of Dicopper(I) Complexes with Bridging Azo and Tetrazine Radical-Anion Ligands. *J. Phys. Chem. A* **2006**, *110*, 4021–4033.
- (206) Remenyi, C.; Reviakine, R.; Kaupp, M. Density Functional Study of EPR Parameters and Spin-Density Distribution of Azurin and Other Blue Copper Proteins. *J. Phys. Chem. B* **2007**, *111*, 8290–8304.
- (207) Fritscher, J.; Hrobárik, P.; Kaupp, M. Computational Studies of Electron Paramagnetic Resonance Parameters for Paramagnetic Molybdenum Complexes. 1. Method Validation on Small and Medium-Sized Systems. *J. Phys. Chem. B* **2007**, *111*, 4616–4629.
- (208) Heise, H.; Köhler, F. H.; Xie, X. Solid-State NMR Spectroscopy of Paramagnetic Metallocenes. *J. Magn. Reson.* **2001**, *150*, 198–206.
- (209) Pennanen, T. O.; Vaara, J. Nuclear Magnetic Resonance Chemical Shift in an Arbitrary Electronic Spin State. *Phys. Rev. Lett.* **2008**, *100*, 133002.
- (210) Paulson, E. K.; Morcombe, C. R.; Gaponenko, V.; Dancheck, B.; Byrd, R. A.; Zilm, K. W. Sensitive High Resolution Inverse Detection NMR Spectroscopy of Proteins in the Solid State. *J. Amer. Chem. Soc.* **2003**, *125*, 15831–15836.
- (211) Chevelkov, V.; Rehbein, K.; Diehl, A.; Reif, B. Ultrahigh Resolution in Proton Solid-State NMR Spectroscopy at High Levels of Deuteration. *Angew. Chem. Int. Ed.* **45**, 3878–3881.
- (212) Knight, M. J.; Webber, A. L.; Pell, A. J.; Guerry, P.; Barbet-Massin, E.; Bertini, I.; Felli, I. C.; Gonnelli, L.; Pierattelli, R.; Emsley, L.; Lesage, A.; Herrmann, T.; Pintacuda, G. Fast Resonance Assignment and Fold Determination of Human Superoxide Dismutase by High-Resolution Proton-Detected Solid-State MAS NMR Spectroscopy. *Angew. Chem. Int. Ed.* **50**, 11697–11701.
- (213) Andreas, L. B.; Marchand, T. L.; Jaudzems, K.; Pintacuda, G. High-resolution proton-detected NMR of proteins at very fast MAS. *J. Magn. Reson.* **2015**, *253*, Special Issue: Recent Achievements and New Directions in Biomolecular Solid State NMR, 36–49.
- (214) Schubeis, T.; Marchand, T. L.; Andreas, L. B.; Pintacuda, G. ¹H magic-angle spinning NMR evolves as a powerful new tool for membrane proteins. *J. Magn. Reson.* **2018**, *287*, 140–152.

- (215) Vasa, S. K.; Rovó, P.; Linser, R. Protons as Versatile Reporters in Solid-State NMR Spectroscopy. *Accounts Chem. Res.* **2018**, *51*, 1386–1395.
- (216) Gan, Z. Isotropic NMR Spectra of Half-Integer Quadrupolar Nuclei Using Satellite Transitions and Magic-Angle Spinning. *J. Amer. Chem. Soc.* **2000**, *122*, 3242–3243.
- (217) Gan, Z. Satellite transition magic-angle spinning nuclear magnetic resonance spectroscopy of half-integer quadrupolar nuclei. *J. Chem. Phys.* **2001**, *114*, 10845–10853.
- (218) Harris, R. K.; Becker, E. D.; Menezes, S. M.C. D.; Granger, P.; Hoffman, R. E.; Zilm, K. W. Further conventions for NMR shielding and chemical shifts IUPAC recommendations 2008. *Solid State Nucl. Mag.* **2008**, *33*, 41–56.
- (219) Bak, M.; Rasmussen, J. T.; Nielsen, N. C. SIMPSON: A General Simulation Program for Solid-State NMR Spectroscopy. *J. Magn. Reson.* **2000**, *147*, 296–330.
- (220) Bodenhausen, G.; Freeman, R.; Turner, D. L. Suppression of artifacts in two-dimensional J spectroscopy. *J. Magn. Reson.* **1977**, *27*, 511–514.
- (221) Jakobsen, H. J.; Hove, A. R.; Hazell, R. G.; Bildsøe, H.; Skibsted, J. Solid-state ^{14}N MAS NMR of ammonium ions as a spy to structural insights for ammonium salts. *Magnetic Resonance in Chemistry*, *44*, 348–356.
- (222) Zaremba, S. K. Good lattice points, discrepancy, and numerical integration. *Ann. Math. Pura Appl., Ser. 4* **1966**, *73*, 293–317.
- (223) Conroy, H. Molecular Schrödinger Equation. VIII. A New Method for the Evaluation of Multidimensional Integrals. *J. Chem. Phys.* **1967**, *47*, 5307–5318.
- (224) Cheng, V. B.; Suzukawa, H. H.; Wolfsberg, M. Investigations of a nonrandom numerical method for multidimensional integration. *J. Chem. Phys.* **1973**, *59*, 3992–3999.
- (225) Perdew, J. P.; Burke, K.; Ernzerhof, M. Generalized Gradient Approximation Made Simple. *Phys. Rev. Lett.* **1996**, *77*, 3865–3868.
- (226) Adamo, C.; Barone, V. Toward reliable density functional methods without adjustable parameters: The PBE0 model. *J. Chem. Phys.* **1999**, *110*, 6158–6170.
- (227) Grimme, S.; Antony, J.; Ehrlich, S.; Krieg, H. A consistent and accurate ab initio parametrization of density functional dispersion correction (DFT-D) for the 94 elements H-Pu. *J. Chem. Phys.* **2010**, *132*, 154104.
- (228) Weigend, F.; Ahlrichs, R. Balanced basis sets of split valence, triple zeta valence and quadruple zeta valence quality for H to Rn: Design and assessment of accuracy. *Phys. Chem. Chem. Phys.* **2005**, *7*, 3297–3305.
- (229) TURBOMOLE V6.2 2010, a development of University of Karlsruhe and Forschungszentrum Karlsruhe GmbH, 1989-2007, TURBOMOLE GmbH, since 2007; available from <http://www.turbomole.com>.
- (230) Neese, F. The ORCA program system. *WIREs Comput. Mol. Sci.* **2012**, *2*, 73–78.

- (231) Heß, B. A.; Marian, C. M.; Wahlgren, U.; Gropen, O. A mean-field spin-orbit method applicable to correlated wavefunctions. *Chem. Phys. Lett.* **1996**, *251*, 365–371.
- (232) Neese, F. Efficient and accurate approximations to the molecular spin-orbit coupling operator and their use in molecular g-tensor calculations. *J. Chem. Phys.* **2005**, *122*, 034107.
- (233) Rappoport, D.; Furche, F. Property-optimized Gaussian basis sets for molecular response calculations. *J. Chem. Phys.* **2010**, *133*, 134105.
- (234) Schmitt, S.; Jost, P.; van Wüllen, C. Zero-field splittings from density functional calculations: Analysis and improvement of known methods. *J. Chem. Phys.* **2011**, *134*, 194113.
- (235) Wolinski, K.; Hinton, J. F.; Pulay, P. Efficient implementation of the gauge-independent atomic orbital method for NMR chemical shift calculations. *J. Amer. Chem. Soc.* **1990**, *112*, 8251–8260.
- (236) Frisch, M. J. et al. Gaussian 09., Gaussian Inc. Wallingford CT, 2009.
- (237) Roos, B. O.; Taylor, P. R.; Siegbahn, P. E. A complete active space SCF method (CASSCF) using a density matrix formulated super-CI approach. *Chem. Phys.* **1980**, *48*, 157–173.
- (238) Malmqvist, P.-A.; Roos, B. O. The CASSCF state interaction method. *Chem. Phys. Lett.* **1989**, *155*, 189–194.
- (239) Angeli, C.; Cimiraglia, R.; Evangelisti, S.; Leininger, T.; Malrieu, J.-P. Introduction of *n*-electron valence states for multireference perturbation theory. *J. Chem. Phys.* **2001**, *114*, 10252–10264.
- (240) Angeli, C.; Cimiraglia, R.; Malrieu, J.-P. *n*-electron valence state perturbation theory: A spinless formulation and an efficient implementation of the strongly contracted and of the partially contracted variants. *J. Chem. Phys.* **2002**, *117*, 9138–9153.
- (241) Ganyushin, D.; Neese, F. First-principles calculations of zero-field splitting parameters. *J. Chem. Phys.* **2006**, *125*, 024103.
- (242) Neese, F. Configuration Interaction Calculation of Electronic g Tensors in Transition Metal Complexes. *Int. J. Quantum Chem.* **2001**, *83*, 104–114.